The University Of Sheffield.

Access To Thesis.

- A bound copy of every thesis which is accepted as worthy for a higher degree, must be deposited in the University of Sheffield Library, where it will be made available for borrowing or consultation in accordance with University Regulations.
- All students registering from 2008–09 onwards are also required to submit an electronic copy of their final, approved thesis. Students who registered prior to 2008–09 may also submit electronically, but this is not required.

Author: Wameath Sh. Abdul-Majeed Dept: Chemical and Biological Engineering

Thesis Title: Development of online, continuous heavy metals detection and monitoring sensors based on microfluidic plasma reactors Registration No: 080241665

For completion by all students:

Submit in print form only (for deposit in the University Library): ☐

Submit in print form and also upload to the *White Rose eTheses Online* server: In full ☑

Edited eThesis ☐

Please indicate if there are any embargo restrictions on this thesis. Please note that if no boxes are ticked, you will have consented to your thesis being made available without any restrictions.

Embargo details: (complete only if requesting an embargo to either your print and/or eThesis)	Embargo required?		Length of embargo (in years)
Print Thesis	Yes ☑	No ☐	5
eThesis	Yes ☑	No ☐	5

Supervisor: I, the supervisor, agree to the named thesis being made available under the conditions specified above.

Name: William BJ Zimmerman Dept: Chemical and Biological Department

Signed: WBZ Date: 25-10-12

Student: I, the author, agree to the named thesis being made available under the conditions specified above.

I give permission to the University of Sheffield to reproduce the print thesis in whole or in part in order to supply single copies for the purpose of research or private study for a non-commercial purpose.

I confirm that this thesis is my own work, and where materials owned by a third party have been used copyright clearance has been obtained. I am aware of the University's *Guidance on the Use of Unfair Means* (www.sheffield.ac.uk/lets/design/unfair)

I confirm that all copies of the thesis submitted to the University (including electronic copies on CD/DVD) are identical in content.

Name: Wameath Sh. Abdul-Majeed Dept: Chemical and Biological Engineering

Signed: W.S.Sal Date: 25-10-2012

For completion by students also submitting an electronic thesis (eThesis):

I, the author, agree that the University of Sheffield's eThesis repository (currently WREO) will make my eThesis available over the internet via an entirely non-exclusive agreement and that, without changing content, WREO may convert my thesis to any medium or format for the purpose of future preservation and accessibility.

I, the author, agree that the metadata relating to the eThesis will normally appear on both the University's eThesis server and the British Library's EThOS service, even if the thesis is subject to an embargo. I agree that a copy of the eThesis may be supplied to the British Library.

I confirm that the upload is identical to the final, examined and awarded version of the thesis as submitted in print to the University for deposit in the Library (unless edited as indicated above).

Name: Wameath Sh. Abdul-Majeed Dept: Chemical and Biological Engineering

Signed: W.S.Sal Date: 25-10-2012

THIS SHEET MUST BE BOUND IN THE FRONT OF THE PRINTED THESIS BEFORE IT IS SUBMITTED

Development of Online, Continuous Heavy Metals Detection and Monitoring Sensors Based on Microfluidic Plasma Reactors

A Thesis

Submitted to the University of Sheffield for the degree of Doctor of Philosophy in the Faculty of Engineering

By

Wameath Sh. Abdul-Majeed

THE UNIVERSITY OF SHEFFIELD

Department of Chemical and Biological Engineering

July 2012

Acknowledgments

First and foremost I express my sincere thanks and gratitude to my research supervisor “Professor William BJ Zimmerman” for his kind support, advice, patience and encouragement throughout the research work and thesis writing. Without him, this thesis and the related published articles would not have been completed.

My sincere thanks and gratitude should be expressed to my sponsor “The Iraqi government / Ministry of higher education and scientific research- IMOHE” for giving me this valuable opportunity, and to their representative “The Iraqi cultural attaché – London” for managing our needs in the UK.

My thanks should also be conveyed to all my colleagues in the microfluidics group for their kind assistance and helpful discussion especially to those who worked in the microplasma team.

Sincere thanks and gratitude should be conveyed to CHELSI INSTITUTE members who supported my work on the biological side and to KROTO INSTITUTE members for their kind assistance in the analysis validation.

I am thankful to the technical staff of the departmental workshop that made a lot of effort to construct the custom designed equipment for the research requirements. I should also thank the technical staff of laboratories and the staff of the departmental and finance offices for their kind assistance.

I cannot end without thanking *my family*, who supported me with constant encouragement, patience, and love throughout the doctoral study period and whole my life. *It is to them that I dedicate this work.*

Summary

This research is dedicated to develop a fully integrated system for heavy metals determination in water samples based on micro fluidic plasma atomizers. Several configurations of dielectric barrier discharge (DBD) atomizer are designed, fabricated and tested toward this target. Finally, a combination of annular and rectangular DBD atomizers has been utilized to develop a scheme for heavy metals determination. The present thesis has combined both theoretical and experimental investigations to fulfil the requirements. Several mathematical studies are implemented to explore the optimal design parameters for best system performance. On the other hand, expanded experimental explorations are conducted to assess the proposed operational approaches. The experiments were designed according to a central composite rotatable design; hence, an empirical model has been produced for each studied case. Moreover, several statistical approaches are adopted to analyse the system performance and to deduce the optimal operational parameters. The introduction of the examined analyte to the plasma atomizer has been achieved by applying chemical schemes, where the element in the sample has been derivitized by using different kinds of reducing agents to produce vapour species (e.g. hydrides) for a group of nine elements examined in this research individually and simultaneously. Moreover, other derivatization schemes based on photochemical vapour generation assisted by ultrasound irradiation are also investigated. Generally speaking, the detection limits achieved in this research for the examined set of elements (by applying hydroborate scheme) are found to be acceptable in accordance with the standard limits in drinking water. The results of copper compared with the data from other technologies in the literature, showed a competitive detection limit obtained from applying the developed scheme, with an advantage of conducting simultaneous, fully automated, insitu, online- real time analysis as well as a possibility of connecting the proposed device to control loops.

Foreword

Most of heavy metals are very dangerous to humans since they can cause significant effects on the human body functions, leading to death in severe cases.

Historically, well known catastrophic accidents occurred due to contamination by heavy metal compounds (e.g. methyl mercury) such as those happened in Japan 1956 and Iraq 1971. The detection and determination of heavy metals is extensively researched for solid and liquid samples of different contamination levels. Nonetheless, the analysis in these researches was conducted inside laboratories by using bulky equipments, which requires pre-concentration procedures and expensive labour skills.

This research is an attempt to design, fabricate and test a miniaturized integrated system based on dielectric barrier discharge plasma atomizers that can be utilized for online – real time determination of heavy metals in different samples of water.

The present work has been described in nine chapters, summarized as follows:

- Chapter one is a general introduction which summarizes the consequences of heavy metals on humans' health, the detailed objectives of the current research and the research hypothesis.
- In Chapter two, the conventional methods used for heavy metal determination are summarized. Reviews on the applications of DBD plasma and the chemical derivatization methods in the field of heavy metals determination are presented. Furthermore, the fundamental principles behind the proposed technology are discussed in detail.
- In chapter three, the proposed technology is mathematically investigated; and several computational models are utilized with the aim of exploring the optimal design parameters required for the best system performance.
- The first experimental investigations in this research are described in chapter four, which explore the performance of the core unit in the proposed technology, the dielectric barrier discharge (DBD) atomizer. An experimental plan and statistical analysis are presented to deduce the optimal operational and spectroscopic parameters for stable system performance. Plasma characteristics were assessed by using spectrometric analysis.

- In chapter five, the application of the proposed technology for mercury determination is described. Samples containing inorganic mercury were examined using two derivatization schemes. The mercury has been determined qualitatively and quantitatively, achieving reasonable accuracy.
- Other heavy metals include hydride forming elements and transition elements are examined individually and simultaneously by applying the hydride generation scheme, as described in chapter six.
- Another developed scheme promoted by the effect of physical factors is presented in chapter seven, in which a pre-treatment stage has been included in the proposed technique.
- In chapter eight, the design of a full version of the integrated system is presented based on the outcomes of early investigations in chapters 3 to 7.
- Chapter nine presents conclusions from the current research and recommendations for future work.

Table of Contents

List of Figures

List of Tables

1. INTRODUCTION

1.1 Preface

Industrial waste water has been considered to be the most dangerous contaminant source of natural surface water. This is attributed to huge quantities of wastewater disposed into water bodies without any treatment or with poor treatment. The heavy metal content in this water is the most important reason for contamination. Such metals can be ingested by the aquatic animals, plants as well as crops on the land, and enters the human body through the food chain *(Ying and Fang, 2006)*. Heavy metals are difficult to biodegrade and normally accumulate in some organs, causing many serious problems to the human body such as the catastrophic effect on the nervous system, brain, and the normal metabolic functions, even when present in small amounts. They also affect the biological structures of some organs leading to deformity or death *(Manahan, 2005)*. The level of toxicity depends on three important parameters: the type of metal, it's biological role, and the type of organisms that is exposed to it *(OhioState-website)*. Therefore, determination of these metals with high accuracy becomes a challenging aim for researchers and legislation authorities.

Heavy metals are most likely present in the wastewater disposal in a soluble form such as ions or unionized organometallic chelates or complexes. They also exist in colloidal, particulate and dissolved phases. Versatility of heavy metal forms leads to difficulties in analysis when adopting a general technique or method. For instance, chromium might be present in two different oxidation states, Cr (III) and Cr (VI), whilst the mercury is possibly present in both inorganic and organic (e.g. methyl mercury) forms. Other metals such as lead could be exist in a non-volatile ionic species or a volatile tetra alkyl lead *(Mach et al., 1996)*.

For the sake of controlling wastewater disposal, an online sample analysis is required to detect most of the heavy metals in their different forms with high accuracy (qualitatively and quantitatively). This kind of highly accurate analysis can be achieved by coupling two powerful techniques, the first technique achieves the separation of the various forms of the element of interest, whilst the second technique conducts the determination of the metal to low detection limits. For instance, the coupling of a high performance liquid chromatography (HPLC) technique with inductively coupled plasma-mass spectrometry has been widely used for mercury elemental speciation *(Zoorob et al., 1998)*.

Although the research centres are keen to develop new equipment in this field, a fully integrated system that can detects most of the toxic heavy metals in their multiple forms is still required. The integration of the whole system provides the advantage of analyzing an online water sample, which eventually leads to better control of the discharges. Thus, it becomes useful to conceive a system that can achieve highly accurate analysis in a small size and with low operational cost. Hence, the current research aims to design and fabricate an integrated system that can be utilized as a sensor for heavy metals determination in different samples of water.

1.2 Heavy metals: definition, sources, standard limits and their consequences on humans health

The term "heavy metals" covers an extremely disparate group of elements, and even more disparate group of compounds of these elements; hence, their biological and toxicological properties are not similar *(Duffus, 2002)*. They include essential elements (e.g. iron) as well as toxic metals such as cadmium and mercury *(Manahan, 2005)*. In general, over 50 of the elements in the periodic table have been classified to be heavy metals but only a quarter of them are considered to be toxic *(OhioState-website)*. Historically, heavy metals are defined in the literature according to the following categories *(Cornelis et al., 2003)*:

- Definitions in terms of the physical and chemical properties such as:
  A metal having a density of 5.0 gm/cm^3 or over; a metal of atomic weight greater than sodium (23); any element with an atomic number greater than 20; metallic elements of high molecular weight.
- Definitions without a clear basis other than the toxicity effects such as:
  Elements commonly used in the industry and generically toxic to animals and to aerobic and anaerobic processes, includes Hg, Cd, As, Sn, Cr, Cu, Pb, Ni, Se, and Zn.

Practically, it is sensible to adopt the toxicity definition for the purpose of this study due to the well known effect of these metals on human life.

Most of heavy metals are toxic in their chemically combined forms; nonetheless, some of them are toxic in their elemental form (such as mercury). The identified reasons for

the toxicity are attributed to a great affinity to combine with several groups, such as the sulphur groups in enzymes in addition to the protein carboxylic acid and amino groups, which consequently leads to disrupting the enzyme and protein functions. Moreover, some of them (e.g. cadmium) bind to the cell membranes and eventually affect the transport processes through the cell wall *(Manahan, 2005)*. In addition to disposal from the industrial wastewater and the sewage treatment plants, other possible sources of heavy metals include pesticide run off from agriculture lands, releases from igneous and metamorphic rocks, decomposition of plant and the animal detritus, and acidic rain. **Table (1-1)** summarizes the possible industrial sources and common health problems. The data are extracted from *(Manahan, 2005)*, *(Cornelis et al., 2003)*, *(Andrews, 2006)*, and *(ATSDR-website)*.

Table 1-1 common heavy metals sources and the most known health problems

Element	Class (*)	Sources	Some of the effects on humans health
Arsenic	Metalloid (VHT)	Mining by product, wastes of chemicals industry	Lung cancer, bladder cancer, liver cancer, renal cancer, and skin cancer. Most toxic: As (III)
Mercury	Metal (MHT)	Industrial wastes of mining & coal industries	Primarily affects the central nervous system. In severe cases, specific anatomical areas of the brain affected, causing irreversible damage. Most toxic: mono methyl mercury (MMHg)
Lead	Metal (MHT)	Industrial waste of mining industry	Destruction of the nervous system characterized by the significant decrease of intelligence quotient. Most toxic: Tetra-alkyllead
Cadmium	Metal (MHT)	Industrial wastes of battery, pigments, coating and plating industries	Bronchitis, Kidney damage, skeletal damage, carcinogenic, affects heart & liver
Chromium	Metal (MHT)	Industrial wastes of metal plating and metal ceramics	Allergic reaction, nose irritations and nose bleeds Most toxic: Cr (VI)
Tin	Metal (LT)	Industrial wastes of can coating and steel container plating industries	Depression, liver damage, malfunctioning of immune systems Most toxic: Tri butyl tin
Zinc	Metal (MHT)	Industrial wastes of iron galvanization & batteries industry	Stomach cramps, skin irritations, vomiting, nausea and anaemia.
Copper	Metal (MHT)	Industrial wastes of electrical equipment, construction and machinery industries	Liver and kidney damage
Nickel	Metal (MHT)	Industrial wastes of alloys, alloy steel, rechargeable batteries, catalysts and plating industries	Lung cancer, nose cancer, larynx cancer and prostate cancer

Although a large number of heavy metals are categorized as toxic, some of them such as cobalt, copper, iron, manganese, molybdenum, vanadium, strontium, zinc and selenium are essential to many organisms *(Andrews, 2006)*. They are required for the normal biochemical processes such as respiration, biosynthesis and metabolism. The shortage of supplying these metals to the human body can lead to a deficiency in the function of organs. For instance, low selenium status may be associated with an increased risk of cancer; however, higher dosages can lead to toxic responses.

The standard limits of heavy metals in the drinking water are shown in **Table (1-2)**. These limits have been recommended by the world health organization (WHO) as well as other authorities such as the European water quality directive (EC). The data are extracted from *(Quevauviller and Thompson, 2006)*, *(WHO, 2008)*, and *(NCSU-website)*.

Table 1-2 the standard limits of heavy metals in drinking water

Element	Guideline value mg/lit	Authority and remarks (**)
Arsenic	0.01 (p)	WHO, (ECD), (N)
Arsenic	0.05	NCU
Cadmium	0.003	WHO, (ID)
Chromium	0.05 (p)	WHO, Total, (N)
Chromium (VI)	0.05	(ECD)
Copper	2.0	WHO, (ECD), (PF)
Lead	0.01	WHO, (ECD), (PF)
Mercury	0.006	WHO, inorganic, (ID)
Mercury	0.001	(ECD)
Nickel	0.07	WHO, (PF)
Nickel	0.01	(ECD)
Zinc	0.005	NCU

*: (VHT): very high toxic, (MHT): moderate to high toxic, (LT): low toxic, (VLT): very low toxic

**: WHO: is the value according to the world health organization, 2008; (ECD) is the value according to European council directive 98/83/EC; NCU represents the value according to north Carolina university code; (p) is the provisional guideline value; (N) is a naturally occurring inorganic chemicals; (PF) refer to contaminants from pipes & fittings; (ID) refer to contaminants from industrial source & human dwellings

1.3 Research objectives

Although substantial work has been done with a voluminous literature in the field of heavy metals detection and determination, an integrated system that can achieve full analysis on a miniature scale is still required. This study is devoted to develop an online – real time – fully automated system that could be utilized for conducting the simultaneous detection and quantification of heavy metals in an online sample of water taken from different sources. The proposed system is principally based on combining chemical derivatization procedures to produce volatile species in the form of hydrides or hydrido metal complexes to be dissociated and atomized through a dielectric barrier discharge (DBD) plasma atomizer, and then detected by using spectrometric analysis. This method has been selected for the sample introduction to the plasma section because of high efficiency (up to 100%) compared with the traditional desolvation/nebulisation technique. Other investigated techniques include integrating physical and chemical effects for better system performance. Nine elements are selected to be examined by the proposed system, include hydride forming elements and transition elements. Several chemical derivatization techniques are investigated for conducting qualitative and quantitative determination individually and simultaneously. The pre-treatment of the examined sample is also considered an important objective of this research since the real water sample possibly contains different types of contaminants. The proposed system is intended to form the basis for producing reliable portable equipment that could be adopted for in-situ analysis as part of the control of wastewater treatment plants.

1.4 Research hypothesis

It is hypothesized in this research that inducing multi physical effects from different resources on a water sample containing heavy metals will enhance the chemical reduction of the analyte and expedite the release of the generated species from the liquid phase; thereby the total efficiency of the process is improved. The general aim of this study is utilizing plasma generated in a dielectric barrier discharge atomizer to develop a miniaturized system for the simultaneous detection and quantification of heavy metals in a sample of water. The proposed hybrid system is principally based on utilizing

chemical derivatization procedures to produce volatile species of the analyte in the form of hydrides or organovolatiles, to be dissociated and atomized by DBD plasma atomizer, and then detected by applying spectrometric analysis. In addition to the traditional chemical reduction procedures, physical effects from ultrasonic irradiation and magnetic field are combined with UV radiation in a DBD atomizer to enhance the reduction efficiency. Online magnetization has been proposed as a preliminary treatment stage due to several advantages of a magnetic field. Ultrasound irradiation is also expected to induce considerable energy, which might enhance the reduction efficiency. UV radiation is well known to be an efficient source able to produce various radicals from the examined bulk, which would be effective on the whole process. Cryogenic separation with aid of liquid nitrogen cold trap is utilized to trap the volatile species before the atomization step for the purpose of species discrimination. The volatiles would be released sequentially by using programmed electrical heating. The challenging task of this study is believed to be the miniaturization of the whole process to be operated and controlled via PC software. The proposed system is aimed to form the basis for producing an integrated scheme for heavy metals determination in different forms.

2. LITERATURE REVIEW

2.1 Preface

The review is presented in four parts. The first part discusses various methods for heavy metals detection and determination, their features and shortcomings. In the second part, the working principle of the core unit in this research, the dielectric barrier discharge (DBD) plasma atomizer, is presented. The discussion also summarizes different design aspects of plasma DBD atomizers applied in the field of spectrochemistry analysis, as presented in the literature. The third part is devoted to discuss the working principles of different derivatization schemes applied in the field of heavy metals determination. The discussion presents some details on the derivatization procedures applied for several element determinations, individually and simultaneously, which has been adopted in the current research. The last part reviews some important principles related to the proposed technology; includes the hydride generation process and the atomization of the generated hydrides in a tubular atomizer, the spectrometric analysis, as well as some important plasma fundamentals. The fundamentals presented in this chapter are utilized in the mathematical investigations in chapter three, the DBD plasma characterization described in chapter four, as well as the experimental investigations and the spectrometric analysis presented in later chapters.

2.2 Conventional methods for heavy metals determination

Analytical methods for heavy metals determination are classified into two categories. In the first category, changes in the chemical properties of specific media are measured due to interactions from external heavy metal species. The second category is based on applying spectrometric analysis to monitor changes in species structure upon being subjected to a thermal radiation from different sources (e.g. quartz cell) or plasma effect. The working principles of these methods are summarized as follows:

2.2.1 Methods based on monitoring the changes in the chemical properties of a specific media

This category includes several methods, which can be illustrated in the following:

2.2.1.1 *Catalytic kinetic spectroscopic techniques (photometry and fluorimetry)*

The working principle of the photometry catalytic kinetic technique relies on utilizing an oxidative coupling reaction as an indicator, in which a heavy metal ion yields a colour derivative as a result of catalytic oxidative coupling of two substrates *(Kumar et al., 2003, Ohno et al., 1996, Gao et al., 2002).* The absorbance of the resulting coloured coupled product (e.g. pink) is measured at a selected wave length for a reagent blank, then a calibration graph is generated to infer the concentration of the analyte. The fluorimetric catalytic kinetic methods rely on the same principle as the photometric methods; i.e. the reaction rate is considered proportional to the concentration of the catalyst; however, fluorimetric techniques are rarely used for heavy metal determination because only few compounds are able to exhibit significant fluorescence. The major shortcoming of the kinetic methods is the poor selectivity *(Safavi et al., 2001)* as several transition metal ions that shows similar catalytic effects.

2.2.1.2 *The electrochemical techniques (anodic stripping voltammetry (ASV) and stripping chronopotentiometry (SCP))*

The working procedure of the anodic stripping voltammetry technique is: (1) preconcentrating the target analyte onto a working electrode (e.g. a mercury electrode), (2) reducing the metal ion to form an amalgam on the electrode (deposition step), (3) distributing the metal inside the mercury, and finally, (4) re-oxidizing the metal during an anodic potential scan, where the current is recorded as a function of the applied potential (stripping step) *(Brainina et al., 2004, Labuda et al., 1994, Manisankar et al., 2006).* The deposition step of stripping chronopotentiometry (SCP) technique is identical to that applied in the (ASV) technique, while re-oxidizing the analyte in the stripping step is usually achieved by the action of a chemical oxidant or by imposing a constant current. The electrochemical techniques (stripping analysis) satisfy most of the requirements for on-site detection of heavy metal ions because of low cost, low power requirements, high speed of analysis, high sensitivity and the instrument compatibility *(Kadara and Tothill, 2004).* Nonetheless, the major drawback of these techniques is the ease of the electrode surface poisoning which has been considered a big limitation to the widespread use of the electrochemical monitoring *(Brett, 2001).*

2.2.1.3 *Thin film techniques*

The chemical of interest is normally adsorbed onto a thin film of a chemically sensitive material; thereby inducing a change on the electrical characteristics of the material, which is consequently attributed to the concentration of the added chemical. Different types of thin film adsorption media are used such as conducting polymers, metal oxides (e.g. SnO_2 or Ga_2O_3) and other materials like gold-thoilate nanoparticle clusters *(Wilson et al., 2001)*. The changes in the electrical parameters are inferred by measuring the resistance (e.g. the chemiresistor sensors) *(Cai and Zellers, 2002)*, or the phase change of a wave propagated across the sensor surface (e.g. the acoustic wave sensors) *(Fang et al., 1999)*. The shortcoming of chemiresistor sensors is the noise produced due to the sensor miniaturization, whereas the operation of acoustic wave sensor requires higher frequencies when being miniaturized, which consequently result in complicating the electronics required *(Wilson et al., 2001)*.

2.2.1.4 *Surface plasmon resonance techniques*

Optical sensors based on surface plasmon resonance (e.g. electrochemical SPR sensors) and fibre optic biosensors which are based on localized surface Plasmon (LSPR) have been developed recently. Electrochemical surface plasmon resonance (SPR) is achieved by depositing mercury onto a surface of gold electrode with a subsequent stripping process using either anodic or cathodic current. During the stripping process, SPR is accomplished by reducing the intensity of the light reflected from the surface due to the effect of coupling evanescent wave with electrons in the sparse medium *(Panta et al., 2009)* , which is eventually utilized to quantify the products of the electrochemical reaction. In optical biosensors, an active bio layer is immobilized onto a nano-particle layer of gold in order to detect the deposited analyte by utilizing LSPR. Localized surface Plasmon resonance (LSPR) is defined to be the absorption of light that occurs if the optical frequency is resonant with the collective oscillation of conduction electrons *(Lin and Chung, 2009)*. The uniqueness of the LSPR sensor is the ability to detect the analyte by using different kinds of detectors such as optical detectors. SPR and LSPR sensors are considered to be efficient devices that could provide very low detection limits, operates with low power consumption and low fabrication cost. However, the

major bottleneck of these sensors is the instability of the surface Plasmon absorbance band that follows immersion of the sensor in aqueous solutions *(Gao et al., 2009)*.

2.2.1.5 *Combined integrated techniques*

The working principle of these systems relies on combining more than one technique to get the advantage of accurate discrimination of heavy metals ions. For instance, *(Cai et al., 2009)* combined the microelectrode array electrochemical technique (MEA) with the light-addressable potentiometric sensor (LAPS) to develop an electronic automated systems to detect a group of heavy metals (Zn(II), Cd(II), Pb(II), Cu(II), Fe(III) and Cr(VI)) in water samples. On the other hand, *(Rudnitskaya et al., 2008)* have used an array of potentiometric chemical sensors (11 sensors) with chalcogenide glass and plasticized PVC membranes for the simultaneous determination of copper, zinc, lead and cadmium ions in sea water. Although low detection limits are obtained from both systems, these devices require a long operation time for one measurement. Moreover, the combination of multi techniques leads to an increase in the system complexity and consequently to higher costs.

For comparison purposes, **Figure (2-1)** illustrates the copper detection limits, obtained with different technologies as well as the detection limits achieved in this research, presented in chapter six.

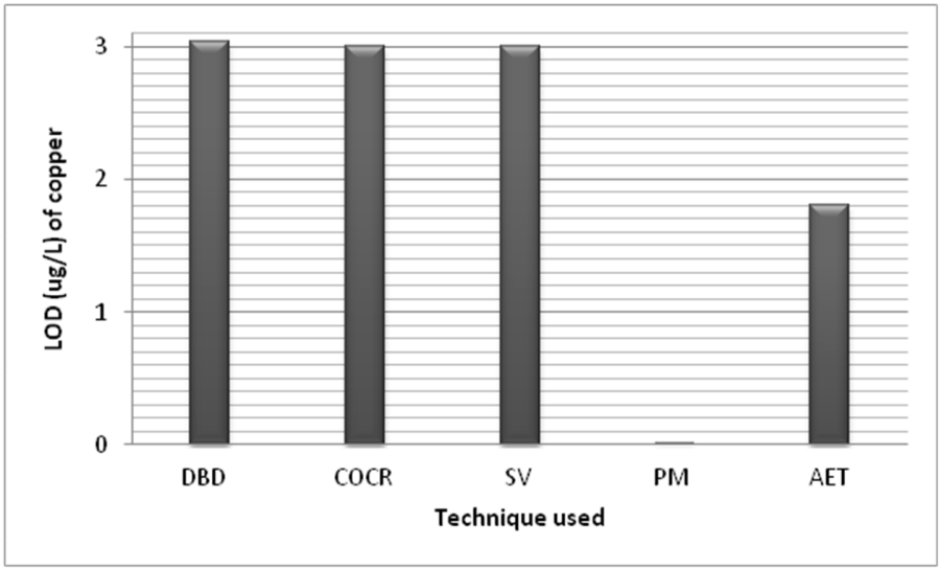

Figure 2-1 the detection limits achieved for copper by using different determination methods;

DBD is the dielectric barrier discharge plasma atomizer adopted in this study in the range up to 100 μg/L , COCR is the catalysed oxidative coupling reaction when applying Cu(II) in the range 8 – 160 μg/L *(Kumar et al., 2003)*, SV is the stripping voltametry technique applied for Cu(II) in the range 5 – 300 μg/L *(Manisankar et al., 2008)*, PM is the array of potentiometric chemical sensors when injecting 0.06 μg/L Cu(II) *(Rudnitskaya et al., 2008)*, and finally AET is the automated electronic tongue which is applied for Cu(II) in the range 2-300 μg/L *(Cai et al., 2009).*

2.2.2 Determination methods based on the atomic spectroscopy analysis

Several analytical techniques based on spectrometry can be applied to detection of heavy metals in water samples, soils, and other matrices. The methods include: flame and graphite furnace atomic absorption spectrometry (FAAS & GFAAS) *(Liu et al., 2007, Naghmush et al., 1994)*, hydride generation- atomic absorption and fluorescence spectrometry (HG-AAS/AFS) *(Leal et al., 2006, Frank et al., 2005)*, inductively coupled plasma optical emission spectrometry (ICP-OES) *(Peña-Vázquez et al., 2005, Matusiewicz and Slachcinski, 2006)*, microwave induced plasma atomic emission spectrometry (MIP-AES) *(Dietz et al., 1999)*, inductively coupled plasma mass spectrometry (ICP-MS) *(Mester et al., 2000)*, ion chromatography *(Beere and Jones, 1994)* and gas chromatography *(Geerdink et al., 2007).* In (FAAS & GFAAS) techniques, the analytes in the sample must undergo desolvation/nebulisation process then vaporization with aid of a high-temperature source such as a flame or graphite furnace to convert them into atoms in order to be determined by the atomic absorption spectroscopy technique. In general, the flame atomic absorption method can only analyze solutions, whereas the graphite furnace atomic absorption can be utilized for solutions, slurries, or solid samples.

The (HG-AAS/AFS) technique has been applied for hydride forming elements (e.g. arsenic, selenium, bismuth, .., etc.) where the hydride of the analyte is usually generated chemically with aid of a reducing agent and then detected after atomization by a spectroscopy technique. Other techniques such as (ICP-OES), (MIP-AES) & (ICP-MS) utilizes the plasma to ionize and break down the chemicals into fragments, to be identified either by the charge to mass ratio (mass spectroscopy) or the wave length of the emission lines (emission spectroscopy). It is well known that the adoption of mass

spectra is more accurate and easier than the optical spectra. The reason is that each analyte has only one charge to mass ratio whereas it could have many emission lines. Therefore the detection limits of ICP-MS technique are reported to be in the range of few parts per trillion, while ICP-OES normally achieves detection limits in the range of parts per billion.

Chromatographic techniques usually utilize an adsorption media in a column to retain the generated volatile species of the analyte and desorb them with time. The analyte's identification is achieved by measuring the releasing time from the adsorption column. It is worth noting that all the above techniques achieves low detection limits (LODs) and have been widely applied inside laboratories. **Figure (2-2)** illustrates the typical detection limits achieved by using the spectrometric methods.

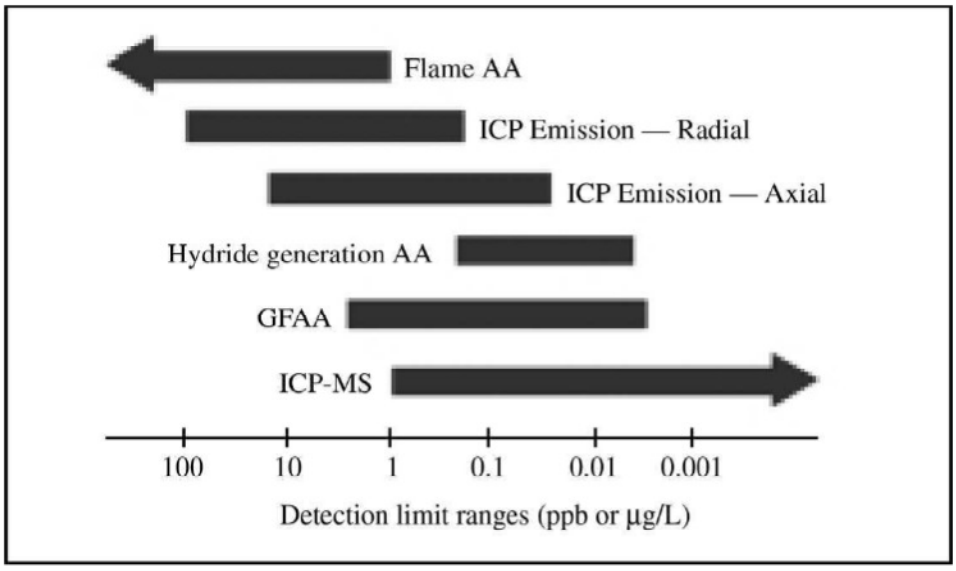

Figure 2-2 the typical detection limit ranges for the major atomic spectroscopy techniques *(Zhang, 2007)*

It is well known that the abovementioned techniques require skilled professional labour, high analytical cost, additional pre-concentration procedures and relatively long operation times. In practice, these techniques are found to be so expensive and not easily miniaturized because they require bulky instruments; hence, they are considered to be impractical for onsite screening or as a portable quantification decision tool *(Kadara and Tothill, 2004).*

2.3 Applications of the dielectric barrier discharge plasma atomizers in the field of heavy metals determination

The non thermodynamic equilibrium plasma, which is classified to be low temperature or cold plasma, is normally formed in low or atmospheric pressure systems. The temperature of electrons in the cold plasma is much higher than the temperature of the heavy particles, the electrons can reach temperatures in the range $10^4 – 10^5$ ^oK while the gas temperature is kept as low as in the range of room temperature. The common types of low-temperature plasma are: direct current, alternating current (AC, 50 – 60 Hz) audio frequency (AF, <100 kHz), radio frequency (RF, 13.56 MHz) and microwave (2.45GHz). The atmospheric pressure plasma can be generated in a large scale such as plasma jet as well as the micro scale such as the resistive barrier discharge. Recent research has been to utilize a microplasma as it offers many advantages. One of the main advantages is the lower operating cost due to limited gas and low power consumption *(Karanassios, 2004)* . Other properties are: light weight, embedding with other components in proximity, and the possibility of using miniaturized power sources *(Valdivia-Barrientos et al., 2009)*. The dielectric barrier discharge microplasma (DBD), also referred to as silent discharge, has been utilized in analytical chemistry research as it offers the ability of miniaturization on a chip. The general configuration of a DBD plasma atomizer assumes a small distance between the electrodes as well as coverage of one or both electrodes with a dielectric material, which prevents direct contact between the plasma gas and the electrodes, and consequently reduces electrode contamination. As soon as a potential is applied, a charge build up is formed on the dielectric surfaces leading to the plasma gas breakdown. The breakdown produces a filament with a high current density for few nanoseconds, which is called a microdischarge. After 100 nano-seconds, the electric field reduces significantly, leading to a reduced charge density and current flow interruption. Hence, the microdischarges form at other positions due to the continuity of the applied field, whereas other microdischarges can only be generated at the former position when the voltage is reversed. As a result of the short discharge duration, no significant heat build up is expected along the DBD surface, which consequently results in cold plasma formation *(Miclea et al., 2001)*. DBD plasma discharge provides sufficient energy for breakdown (1-10 eV), which is considered to be ideal for spectrochemical analytical applications. The energetic electrons collide with

the molecules in the ambient gas, forming various ions, atoms, molecular fragments and free radicals *(Zhu et al., 2006a, He et al., 2007)*. DBD atomizers are usually powered by applying an AC source of 1-100 kV and a frequency range up to several megahertz. Practically, DBD microplasma is still in the research stage and it has not been extended yet for wider applications in the field of spectrochemical analytical devices.

The last decade has experienced extensive applications of DBD microplasma in the fields of analytical chemistry. **Table (2-1)** summarizes the recent researches in this field.

2.4 Applications of the chemical derivatization methods in the field of heavy metals determination

Analyte derivatization is the process of the controlled conversion of species originally present in a sample into another form of improved separation coefficient, without changing the original chemical structure *(Cornelis et al., 2003)*. Hence, the derivatization procedures are used to transform a chemical compound into product of similar chemical structure, called a derivative. The main objectives of the derivatization procedures are: increasing the compound volatility, decreasing the compound polarity, increasing the thermal stability of the compound, as well as increasing the detection efficiency by incorporating functional groups, which consequently improves the element separation efficiency and eventually leads to a higher signal intensity *(Zhang, 2007)*.

The working principles of the derivatization methods rely on one or more of the following procedures:

- Conversion of inorganic and small organometallic ions to volatile compounds (e.g. hydrides or fully ethylated species) in aqueous media.
- Conversion of large alkylmetal cations ($R_nPb^{(4-n)+}$) to saturated nonpolar species.
- Conversion of ionic species to volatile chelates (e.g. dithiocarbamate) or other compounds.

The most common chemical derivatization techniques are cold vapour generation (CVG) and hydride generation (HG) for hydride forming elements; alkylation by using alkylborates and derivatization procedures by applying Grignard reagents.

Table 2-1 the applications of DBD microplasma in the analytical chemistry fields

Used technique	Detection of	DBD geometry	Electrodes	Power	Ref.
DBD - DLS (Argon or Hellium)	Halogenated hydrocarbons	A rectangular, two flat glass plates. The channel was formed by two glass spacers with the following dimensions: 60 mm length x 1mm width. The distance between the electrodes including the dielectric layers is 1 mm	50 mm long x 0.8 mm width x 0.1 mm thickness aluminium electrodes covered with 20 µm glass layer	0.5 – 1 watts 750 V AC 5 - 20 kHz 11.5 kHz modulation frequency	*(Miclea et al., 2001)*
HG - DBD - AAS (Helium)	As(III), As(V), MMA, DMA	A rectangular, two flat glass plates 1 mm thick. The channel was formed by two glass spacers with the following dimensions: 70 mm length x 10 mm width, with an entrance channel in the midline of the cell. The distance of the two glass plates was 2 mm	50 mm long x 10 mm width flat copper plates attached to the top and the bottom surface of the cell	5 watt 3700 V AC 20.3 kHz	*(Zhu et al., 2006a)*
HG - DBD - AAS (Argon)	Se, Sb, Sn	A rectangular, two flat glass plates 1 mm thick. The channel was formed by two glass spacers with the following dimensions: 70 mm length x 8 mm width, with an entrance channel in the midline of the cell. The gap between the two glass plates was 3 mm	50 mm long x 8 mm width flat copper plates attached to the top and the bottom surfaces of the cell	5 watt 3500 – 4000 V AC 20.3 kHz	*(Zhu et al., 2006b)*
CVG - DBD - AES (Argon or Hellium)	Hg (II)	A rectangular, two flat glass plates 190 µm thick. The channel was formed by two glass spacers, 1 mm thick, with the following dimensions: 15 mm length x 5 mm width, with an entrance port for the gas midline of the cell. The thickness of the plasma channel was 0.6 mm	10 mm long x 5 mm width copper electrodes attached to the top and bottom surface of the cell	5 watt 3700 V AC 30 kHz	*(Zhu et al., 2008a)*

HG - DBD - AFS (Argon)	As (III)	A cylindrical, two concentric quartz tubes with inner tube diameter of 4 mm and 7 mm ID for outer tube. A 2 mm discharge gap is present between the quartz rod and the inner quartz tube. The effective discharge length was 20 mm.	A copper wire embedded inside a quartz rod as a central electrode in addition to an outer aluminium foil wrapped around the outer surface of the inner tube as the second electrode	13.5 watt 4300 - 7000 V AC 20 kHz	*(Zhu et al., 2008c)*
HG - DBD – AFS (Argon)	Se, Pb & Sb	Same design of *(Zhu et al., 2008c)*	Same design of *(Zhu et al., 2008c)*	Same conditions of *(Zhu et al., 2008c)*	*(Zhu et al., 2008b)*
CVG - DBD - OES (Argon)	Hg (II)	A rectangular, two quartz plates 50 mm length x 15 mm width x 1.2 mm thick were used for outer shell. 50 mm length x 5 mm width x 1mm thick channel was formed between the outer shell by using two glass spacers	Two aluminium foils 5 mm x 30 mm were attached to the outside surfaces of the outer shell	13.5 watt 1200 - 1350 V AC 35 kHz	*(Yu et al., 2008a)*
GC – DBD-CL (Nitrogen)	Volatile chlorinated hydrocarbons	A cylindrical, glass tube 1 mm ID x 40 mm length covered with a rubberized fabric	Copper rod 0.45 mm OD x 30 mm length along tube centre line as inner electrode plus copper wire 0.45 mm OD x 50 mm length wrapped around the outside surface of the tube as the second electrode	5 watt 1400 - 2700 V AC 20 kHz	*(Li et al., 2008)*
HG - DBD – AFS (Argon)	As(III)	Lab on valve DBD atomizer, 4 quartz plates with 1.2 mm thickness formed an atomization chamber 50 mm length x 4 mm width x 3 mm depth	Two aluminium foils 30 mm length x 4 mm width	Neon power supply, discharge voltage = 60 volt	*(Yu et al., 2008b)*
HG - DBD - AFS (Argon)	Bi	Programmable intermittent DBD reactor	NA	2-22 watts	*(Xing et al., 2009)*

Integrated chromatograp -hic approach including capillary flow and DBD atomizer (Argon)	Measurement of arsine and phosphine in hydrocarbons such as propylene	A commercial dielectric barrier discharge detector operating in argon mode was used	NA	NA	*(Gras et al., 2010)*
HG – DBD - AAS	Inorganic mercury and methyl mercury	A rectangular configuration consists of two glass plates, 1 mm thickness. The discharge channel dimension was 70mm length x 10mm width x 1mm depth	Two aluminium foils 50mm length x 10 mm width	5 watt	*(Zhu et al., 2010)*
VG-DBD-ICP-OES	Inorganic mercury	Concentric cylinders configuration, the outer cylinder is a quartz tube (5 mm ID, 7 mm OD, and 10 cm length) whereas the inner cylinder is a smaller diameter quartz tube	1 mm copper wire inserted in the inner cylinder. 1 mm copper wire formed the outer electrode and wrapped on the outer cylinder	High voltage power supply Input voltage = 20 volt	*(Wu et al., 2011)*
DBD - GC	halo-hydrocarbons	A cylindrical configuration, a small quartz tube (3.0 mm ID, 5.0 mm OD and 50 mm length)	A copper wire electrodes, inner electrode diameter (1.7 mm) and outer electrode diameter (1.2 mm)	High voltage power supply voltage = 4 kV, 20 kHz	*(Li et al., 2011)*
DBD – OES	Inorganic mercury	A rectangular configuration, plasma channel dimensions (4 cm length, 1 cm width, and 1 mm depth)	Aluminium foils, 0.5 mm thickness, were used for electrodes	High voltage power supply (up to 12 Kv)	*(Abdul-Majeed et al., 2011, Abdul-Majeed and Zimmerman, 2012a)* (the current research)

DLS: diode laser spectrometry, HG: hydride generation technique, AAS: atomic absorption spectroscopy, CVG: cold vapour generation, AES: atomic emission spectroscopy, AFS: atomic fluorescence spectroscopy, OES: optical emission spectroscopy, GC: gas chromatography, CL: chemiluminescence, VG: vapour generation, ICP: inductively coupled plasma, MMA: monomethyl arsenic, DMA: dimethyl arsenic

Other derivatization techniques utilize UV light and ultrasonic irradiations to produce radicals that are able to reduce the analyte and produce the volatile species *(Wu et al., 2010).* It is worth noting that the utilization of chemical derivatization methods in plasma spectrochemistry devices could ameliorate the analyte transport efficiency and their introduction to the plasma bulk by more than 90% compared with the conventional pneumatic nebulisation method, which normally achieves no more than 5% efficiency *(Liu et al., 2011).* Consequently, the limits of detection could be improved up to several orders of magnitude. It is also important to refer to the ability of coupling the chemical derivatization methods with various detection schemes, which eventually facilitate the determination procedures.

2.4.1 Chemical derivatization techniques (CVG & HG)

The working principle of the cold vapour generation (CVG) and hydride generation (HG) techniques is to reduce the element into a lower oxidation state by using a reducing agent. Applying the cold vapour generation process results in liberating the analyte elemental form at room temperature, which can be detected by spectroscopic analysis, while the hydride generation technique involves the reduction of the element from the higher oxidation state to its lowest state (usually II or III), which appears ultimately as the volatile hydride. The advantages of these techniques are: rapid reaction kinetics, high and reproducible reaction efficiency and a stable analyte species during transport. The generated volatile hydrides require an atomization step in order to be converted to the free atoms which can be detected by spectroscopic methods. The cold vapour generation technique is reported to be applicable for mercury species, in which inorganic mercury Hg (II) is converted to elemental mercury Hg (0). The formation of cadmium free atoms at room temperature has also been reported as possible *(Cornelis et al., 2003, y Temprano et al., 1994).* Mercury and cadmium are chemically reduced to the free atomic states Hg (0) and Cd (0) directly or indirectly through reaction with a strong reducing agent like sodium tetrahydroborate ($NaBH_4$). The volatile-free atoms are then driven from the reaction chamber by a carrier gas to the absorption cell, to be detected by atomic absorption spectrometry. The detection limit of mercury using the cold vapour technique, is reported to be sub ppb with 100% release efficiency *(Zhang,*

2007). Other metals and metalloids classified to be hydride forming, include arsenic, antimony, bismuth, germanium, lead, selenium, tellurium and tin. The range has been extended recently to include the noble and transition metals, platinum, cobalt, silver, copper, rhodium, palladium, osmium, chromium, gold, nickel, indium, thallium, and manganese *(Feng et al., 2001, Pohl and Prusisz, 2007)*. The metals react with a reducing agent (usually $NaBH_4$) to produce volatile species (e.g. AsH_3, SbH_3, BiH_3, GeH_4, PbH_4, SeH_2, TeH_2 and SnH_4) *(Dedina and Tsalev, 1995)*. In some cases reduction doesn't take place; for example inorganic As (III) remains in the same oxidation state passing from H_3AsO_3 to AsH_3. The generated molecular species transfer from the aqueous phase to the gas phase at moderate to high efficiency, up to 95% for arsenic *(Le et al., 1992)*, and partially dissociate through the atomizer. Hydrides generation could be conducted using either batch operation, continuous flow or flow injection, where the volatile hydrides are scavenged from the sample solution with aid of a carrier gas (usually argon) into the atomization cell. The cell is heated either electrically or by a flame in order to atomize the element. Several reducing agents have been applied including Zn/HCl, $SnCl_2$/HCl-KI, Mg/HCl-$TiCl_3$ and tetrahydroboride (THB).

Sodium tetrahydroborate ($NaBH_4$) stabilized by NaOH or KOH is almost exclusively used as an efficient derivatizing agent due to exceptional reducing and hydride transfer properties. In this regard, several mechanisms proposed in the literature have contemplated the formation of the volatile hydrides *(D'Ulivo et al., 2005, D'Ulivo et al., 2007, Ramesh Kumar and Riyazuddin, 2005)*, summarized as follows:

a) assuming the evolution of the nascent hydrogen from acidic hydrolysis of THB

The mechanism of the hydride generation process is represented by the following reaction:

$$NaBH_4 + 3H_2O + HCl \xrightarrow{K_1} H_3BO_3 + NaCl + 8H^{\bullet} \xrightarrow{A^{m+}} AH_n + H_2 \uparrow \qquad (2\text{-}1)$$

Where;

A: the analyte, m^+: the oxidation state of the analyte, *n*: the coordination number of the hydride, $H^{\bullet}$: the nascent hydrogen

The active specie in the reduction process is the atomic (nascent) hydrogen which forms during the acid hydrolysis of THB. The decomposition of THB in a pure aqueous solution is represented by the following mechanism:

$$
\left.
\begin{aligned}
BH_4^- + H_2O + H^+ &\rightarrow H_2O{-}BH_3 + H_2 \\
H_2O{-}BH_3 + H_2O &\rightarrow H_2O{-}BH_2OH + H_2 \\
H_2O{-}BH_2OH + H_2O &\rightarrow H_2O{-}BH(OH)_2 + H_2 \\
H_2O{-}BH(OH)_2 + H_2O &\rightarrow B(OH)_3 + H_2 + H_2O \\
\text{----------} & \\
BH_4^- + 3H_2O + H^+ &\rightarrow B(OH)_3 + 4H_2
\end{aligned}
\right\} \quad (2\text{-}2)
$$

b) assuming the formation of the hydride occurs due to the action of the hydrogen that directly links to the boron through the formation of some hydroboron intermediates

The mechanism is illustrated in the following reactions:

$$
\left.
\begin{aligned}
THB + H_3O^+ + 2H_2O &\rightarrow Intermediates \rightarrow H_3BO_3 + H_2 \\
THB/Intermediates + Analyte &\rightarrow Hydride
\end{aligned}
\right\} \quad (2\text{-}3)
$$

The oxidation state of the analyte imposes a pronounced effect on the generation of the hydride. In practice, producing the hydride from the analyte at low oxidation state is more effective for analytical purposes. For example, the reduction of Sb (III) into stibine (SbH_3) is found to be faster, more reliable, and higher yielding in comparison with stibine produced by Sb (V) reduction. Thus, an element at a high oxidation state should be pre-reduced to the lower state before being reduced to the hydride form. The most common pre-reducing agents are: L-cysteine, ascorbic acid and thiourea. Some of these reagents enhance the analyte signal by eliminating the interferences produced from other compounds in the reaction bulk. L-cysteine ($C_3H_7NO_2S$) is capable of speeding up the rate of hydroborate reaction, thereby increasing the sensitivity. The signal amelioration is attributed to an intermediate compound formed due to the reaction between $NaBH_4$ and the SH group of L-cysteine, which is found to be more effective than $NaBH_4$ alone.

$$BH_4^- + RSH \rightarrow RS{-}BH_3^- + H_2 \quad (2\text{-}4)$$

On the other hand, sample acidity and the concentration of the reducing agent are reported to have significant effects on hydride generation efficiency. Hydrogen ions in the reaction bulk also have an important role in the activation of the analyte to a suitable chemical form in addition to their role in THB hydrolysis. Generally speaking, a higher value of acid concentration results in better control of interferences from the transition metals; hydride generation for an analyte present at a higher oxidation state (e.g. As (IV)) requires a very limited acidic range (PH = 0.3-0.5). Furthermore, the reductant concentration is also a sensitive parameter, depending on the hydride generation technique used. For instance, (0.1-0.2%, 0.2-1.0% and 1-3% m/v) $NaBH_4$ concentrations has been utilized for antimony reduction using flow injection, continuous and batch systems respectively *(Dedina and Tsalev, 1995)*.

2.4.2 The alkylborates and Grignard reagents

The most commonly used alkylborate reagents are sodium tetraethylborate ($NaBEt_4$), sodium tetraphenylborate ($NaBPh_4$) and sodium tetrapropylborate ($NaBPr_4$). Ethylation, using sodium tetraethyl borate can be applied in aqueous media, in which the reduction and the extraction procedures are conducted in the same step. Such ethylation is used for Sn, Se, Hg and Pb which enables the simultaneous reduction of organo (Sn, Hg and Pb) compounds *(Cornelis et al., 2003)*. Moreover, ethylation by sodium tetraethylborate is reported applicable for cadmium *(y Temprano et al., 1994, D'Ulivo and Chen, 1989)*. The application of ethylation in the aqueous phase is found to be unable to distinguish between the organic species (ethyl lead, ethyl mercury) and ionic inorganic mercury and lead. Alternatively, both ($NaBPh_4$) and ($NaBPr_4$) were found to be more stable compared with $NaBEt_4$, which has provided the possibility to distinguish between ethyl- and inorganic mercury and lead derivatives. Grignard reagents (e.g. ethyl magnesium bromide) are efficient agents for mercury, organotin and organolead speciation. However, some shortcomings are reported when using Grignard reagents such as their atmospheric instability and their hydrolysis in the presence of water, leading to the formation of $Mg(OH)_2$. Therefore the target species must be extracted into a non-polar solvent as a first stage and then dried prior to derivitized with Grignard reagent *(Grinberg et al., 2003)*.

2.4.3 Application of chemical derivatization methods stimulated by UV light and ultrasound irradiation

Photo-chemical reduction/oxidation reactions are utilized in various fields such as wastewater treatment and some industrial applications. In the analytical chemistry, photochemical derivatization procedures are used to conduct the photochemical pre-reduction of Se (VI) to Se (IV) *(Fragueiro et al., 2006)*. In later studies, a photochemical vapour generation procedure was utilized for other elemental (e.g. Hg, As, …, etc.) reductions. 30 % of the elements in the periodic table could be converted into volatile species upon being subjected to sufficient UV radiation in presence of low molecular weight acids *(Vieira et al., 2007, McSheehy et al., 2005, Guo et al., 2005)*. The concept of the photochemical vapour generation (PVG) process relies on utilizing the reducing radicals generated from inducing a UV radiation on low molecular weight organic compounds (e.g. carboxylic acids or alcohols).
The photolytic cleavage of low molecular weight organic acids by the UV radiation is represented according to the following equations *(Bendl et al., 2006)*.

$$RCOOH + hv \rightarrow R^* + COOH^* \qquad (2\text{-}5)$$

Another pathway for the photolytic decomposition of aliphatic acids was suggested to be as in the following form *(Guo et al., 2005)*:

$$R - COO \xrightarrow{hv} R^* + COOH^* \rightarrow RH + CO_2 \quad , (R = C_nH_{2n+1}, n = 0,1,2) \qquad (2\text{-}6)$$

For instance, the photo-dissociation of formic and acetic acids which promotes the generation of mercury vapour species is described as follows:

$$\left.\begin{aligned} HCOOH + hv &\rightarrow HCOOH^* \rightarrow H_2O + CO \\ CH_3COOH + hv &\rightarrow CH_3COOH^* \rightarrow H_2O + CH_2CO \\ Hg\ (II) + reducing\ species\ (radicals) &\rightarrow Hg(0)_{sol} \rightarrow Hg\ (0)_{gas} \end{aligned}\right\} \qquad (2\text{-}7)$$

Investigations into applying PVG schemes for arsenic show that As (III) acts as a scavenger leading to a recombination with hydrocarbon radicals and the formation of stable methylation products as follows:

$$3RCOOH + H_3AsO_3 \underset{R = C_nH_{2n+1}}{\overset{hv}{\rightarrow}} 3CO_2 + R_3As + 3H_2O \qquad (2\text{-}8)$$

Subjecting an aqueous phase to ultrasound irradiation leads to the formation of cavitation bubbles. Each cavitation bubble acts as a microreactor which consequently generates a collapse bulk with very high localized temperature and pressure (4000 ^{o}K and 200 Bar). The collapse of the bubble may occur in different ways which produces shock waves and consequently results in a turbulent flow at the bubble interface (in the case of symmetrical cavitations) or formation of micro jets in the case of asymmetric cavitations. When a water sample is affected by sufficient ultrasound irradiation, many radicals (e.g. $H^*$and OH^*) form at the gas-phase interface of the cavitation bubbles, and to a lesser extent, in the bulk solution. The generated radicals are responsible for the reduction properties of the ultrasound irradiation process. Sonic decomposition of low molecular weight organic compounds (e.g. acetic or formic acid) results in the formation of reducing radicals which consequently reduces the analyte into a lower oxidation state. The formation of mercury vapour species due to ultrasonic irradiation in presence of formic acid (sono-chemical reduction) is by the following mechanism *(Gil et al., 2008)*.

$$\left.\begin{aligned} H_2O \rightarrow OH^* + H^* \\ HCOOH + OH^*\,(H^*) \rightarrow COOH^* + H_2O\,(H_2) \\ 2HCOOH \rightarrow CO + CO_2 + H_2O + H_2 \\ Hg\,(II) + reducing\ species\ (radicals, gases) \rightarrow Hg(0)_{sol} \rightarrow Hg\,(0)_{gas} \end{aligned}\right\} \qquad (2\text{-}9)$$

UV-induced photochemical vapour generation can be used for selenium determination, where different UV light sources were used and several mechanisms presented *(Guo et al., 2003, Sun et al., 2006)*. Later studies investigated other elements such as mercury *(Wu et al., 2011)*, arsenic, tin, cadmium , lead *(Zheng et al., 2010a)*, and nickel *(Zheng*

et al., 2009). In all these studies, the detection limits are found to be quite competitive with the traditional HG technique.

Ultrasonic irradiation has been utilized for sample pre-treatment for extracting different kinds of species from various samples *(Bentlin et al., 2007, Marin et al., 2001)*. Ultrasonic chemical vapour generation is reported to be applicable to inorganic mercury and methyl mercury reduction *(Gil et al., 2006, Gil et al., 2008, Ribeiro et al., 2007)* where micro-sonic probes and a sonic water bath were used to induce different levels of ultrasonic irradiation. Although *(Ribeiro et al., 2007)* stated that the methodology could be extended to apply to other elements (As, Se, Cd, and Zn), ultrasonic cold vapour generation of mercury is found to be a restricted process *(Capelo et al., 2000)* because of the presence of chloride and amino acids (normally used for the sample digestion), which ultimately suppresses the signal of Hg (II) and Hg (0).

It is worth noting that to the best of knowledge, no other elements have been investigated using this technique. However, *(Ribeiro et al., 2007)* suggested that UV radiation of aqueous solutions containing strong oxidants (e.g. O_3 or H_2O_2) gives rise to the formation of lower residual oxidants which could be utilized for sample digestion without signal suppression. This envisages the possibility of integrating both UV and ultrasonic irradiations for sample pre-treatment and analyte reduction, which has been applied in the current research (**Section (7-6)**).

In practice, a significant sonic effect could be imposed on the examined sample by using a suitable transducer (e.g. immersion) *(Li et al., 2009, BPO-Website)*.

2.5 The chemical derivatization procedures for the most common heavy metals

In this section, the chemical derivatization procedures for the most common heavy metals are reviewed. The review covers nine elements, selected to be examined in this research, including hydride forming elements (Hg, As, Sn, Cd, Pb) and other transition elements (Cu, Ni, Zn, Cr). The reason for selecting these elements is to investigate a wider range of the derivatization conditions and different categories in the periodic table.

In addition to the selected nine elements, other elements are also included for completeness. It can be observed in **Figure (2-3)** that the element responses to the

chemical derivatization procedures are widely different, in which several forms can be produced even from the same element. For instance, Hg (II) produces free atoms at room temperature whereas methyl mercury produces methyl mercury hydride. Other elements (e.g. As (V)) require to be pre-reduced to a lower oxidation state before conversion to the volatile species, whereas Pb (II) requires to be oxidized into higher oxidation state before producing the volatile species.

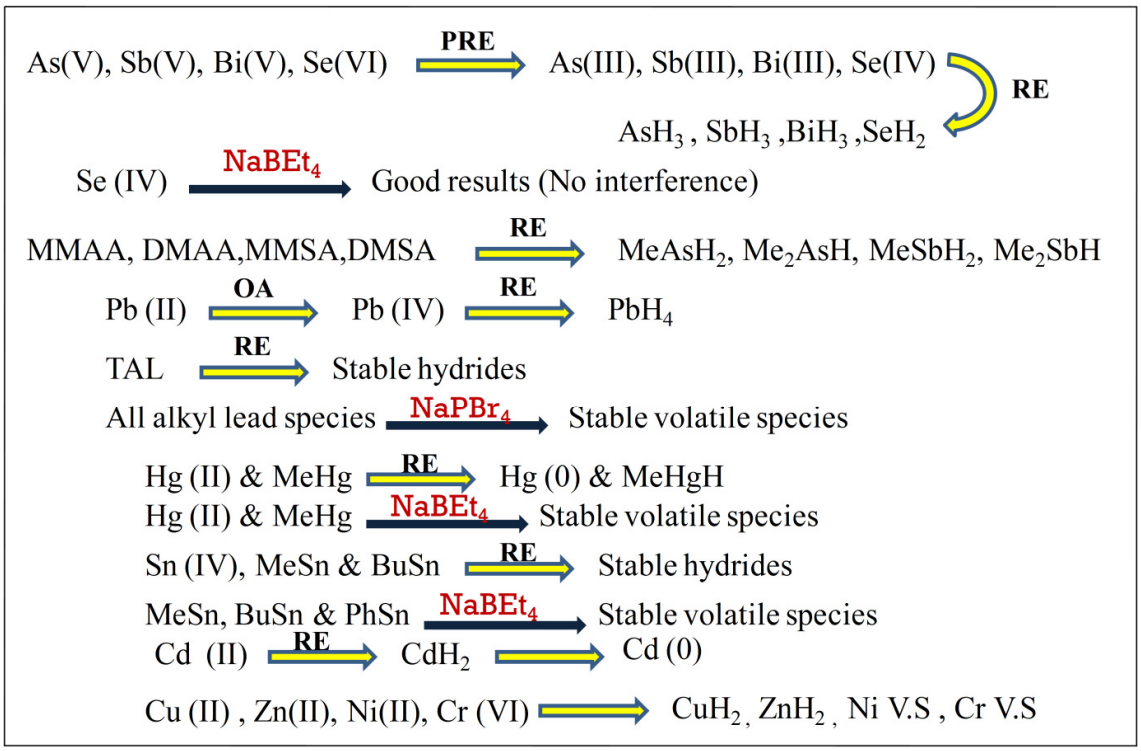

Figure 2-3 summary of the derivatization procedures for the volatile species forming elements;
PRE & RE indicate pre-reducing & reducing agents respectively, whereas OA denotes an oxidizing agent. The yellow arrow represents the derivatization procedure by applying the hydride generation technique while the blue arrow illustrates alternative derivatization procedure by applying the alkylborates reagents.

As: arsenic, Sb: antimony, Bi: bismuth, Se: selenium, MMAA: monomethylarsonic acid, DMAA: dimethylarsenic acid, MMSA: monomethylated species of antimony, DMSA: dimethylated species of antimony, TAL: tetra alkyl lead compounds, MeSn: methylated tin, BuSn, butylated tin, PhSn: phynelated tin

2.5.1 Mercury

The important chemical forms of mercury include: the elemental mercury Hg^0, the inorganic mercuric Hg^{2+}, monomethylmercury (CH_3Hg^+), dimethylmercury (CH_3HgCH_3) and mono ethyl mercury MEtHg *(Mach et al., 1996, Leermakers et al., 2005)*. The monomethylmercury compounds are relatively more toxic than elemental mercury and its inorganic salts.

Derivatization of mercury species has been applied by using either the cold vapour generation technique ($NaBH_4$ or $SnCl_2$) or other procedures such as the aqueous phase ethylation with ($NaBEt_4$) or Grignard reagents. In general, cold vapour atomic absorption spectrometry (CV-AAS) offers many advantages such as high sensitivity, absence of spectral interferences, simplicity, and low operational costs *(Rio-Segade and Bendicho, 1999)*. Practically, using any of the aforementioned derivatization techniques produces volatile species of mercury such as elemental Hg^0 and methyl mercury hydride, as illustrated by the following schemes:

- Sodium tetrahydroborate

$$\left.\begin{aligned} Hg^{2+} + 2NaBH_4 + 6H_2O &\rightarrow Hg^0 + 7H_2 + 2H_3BO_3 + 2Na^+ \\ MeHg^+ + NaBH_4 + 3H_2O &\rightarrow MeHgH + 3H_2 + H_3BO_3 + Na^+ \end{aligned}\right\} \quad (2\text{-}10)$$

The elemental mercury Hg^0 can be determined at room temperature using the atomic absorption spectroscopy method; however, the total determination of mercury species requires a heat source (e.g. quartz tube furnace or plasma atomizer) for achieving the decomposition of MeHgH *(Zhu et al., 2010)*. On the other hand, the direct reduction of $MeHg^+$ to Hg^0 was achieved under specific conditions *(Rio-Segade and Bendicho, 1999, Capelo et al., 2000)*. Concentration of sodium borohydride is mentioned to be a critical factor in the determination of mercury species via cold vapour generation; therefore, it is specified within (0.01- 0.1%, m/v) when processing inorganic mercury and (0.01- 0.75% m/v) in the case of methyl mercury. It is also reported that the reagent solution should be prepared by adding NaOH in order to stabilize the solution.

- Tin chloride ($SnCl_2$)

$SnCl_2$ is usually used for the reduction of inorganic mercury; however, it can also be used for the reduction of organic mercury species into Hg^0 by using the ultrasonic chemical vapour generation technique, where the organic mercury is converted to a hydride (e.g. the conversion of CH_3Hg^+ into CH_3-HgH) *(Capelo et al., 2000)* . A procedure applied to differentiate between inorganic and organic mercury depends on the sonic source. For instance, if the sonic irradiation source is turned on, the signal indicates the total mercury; conversely if it is turned off, the signal refers to the inorganic mercury. Therefore, the organic mercury can be inferred from the difference between the two determinations.

- Sodium tetraethylborate

$$\left.\begin{aligned} Hg^{2+} + 2NaB\,(C_2H_5)_4 &\rightarrow (C_2H_5)_2\,Hg + 2Na^+ + 2B\,(C_2H_5)_3 \\ CH_3Hg^+ + NaB\,(C_2H_5)_4 &\rightarrow CH_3HgC_2H_5 + Na^+ + B\,(C_2H_5)_3 \end{aligned}\right\} \quad (2\text{-}11)$$

The advantages of using an aqueous phase reducing agent such as (NaBEt) rely on conducting the whole derivatization process simultaneously, i.e. the analytes can be separated from the matrix, derivitized and extracted into an organic solvent in one-step *(De Smaele et al., 1998)*. Nevertheless, sodium tetraethylborate cannot be used for the simultaneous discrimination of inorganic mercury and methyl mercury because it produces similar volatile species $HgEt_2$ after ethylation. Alternatively, a phenylation technique by using sodium tetraphenylborate *(Abrankó et al., 2005)* and a propylation technique by using sodium tetrapropylborate *(Grinberg et al., 2003)* have been applied for the same purpose.

2.5.2 Cadmium

Cadmium is considered, together with mercury, to be the most toxic of the heavy metals group *(y Temprano et al., 1994)*. Cadmium is derivitized into cadmium hydride (CdH_2) by applying the hydride generation technique using either $NaBH_4$ or KBH_4 as a reducing agent. Both atomic and molecular cadmium species are probably generated when applying the reduction process. However, the efficiency of molecular cadmium

generation does not exceed 5% *(Arbab-Zavar et al., 2006)*, which is attributed to the instability of the hydride at temperatures above the liquid nitrogen boiling point. Although cadmium hydride is an unstable species, it is considered to form the major volatile product of cadmium. In practice, CdH_2 could be produced by reacting Cd^{2+} solution with $NaBH_4$ in a medium of surfactant-based organized assemblies such as didodecyldimethylammonium bromide (DDAB) vesicles or organic medium such as dimethylformamide *(y Temprano et al., 1993)*. An important advantage of using the organized assemblies is the improvement of the spectral characteristics of the colored or fluorescent compounds *(Sun et al., 2002)*. Generally speaking, producing the cadmium hydride is not a preferred route for cadmium detection by the spectroscopic methods due to the hydride instability at room temperature. The efficiency of cadmium vapour generation is improved by applying assisting chemicals such as pre-reducing agents (e.g. thiourea), surfactant reagent (DDB), halogenated compounds (e.g. $NaBrO_3$ or $NaIO_3$) which result in low detection limits in the range of pg/ml *(Li et al., 2004)*. In other studies, derivatization of cadmium is achieved by using alkyl borate agents, obtaining low detection limits in the range of sub-ng/ml *(y Temprano et al., 1994)*. The alkyl borates technique is mentioned to be useful for eliminating the scattering problem and consequently achieves adequate sensitivity and precision, therefore, $NaBEt_4$ is reported to be more relevant for cadmium derivatization compared with hydroborate scheme.

2.5.3 Arsenic

Arsenic may exist in either inorganic (e.g. As_2O_3) or organic forms. The commonly reported organic forms includes monomethyl arsonic acid (MMAA), diemethylarsenic acid (DMAA) and trimethylarsine oxide (TMAO) as well the organometallic species such as: $MeAsO(OH)_2$, $Me_2AsO(OH)$ and Me_3AsO *(Weber, 1997)*. Furthermore, it may exist in bio-incorporated forms such as arsenobetaine (AB) and arsenocholine (AC) *(Mach et al., 1996)*. The toxicity of arsenic is reported to be totally dependent on the species forms, i.e. inorganic arsenic is found to be more toxic than the organic forms whereas the inorganic form As (III) is shown to be more toxic than As (V). The hydroborate reagents (e.g. $NaBH_4$) are reported capable of derivitizing inorganic arsenicals such as As (III) and As (V) to form arsine (AsH_3). It is also found applicable

for organic arsenicals $Me_nAsO(OH)_{3-n}$ (n= 1-3) to form methylarsenic (III) hydrides and trimethylarsenic (III), as illustrated in the following reactions *(Weber, 1997)*.

$$\left.\begin{array}{l} Me_nAsO(OH)_{3-n} + NaBH_4 \rightarrow Me_nAsH_{3-n}\ ,\ (n = l\text{-}3) \\ Me_3AsO + NaBH_4 \rightarrow Me_3As \end{array}\right\} \quad (2\text{-}12)$$

The total arsenic determination by using the chemical vapour generation technique requires a pre-reduction of As (V) into As (III) before reducing As (III) into the arsenic hydride (AsH_3). This step is normally achieved by using pre-reducing agents such as L-cysteine, thiourea, potassium iodide or thioglycolic acid. Most of the pre-reducing agents require specific reaction conditions (e.g. potassium iodide should be added 30 minutes before the addition of the reducing agent). On the other hand, thiourea has been applied for pre-reducing the arsenic species but failed to derivitize the methylarsine MAs (V) *(Musil and Matousek, 2008)*. Alternatively, L-cysteine is reported as an efficient pre-reducing agent; however, its reaction with some arsenic species was shown to be very slow at room temperature (1 hr) *(Howard and Salou, 1998)*. Moreover, thioglycolic acid was demonstrated to be an efficient and fast pre-reducing agent and suitable for online reductions at room temperature *(Musil and Matousek, 2008)*.

2.5.4 Tin

Inorganic tin is reported to have negligible toxicity effect, while the major toxicity hazards has been attributed to the organic tin compounds, especially tributyltin (TBT) which is found to be highly toxic *(Cai et al., 1993)*. Tin compounds (stannane, methyltin and butyltin) are reported to occur naturally by unknown processes without a need of derivatizing agent *(Weber, 1997)*. However, the hydride generation technique using $NaBH_4$ was used for inorganic tin Sn (IV) derivatization, targeting SnH_4 (named as Stannane) production, as well as organic compounds derivatization according to the following reaction *(Nsengimana et al., 2009)*:

$$Bu_3SnCl\ (aq.) + 2NaBH_4 + HCl \rightarrow Bu_3SnH + 2BH_3 + 2NaCl + H_2 \quad (2\text{-}13)$$

It is also reported that applying the hydridization process to an aqueous sample with a high metals content, such as the industrial wastewater, may inhibit tin hydride

formation. For example, the derivatization of butyl-tin compounds in the wastewater by $NaBH_4$ is prone to interferences due to presence of other metals. The metals would probably lead to several interferences through the formation of inorganic species (metal borides) which react with the organotin hydrides by attacking the Sn-H bonds.
Other possible derivatizing agents for organotin compounds are either Grignard reagents (RMgX) in a suitable solvent or tetralkylborates. The reaction mechanisms of both abovementioned reagents were shown to be as follows *(Nsengimana et al., 2009)*:

$$\left.\begin{array}{ll} Bu_3SnCl + EtMgBr \rightarrow Bu_3SnEt + MgClBr & \text{(Grignard reagents)} \\ Bu_3SnCl\,(aq) + NaEt_4B \rightarrow Bu_3SnEt + Et_3B + NaCl & \text{(Alkyl borates)} \end{array}\right\} \quad (2\text{-}14)$$

2.5.5 Lead

Lead may present in two possible oxidation states, inorganic lead Pb^{2+} and metastable Pb^{4+}; however, the organic forms of Lead are considered to be more harmful to the humans health than the inorganic lead *(Mach et al., 1996)*. Tetra alkyl lead compounds which consist of tetramethyllead $(CH_3)_4Pb$, tetraethyllead $(C_2H_5)_4Pb$ or mixed tetra ethylmethyl lead, are the most anthropogenic Lead compounds, can be transferred to aquatic surfaces from the atmosphere. Other organoLead compounds are: trimethyllead $(CH_3)_3Pb^+$, dimethyllead $(CH_3)_2Pb_2^+$, triethyllead $(C_2H_5)_3Pb^+$ and diethyllead $(C_2H_5)_2Pb_2^+$ *(Heisterkamp and Adams, 1999)*. Lead hydride (PbH_4, known as plumbane) is produced by the reduction of Pb(IV) using hydroborate agents. Since the hydride of Pb (IV) is the only stable form, Pb (II) is required to be oxidized into Pb (IV) before being reduced into the hydrides *(Maleki et al., 1999)*. Commonly used oxidizing agents are: potassium dichromate, hydrogen peroxide, and ammonium peroxodisulfate which is proved to be the best oxidant for Pb (II) *(Chen et al., 1995)*. In addition to these oxidizing agents, chelating agents such as peroxide potassium ferricyanide (K_3 Fe $(CN)_6$, 5% m/v) and Nitroso R salt solution (1.6% m/v) have been used to enhance the lead signal obtained from applying the hydride generation- atomic spectroscopy technique. The hydride generation technique is considered to be unsuitable for organolead speciation due to the instability of alkyl lead hydride molecule and the hydrogen-alkyl exchange *(Rapsomanikis et al., 1986)*. The Tetraalkyl lead compounds (R_4Pb) are

known to be dramatically degraded into inorganic lead according to the following scheme:

$$R_4Pb \rightarrow R_3Pb^{+} \rightarrow R_2Pb^{2+} \rightarrow Pb^{2+} \qquad (2\text{-}15)$$

Where; $R = CH_3$ *or* C_2H_5, in a single or combined form

OrganoLead species can be reduced by using either alkylation with appropriate Grignard reagent or through tetraalkylborates reagent. The ethylation reactions of Lead compounds are represented as follows *(Rapsomanikis et al., 1986)*:

$$\left.\begin{aligned} Pb^{2+} + 2NaBEt_4 &\rightarrow Et_2Pb^{II} \\ 2Et_2Pb^{II} &\rightarrow Et_4Pb^{IV} + Pb^{o} \\ Me_3Pb^{+} + NaBEt_4 &\rightarrow Me_3EtPb \\ Me_2Pb^{2+} + NaBEt_4 &\rightarrow Me_2Et_2Pb \end{aligned}\right\} \qquad (2\text{-}16)$$

2.5.6 Copper

Copper derivatization by using hydroborates is reported in several studies. For instance, *(Sturgeon et al., 1996)* applied $NaBH_4$ for producing copper volatile species to be atomized and detected by ICP-ES. Presumably, CuH or CuH_2 species could be determined; however, the exact identity of the volatile copper species has not been identified certainly. Nonetheless, they reported that the volatile species of copper are most likely molecular in nature rather than atomic.

2.5.7 Nickel

Nickel is investigated with a lot of concern as a result of its toxicological effects. Nickel vapour derivatives can be generated chemically by using either $NaBH_4$–CO system or $NaBH_4$–HCl system. Since nickel is a transition metal, it has the ability to form carbonyl derivative, named as nickel tetracarbonyl Ni $(CO)_4$, through reaction with carbon monoxide under ambient conditions. The main principle relies on reducing the dissolved nickel ion by $NaBH_4$ to produce free atoms which subsequently combines the

carbon monoxide to form gaseous $Ni(CO)_4$. This has been utilized for analytical purposes. Since nickel carbonyl is extremely toxic, other researchers have tried to find alternative paths to achieve the reduction of nickel without using the poisonous gas. For example, *(Guo et al., 2000)* produced volatile nickel at room temperature without using carbon monoxide by applying potassium borohydride under appropriate conditions.

2.5.8 Zinc

Zinc derivatization has been reported in several studies by using hydroborates agents. For instance, *(Sun et al., 2002)* derivatized zinc in acidic aqueous solution by using KBH_4 and detected the hydride after atomization by atomic fluorescence spectroscopy. They added a cationic surfactant (cetyltrimethylammonium bromide) to improve the analytical reaction and the performance of the analytical method. They reported that the presence of the surfactant agent improves the kinetics of the hydride generation process; however, increasing the level of the surfactants leads to foam formation, which is not permissible for the detection process.

2.5.9 Chromium

Chromium mainly exists in two oxidation states, Cr (III) and Cr (VI); nonetheless, Cr (VI) is considered to be highly toxic. In contrast, Cr (III) is essential to the normal carbohydrate and protein metabolism. According to the literature, chromium is detected by several analytical methods; most of them isolate the trivalent form from the hexavalent form in the first stage by using a specific separation process such as ion pair high performance liquid chromatography *(Mach et al., 1996, Hagendorfer and Goessler, 2008, Chen et al., 2010)*. The eluent stream from the separation column is either subjected to atomization followed by spectroscopic analysis or injected with a chemiluminescence reagent (luminal) and detected by a special chemiluminescence detector. Although chromium is considered to be a transition metal, some researchers contemplated the possibility of generating vapour species for chromium by using hydroborate as a reducing agent *(Pohl and Zyrnicki, 2001, Matoušek, 2007, Pohl and Prusisz, 2007)*. Nonetheless, the chemical vapour generation process for chromium and

other transition metals is reported to be strictly related to the efficiency of the gas – liquid separation stage and the stability of the metal hydrides or the hydrido metal complexes formed in the reaction.

2.5.10 Multi elements determination

There is a necessity for a simple, sensitive and accurate method for determining multi metal samples these metal samples down to the trace levels. Although several techniques are adopted in such studies, including HG-AAS, HG-AFS, ICP-AES, MIP-AES, and heated quartz tube atomizer atomic absorption spectrometry (QTA-AAS), only a few studies investigated the simultaneous determination of multi elements in environmental samples. This is due to the difficulty of achieving this kind of analysis. Hence, a protocol for sample pre-treatment and analysis is required where several elements exist in one sample *(Grotti et al., 2005). Grüter et al., (2000)* investigated the simultaneous speciation of organic compounds of twelve elements using a coupled system of HG-GC-ICPMS, and determined 31 compounds of these elements in soil samples from municipal deposits. The volatile species of different compounds were dried and retained in a liquid nitrogen cryogenic trap, then released by sequential heating making use of the difference in boiling points of the retained compounds (a range of -88.5 and 250 ^{o} C with a difference of more than 14 ^{o} C between any two species). Their results indicated the possibility of analyzing metal/metalloid organic compounds (element hydrides, methylated species and compounds of lower organic groups) simultaneously in a few minutes, achieving low detection limits. In another study, the simultaneous determination of hydride forming elements was achieved by coupling the HG technique with cryogenic trapping followed by MIP-AES *(Dietz et al., 1999)*. Two important results were found; the reductant concentration ($NaBH_4$) is a very sensitive factor in the reduction process and should be accurately controlled through the process and the acidic concentration is an important factor in the process. *(Grotti et al., 2005)* studied the simultaneous determination of a group of hydride forming elements by coupling the chemical vapour generation process with ICP-OES. The effect of different parameters, $NaBH_4$ and HCl concentrations as well as the argon gas flow rate, on the detection efficiency were deduced through a multi-variable second order model.

The model indicated that a limited effect on the derivatization efficiency could result from a change in HCl concentration. The model also demonstrated a significant role for the combined effect of reductant concentration and argon gas flow rate on increasing the intensity ratio. This result is attributed to the hydrogen produced in the system, which ultimately improved the excitation and ionization of the ICP source due to the existence of sufficient hydrogen radicals.

The dielectric barrier discharge atomizer has been utilized recently in the determination of multi heavy metals in different samples. *(Zhu et al., 2006b)* derivitized a mixture of multi hydride forming elements using ($NaBH_4$) and atomizing the volatile species through a rectangular channel DBD atomizer and detecting by atomic absorption spectrometry. Their results show that the plasma is only temporarily and spatially active and depends on several factors such as the discharge power, gas flow and gas composition. The study also demonstrated that a hydrogen concentration, which is normally generated from the hydroborate decomposition, is necessary to generate the hydrogen radicals. These radicals are required for hydride atomization; however, extra hydrogen leads to a dilution of the analyte and consequently results in analyte signal depression. In a later study, *(Zhu et al., 2008b)* coupled the DBD atomizer with AFS for the simultaneous determination of another group of hydride forming elements using KBH_4 as a reducing agent. The results indicate that an increase in signal intensity occurs with an increase in KBH_4 concentration up to 2%, and attributed this to the presence of hydrogen in the system. Further increase in the hydrogen concentration leads to a signal depression as mentioned previously.

2.6 Fundamental principles

This section is dedicated to review the principles of the applied detection strategy. The review has included the fundamentals of hydride generation, spectrometric analysis, and some plasma fundamentals.

2.6.1 The hydride generation (HG) process

The determination of hydride forming elements and other elements by applying the hydride generation technique coupled with spectrometric analysis is normally conducted in three steps, as follows *(Dedina and Tsalev, 1995)*:

1- Generating the hydride, where the target analyte is reduced to the hydride in acidic aqueous media, and then released to the gaseous phase.
2- Transporting the released hydride with aid of a carrying (purge) gas to a suitable atomization cell.
3- Detecting the atomized species by applying spectrometric methods.

The efficiency of the HG process is measured by the fraction of the analyte successfully transported in the form of hydride to the atomizer, as represented by the following formula:

$$E_g = \frac{N_0}{c_0 V_s} \quad (2\text{-}17)$$

Where;
N_o : the total number of analyte atoms supplied in the form of hydride to the atomizer
c_o : the analyte concentration in the sample
V_s : volume of the sample

Alternatively, the efficiency can be defined for each individual step as follows:

$$E_r = \frac{N_{released}}{c_0 V_s} \quad (2\text{-}18)$$

E_r : hydride releasing efficiency
$N_{released}$: the total number of analyte atoms released from the liquid sample in the form of hydride

$$E_t = \frac{N_0}{N_{released}} \quad (2\text{-}19)$$

E_t : the hydride transporting efficiency, which represents the fraction of the released hydride that transported to the atomizer

Thus, the efficiencies of the individual stages are correlated by the following formula:

$$E_g = E_t E_r \quad (2\text{-}20)$$

The purge gas strips the hydride out of the sample solution as well as transporting it to the atomizer. The most commonly used purge gas is argon; however, other gases such as nitrogen and helium have also been used.

The general form of the hydride generation reaction is shown as follows:

$$A^{m+} + (m+n)H \rightarrow AH_n + mH^+ \quad (2\text{-}21)$$

Where;
A : the analyte
m & n : the valence of the analyte in the sample solution and the hydride respectively

The hydrogen which is required for the reduction of the analyte is obtained by the decomposition of several kinds of reagents such as hydroborate.
The performance of the hydride generator is normally assessed according to the following parameters:

- *S (t)*: The hydride supply function which represents the number of the analyte atoms delivered to the atomizer in the form of hydride per unit time.
- *F (t)*: gas flow rate.
- The generator outlet function which represents the relation between the amount of the injected hydroborate and the hydride releasing efficiency.

If no significant changes in the acidity, volume, or temperature are assumed during the hydride generation reaction; the hydroborate consumption, c_B, with time is considered to be a pseudo-first order reaction. Accordingly, the reduction reaction can be represented by the following formula:

$$c_B = q \exp(-k_1 t) \quad (2\text{-}22)$$

Where;
q : the mass of hydroborate added per unit of sample volume, k_1 : pseudo-first order reaction rate (1/time), t : time

On the other hand, if the hydride release is considered to be a second order process with a rate constant k_2 (1/conc./time), the analyte concentration in the reaction mixture, c, is expressed by the following formula:

$$\frac{dc}{dt} = -k_2 \; c \; c_B \quad (2\text{-}23)$$

Solving equations (2-22) and (2-23) for *c* leads to the following formula which can be used to determine the analyte concentration in the reaction mixture:

$$c = c_0 \exp\left(-\frac{q\ k_2}{k_1}\right) \quad (2\text{-}24)$$

Equation (2-24) is utilized to determine the amount of the hydroborate which is required for any targeted hydride releasing efficiency, expressed by:

$$E_r = \frac{c_0 - c}{c_0} = 1 - \exp\left(-\frac{q\ k_2}{k_1}\right) \quad (2\text{-}25)$$

The complete hydride release is achieved when $(q \gg k_2/k_1)$; therefore it becomes obvious that a complete hydride release is totally dependent on the ratio (k_2/k_1).
As soon as the hydride enters the atomizer, the atomization process proceeds via thermal decomposition *(Ramesh Kumar and Riyazuddin, 2005)*.

$$AH_{n(g)} \rightarrow A_{(g)} + n/2\ H_{2(g)} \quad (2\text{-}26)$$

Other studies show that the species atomization occurs due to the presence of radicals in the atomizer. The amount of oxygen and hydrogen in a quartz cell atomizer has a great effect on the sensitivity of the analyte signal. Presence of hydrogen gas in the atomizer, produced from the acid decomposition of THB or added to the reaction mixture, leads to the formation of radicals, collisions of the analyte hydride with the hydrogen free radicals, and consequently to analyte atomization at 1000 ^{o}C. The presence of oxygen gas can enhance the formation of hydrogen free radicals and supports the atomization process. In the absence of hydrogen, the atomization process is not be initiated until 1700 ^{o}C. The atomization of volatile hydrides in a heated quartz cell was described by the following mechanism *(Ramesh Kumar and Riyazuddin, 2005)*:

$$\left.\begin{aligned} AH_x + H &\rightarrow AH_{x-1} + H_2 \\ AH + H &\rightarrow A + H_2 \end{aligned}\right\} \quad (2\text{-}27)$$

Hydrogen radicals would be generated according to the following:

$$\left.\begin{aligned} H^{\bullet} + O_2 &\leftrightarrow OH^{\bullet} + O \\ O^{\bullet} + H_2 &\leftrightarrow OH^{\bullet} + H^{\bullet} \\ OH^{\bullet} + H_2 &\leftrightarrow H_2O + H^{\bullet} \end{aligned}\right\} \qquad (2\text{-}28)$$

The radical's recombination is considered to be a slow process; therefore, the concentration of the free hydrogen radicals is usually maintained above the equilibrium concentration. Despite the fact that $OH^{\bullet}$ is produced with lower concentration compared with $H^{\bullet}$, it is speculated to act as an effective parameter in the decomposition reaction, taking the role of a catalyst.

In order to find the distribution of free atoms inside the atomizer, the following assumptions are taken into consideration *(Dedina and Tsalev, 1995)*:

- The atomizer is assumed to be a tubular section with a T-shape configuration, **Figure (2-4)**, represented by two cylindrical coordinates (*r & l*). The released hydrides from the reactor are removed with aid of purge gas and transported to the atomizer via the central tube.

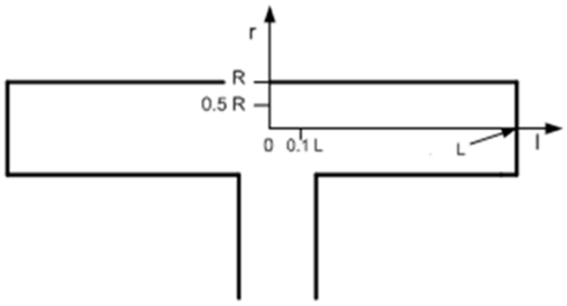

Figure 2-4 a configuration of the tubular atomizer

- The atomization efficiency is 100%, which indicates the hydride is fully atomized at any point in the atomizer.
- The free atoms are removed from the atomizer by the combined action of the forced convection and decay on the surface. This decay is considered to be a first order process *(Dedina and Tsalev, 1995)*:

$$J(t,l) = -k_{het}\, n(t,l,r=R) \quad (2\text{-}29)$$

Where;
J : the decay flow of the atoms per unit volume
k_{het} : the rate constant of the heterogeneous reaction, which is considered to be constant over the whole surface
n : the free atom density
t : time

- No gas temperature change occurs inside the atomizer; accordingly, the gas flow rate through the atomizer is corrected by the following formula:

$$F' = \frac{F \times T_a}{300} \quad (2\text{-}30)$$

Where;
F: flow rate of the supplied gas to the atomizer, T_a: gas temperature in the atomizer (^{o}K)

The analyte atom distribution through the atomizer has been described by several models. The laminar flow model assumes a strictly laminar flow for the gas in the longitudinal direction, whilst the transport in the radial direction occurs by diffusion. The linear velocity of the free atoms in the atomizer is expressed by the following parabolic form *(Dedina and Tsalev, 1995)*:

$$v(r) = \frac{F'}{\pi R^2}\left[\frac{\pi R^2 - \pi r^2}{\pi R^2}\right] \quad (2\text{-}31)$$

Ultimately, the distribution of the free analyte atoms in the cylindrical tube atomizer is represented by the following partial differential equation, assuming uniform diffusion coefficient (D_k) and non uniform atom density:

$$\frac{\partial n(l,r)}{\partial t} + \frac{\partial n(l,r)v(r)}{\partial l} = D_k \frac{\partial}{\partial r}\left[\frac{1}{r}\frac{\partial n(l,r)}{\partial r}\right] \quad (2\text{-}32)$$

If the change of the hydride supply function is considered to be negligible with time, and the transfer of the free atoms only occurs in the longitudinal direction (l), then equation (2-32) can be reduced to the following form:

$$v(r)\frac{\partial n(l,r)}{\partial l} - D_k \frac{\partial}{\partial r}\left[\frac{1}{r}\frac{\partial n(l,r)}{\partial r}\right] = 0 \quad (2\text{-}33)$$

The boundary conditions are described as follows *(Dedina and Tsalev, 1995)*:

$$\left.\begin{aligned} n(0,r) &= \frac{S(t)}{F\prime} \\ \frac{\partial n(l,0)}{\partial r} &= 0 \\ -D_k\left[\frac{1}{r}\frac{\partial n(l,R)}{\partial r}\right] &= K_{het}\ n(l,R) \end{aligned}\right\} \qquad (2\text{-}34)$$

The distribution of the free atoms is interpreted upon solving (eq. 2-33) numerically, as presented in **Section (3.6.1)**.

The hydride generation process is usually conducted in one of two basic modes; the collection mode and the direct mode. In the collection mode, the hydride is trapped in a collection section, which is actually a part of the generator. After collecting all evolved hydrides, they are released and transported to the atomizer in one step within a very short period. The most common method used for the hydride trapping is a cold trap and graphite furnace. In the direct transfer mode, the released hydride from the sample solution is directly transported to the atomizer using batch, flow injection (FI), or continuous flow (CF).

- ***Batch mode***

In the batch generator, the reaction and the gas-liquid separation stages are happen in the same section. The acidified sample solution is placed inside the reaction section and the reducing agent is introduced by syringe or a pump. The purge gas is normally introduced below the liquid level to improve the stripping of the hydride out of the reaction mixture; however, it can be introduced into the head space above the sample solution. The released hydrides are transported to the atomizer to produce free atoms. If hydroborate is used as reducing agent, then the concentration of THB in the reaction mixture can be described by equation (2-35), assuming that the released hydrides in the head space are well mixed. Other assumptions are the existence of a homogeneous reacting media and negligible volume of tubing that connects the gas liquid separator with the atomizer.

$$\frac{dc_B}{dt} = -k_1\, c_B + \frac{f_B}{V_s} \quad (2\text{-}35)$$

Where;
c_B: THB concentration in the reaction mixture, f_B: THB mass flow rate, V_s: sample volume = volume of the reaction mixture, k_1: first order reaction rate (1/time)

Solving equation (2-35) gives the predicted change of c_B concentration through the batch time:

$$C_B = f_B \left(\frac{1-\exp\,(-k_1\, t)}{V_s\; k_1}\right) \quad (2\text{-}36)$$

- ***Continuous flow and flow injection modes:***

In the continuous flow generator, a constant mass flow rate of pure THB (f_B), constant volume flow rates of the sample solution (f_s) and the purge gas (F_o) are mixed in the reaction coil. The mixed stream is directed into a gas-liquid separator where the gaseous hydrides and the evolved hydrogen from the reaction travel to the atomizer, and the liquid residue is released out of the separator. The reaction mixture can be treated as an isolated segments passing through the generator, in which each segment has enough time to finish the reaction before reaching the gas-liquid separator. Therefore, the concentration of THB in a segment can be described by the following equation:

$$q = \frac{f_B}{f_s} \quad (2\text{-}37)$$

The analyte concentration in the liquid phase of a segment is described by equation (2-24)

$$c = c_0 \exp\,(-\frac{q\; k_2}{k_1})$$

The hydride supply function *S(t)* represents the number of analyte atoms delivered to the atomizer in the form of hydride per unit time; therefore, it can be expressed by the following formula:

$$S(t) = E_r\, E_t\, f_s\, c_0 \quad (2\text{-}38)$$

If a sufficient THB inflow is available, the releasing efficiency may approach unity; therefore:

$$S(t) = E_t f_s c_0 \quad (2\text{-}39)$$

The total gas flow rate is represented by the sum of the purge gas flow rate and the hydrogen flow rate liberated from THB decomposition.

$$F = F_0 + f_B V_{Hydrogen} \quad (2\text{-}40)$$

Where; $V_{Hydrogen}$ represents the hydrogen volume liberated per unit mass of THB rate (ml/g)

The experimental arrangement of the flow injection mode is mostly similar to the continuous flow mode with a difference of using an acidic carrier stream at constant flow for the sample. Basically, the sample is injected and dispersed into the acidic carrier stream, and then the sample/acidic stream is mixed with a constant flow of THB solution and of the purge gas. The generated hydrides with the liberated hydrogen are separated from the liquid residuals in a gas liquid separator and travel to the atomizer.

2.6.2 Fundamentals of spectrometric analysis

2.6.2.1 *Atomic spectra*

The atom has a number of discrete energy levels each of them represents an orbit that could be occupied by electrons if gaining sufficient energy to move from the ground state *(Broekaert and Wiley, 2005)*. An unexcited atom has electrons in the lowest permitted energy level. If the atom is excited, the electrons become able to move from the low-energy orbital to an orbital with higher energy (an excited state, known as absorption). Because the excited state is unstable, the electron returns back to a lower-energy state with the emission of a photon of energy (emission). Both absorption and emission processes occur at selected frequencies, wavelengths or energies *(Dean, 2005)*. When a change in the orbit occurs, another energy level is reached and the excess energy is emitted in the form of electromagnetic radiation, which is related to the wavelength according to Planck's law:

$$\Delta E = E_1 - E_2 = h\,v = h\ \frac{c_l}{\lambda} \qquad (2\text{-}41)$$

Where;
E_1 *and* E_2: higher and lower energy states, (erg), h: Planck's constant = 6.623 x 10^{-27} (erg . sec), v: the wave number or frequency which is defined as the number of wave cycles that travel past a fixed point per unit time and is usually described by cycles per second or hertz (Hz), c_l: speed of light = 3 x 10^{10} (cm / sec), λ: wavelength, which is defined to be the distance between two adjacent peaks of electromagnetic radiation (cm)

The energy of radiation is directly proportional to the frequency and inversely proportional to the wavelength as shown in **Figure (2-5)**:

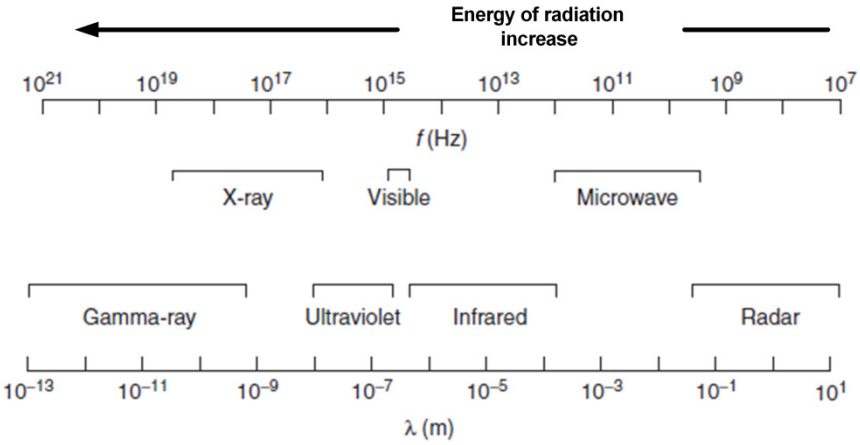

Figure 2-5 the electromagnetic radiation spectrum *(Dean, 2005)*

Infrared (IR) radiations are associated with transitions within the molecule (vibrational and rotational sublevels), where the photons in the (IR) region acquire a limited energy that may only cause vibrations in the molecules, while the photons in the visible/UV regions are more energetic and may causes the electron to be ejected from the molecule, leading to molecule ionization. More possible ionization can occur with existence of higher energy such as UV radiation, while the microwave radiation cannot excite vibrations but can only cause molecules to rotate.

Each electronic transition results in either emission or absorption of energy, which represents a narrow interval of wavelength in the spectrum.

The population of free atoms may exists at various electronic energy levels; accordingly, the distribution of the free atoms in the energy levels has been described

according to Boltzmann distribution equation *(Rouessac and Rouessac, 2007, Cantle, 1982)*:

$$\frac{N_2\,\Delta E}{\tau} = \frac{N_1\,\Delta E\,g_1}{\tau\;g_2}\;exp\left(\frac{-\Delta E}{k\,T}\right) \qquad (2\text{-}42)$$

Where;
N_1 *and* N_2 : the number of atoms in the ground and excited states respectively
g_1 *and* g_2 : the statistical weights of the atoms in the ground and excited states respectively, $g = 2J + 1$, J = the total electronic angular momentum quantum number *(Hill, 2006)*, ΔE : the energy difference between the ground state and the excited state (joules), τ : life time in the excited state, k : Boltzmann constant = 1.38 x 10^{-23} (J/ ^{o}K)
T : absolute temperature in ^{o}K

In principle, the equilibrium between the atoms in two different energy states depends on the energy required to excite the atoms and the temperature of the system. For instance, if a high energy level exists then a small number of excited atoms are produced. In contrast, high temperatures in the system result in an increased number of excited atoms.

2.6.2.2 *Analytical spectroscopic methods*

Spectrometric analysis can be utilized to identify an analyte qualitatively and quantitatively. The light emitted from an excited analyte, which is generated upon subjecting the sample to a highly energetic source (e.g. plasma), can be used for qualitative determination based on monitoring the intensity of the spectral line of interest. For quantitative determination a specific radiation, of similar wavelength to the examined analyte, is allowed to pass through the sample containing the analyte of interest, and the reduction in the imposed light intensity is proportional to the concentration of the analyte. Two types of spectroscopic methods are known; molecular and atomic. In molecular spectroscopy, a low to moderate energy radiation (IR, visible, UV) is required to force the molecule to vibrate, rotate or to transit an outer electron (valence electron) from a lower to a higher energy state.
The molecular energy is normally represented by the sum of three quantities:

$$E_{total} = E_{rotation} + E_{vibration} + E_{electronic} \qquad (2\text{-}43)$$

Molecular spectroscopy is applicable for determination of inorganic or organic molecules in solution in the UV–VIS region or in other forms such as solution, gas, or solid in the IR region. Higher energy levels are required in atomic spectroscopy to achieve the transition of inner electrons within the atom because the atom cannot rotate or vibrate in a similar way to a molecule *(Zhang, 2007)*.

In atomic spectroscopy, various types of high energy sources are applied including: high temperature flames, graphite furnace, plasma, and X-ray. They are utilized to identify and quantify a large number of elements in different media. In this regard, three types of spectroscopic techniques have been developed: Atomic absorption spectroscopy (AAS), atomic emission spectroscopy (AES) and atomic fluorescence spectroscopy (AFS), their principles illustrated in **Figure (2-6)**.

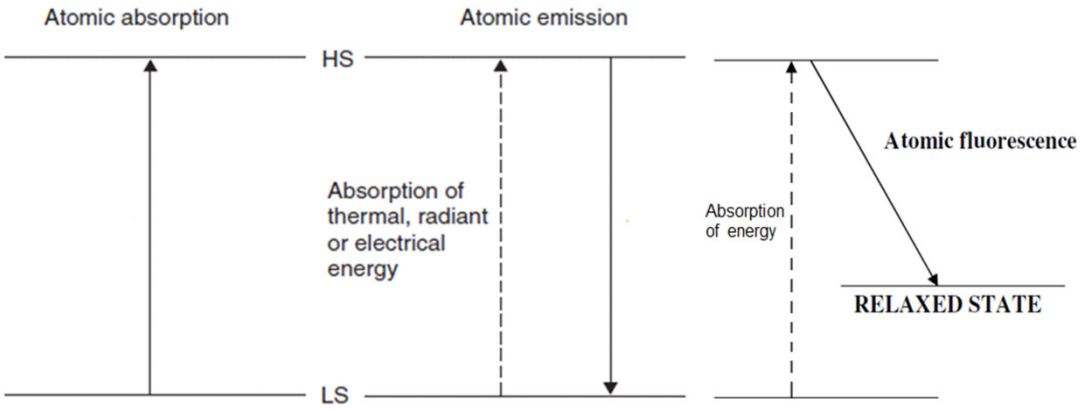

Figure 2-6 the energy transition in the atomic spectroscopy;
Where: HS & LS are the higher and lower energy state respectively

The absorption and emission steps for the analyte (M) are shown as follows:

$$\left.\begin{array}{ll} M + h\nu \rightarrow M^{*} & \text{(atomic absorption spectrometry)} \\ M^{*} \rightarrow M + h\nu & \text{(atomic emission spectrometry)} \end{array}\right\} \qquad (2\text{-}44)$$

For instance, if the analysis of $CaCl_2$ solution is conducted in a flame atomizer, then the possible fragmentation paths can be illustrated in **Figure (2-7)**:

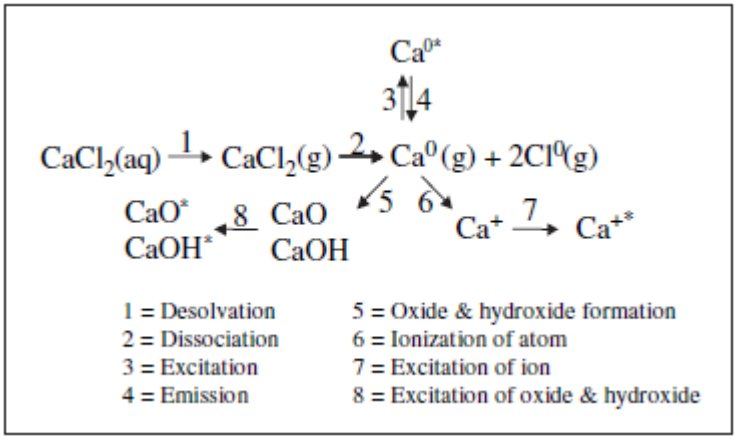

Figure 2-7 the fragmentation of $CaCl_2$ solution in a flame atomizer *(Zhang, 2007)*

If (Ca) is analyzed by applying atomic absorption spectroscopy technique, the radiation absorbed by the gaseous atom (Ca^0) is measured; in contrast, the emission from (CaO*) is measured in using the emission spectroscopy technique. The steps (1, 2, and 3) are desired pathways to the formation of gaseous atoms in the excited state, whilst other steps (4-8) are undesired and may produce interferences.

a) Atomic absorption spectroscopy (AAS)

The AAS technique utilizes the amount of light absorbed by the examined analyte to infer its concentration. This technique is applicable for liquid and solid samples as well as gas samples, in which the analyte should be heated enough (at least to 2000 ^oC) to dissociate all the sample. The produced gas atoms are then subjected to radiation from a light source (185-1100 nm) to make the required transition into higher electronic energy levels. The concentration can be inferred by measuring the light absorbed by the vaporized ground state atoms in the absorption cell, which irradiates from the excited atoms of the element of interest. The relation between the absorbed light and the concentration of the analyte is described by Beer- Lambert's law *(Rouessac and Rouessac, 2007)* which presumes a linear relationship between the concentration of the analyte and its absorbance:

$$A = \varepsilon \; l \; C \qquad (2\text{-}45)$$

Where;

A: absorbance, also called molar absorptivity (dimensionless), ε: the molar absorption coefficient (L/mol/cm) at a specific wavelength, at which the measurement is conducted l: the path through which the incident light pass (cm), C: the molar concentration (mol/L)

In practice, the accuracy of absorption spectroscopy depends on the value used for the analyte molar absorption coefficient; where a value ($\varepsilon \geq 10000$) is expected for the compounds of strong absorption, while (ε = 10 to 100) if the absorption is weak.
The fraction of the original light that passes through the sample is called transmittance (T) which relates to the absorbance (A) by the following relation:

$$A = -log_{10}\,(T) \tag{2-46}$$

$$T(\%) = \frac{I}{I_0} \times 100\% \tag{2-47}$$

Where;
I_o: intensity of the incident light, I: intensity of the transmitted light
Then;

$$A = -log_{10}\,(T) = \; log_{10}\left(\frac{I_0}{I}\right) \tag{2-48}$$

If the sample cell (e.g. an atomizer) has a reproducible path length (l), then Beer's law applies, subject to availability of a homogeneous analyte. Where a flame is used for atomization, the population of free atoms in the flame is far from homogeneous, therefore another description for the absorbance is presented by the following equation *(Cantle, 1982)*:

$$l_A = \frac{\pi\, e^2}{m\; c_l}\, N\, f \tag{2-49}$$

Where;
l_A : the total amount of the absorbed light, e : charge of the electron, m : mass of the electron, c_l : speed of light , N : the total number of atoms in the light path
f : the oscillator strength, which is an indication of how strongly each atom will absorb at that wavelength. For a given element the oscillator strength is highest for the transitions between the ground state and the first excited state; thus, this transition is the most sensitive analytically.

The atomic absorption spectroscopy technique is a combination of analyte atomizer, light source and detection devices. In general, hollow cathode lamps are used as a light source in which the metal of interest is used as a material for the cathode. On arrival at the cathode, the positively charged ions strike the cathode and stimulate the atoms of the cathode to be ejected (sputtered). The sputtered atoms are excited and consequently emit radiation equivalent to the cathode metal *(White, 2011)*. If a mercury lamp is used as a light source and the measuring cell is loaded with a mercury sample, then a presence of mercury atoms in the optical path leads to absorb such amount of light depends on the concentration of mercury atoms; thereby attenuates the light intensity received by the detector.

Absorption line widths are extremely narrow and can only be isolated using instruments with very high spectral resolution. It is difficult to isolate a natural line width ($\approx 10^{-5}$ nm) that is not exposed to any broadening effects. Practically, the natural line width is broadened as followings *(Cantle, 1982, Yubero et al., 2006)*:

- Doppler effect $\Delta\lambda_D$, caused by the motion of the absorbing atoms in their bulk. Due to this effect, the atoms absorb the radiation at slightly different wavelengths which consequently causes a broadening of the absorption line.
- Van der Waal broadening $\Delta\lambda_w$, occurs when the emitting particle is perturbed by dipolar forces from other molecules in the bulk, which disrupts the spectral line. This effect occurs due to non-uniform distributions of positive and negative charges on various atoms, which results in different electro negativity and consequently disturbs the emitting particle over a very small distance.
- Lorentz broadening, which is a consequence of collisions between the absorbing atoms and other species. The collisions may cause atom relaxation and consequently leads to a short lifetime ($\Delta\tau$) and increased energy (ΔE), according to the following equation:

$$\Delta E = \frac{h}{2\,\pi\,\Delta\tau} \qquad (2\text{-}50)$$

- Stark broadening,$\Delta\lambda_S$, occurs due to the fast movement of the electrons close to the atoms. This movement results in a strong varying electric field and leads to splitting the electron levels of the atoms.

- Zeeman broadening which occurs by variations of the magnetic field in the vicinity of the atoms.
- Other broadening effects are attributed to optical instrumental error and referred to as the instrumental broadening ($\Delta\lambda_I$).

Spectral lines at pressures higher than 100 Torr have particular profiles; Gaussian profile ($\Delta\lambda_G$) which combines the effects from Doppler and instrumental broadening, and the Lorentzian profile ($\Delta\lambda_L$) which includes Stark and Van der Waals broadening, equation (2-51). The effects from other broadenings sources, can be neglected at pressures > 100 Torr *(Calzada, 2005)*.

$$\left.\begin{aligned} \Delta\lambda_G^2 &= \Delta\lambda_D^2 + \Delta\lambda_I^2 \\ \Delta\lambda_L &= \Delta\lambda_s + \Delta\lambda_w \end{aligned}\right\} \qquad (2\text{-}51)$$

The combined effects from multiple broadening sources has been described by the Voigt profile which represents the contribution from different broadenings (Lorentzian and Gaussian profiles). The Voigt profile has the following formula *(Torres et al., 2003, Luque et al., 2005)*:

$$\Delta\lambda_{voigt} \approx \left[\left(\frac{\Delta\lambda_L}{2}\right)^2 + \Delta\lambda_G^2\right]^{1/2} + \frac{\Delta\lambda_L}{2} \qquad (2\text{-}52)$$

The above reasons may lead to broadening the line width to a value of ($\approx 10^{-3}$ nm) which is a considerable increase over the natural line width. Even so, the line width is still very narrow and so difficult to observe by conventional instruments. Therefore, it is essential that the light source emits at exactly the same wavelength as the sample atoms, which absorb only at their own characteristic wavelengths. Although the atomic absorption lines of each element are very narrow and easily distinguished, error can be produced from broadband (or background) absorption which is due to many reasons (e.g. presence of water molecules). Several methods are applied for background correction such as Zeeman background corrector. All rely on measuring the absorption

of the resonance line which represents the desired signal plus the background absorption. Then a second measurement due solely to the background is measured and the difference between the two measurements represents the true atomic absorption measurement. In the case of the Zeeman correction, the sample is exposed to an alternating magnetic field, where the sample atoms absorb at the resonance line when the magnetic field is turned off; and the background is measured when the magnetic field is turned on. From the combined data, the net atomic absorption is inferred.

b) Atomic emission spectroscopy (AES)

In this technique, the sample is subjected to a very high energetic level which results in excitation and/or ionization of the sample atoms. When the excited species leave the high temperature region, energy is released in the form of visible and ultraviolet photons due to the transition of the excited atoms into lower energy levels or to the ground electronic state. The intensity of the light emitted at a wavelength specific to the element of interest is measured to infer the element identity. In the emission spectroscopy technique, the ability of atoms to emit radiation is identified by the oscillator strength (f) value, which relates to the transition probability of atoms between the energy levels according to the following equation *(Cantle, 1982)*:

$$A_{ij} = \frac{8\,\pi^2\, e^2\, f_{ij}}{\lambda^2\, m\, c_l} \qquad (2\text{-}53)$$

Where;
A_{ij}: the transition probability between the energy levels i and j, f_{ij} : the oscillator strength of the associated emission line at wavelength (λ) which represents a measure of how closely an atom resembles a classical oscillator in its ability to emit radiation (i.e. higher f_{ij} lead to greater emission intensity), e : charge of the electron, m : mass of the electron, c_l : speed of light

Spectral lines at short wavelengths require higher energy to be excited. The absolute intensity (I_{qp}) of a spontaneous emission line originated due to an electronic transition from a higher state (q) to lower state (p) is represented by the following equation *(Hill, 2006, Marcus et al., 2003)*:

$$I_{qp} = A_{qp}\, h\ \ v_{qp}\ \ n_q \qquad (2\text{-}54)$$

Where;
I_{qp} : absolute intensity, h: Planks' constant, v_{qp}: transition frequency, n_q: the number of the excited level species, A_{qp} : line transition probability

n_q can be related to the temperature (T) through the Boltzmann distribution, (eq. 2-42), which is used to describe the equilibrium between the population of various energy levels within the same ionization state, including both excited and ground states. Boltzmann distribution for a level (q) is described as follows:

$$\frac{n_q}{N} = \frac{g_q}{Z(T)}\ exp\left(-\frac{E_q}{k\,T}\right) \qquad (2\text{-}55)$$

Where;
N: the total number of analyte species (ion or atom), g_q: is the statistical weight of the level (q), $g = 2J + 1$, J = the total electronic angular momentum quantum number
E_q : is the excitation energy of the level (q), $Z(T)$: is the partition function (a function of temperature).

$$Z = g_0 + g_1\, exp\left(-\frac{E_1}{k\,T}\right) + \cdots + g_q\, exp\left(-\frac{E_q}{k\,T}\right) \qquad (2\text{-}56)$$

In practice, (Z) represents the relation between the populations at the excited level and the total population of the atoms or ions. It is reported that in the range 3000-7000 ^{o}K, a limited effect of temperature on the partition function is observed, therefore it can be neglected *(Hill, 2006)*.

The intensity of the selected line can be related to the concentration of the emitting species. The intensity of the emission line is proportional to the following factors:

- the energy difference between the upper (q) and the lower (k) transition levels
- the electrons in the upper level, n_q
- the transition probability between the levels per unit time, (A)

Therefore;

$$I \propto \left(E_q - E_k\right) A\, n_q \qquad (2\text{-}57)$$

Since $(E_q - E_k) = h\ v = h\ \frac{c}{\lambda}$, and ($n_q$) could be related to the total population (N) through (eq. 2-55); hence, the intensity (I) could be described by the following equation:

$$I = \Phi \left(\frac{h\,c\,g_q\,A\,N}{\lambda\,Z}\right) exp\left(\frac{-E_q}{k\,T}\right) \quad (2\text{-}58)$$

Where; Φ represents the emission coefficient

If a stable radiation source is applied at a constant temperature, then (Z) remains constant and the number of atoms (or ions) becomes proportional to the concentration of the analyte. Since the values of (g_q, A, λ, and E_q) are constant for a given line of element, the intensity (I) is proportional to the total number of analyte species, which enables quantitative analysis.

The AES technique requires a high energy source like an inductively coupled plasma (ICP) to provide the analyte with the energy required for excitation. The emitted light from the plasma is viewed either radially or axially; however, *(Zhang, 2007)* has indicated that axial viewing from an ICP–OES source provides better detection limits.

In practice, applying AES techniques offers the possibility of exciting and detecting all the analyte elements simultaneously; nonetheless, a considerable shortcoming of AES techniques (e.g. ICP-AES) is the production of a large number of emission lines and much potential for spectral interferences.

c) Atomic fluorescence spectroscopy (AFS)

In atomic fluorescence spectroscopy, a fluorophore, the functional group in a fluorescing molecule, absorbs energy at a specific wavelength and emits a longer wavelength at lower energy which is measured *(Zhang, 2007)*. The AFS technique is illustrated in **Figure (2-8)**.

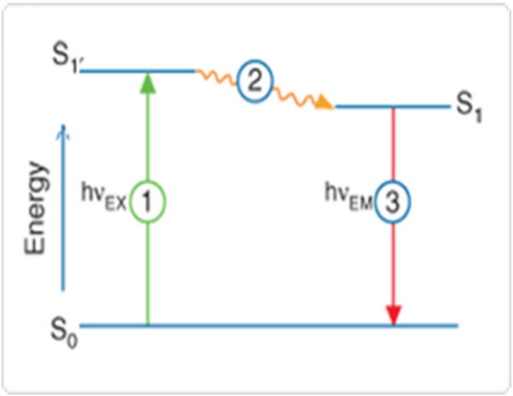

Figure 2-8 Jablonski diagram illustrate AFS steps *(invitrogen-website)*;
S_o represents the ground state, S_1' is the excited electronic singlet state and S_1 is the relaxed singlet excited state.

The energy $h\nu_{EM}$ of the emitted photon is, in principle, less than the energy of the excited photon $h\nu_{EX}$; however, it has longer wave length. The difference in the energy ($h\nu_{EX} - h\nu_{EM}$) is called the Stokes shift which allows the emission photons to be detected separately from the excitation photons. In practice, applying (AFS) leads to highly accurate results because the wavelength and the energy of the fluorescence radiation is specific. The advantages of fluorescence measurements over the absorption measurements are a greater sensitivity and low interference levels.

2.6.3 Plasma fundamentals

Plasma is an electrically neutral, highly ionized gas that consists of several species *(Dean, 2005)*. Plasmas are classified according to their energy level, electron density and temperature, which alter the properties of the plasma. These are governed by the source and the amount of the energy supplied. Another classification is based on the local thermodynamic equilibrium in the plasma bulk *(Bellan and Ebrary, 2006)*. Accordingly, two types are classified; localized thermal equilibrium (LTE) plasmas and non-localized thermal equilibrium (n-LTE) plasmas. In LTE plasma, the transitions and the chemical reactions are governed by collisional processes. LTE plasmas acquire the ability to balance all types of collisions (e.g. excitation/de-excitation, ionisation/recombination,...,etc.), therefore the electron temperature (T_e) exists in equilibrium with the gas temperature (T_g). In contrast, the electron temperature in (n-LTE) plasmas can reach temperatures of 1-10 (eV) while the gas temperature is kept as low as room temperature. Non-thermal plasmas are normally classified into several types:

- DC glow discharge
- AC discharges: frequency values up to 100 KHz applies within this category
- Radio frequency (RF) discharges: (100 kHz $\leq f \leq$ 100 MHz)
- Microwave discharges (MW): $f >$ 100 MHz

2.6.3.1 *DC glow discharge*

Glow discharges can be sustained over a pressure range 10^{-2} mbar to atmospheric pressure, and can be formed by applying a DC field into the gap between two metal electrodes *(Marcus et al., 2003, Avtaeva et al., 2010)*. DC glow discharge is utilized in many applications such as fluorescent light tubes, sputtering sources (e.g. magnetrons), as well in spectrochemistry *(Dean, 2005)*. In a fluorescent tube, the pressure is kept around 0.3 atmospheres. When a voltage is applied between two electrodes at low pressure, a continuous current flow gives rise to the formation of glow discharge caused by the excited neutral atom and the excited species. Electrons, accelerated by the electric field, collide with the gas atoms leading to excitation. The excitation/collisions series is followed by de-excitation/emission of characteristic radiation. The ionisation collisions lead to the formation of new electrons and ions. Ions are directed toward the cathode due to the effect of the applied electric field, where new secondary electrons are generated. At the same time, the original electrons activate a new series of ionization collisions leading to a new generation of ions and electrons. This leads to a self sustaining glow discharge. The ionized atoms can be detected by mass spectrometry analysis while the excited atoms/ions emit photons, normally detected by emission spectroscopy.

The direct current glow discharge do not resembles a radio frequency (Rf) plasma. However, it is worth noting that the difference between DC plasma and RF plasma is not significant at high pressure; therefore, both sources (AC and DC) are capable of producing high temperature plasmas (12000-20000 ^{o}K), *(Mollah et al., 2000)*. The general characteristics (voltage – current) of DC glow discharge are shown in **Figure (2-9)**.

According to Paschen's law, the value of $(p \times d)$, the applied pressure multiplied by the distance between the electrodes, is a limiting parameter controlling the characteristics of the glow discharge and its consistency. Hence, in order to generate the discharge under atmospheric pressure conditions, the gap between the electrodes must be reduced to optimal limit which ultimately results in a value $(p_1 \times d_1)$ corresponding to the value of $(p_2 \times d_2)$ in a vacuum. Typically, Paschen's law applies at $(p \times d)$ values less than 1000 (Torr cm) or gaps in the limit of 1.0 cm at 1.0 atm *(Radmilovi -Radjenovi et al.,*

2010). Furthermore, the $(p \times d)$ value can be utilized to estimate the required breakdown voltage in different gases as represented by **Figure (2-10)**.

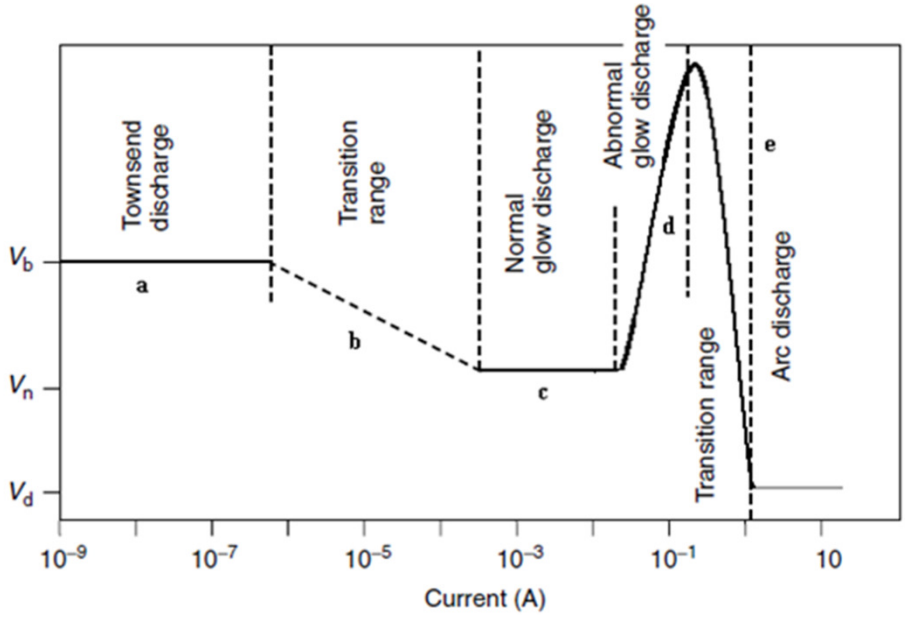

Figure 2-9 the voltage – current diagram;
which illustrates the characteristics of a self sustaining DC glow discharge *(Marcus et al., 2003)*; V_b is the breakdown voltage, V_n is the normal operating voltage, whereas V_d represents the operating voltage of the arc disc

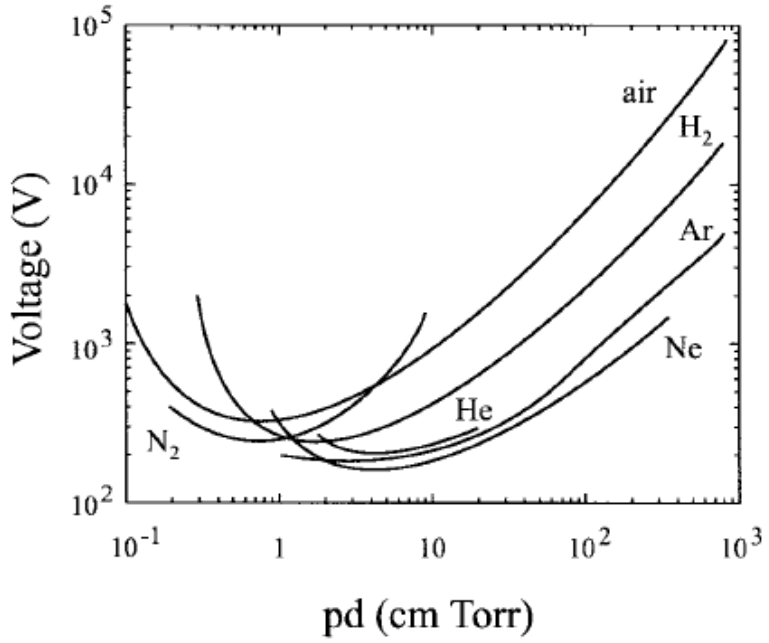

Figure 2-10 the breakdown potential versus pd for a plane-parallel electrode;
pd = is the multiplication of pressure and inter-electrode distance, *(Schutze et al., 1998)*

2.6.3.2 *Atmospheric pressure discharges*

Atmospheric non-thermal plasmas produced by various AC or DC discharge schemes possess certain common properties such as average electron temperature (2-5 eV), electron density (above 10^{12} cm^{-3}) and a relatively low gas kinetic temperature (close to the room temperature) *(Napartovich, 2001)*. This kind of discharge has been widely applied in the industrial applications. For instance, a non-equilibrium air plasma is applied to control air pollution and surface treatment. The general characteristics of some atmospheric discharges are shown in **Table (2-2)**.

Table 2-2 atmospheric discharges categories *(Napartovich, 2001)*

Class (*)	P, W/cm^3	T_{max}, ^{o}K	u m/sec	h, mm	f, kHz
Pulsed corona	1-50	room	≤ 50	≤ 350	1-1000
Pulsed glow discharge	10-500	≤ 600	10-200	10-50	0.05-5
Glow discharge	50-500	room	10-150	5-20	DC
Micro-hollow cathode discharge	$\leq 10^4$	≈ 2000	slow	1-2	DC,RF
Plasma torch	$\approx 10^4$	≈ 3000	100	20	DC
DBD (I)	1-50	room	slow	1-3	0.05-100
DBD (II)	1-50	room	slow	1-5	1-5
RF discharge	3-30	≤ 600	5-10	1-2	13560
Microwave discharge			≈ 10		2.45×10^6

DC glow discharge and DBD regimes are the two techniques which are distinguished by their technical simplicity and attractive properties such as low gas temperature, low sensitivity to the gas composition and low power requirement. A DC glow discharge is able to excite the gas more extensively than a DBD regime, whereas DBD can be operated at lower power. The characteristic of a DBD configuration is a presence of at least one dielectric layer between the electrodes as illustrated in **Figure (2-11)**.

It is worth noting that DBDs configurations cannot be driven by DC voltage. The reason is the requirement for a capacitive coupling of the dielectric which requires alternating voltage to drive a displacement current *(Nehra et al., 2008)*. In a DBD regime, several parameters, such as the composition of the gaseous mixture, the electrodes configuration, the applied voltage and frequency, determine whether the discharge is filamentary or homogeneous (also referred to as atmospheric pressure glow discharge, APGD).

*: P: the power density, T_{max}: the maximum value of gas temperature, u: the gas flow velocity, h: the discharge gap length, f : frequency

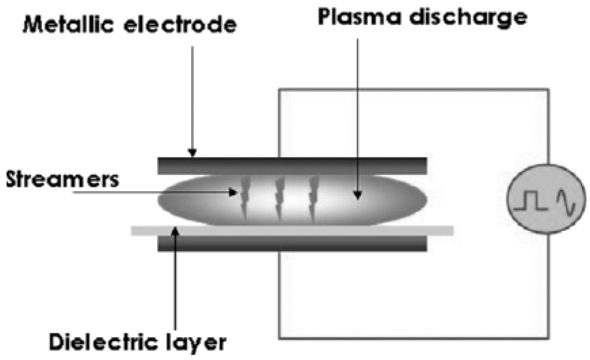

Figure 2-11 DBD plasma configuration *(Tendero et al., 2006)*

It is reported that APGD is found in either Townsend discharge (e.g., APGD in N_2) or glow discharge (e.g., APGD in noble gases). The difference between the two regimes is the DBD in the Townsend regime is characterized by the positive net charge, low densities of charged particles, and the absence of the quasi-neutral plasma (positive column); therefore the highest light intensity is localised near the anode. In contrast, a glow discharge regime is characterized by the formation of cathode sheath as well as the presence of a quasi-neutral plasma region. Therefore the structure of glow discharge shows three distinguished areas (a positive column, Faraday dark space, cathode and negative glow, which are not separated at atmospheric pressure); hence, the bright glow is near the cathode *(Chiper et al., 2005, Golubovskii et al., 2004)*. Generally speaking, Townsend discharge is reported to be highly stable when an inert gas (e.g. Helium and neon) is applied; however, a transition could occur from a Townsend to filamentary discharge when an alteration in the frequency is applied. For instance, the molecular gases (e.g. Nitrogen) require frequency values in the range of some kilohertz which applies a change to the filamentary discharge. It is reported that glow discharge has not been observed with homogeneity due to instability relative to radial perturbations *(Golubovskii et al., 2003)*. In practice, operation under high pressure in small gaps between the electrodes most likely resembles the streamer regime which is characterised by narrow discharge filaments. The discharge regime can only be elucidated with high certainty by producing the Lissajous figure, as presented in chapter four, **Section (4-4).**
DBD plasma is usually operated under atmospheric pressure with an oscillating voltage (1-100 kV), which provides an operational sustainability at kilohertz frequencies. DBD

(I), **Table (2-2),** also called the silent discharge, is the common form of discharge which composes of several micro-discharges (streamers) with non uniform distribution along the electrode surface, while DBD (II) is the homogeneous distribution form of a DBD discharge. It is reported *(Golubovskii et al., 2004)* that a homogeneous glow discharge can be obtained when using a custom made dielectric layer (e.g. polymer, PET, in contact with a fine mesh of metal) while supplying a low frequency voltage (50 Hz). Thus it can be concluded that both the dielectric material and the applied frequency significantly affect the type of generated plasma.

2.6.4 Plasma characteristics

Conventional plasmas (e.g. industrial) are defined to be a quasi-neutral collection of mutually interacting species *(Bellan and Ebrary, 2006)*. The plasma can be approximated by a multi-component fluid composed of two dominant species; electrons and ions in addition to other species. Plasma dynamics have been described by coupling species transport with the electric field and electron energy. The electron conservation equation combines the electron density continuity equation with the electron flux, as follows *(Jayaraman et al., 2008)*:

$$\frac{\partial n_e}{\partial t} + \nabla \bullet \vec{\Gamma}_e = S_e \qquad (2\text{-}59)$$

Where: n_e is the electron density, S_e represents the source of electron creation or destruction due to ionization, Γ_e is the electron flux, described by drift - diffusion approximation equation:

$$\vec{\Gamma}_e = \mu_e n_e \nabla \varphi - D_e \nabla n_e \qquad (2\text{-}60)$$

μ_e is the electron mobility, D_e is the electron diffusion coefficient, φ represents the electrostatic potential.

The electron energy conservation equation is expressed according to the following form *(Farouk, 2009)*:

$$\frac{3}{2}\frac{\partial}{\partial t}\left(n_e T_e\right) + \nabla \bullet \left(\frac{5}{2} T_e \vec{\Gamma}_e - \chi \nabla T_e\right) = P - n_e \sum_i n_k \eta_k \qquad (2\text{-}61)$$

$\chi = \frac{5}{2} n_e D_e$ is the thermal diffusivity, n_k is the heavy particle density, while η_k represents the rate coefficient for energy loss. The first term to the right hand side (P) represents the energy gain due to the electron joule heating, while the second term refers to the inelastic collision of electrons with species k.

Energy transfer in plasma discharge is dominated by convection and thermal diffusion. Consequently, an increase in the internal energy of the species occurs and leads to an increase in the gas temperature. The general heat transfer equation in plasma discharge is of the following form *(Lozano Parada, 2007)*:

$$\rho_m c_p \left[\frac{\partial T}{\partial t} + (v.\nabla)T \right] = k\nabla^2 T + \sigma E^2 + S_{jE} \qquad (2\text{-}62)$$

ρ_m & c_p refer to the heavy particles density and specific heat respectively, k is the thermal conductivity, E is the electric field, σ is the electrical conductivity, while S_{jE} represents the heat source. The right hand side of the equation includes the thermal diffusivity and joule heating terms respectively whereas the left hand side combines the heat accumulation and the convection terms.

Some important characteristics of plasmas are described as follows:

2.6.4.1 *Plasma temperatures*

All plasmas can be characterized by their electron and ion densities as well as their temperature; however, it is not possible to characterize a single temperature for a non thermal equilibrium plasma since it is not at thermodynamic equilibrium. Therefore characterizing a plasma is achieved by measuring four temperatures: excitation, ionization, electron and gas. The excitation temperature is the energy of the excited particles in the plasma, whilst the population density in such an ionization state is referred to as the ionization temperature which characterizes the energy of ionization. The electron and gas temperatures indicate the kinetic energy of the electrons and atoms respectively *(Dean, 2005)*. The rotational temperature, T_{rot}, indicates the vibrational – rotational excitation of the molecules. In practice, plasma temperatures cannot be measured by using common instrumentations for temperature measurement because it

exists out of the measuring range of these devices; therefore these temperatures are normally inferred using spectrometric methods. Two types of methods are applied, passive and active *(Hill, 2006)*. The passive method measures the line emission intensities without any interaction with the plasma (e.g. Boltzmann's distribution), whereas inducing a perturbation such as laser scattering is applied in the active methods. **Figure (2-12)** illustrates the range of various temperatures measured by using ICP.

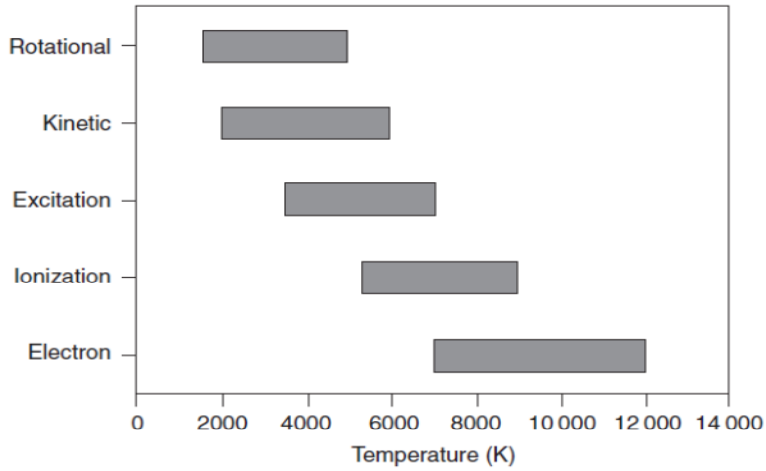

Figure 2-12 the range of the various temperatures observed in the analytical ICP *(Hill, 2006)*

Although the excitation temperature can be deduced from equation (2-58), an alternative method based on the Boltzmann plot is easier due to several difficulties when measuring the absolute line intensity. The Boltzmann plot assumes the existence of localized thermal equilibrium in the plasma, thereby eliminating the need for estimating several temperatures of plasma. The method is based on using different spectral lines of a given element within the same ionization state. Consequently, the necessity to identify the values of the number density (N) and the partition function (Z) is eliminated since these values are constant for the same element, provided that the partition function is independent of temperature.

Therefore the temperature can be deduced from a plot of: $ln\left(\frac{I\,\lambda}{g\,A}\right)$ versus E_{exc}

The plot, in most cases, produces a straight line; thus, the excitation temperature can be inferred from the slope which equals the reciprocal of ($k \times T$). In order to obtain an accurate excitation temperature, it is essential to use an expanded range of excitation energies (E_{exc}) with known values of transition probabilities (A). Thus, the excitation

temperature can be deduced from the slope of the line which equals to (-0.625 / T_{exc}) if the values of E_{exc} are estimated in (cm^{-1}) *(Hill, 2006)*.

The excitation temperature is usually determined using atoms of the discharge gas or atoms of the injected analyte as emitting species *(Gielniak et al., 2011)*. In any case, it is recommended that the examined species should have close emission lines, thereby giving the ability for simultaneous measurement. There should be considerable differences in the excitation energy of the selected emission lines to achieve accurate measurements. In the case of argon plasma, a lot of emission lines are available for the spectrometric analysis. In the case of other plasmas (e.g. helium plasma), limited spectral lines are available which then requires the injection of another analyte (e.g. Fe).

The ionization temperature is normally estimated by utilizing the combination of Saha and Boltzmann equations under the assumption of localized thermal equilibrium condition, as expressed by equation (2-63).

$$\frac{I_{qp}^{+}}{I_{ji}} = \frac{2\, g^{+}\, A_{qp}^{+}\, \lambda_{ji}}{n_e\, g_i\, A_{ji}\, \lambda_{qp}} \left(\frac{2\,\pi\, m_e\; k\, T}{h}\right)^{3/2} exp\left(\frac{-(E_q^{+} - E_i + E_{ion} - \Delta E_{ion})}{k\, T}\right) \qquad (2\text{-}63)$$

Where;

q, p, j, i : indicates the upper and lower energy levels of ions and electrons respectively

$+$: indicates the values of the ions, I : the intensity of the observed line, A : indicates the transition probability for spontaneous emission, g : statistical weight of the level, n_e: the electron number density, m_e : mass of the electron

k, h, T : indicates Boltzmann and Planck constants as well as the temperature respectively, E_q and E_i : the excitation energies of the respective levels

E_{ion} : the ionization potential of the element, ΔE_{ion}: a correction factor for E_{ion}

The plasma rotational temperature can be estimated by utilizing thermometric species (e.g. OH and N_2), and most likely produces a result similar to the gas temperature. This is due to a rapid energy exchange between the rotational and translational levels and the low energy involved in the rotational processes. The rotational temperature is normally determined from the slope obtained from plotting the intensity versus the rotational quantum numbers. These quantum numbers are related to the upper and lower states for a number of rotational lines in the same vibrational band, as illustrated in chapter four.

2.6.4.2 *Electron number density*

Estimation of the electron number density (n_e) is normally achieved by measuring stark broadening of the emission lines. It is also achieved by applying Thomson scattering of laser light or using a current probe *(Gielniak et al., 2011)*. Stark broadening, which originates by interactions of charged particles in the plasma, depends on electron density (n_e) and temperature (T_e). Therefore, n_e can be deduced through analysis of atomic line broadening. In Stark broadening, the hydrogen (H_β) emission line at 486.13 (nm) is broadened due to the effect of the electric field, which is utilized to estimate the electron number density. This technique may require injecting hydrogen gas into the plasma which may lead to changes in plasma conditions. Moreover, the resolution of the spectrometer should be high enough to differentiate between the recorded bands.

In order to obtain an accurate value of Stark broadening, the estimated value of the Doppler broadening and other effects should be subtracted from the measured value of the full width at half maximum (FWHM). Accordingly, the electron number density can be estimated from the following formula *(Jovievi et al., 2000)*:

$$n_e = 10^{16} \left(\frac{W}{4.7333}\right)^{1.49} \tag{2-64}$$

Where; W represents the corrected full width at half maximum of H_β line, in angstroms

It can also estimated by applying the following formula *(Yubero et al., 2006)*:

$$\Delta\lambda_s(H_\beta) = 4.8\ \text{nm} \left(\frac{n_e}{10^{23}\text{m}^{-3}}\right)^{0.68116} \tag{2-65}$$

The Thompson scattering method is difficult to implement in small dimension plasmas and requires a powerful laser system, which makes the method expensive *(Torres et al., 2003)*.

2.6.4.3 *Plasma reactions*

The most probable principal ionization mechanisms are summarized by the following reactions *(Dean, 2005, Hill, 2006, Fridman, 2008, Nehra et al., 2008)*:

$$\left.\begin{array}{ll} M + e\,(fast) \rightarrow M^+ + e\,(slow) + e\,(slow) & \text{(electron impact)} \\ M + Ar^m \rightarrow M^+ + Ar + e & \text{(Penning ionization)} \\ M + Ar^+ \rightarrow M^+ + Ar & \text{(charge exchange)} \end{array}\right\} \quad (2\text{-}66)$$

Where;
M: represents the analyte atom, Ar^m: represents an excited (meta stable) state argon atom, Ar^+: indicates argon ions, M^+ indicates the excited ionized atom

The main excitation processes for the analyte atom are illustrated as follows *(Hill, 2006)*:

$$\left.\begin{array}{ll} e + M \rightarrow M^* + e & \text{(electron impact excitation)} \\ e + M^* \rightarrow M + 2e + hv & \text{(de-excitation)} \\ M^+ + e \rightarrow M^{+*} + hv & \text{(ion-electron radiative recombination)} \end{array}\right\} \quad (2\text{-}67)$$

In principle, ionization by electron impact is subdivided into direct and stepwise ionization. Direct ionization is found in non-thermal plasmas, in which the exerted electric field enhances the electron energy while keeping the excitation of the neutral species at a medium level. Stepwise ionization is where a high concentration of excited neutrals exist simultaneously with the availability of high energy levels, which imposes the highly excited neutrals to be ionised by step-wise collisions.

Other ionization mechanisms are classified as follows:

- Due to collision with heavy particles, that occurs when the total energy of the collision partner exceeds the potential required for ion-molecule or ion-atom collisions.

- Photon ionization, in which the collision takes place between neutral species and photons. Consequently, an electron-ion pair forms.
- Surface ionization, which occurs due to collisions between highly energized particles (e.g. electrons, ions or photons) and the surface. These collisions may lead to the surface heating.

Other significant plasma reactions are attributed to the presence of positive and negative ions in the plasma bulk. Although the activity of the ions is much lower than the electrons, their exothermic reactions with the neutrals can provide an important contribution to the whole reaction series.

The positive ion reactions can be summarized as follows:

$$\left.\begin{array}{ll} e + AB^+ \rightarrow AB^* \rightarrow A + B^* & \text{(dissociative electron-ion recombination)} \\ e + e + A^+ \rightarrow A^* + e & \text{(three body electron-ion recombination} \\ e + A^+ \rightarrow A^* \rightarrow A + \Delta E & \text{(radiative electron recombination)} \end{array}\right\} \quad (2\text{-}68)$$

The negative ion reactions can be summarized as follows:

$$\left.\begin{array}{ll} e + AB \rightarrow (AB^-)^* \rightarrow A + B^- & \text{(dissociative electron attachment)} \\ e + A + B \rightarrow A^- + B & \text{(three body electron attachment)} \end{array}\right\} \quad (2\text{-}69)$$

Other mechanisms are attributed to the destruction of the negative ions and recombination of negative-negative ions as follows:

$$\left.\begin{array}{ll} A^- + B \rightarrow (AB^-)^* \rightarrow AB + e & \text{(associative detachment)} \\ e + A^- \rightarrow A + e + e & \text{(electron impact detachment)} \\ A^- + B^* \rightarrow A + B + e & \text{(detachment in collisions with excited particles)} \\ A^- + B^+ \rightarrow A + B^* & \text{(binary collisions)} \\ A^- + B^+ + M \rightarrow A + B + M & \text{(binary collisions)} \end{array}\right\} \quad (2\text{-}70)$$

2.7 Summary

In this chapter, many aspects related to the field of heavy metals detection and determination are presented. The review of the technologies applied in this field, other than those based on spectrochemistry, has shown reasonable accuracy can be obtained; however, different shortcomings and operational drawbacks are also addressed. Technologies based on plasma spectro-chemistry (e.g. ICP-OES) are shown to be highly accurate and more stable. However, these devices are impractical for miniaturization purposes. Hence, a configuration based on DBD plasma atomization is most appropriate for the research objective since high electron energy is available while the gas temperature is kept at room temperature. Moreover, the chemical derivatization procedures are shown to be the most efficient way (> 95%) for sample introduction to the plasma compared with the traditional desolvation procedures (< 5%).

Accordingly, it is decided to adopt the chemical derivatization procedures coupled with DBD plasma atomization to produce a miniature portable device that could be utilized for in situ – online – real time analysis. On this basis, the fundamentals of the proposed technology were presented, and these will be utilized in mathematical and experimental investigations presented in later chapters.

3. MATHEMATICAL INVESTIGATIONS

3.1 Preface

This chapter is dedicated to applying mathematical simulation studies to explore the proposed technology with the aim of determining the optimal design parameters. The proposed detection method relies on applying a chemical derivatization procedure (HG technique) which is integrated with an atomization stage for detecting heavy metals with aid of spectrometric analysis. The HG derivatization technique is utilized to produce volatile hydrides from the examined analytes. The analyte hydride (in the gaseous form) is assumed to be generated in a helical tubular reactor, separated from the liquid residue in a gas liquid separator, and then transported with a carrier gas to the specified atomizer. Several mathematical investigations are conducted in the current work; the first study investigates the process of generating the analyte hydride according to well known hypotheses, while the second study explores the separation of the generated hydride through a helical tubular section and hydride separation efficiency. In the third study, a simulation of a nebulizer gas liquid separator is carried out to determine the optimal operating parameters for the best separation results, whereas hydride atomization in a quartz cell and dielectric barrier discharge atomizers are investigated in the fourth study to illustrate the formation and distribution of the free atoms along the atomizer. The outcomes of the studies reveal some important aspects that contribute to the design and operation of a fully integrated system for heavy metal detection in water samples.

3.2 The working principles

The working principle of the hydride generation technique involves the reduction of the element from the higher oxidation state to its lowest state (usually II or III), which ultimately appears as the volatile hydride. The generated hydrides transfer with aid of carrier gas to an atomization cell where the hydride molecules dissociate into analyte atoms in order to be detected by spectrometric analysis. As mentioned earlier, the mechanism of the hydride generation process has been studied thoroughly by different research groups *(Dedina, 1986, Wang, 1986, Wang and Barnes, 1987)* who proposed different hypotheses and perspectives. The first hypothesis presumes atomic hydrogen to be the active specie in the derivatization process. The atomic hydrogen, also referred

to as ”nascent hydrogen”, forms during the acidic hydrolysis of the hydroborate compound (e.g. $NaBH_4$). The second hypothesis denies the need for intermediate reactive species and presumes the formation of the hydrides, in a pH range 4.7 to 12.7, occurs due to the action of borohydride compounds (BH_4 or X-BH_3 where X = Cl, Br, I) on the analyte. On the other hand, another experimental study *(D'Ulivo et al., 2005)* demonstrated the formation of molecular hydrogen and hydroboron species during the hydrolysis of tetrahydroborate and claimed that the hydrogen atoms bonding to the boron species are released leading to molecular hydrogen formation. Although the second hypothesis and the experimental evidences presented solid arguments against the first one, the mechanism of nascent hydrogen formation is still valid and accepted as a model by several researchers *(D'Ulivo et al., 2004, D'Ulivo et al., 2011)*. The most important link between the abovementioned hypotheses is: they agree that a hydrogen gas is generated as one of the final products of the hydride generation reaction due to decomposition of hydroborate (THB). The decomposition of THB is considered to be a second order reaction that might last for few microseconds *(Dedina and Tsalev, 1995)*, whereas the generation and transfer of the hydrides from the liquid phase to the gaseous phase are a first order reaction *(Van Wagenen et al., 1987)*.

The atomization process of the hydride has also been studied by many researchers *(Welz and Melcher, 1983, Welz and Schubert-Jacobs, 1986, Ramesh Kumar and Riyazuddin, 2005, Dedina and Rubeka, 1980)*. The general opinion supports atomization by thermal decomposition such as in the case of electro-thermal atomization in a heated quartz tube. However, this theory is found difficult to apply as a general case due to variations in the atomization temperature which is strongly related to the type of equipment. For instance, arsenic atomization is reported to occur at approximately 800 ^{o}C in a heated quartz tube, whereas it is reported to atomize at 1700-1800 ^{o}C in a graphite tube furnace. In addition to the thermal decomposition theory, the atomization mechanism is attributed to the effect of the free hydrogen radicals and the assistance of oxygen radicals in the atomizer. Generally speaking, the hydrogen radicals are found to be the most effective factor on the atomization process. As mentioned in **Section (2.6.1)**, oxygen radicals are also an important factor, in which the hydride decomposition occurs in presence of oxygen radicals alone; nevertheless, no atomization could be achieved at temperatures below 1700 ^{o}C *(Ramesh Kumar and Riyazuddin, 2005)*. On the other hand, OH radicals are reported to play a powerful catalytic role on the hydride generation

process. In practice, the recombination of radicals is reported to be slower than the onward radical generation; therefore, the population of hydrogen radicals is always expected above the equilibrium value.

3.3 Study of the hydride generation process in a tubular reactor

3.3.1 Process description

The hydride generation reaction is investigated in this study by assuming a sample of water contains 0.02 mg/L of arsenic,As(III), with the aim to be converted to arsenic hydride AsH_3 upon being reacted with a reducing agent ($NaBH_4$). The reactant streams are assumed to be injected into a tubular helical coil (2.4 mm diameter) through a T-junction. The inlet streams are assumed to have the following specification on the basis that the feed rate of the reagents (THB and HCL) to the HG generator is normally applied in a ratio 1/1 *(Pohl et al., 2007)*.

Stream 1: 2 ml/min H_2O aqueous solution contains (0.2 % m/v) sodium tetrahydroborate (THB) stabilized by using (0.1% m/v) NaOH

Stream 2: 2 ml/min H_2O aqueous solution contains 0.02 mg/L As(III) and acidified by using 0.1 (M) HCl

3.3.2 Chemical reaction mechanisms

3.3.2.1 *Assuming the evolution of nascent hydrogen from the acidic hydrolysis of THB*

The mechanism of the hydride generation process is represented by the following reaction *(Dedina and Tsalev, 1995)*:

$$NaBH_4 + 3H_2O + HCl \overset{K_1}{\rightarrow} H_3BO_3 + NaCl + 8H^{\bullet} \overset{A^{m+}}{\longrightarrow} AH_n + H_2 \uparrow \qquad (3\text{-}1)$$

Where;
A: the analyte, m^+: the oxidation state of the analyte, n: the coordination number of the hydride, $H^\bullet$: the nascent hydrogen

The general form of the reaction which leads to the formation of the hydrides is described as follows:

$$A^{m+} + (m+n)H \rightarrow AH_n + mH^+ \quad (3\text{-}2)$$

The excess of the un-reacted atomic hydrogen is mentioned to form the molecular hydrogen, which is one of the final products of the acidic hydrolysis of tetrahydroborate, as follows *(D'Ulivo et al., 2005)*:

$$H + H \rightarrow H_2 \quad (3\text{-}3)$$

$$H + H_2O \rightarrow H_2 + OH \quad (3\text{-}4)$$

Another general form is proposed as follows *(Ramesh Kumar and Riyazuddin, 2005, Laborda, 2002)*:

$$A^{m+} + \frac{(m+n)}{8} BH_4^- + 3\frac{(m+n)}{8} H_2O \rightarrow AH_n + \frac{(m+n)}{8} H_3BO_3 + 7\frac{(m-n)}{8} H^+ \quad (3\text{-}5)$$

In this part of study, the generation of arsenic hydride is represented by the following equations according to the nascent hydrogen hypothesis *(D'Ulivo et al., 2011)*, (1st mechanism in the current study), assuming *m=3* and *n=3* and the hydrogen gas is generated directly:

$$BH_4^- + 3H_2O + H^+ \xrightarrow{K_1} H_3BO_3 + 8H^\bullet \quad (3\text{-}6)$$

$$As(III) + 6H^\bullet \xrightarrow{K_2} AsH_{3(aqueous)} + 1.5\, H_2 \uparrow \quad (3\text{-}7)$$

$$AsH_{3(aqueous)} \xrightarrow{K_3} AsH_{3(gas)} \quad (3\text{-}8)$$

Where;
K_1 : 2^{nd} order decomposition rate constant = 1.22 $\times 10^8$ L/mol/min = 2033.3(m^3/mol/sec) *(Dedina and Tsalev, 1995).*
K_2 : the rate constant of the arsenic hydride formation. According to *(Van Wagenen et al., 1987)* , the formation of arsenic hydride was found to be a first order reaction with a rate constant equal to 32 (sec^{-1}).
K_3 : 1^{st} order rate constant of arsenic hydride release from the liquid phase, which was estimated equal to 3.5 (sec^{-1}) *(Van Wagenen et al., 1987)* in a three neck round bottom flask hydride generator.

It is assumed that the value and units of the rate constants mentioned above are applicable for the reactions described in the current case study, and that no changes in the rate constants will occur throughout the reaction series. Moreover, the concentration of (*HCl*) is considered to be equivalent to 10% of ($NaBH_4$) concentration in the description of hydroborate decomposition rate (R_1); this is to obtain the highest As signal to background ratio as demonstrated by *(Pohl et al., 2007).*
Thus; the reaction rates, for the current case, are described as follows:

$$R_1 = K_1 \times 0.1 \times C_A^2 \;\; ; \;\; R_2 = K_2 \times C_C \times C_B^6 \;\; ; \; R_3 = K_3 \times C_E$$

The notations used for the species are shown below:

A=THB(i.e. $NaBH_4$) , B = $H^{\bullet}$, C = As(III), D = H_2 , E = $AsH_{3\,(aqueous)}$, F = $AsH_{3\,(gas)}$,

The concentration gradients of the reactants and the products are described as shown in the following equations:

$$\frac{dC_A}{dt} = -R_1 \qquad (3\text{-}9)$$

$$\frac{dC_B}{dt} = R_1 - R_2 \qquad (3\text{-}10)$$

$$\frac{dC_C}{dt} = -R_2 \qquad (3\text{-}11)$$

$$\frac{dC_D}{dt} = 1.5\,R_2 \qquad (3\text{-}12)$$

$$\frac{dC_E}{dt} = R_2 - R_3 \qquad (3\text{-}13)$$

$$\frac{dC_F}{dt} = R_3 \qquad (3\text{-}14)$$

In order to find the optimal reactor length, further ordinary differential equations are added to the described system, , which aims to simulate the velocity and the position required for the optimal conversions, as follows, *(Zimmerman, 2006)* :

$$\frac{du}{dt} = -R_1 \frac{u}{C_{A0}} \quad (3\text{-}15)$$

$$\frac{dx}{dt} = u \quad (3\text{-}16)$$

Where; u = velocity (m/sec), x = position (m), and C_{A0} = the initial concentration of hydroborate.

The above system of eight ordinary differential equations has been analyzed using the ordinary differential equation solver (ode 23) in Matlab, **Appendix 11.1**, which is principally based on the explicit Runge-Kutta method. The initial conditions are applied as follows:

(C_{THB} = 1.347 mol/m^3, $C_{As(III)}$ = 2.66x10^{-4} mol/m^3 , other species = 0 mol/m^3).

The computations have produced the gradients of species concentration shown in **Figure (3-1)**, which represents a comparison between the results obtained from the analytical solutions of both hypotheses.

3.3.2.2 *Assuming the stepwise decomposition of hydroborate and formation of hydroboron intermediate species*

Other analytical evidence *(D'Ulivo et al., 2004, Wang and Jolly, 1972, D'Ulivo et al., 2011)* supports the hypothesis of forming the hydroboron species with life time longer than the life time of the hydroborate (BH_4^-). The borane complex $[BH_3Y]^n$, where Y represents a neutral or anionic ligand, is hydrolysed in the aqueous phase catalyzed by acid and eventually decomposes to give molecular hydrogen according to the following reaction path *(D'Ulivo et al., 2011)*:

$$[BH_3Y]^n + H_2O \Leftrightarrow [BH_4Y]^{n+1} + OH^- \quad (3\text{-}17)$$

$$[BH_4Y]^{n+1} \rightarrow [BH_2Y]^{n+1} + H_2 \quad (3\text{-}18)$$

The overall hydrolysis rate constant K_{Hyd} of THB (second-order reaction) is estimated equal to 1.6 x10^6 (L/mol/sec) at 25 °C; where H^+ applied in the range (0.2 M – 10 M) *(D'Ulivo et al., 2004).*

The following reactions are adopted in the current case study to investigate the arsenic hydride generation according to the hydroboron intermediates theory, where the formation of arsenic hydride occurs due to the reaction of the analyte with the hydrogen atoms that are released from the intermediate species,$[BH_3Y]^n$,

$$BH_4^- + H^+ + 3H_2O \xrightarrow{K_{Hyd}} 4H_2 + [BH_3Y]^n \quad (3\text{-}19)$$

$$As(III) + [BH_3Y]^n \xrightarrow{K_1} AsH_{3(aqueous)} + [BY]^{n+1} \quad (3\text{-}20)$$

$$AsH_{3(aqueous)} \xrightarrow{K_2} AsH_{3(gas)} \quad (3\text{-}21)$$

Where;

K_{Hyd} = 1.6 x10^6 L/mol/sec = 1600 m^3/mol/sec, $[H^+] = 1$ M, and K_2 = 3.5 sec^{-1}

As mentioned in **Section (*3.3.2.1*)**, the value of (K_1 = 32 sec^{-1}) has been utilized to describe the reaction rate by assuming that the value and units of K_1 are applicable for the current case; moreover, $[H^+]$ is assumed equal to 10% of $NaBH_4$ concentration; this is in order to envisage the case where a stable acidity undertaken throughout the reaction series.

In light of the hydroboron intermediates hypothesis (2nd mechanism in the current study), the reaction rates that contribute to the arsenic hydride production can be approximated according to the following equations:

$$R_1 = K_{Hyd} \times C_B \times H^+ = K_{Hyd} \times 0.1 \times C_B^2 \; ; \; R_2 = K_1 \times C_C \times C_D \; ; \; R_3 = K_2 \times C_E$$

The notations used for the species are shown below:

$B = BH_4^-$, $C = [BH_3Y]^n$, $D = As(III)$, $E = AsH_{3\,(aqueous)}$, $F = AsH_{3\,(gas)}$, $G = H_2$, $J = [BY]^{n+1}$;

The concentration gradients of the reactants and products are described as follows, where the last two equations are added to estimate the optimal reactor length:

$$\frac{dC_B}{dt} = -R_1 \quad (3\text{-}22)$$

$$\frac{dC_C}{dt} = R_1 - R_2 \quad (3\text{-}23)$$

$$\frac{dC_D}{dt} = -R_2 \quad (3\text{-}24)$$

$$\frac{dC_E}{dt} = R_2 - R_3 \quad (3\text{-}25)$$

$$\frac{dC_F}{dt} = R_3 \quad (3\text{-}26)$$

$$\frac{dC_G}{dt} = 4\,R_1 \quad (3\text{-}27)$$

$$\frac{dC_J}{dt} = R_2 \quad (3\text{-}28)$$

$$\frac{du}{dt} = -R_1\,\frac{u}{C_{A0}} \quad (3\text{-}29)$$

$$\frac{dx}{dt} = u \quad (3\text{-}30)$$

The above system of nine ordinary differential equations has been analyzed by using the ordinary differential equation solver (ode 23) in Matlab, **Appendix 11.1**. The initial conditions are considered to be (C_{THB} = 1.347 mol/m^3, $C_{As(III)}$ = 2.66x10^{-4} mol/m^3 , other species = 0 mol/m^3).

The results obtained from the analytical solution of the two hypotheses are shown in **Figure (3-1)**, in which the plots to the left represent the gradients according to the nascent hydrogen hypothesis whereas the plots to the right refer to the gradients according to the hydroboron intermediates hypothesis.

(A)

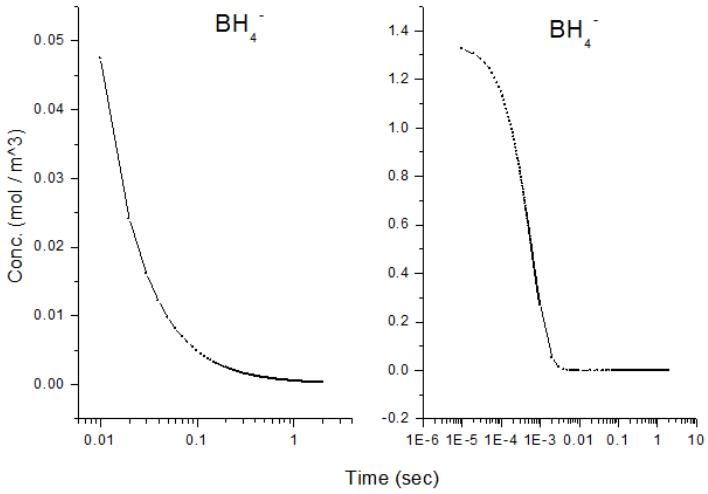
BH4-
BH4-
Conc. (mol / m^3)
Time (sec)

(B)

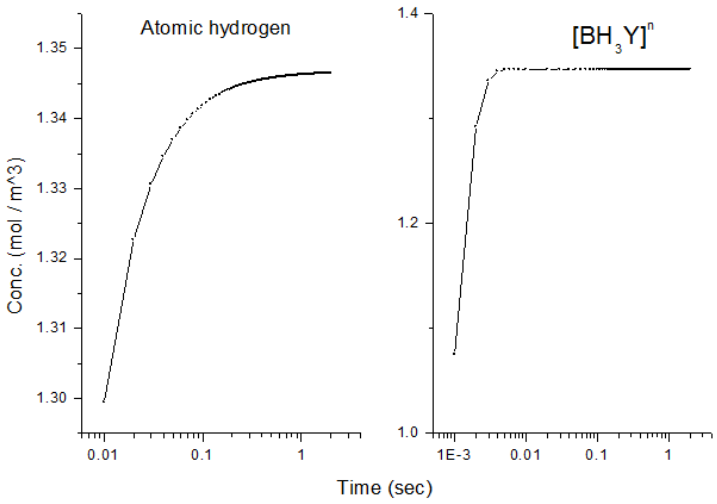
Atomic hydrogen
[BH3Y]n
Conc. (mol / m^3)
Time (sec)

(C)

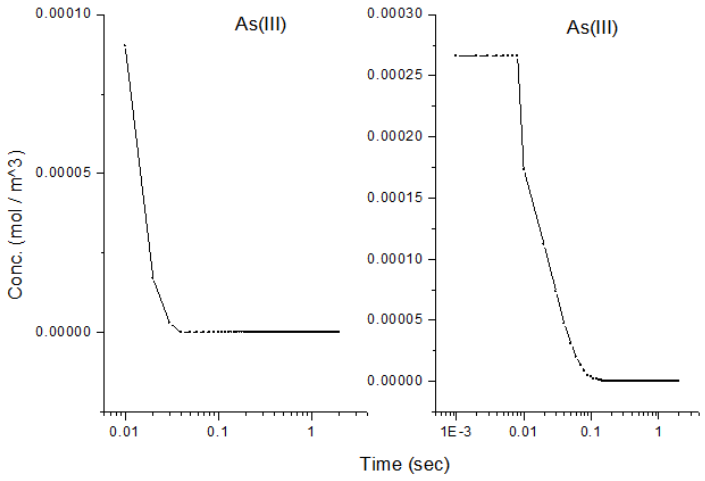
As(III)
As(III)
Conc. (mol / m^3)
Time (sec)

(D)

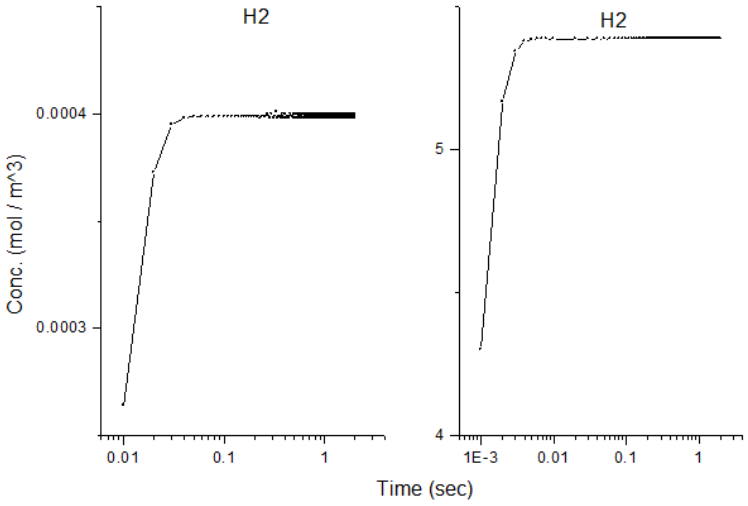
H2
H2
Conc. (mol / m^3)
0.0004
0.0003
5
4
0.01
0.1
1
1E-3
0.01
0.1
1
Time (sec)

(E)

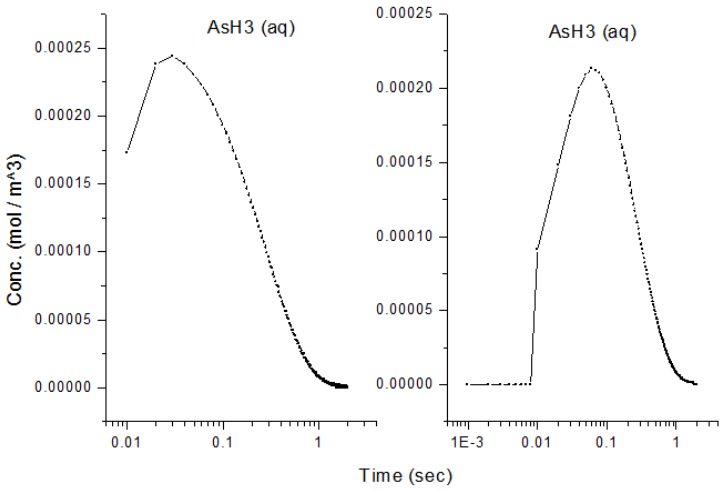
AsH3 (aq)
AsH3 (aq)
Conc. (mol / m^3)
0.00025
0.00020
0.00015
0.00010
0.00005
0.00000
0.01
0.1
1
1E-3
0.01
0.1
1
Time (sec)

(F)

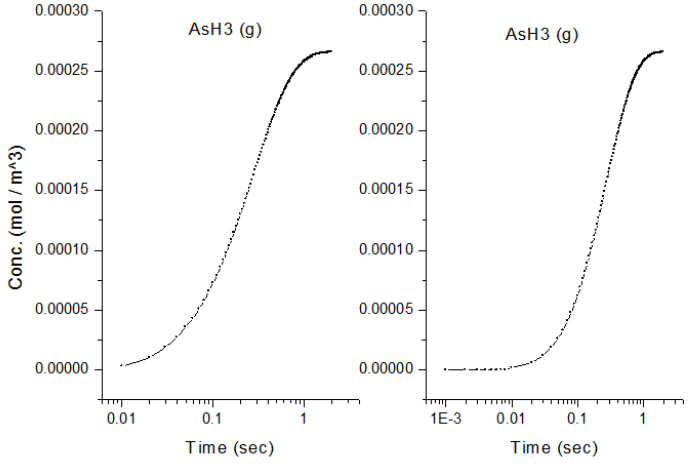
AsH3 (g)
AsH3 (g)
Conc. (mol / m^3)
0.00030
0.00025
0.00020
0.00015
0.00010
0.00005
0.00000
0.01
0.1
1
Time (sec)
1E-3
0.01
0.1
1
Time (sec)

(G)

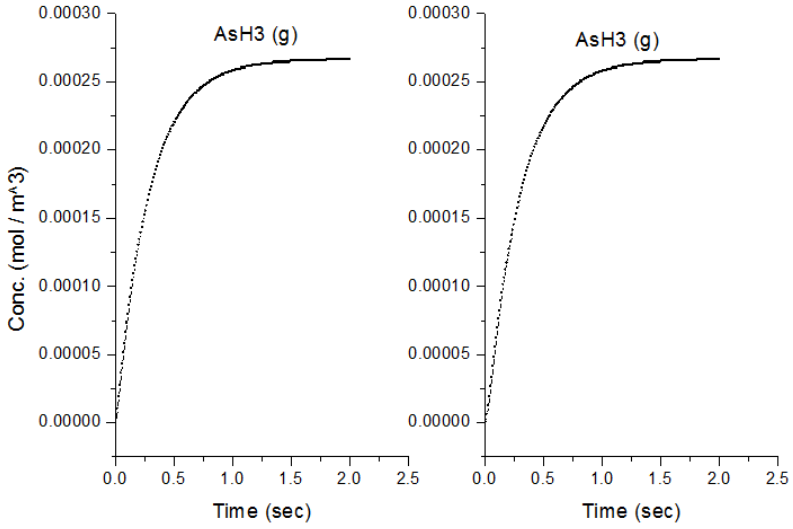

Figure 3-1 the gradients of species concentration with time according to the hypotheses of nascent hydrogen (left side plots) and the hydroboron intermediates (right side plots); ***(A,B,C,D)*** plots illustrate the decomposition of hydroborate, dissipation of the analyte As (III), and formation of the side products and the hydrogen gas respectively, ***(E,F)*** plots illustrate the formation of the intermediate arsenic hydride (in the aqueous phase) and its release to the gas phase (in logarithmic time scale) respectively, ***(G)*** plots illustrate the formation of the arsenic hydride in the gaseous phase (normal time scale).

It can be observed in the plots shown in **Figure (3-1)** that a time slot of 2 seconds has been selected for the analysis. A general overview on the analytical solutions shows that the second mechanism has a faster decomposition by approximately two orders of magnitude (**Figure (3-1/A)**)**.** Since the hydroborate decomposition in both mechanisms is considered to be a second order reaction; decomposition rates occur within 0.1 and 0.005 seconds for the first and second mechanism respectively. The results of the second mechanism are found to be in agreement with the data in the literature (e.g. $14x10^{-6}$ second for 0.2 M $[H^+]$) *(D'Ulivo et al., 2004)*. The results also show that the intermediate species, represented by the atomic hydrogen in the first mechanism and the intermediate complex $[BH_3Y]^n$ in the second mechanism, saturates to a maximum and become stable within 1.0 second in the first mechanism, and within less than 0.01 second in the second mechanism, as shown in **Figure (3-1/B)**. Other differences between the examined mechanisms are found in the depletion of arsenic, the generated hydrogen, the formation of the intermediate arsenic hydride (in the aqueous phase), and their release to the gas phase, as presented in **Figure (3-1/C – E)**. The arsenic

concentration totally depletes from the reaction bulk within 0.03 second in the first mechanism whereas it takes approximately 0.1 second according to the second mechanism. In contrast, the peak value of the generated hydrogen is reached after 0.03 second in the first mechanism compared with 0.003 second in the second mechanism. Moreover, the second mechanism shows that a higher amount of hydrogen is generated due to the hydroborate decomposition by approximately 4 orders of magnitude and this is in agreement with the finding of *(Pohl et al., 2007)* who reported that a hydrogen gas value of 0.6 ml/min is generated from only 0.1 m/v $NaBH_4$ decomposition. Furthermore, both mechanisms show that the aqueous arsenic hydride generates after 0.001 second of the reaction start up and totally depletes within approximately 1 second. However, the first mechanism show that 0.03 second is required to reach the peak $AsH_{3(aqueous)}$ concentration, whereas the second mechanism required more time (about 0.1 second). Both mechanisms exhibit arsenic hydride in the gaseous phase after 0.01 seconds, increasing relatively with time, and reaching maximum values after approximately 1.8 second (**Figure (3-1/F-G)**). This result indicates that the first 5 cm of the reaction tube is required to achieve the full conversion of arsenic to arsenic hydride. The next portion of the reaction tube is where the gaseous phase separates from the liquid phase. In conclusion, the results of the second mechanism have shown greater agreement with the observations reported in literature; thus, the results from the second mechanism are adopted to study the separation of the gaseous hydrides in the helical tubular section.

3.4 Release of the generated arsenic hydride

The second reaction mechanism presumes the arsenic hydride and other side products (H_2, and $[BY]^{n+1}$) to be produced as final products. As mentioned earlier, the second part of the reaction tube, which begins after 5 cm, is where separation occurs. A helical tubular section has been adopted to utilize the beneficial effect of the secondary flow to enhance the releasing efficiency. The secondary motion (flow perpendicular to the main flow direction) is generated in the curved section of the tube due to the centripetal action which forces the liquid phase towards the tube wall. This phenomenon occurs due to a greater density and inertia of the liquid phase compared with the gaseous phase.

As a result, the attraction force between the two phases reduces and leads to the gaseous species separating.

The effect of using two turns of a helical coil is studied by assuming the following conditions, taking into consideration the main products from the hydride reaction (AsH_3 and H_2) and neglecting the side product ($[BY]^{n+1}$) to simplify the computations:

- 2 ml/min water stream contains 2.66 x10^{-4} (mol/m^3) AsH_3 and 5.38 (mol/m^3) H_2 is introduced to the helical coil. These values refer to the species concentration after passing the first part of the reaction tube, **[Figures (3-1)/D&G]**.
- Two turns of a helical coil (2.4 mm ID) with a top and bottom turn radius of 1 cm, is applied. The total height of the spiral is 2 cm and the total length of the assembled tubular section is 12.56 cm.

The coil configuration is shown in **Figure (3-2)**.

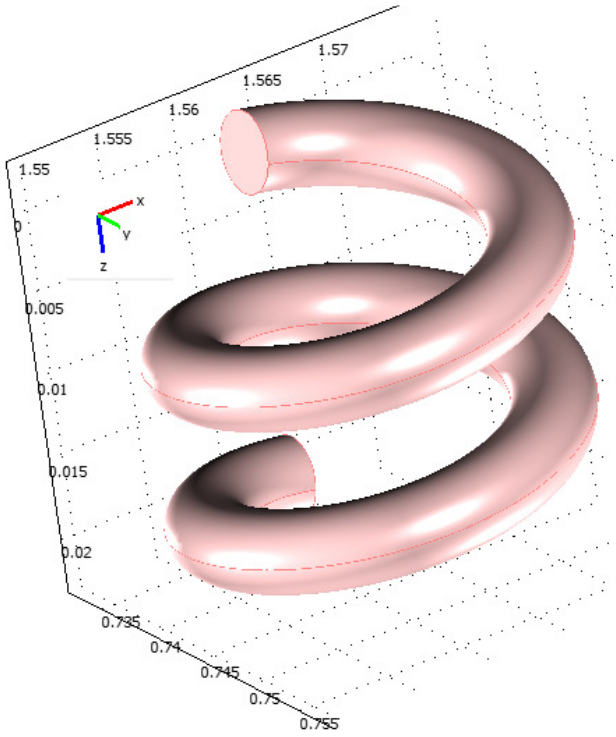

Figure 3-2 the geometry of the helical section

A geometry in three dimensions, representing the helical tube was built in Autocad software and exported to Comsol Multiphysics 3.5a software to conduct the computations. Two models were used in Comsol to investigate the separation process inside the helical section. The fluid flow is described by incompressible Navier-Stokes equations, in which a laminar flow regime and a constant fluid density describe the system in a steady state condition according to the following equations:

$$-\nabla.\eta(\nabla u + (\nabla u)^{T}) + \rho u.\nabla u + \nabla p = F \quad (3\text{-}31)$$

$$\nabla.u = 0 \quad (3\text{-}32)$$

Where η denotes the dynamic viscosity (Ns/m^2), u the velocity (m/s), ρ the density of the fluid (kg/m^3), p the pressure (Pa), and F is a body force term (N/m^3).

The boundary conditions are taken as follows: at the inlet of the tubular section, the velocity vector is normal to the boundary, i.e. $u.n = u_0$; whereas the pressure at the outlet boundary is set ($p = p_0 = 0$). Moreover, a flow is considered to be running down along the bottom half of the tubular section with a specific velocity, u, whereas the top half of the tubular section is considered at no-slip boundary ($u = 0$).

The mass transfer process in the studied helical section is modeled as a convection-diffusion equation:

$$\nabla.(-\mathrm{D_i}\nabla C_i + C_i u) = R_i \quad (3\text{-}33)$$

Where C_i and D_i represents the concentration (mol/m^3) of specie (i) and the diffusion coefficient (m^2/s) respectively, whereas R_i denotes the reaction term (mol/m^3/sec).

At the inlet section of the tubular helical section, the boundary condition is assumed to be ($C_i = C_{i0}$), which equals the initial concentration. The outlet boundary conditions presume that no mass flux occurs due to diffusion, hence is dominated by convection, therefore the total flux is described by:

$$N_i.n = c_i u.n \quad (3\text{-}34)$$

Zero mass transfer is imposed at the interior surfaces due to the assumption of impermeable boundaries. The computations are conducted numerically by applying the finite element method treated by (lagrange – P_2 P_1) elements for pressure stability.

The mesh is refined manually by changing the element size, which results in increasing accuracy. The accuracy of the solution is inferred by estimating a specific parameter (concentration of AsH_3) at a specific point along the helical tube.

A numerical error estimation study is conducted to infer the appropriate grid size for higher solution accuracy. Eventually, a very fine mesh of 84194 elements and 826978 degrees of freedom was applied in the computations, which produced the lowest relative error (*% RE ≈ 2%). The computation results of the finest grid size (0.2175 mm) are adopted for discussion. **Figure (3-3)** illustrates the simulation results represented by the velocity field distribution and the change of species concentration along (z) coordinate.

The results show that a gradual increase in the velocity field along (z) coordinate occurs, which could be attributed to the effect of the secondary motion on the momentum transfer. Moreover, a concentration depletion occurs for all species through the helical section which indicates species transfer from the liquid phase to the gaseous phase as a result of high diffusion rate. The results also show that both AsH_3 and H_2 are completely depleted from the liquid phase within the tested length of the helical coil. However, the hydrogen gas is shown to be depleted faster than the arsenic hydride, and this is clearly attributed to a higher diffusion coefficient of hydrogen ($1.32x10^{-7}$ cm^2/sec) compared with the arsenic hydride diffusion coefficient ($3.45x10^{-10}$ cm^2/sec), where the diffusion coefficients are estimated according to the details given in **Appendix 11.2**. The diffusion coefficients also result in big differences between the estimated Peclet numbers of the examined species at a specific point along the tubular section (1.5×10^8 for AsH_3 and 4×10^5 for H_2 estimated at x= 1.5675, y= 0.745, and z =0.0115), where Peclet number is defined as the ratio of the rate of advection of a physical quantity by the flow to the rate of diffusion of the same quantity driven by an appropriate gradient.

$$Pe_L = Re_L \,.Sc = \frac{L\,V}{D} \qquad (3\text{-}35)$$

Where; Re = Reynolds number , Sc = Schmidt number, L = characteristic length, V= velocity, and D = mass diffusion coefficient

*% RE is the relative error percentage = [(the estimated conc. of the examined grid size – the estimated conc. of the finest grid size) / the estimated conc. of the examined grid size] × 100

(A)

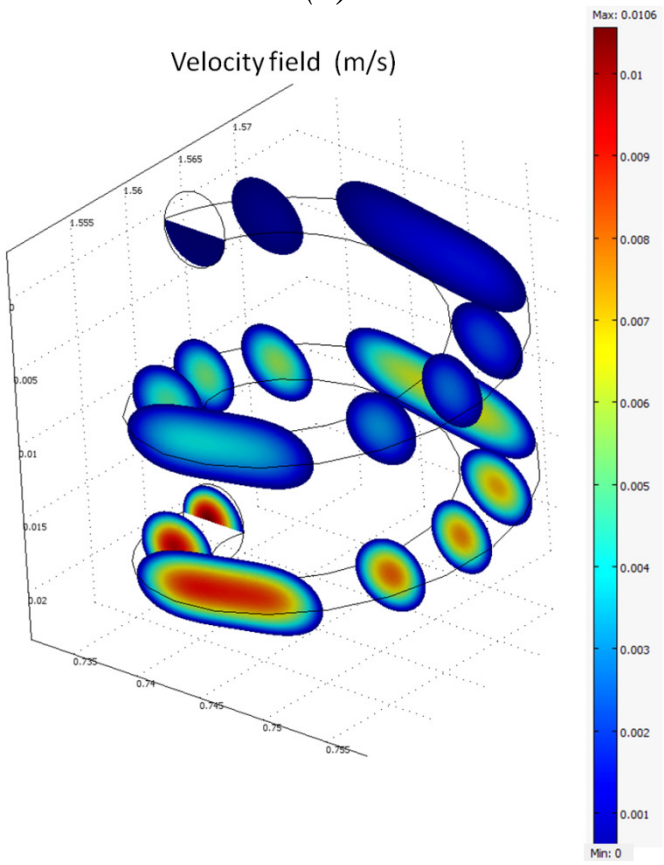

(B)

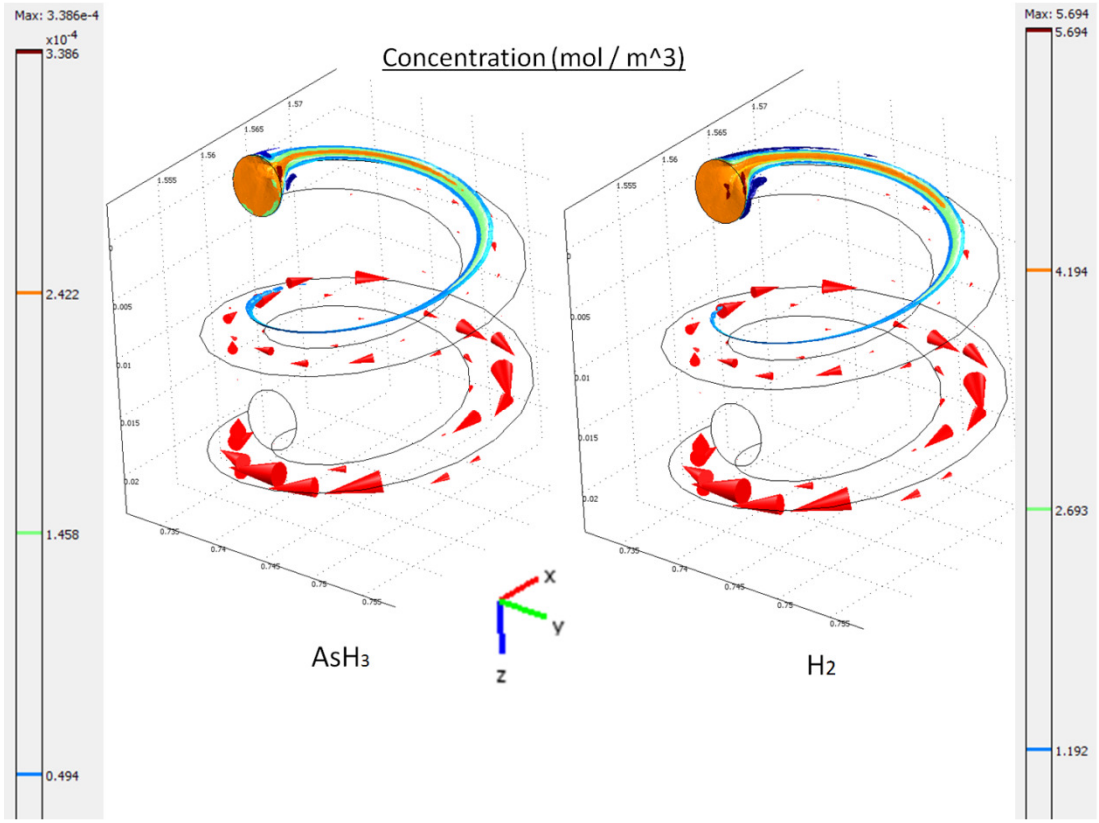

Figure 3-3 the simulation results of the helical tubular section (three dimensions visual representation);

(A) the velocity fields distribution along the helical section, (B) the concentration distribution of the examined species, where the red arrows indicate the velocity fields.

3.5 Simulation of a nebulizer-gas liquid separator

A design for a nebulizer-gas liquid separator is presented in the current study to be utilized for the gas- liquid separation and gas dilution. Due to the effect of the hydrogen gas on DBD plasma consistency, discussed in **Section (5-4)**, the aim of the current simulation is to estimate the optimal helium gas flow rate that is required to dilute the released hydrogen gas and the accompanying alkaline mist into acceptable limits in later DBD atomization stage. The details of the inlet streams are illustrated in **Figure (3-4)**. Stream (1) represents the connection point with the end of the helical tubular section, described in **Section (3-4)**. According to the assumptions made in **Section (3-3)**, stream (1) is flowing at 4 (ml/min) and mainly consists of water as a liquid phase. Further assumption is that stream (1) contains 2.66×10^{-4} (mol/m^3) AsH_3 and 5.388 (mol/m^3) H_2 in the gaseous phase. On the other hand, stream (2) is a helium gas (1000 mol/m^3) flowing at 35 ml/min and 0.3 barg, which is applied to increase the velocity of injection and to fulfil the nebulisation effect at the tapered end of the central tube. Since the hydrogen is the lighter gas in the examined separator bulk (H_2 density is approximately equal half of helium density at 20 ^oC), therefore there is a high probability for hydrogen transfer to the plasma atomizer before other gases exists. Moreover, streams (3) and (4), mainly consist of helium gas at 0.3 barg and 1000 (mol/m^3), are assumed to be injected to the second domain of the separator to dilute the released hydrogen gas in the expanded section. As previously mentioned, the aim of this study is to find the optimal quantity of helium which could result in better hydrogen dilution and eventually lead to a stable plasma performance.

The geometry shown in **Figure (3-4)** is simulated through Comsol Multiphysics 3.5a by applying two domains; the first domain has included the central tube (nebulizer), whereas the second domain has combined the sections around the central tube in addition to the expanded section. The expanded section has been separated into two phases, the top phase is assumed majorly dominated by a helium gas, while the bottom phase is assumed totally occupied by water residues.

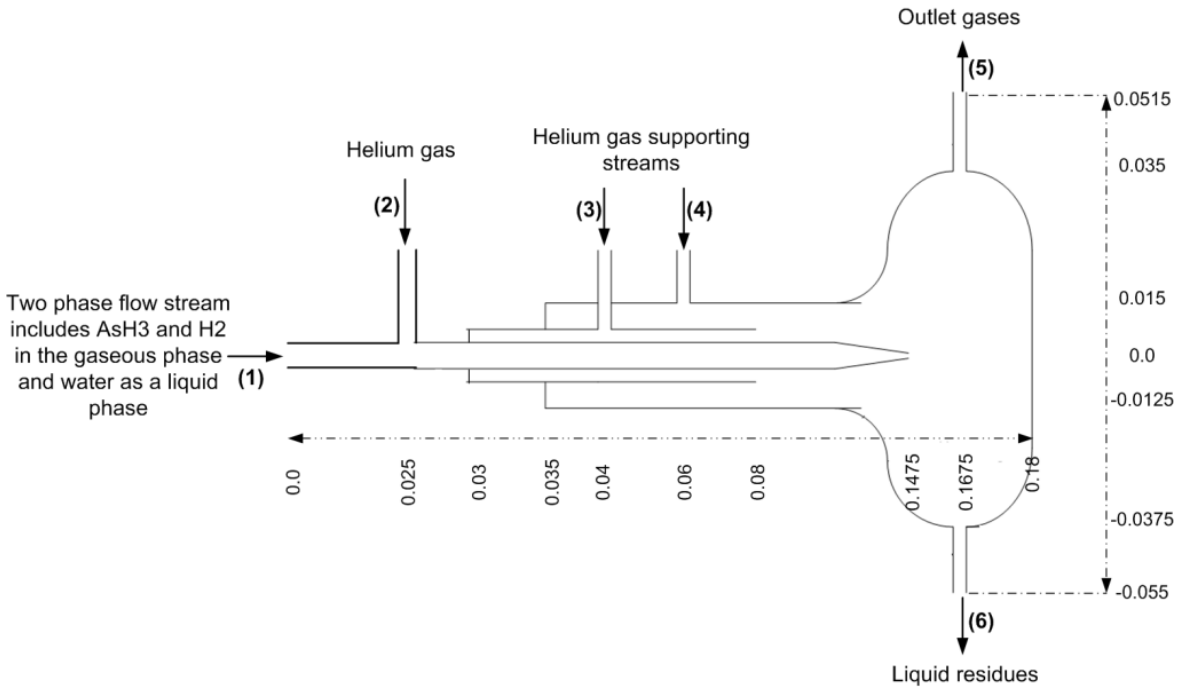

Figure 3-4 a schematic diagram illustrates the working principles and the dimensions of nebulizer gas liquid separator;
(not to scale – all coordinates are described in meter). An annular section (16 mm ID and 20 mm ID for the central and the bounded sections respectively) is connected with streams (3) and (4). A central tube (5 mm ID) with a tapered end is applied to introduce streams (1) and (2). All compartments are connected with an expanded section (20 mm ID). The inlet tube of stream (2) is 3 mm ID whereas 6 mm ID is adopted for streams (3 and 4).

A finite element method is applied in the computations; ultimately, a very fine mesh of 31311 elements and 356231 degrees of freedom was applied to obtain the results with considerable accuracy. To simplify the computations, the central domain is assumed to be a single phase (water) which is injected with the helium gas through stream (2). The momentum transfer is treated in the central tube by applying (k-ε turbulence model), while incompressible-Navier stokes model applied in the second domain. The fluid flow in the second domain, which combines all sections except the central tube, is described by a laminar flow regime and a constant fluid density as shown previously by equations (3-31 and 3-32). The boundary condition assumes the velocity vector is normal to the boundary, i.e. $u.n = u_0$ at the inlet sections for streams (3 and 4), whereas zero pressure is adopted at the outlet boundaries from the expanded section ($p = p_0 = 0$). Another inlet stream to the second domain is applied from the outlet of the central domain (at the

tapered end), in which the velocity is considered proportional to velocity of the central domain.

The turbulent flow mode, which is applied in the central domain, assumes Newtonian incompressible flow which is theoretically guided by incompressible Navier-Stokes equations, represented by the following forms at a steady state condition:

$$\rho(u.\nabla)u = \nabla.[-pI + \eta(\nabla u + (\nabla u)^T)] + F \quad (3\text{-}36)$$

$$\nabla.u = 0 \quad (3\text{-}37)$$

Once the flow regime becomes turbulent, all quantities fluctuate in time and space, therefore the equations shown above should be converted to the form of Reynolds-averaged Navier-Stokes (RANS) equations by inserting the averaged and the fluctuating parts *(Comsol, 2008)*:

$$\rho\, U.\nabla \mathrm{U} + \nabla.(\rho u'(\times)\, u') = -\nabla \mathrm{p} + \nabla.\eta(\nabla U + (\nabla U)^T) + F \quad (3\text{-}38)$$

$$\nabla.U = 0 \quad (3\text{-}39)$$

Where;

U is the averaged velocity field, $(\times)$ is the outer vector product, and u' indicates the velocity of the fluctuating part.

A commonly used turbulence model is the $(\kappa - \epsilon)$ model; where κ is the turbulent kinetic energy and ϵ is the dissipation rate of the turbulence energy. The turbulent viscosity is represented by:

$$\eta_T = \rho\, C_\mu \frac{\kappa^2}{\epsilon} \quad (3\text{-}40)$$

Where; C_μ is a model constant = 0.09

The transport equations for κ and ϵ in a steady state condition are shown as follows *(Comsol, 2008)*:

$$-\nabla.\left[\left(\eta + \frac{\eta_T}{\sigma_\kappa}\right)\nabla\kappa\right] + \rho\, U.\nabla\kappa = \frac{1}{2}\,\eta_T\,(\nabla u + (\nabla u)^T)^2 - \rho\epsilon \quad (3\text{-}41)$$

$$-\nabla.\left[\left(\eta+\frac{\eta_T}{\sigma_\epsilon}\right)\nabla\epsilon\right]+\rho\, U.\nabla\epsilon=\frac{1}{2}\,C_{\epsilon1}\frac{\epsilon}{\kappa}\,\eta_T(\nabla u+(\nabla u)^{\,T})^{\,2}-\rho\,C_{\epsilon2}\,\frac{\epsilon^2}{\kappa} \qquad (3\text{-}42)$$

$$\sigma_\kappa=1.0\ ,\qquad \sigma_\epsilon=1.3\ ,\qquad C_{\epsilon1}=1.44\ ,\ C_{\epsilon2}=1.92$$

The inlet boundary conditions are assumed similar to those described for incompressible Navier-Stokes, as shown in the case of laminar flow conditions. In addition, the values of the turbulent quantities are set to be ($\kappa = 0.005\ m^2 s^{-2}\ and\ \epsilon = 0.005\ m^2\ s^{-3}$). The outlet boundaries are assumed similar to those described for incompressible Navier-Stokes, where convective flux conditions are prescribed for the turbulence variables:

$$n.\nabla\kappa=0\quad,\quad n.\nabla\epsilon=0 \qquad (3\text{-}43)$$

A slip boundary is assumed at the interior surface in which no viscous interaction between the wall and the fluid is expected.

The concentration distribution of the species along the simulated nebulizer - GLS is estimated by coupling the mass and momentum transfer models.

The mass transfer in the studied domains is described through a convection-diffusion process, where the mass balance equation of a steady state condition is shown by equation (3-33). Both domains are coupled in the computations of the mass transfer model by applying helium gas as the dominant component in the second domain and water in the central domain. At the inlet boundary, the concentration is assumed equal to the initial concentration of the examined species, and no mass flux occurs through diffusion at the outlet boundary, which means the mass flux is dominated by convective flux. Therefore the total flux is described according to equation (3-34). A trial and error procedure is adopted in the solution strategy to infer the optimal helium flow rate that is required for the best hydrogen dilution. In each run, a value of the helium flow rate (stream 3 + stream 4) is assumed and the velocity of streams (3 and 4) estimated and applied in the computational model. The calculated velocity fields in both domains are combined in the picture shown in **Figure (3-5)**.

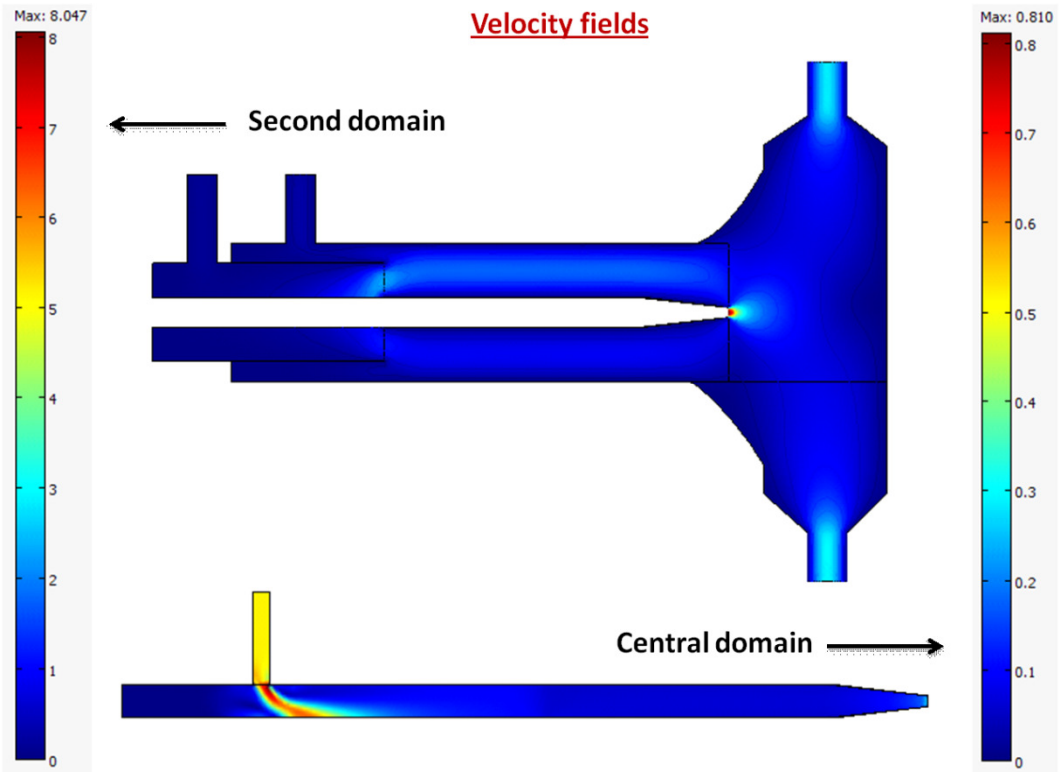

Figure 3-5 the estimated velocity fields for two domains of a nebulizer-gas liquid separator;
the picture has been produced by combining the results from both domains

The computations show that a significant reduction in hydrogen gas concentration would be obtained when applying 216 (ml/min) of helium gas through streams 3 and 4. Applying the helium from the side streams at the abovementioned rate in addition to the helium injected in the central tube results in a dilution ratio (0.26 H_2 / 250 He ≈ 1/1000) which would affect the system performance to a considerable level. The estimated concentration of the hydrogen gas along (x and y) coordinates is shown in **Figure (3-6)**.

(A)

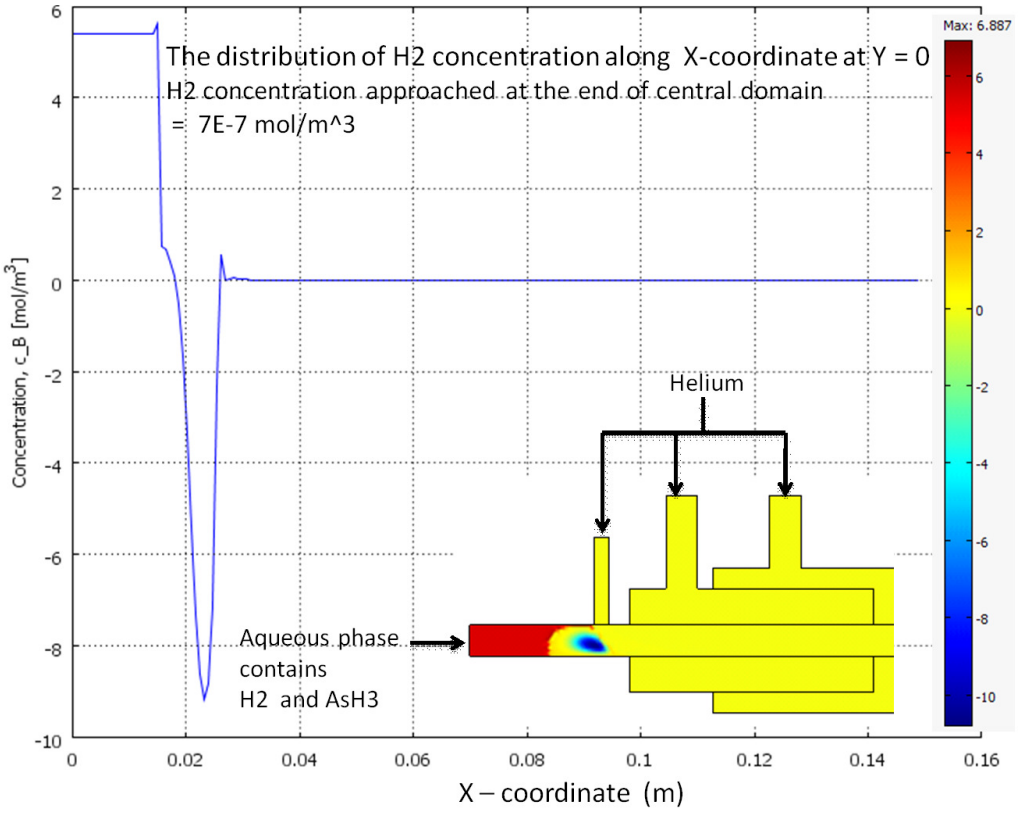
The distribution of H2 concentration along X-coordinate at Y = 0
H2 concentration approached at the end of central domain
= 7E-7 mol/m^3
Helium
Aqueous phase
contains
H2 and AsH3
Max: 6.887
Concentration, c_B [mol/m^3]
X – coordinate (m)

(B)

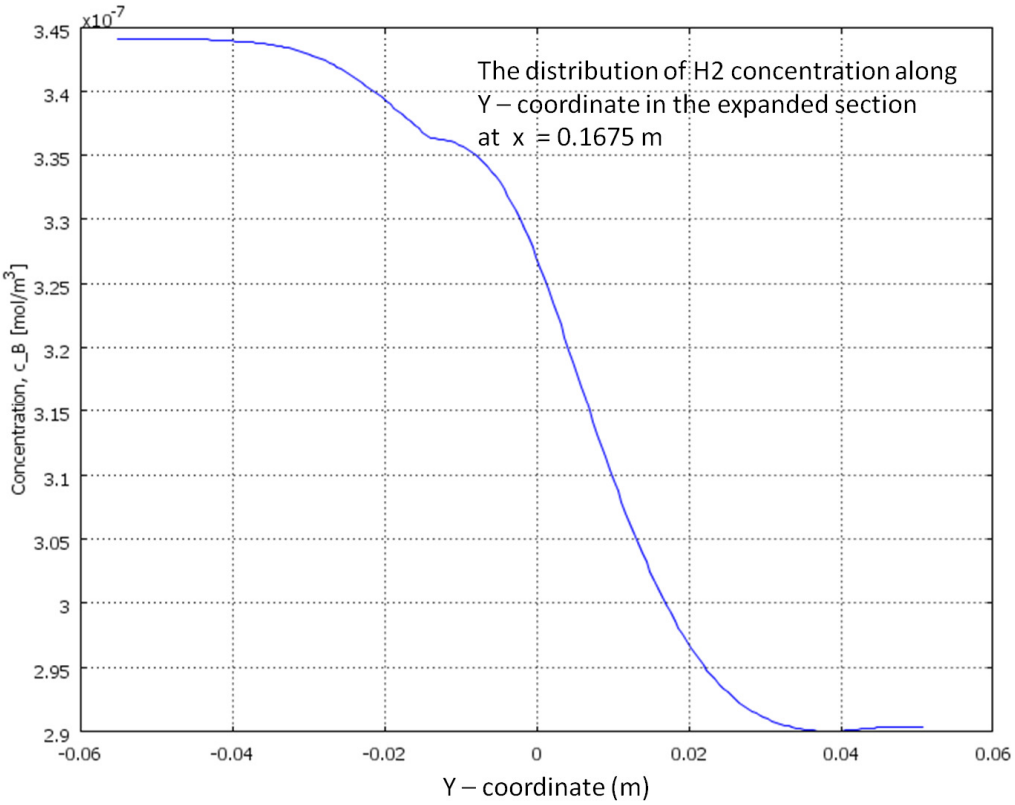
x10^-7
The distribution of H2 concentration along
Y – coordinate in the expanded section
at x = 0.1675 m
Concentration, c_B [mol/m^3]
Y – coordinate (m)

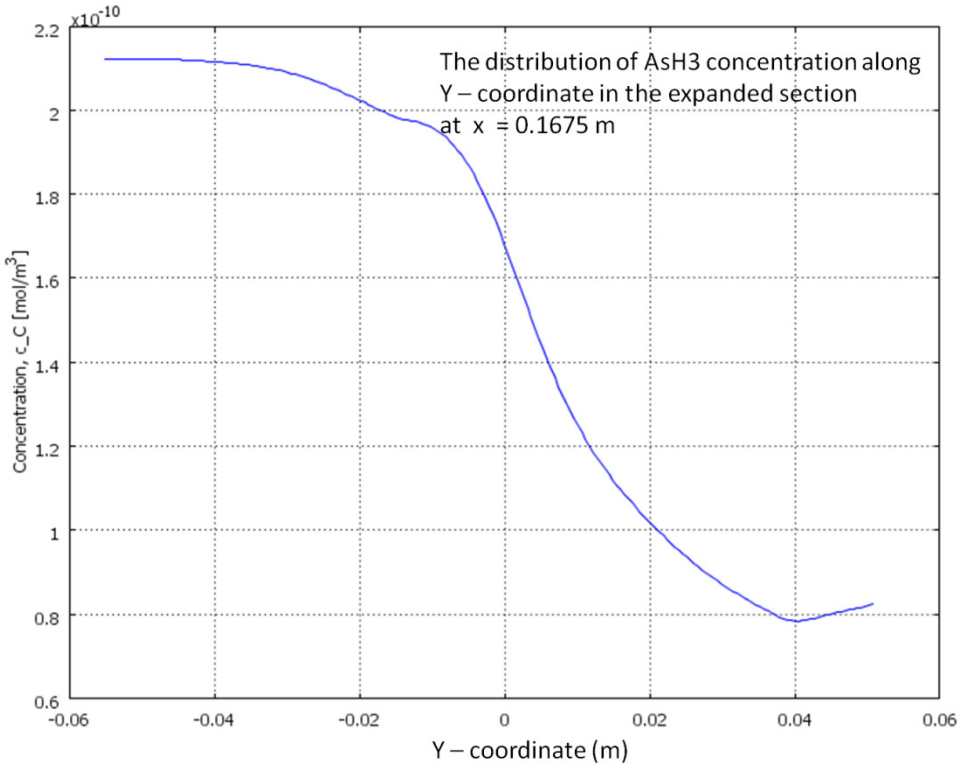

Figure 3-6 the distribution of H_2 and AsH_3 concentration along the nebulizer – gas liquid separator;
(A) H_2 concentration along x-coordinate, (B) H_2 concentration along y-coordinate, (C) AsH_3 concentration along y-coordinate. The helium flow rate in streams (3 and 4) is assumed to be 216 (ml/min), while 35 (ml/min) helium is injected in the central domain.

It can be observed in **Figure (3-6/A)** that hydrogen concentration reduces by seven orders of magnitudes in the central tube before being nebulised into the expanded section. This might indicate a low or negligible effect is induced from the helium injected through the supporting streams (3 and 4). Despite the achieved reduction in the hydrogen concentration along the x – coordinate, the effect of injecting extra helium through streams 3 and 4 is more obvious in the distribution estimated along the y-coordinate. Hence, in **Figure (3-6/B)** the hydrogen concentration in the expanded section reduces gradually as a result of dilution by helium upon transferring from the centre to the top end of the expanded section. In contrast, the hydrogen concentration increases when moving toward the bottom end of the expanded section. This may indicate a portion of the hydrogen gas would be re-dissolved in the water and exit from the bottom end of the expanded section. The computations also show that a significant

reduction (by six orders of magnitude) occurs in the concentration of arsenic hydride upon dilution by helium. Practically, although the plasma may become more consistent and stable due to the hydrogen dilution in the system, the reduction in AsH_3 concentration may lead to a relative reduction in the arsenic signal, which is in contrast to the aim of the current study. To sum up, the computation results have shown some discrepancy (a reduction by seven orders of magnitudes has occurred in the concentration of H_2 and AsH_3 from applying only 35 ml/min helium in the central domain, whereas the application of higher quantities of helium in the second domain results in only limited effect). This result might be attributed to the assumption made for the flow regime in the central domain (presence of a single phase). Nonetheless, the proposed design might lead to stable system performance upon optimizing the real experimental conditions, which will be discussed in **Section (5-5)**.

3.6 The Study of the atomization of arsenic hydride and the distribution of the free analyte atoms in a heated quartz cell and DBD atomizers

This part of study is devoted to investigate arsenic hydride atomization in two types of atomizers. The first one is a heated quartz cell working at 1000 ^{o}K, whereas the second is a dielectric barrier discharge atomizer. The aim of this analysis is to elucidate the processes of formation and subsequent distribution of the produced free arsenic species through the two atomizers.

3.6.1 Atomization of the volatile hydride in a heated quartz cell

The distribution of the free analyte atoms in the cylindrical tube atomizer is described by equation (2-32), assuming a uniform diffusion coefficient (D_k) and non uniform atomic density:

$$\frac{\partial n(l,r)}{\partial t} + \frac{\partial n(l,r)v(r)}{\partial l} = D_k \frac{\partial}{\partial r}\left[\frac{1}{r}\frac{\partial n(l,r)}{\partial r}\right]$$

If a negligible change in the free atoms velocity in the axial direction is assumed, the equation can be reduced to the following form:

$$Dn_t + vn_l - D_k \nabla \cdot (\frac{1}{r} \nabla n) = 0 \quad (3\text{-}44)$$

The values shown below are used in this work, assuming a length of 4 cm and 1 mm diameter for a tubular atomization channel is applied. The other assumption is that the diffusion coefficient of the transferred gases to the atomizer is equal to the hydrogen gas diffusion coefficient in a gas phase.

$D = 1$, $v = 0.084$ m/sec , $D_k = 1.132 \times 10^{-4}$ m^2/sec (for hydrogen – **Appendix 11.2**)

The boundary conditions are described by equation (2-34), **Section (2.6.1)**, as follows:

$$n(0, r) = \frac{S(t)}{F\prime}$$

$$\frac{\partial n(l,0)}{\partial r} = 0$$

$$-D_k \left[\frac{1}{r}\frac{\partial n(l,R)}{\partial r}\right] = K_{het}\ n(l, R)$$

The distribution equation (2-32) shown above is a single partial differential equation in two dimensions, which can be categorized as a parabolic equation with the following general form *(Howard, 2005)*:

$$D\, u_t - \nabla \cdot (c\, \nabla u) + au = f \quad (3\text{-}45)$$

u_t is the partial derivative of the variable (u) with time.

In the axial (l) and radial (r) directions, the general form is written as follows considering the main variable is the free atoms concentration (n):

$$D(t, l, r)n_t - \nabla.(c\,(t, l, r)\nabla n) + a(t, l, r)n = f(t, l, r) \quad (3\text{-}46)$$

The boundary conditions, shown above, are reformulated according to the following assumptions:

1- Dirichlet boundary condition [*n(t; l; r)*]:

$$n(t, 0, r) = \frac{S(t)}{F\prime} = 0.001 \quad (3\text{-}47)$$

F' represents the total gas flow rate flowing within the atomizer optical tube, i.e. it is the total gas flow rate entering the atomizer corrected to the atomizer temperature.
In the current case study the ratio of the analyte atoms (delivered to the atomizer in the form of hydride) to the total gas flow rate flowing within the atomizer optical tube is assumed equal to 1/1000.

2- Neumann boundary conditions, according to the following equation:

$$j^{\wedge} \cdot c\nabla u + q\,u = g \tag{3-48}$$

where; $j^{\wedge}$ represents a unit vector normal to the domain

at $r = 0$ (at the tube centre) ,

$$n_r'(t, l, 0) = 0 \rightarrow q = 0 \;\&\; g = 0 \tag{3-49}$$

at $r = R$ (at the tube inside wall surface) ,

$$n_r'(t, l, R) = -\frac{K_{het}}{D_k} \cdot n(t, l, r) \tag{3-50}$$

The conversion of arsenic hydride into arsenic free atoms is found to be a fast reaction with a rate constant equal to 62 sec^{-1} *(Van Wagenen et al., 1987)*. This value has been utilized in this study by assuming the value and units of (K) are applicable for $(-K_{het})$. Applying the above mentioned values, the term (K / D_k) is estimated equal to 5.47×10^5 m^{-2};
So that,

$$q = 0 \;\&\; g = 5.47\text{x}10^5$$

It should be noted that a value (c = 1) is applied in the general equation as well as the boundary conditions. Moreover, the initial atom density is assumed, $n(t_0) = 0.001\ atoms/m^3$. The above conditions are applied to analyse the proposed atomizer, where the geometry has been set using the graphical user interface in Matlab software. The results of the free analyte density distribution in the adopted atomizer are shown in **Figure (3-7)**. The distribution indicates that a maximum value in the order of 10^8 atom m^{-3} ($\simeq 10^{-15}$ mol m^{-3}) is generated in the centre of the atomization cell, whereas it vanishes at the outlet end. This result is informative because it clearly indicates that the centre of the atomization cell is the appropriate position for spectrometric data

acquisition, which consequently denotes only radial data acquisition is possible in this case.

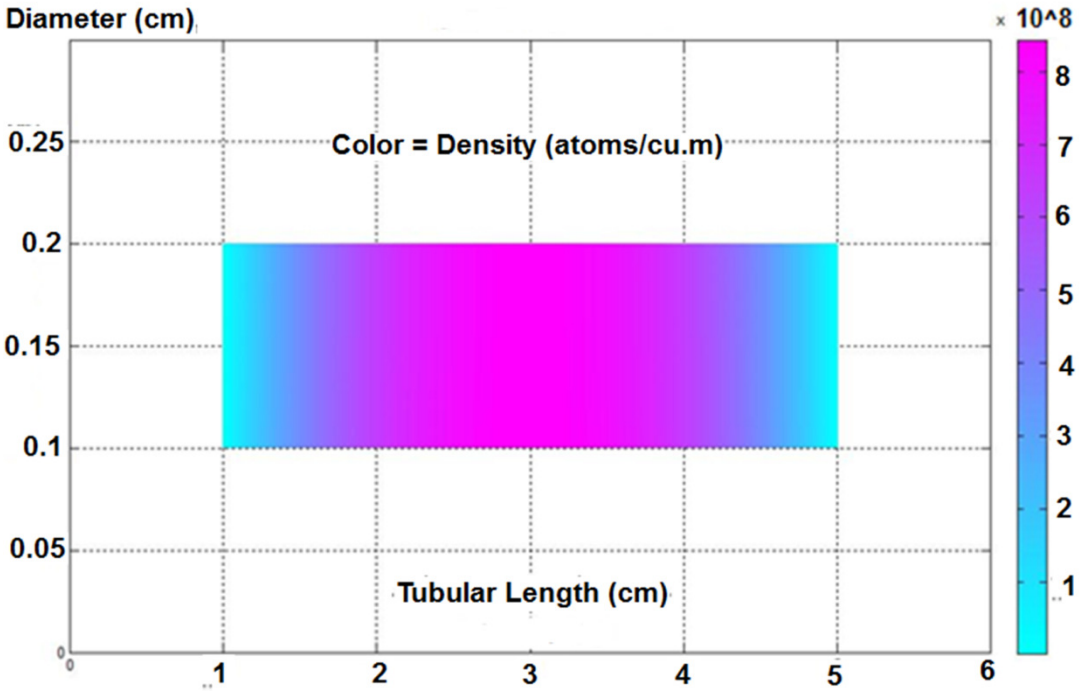

Figure 3-7 the distribution of the free arsenic atoms in a tubular atomizer; the maximum concentration obtained in 3 seconds is in the order of 10^8 atoms. m^{-3}

Further investigations were conducted on a quartz cell atomizer at a steady state condition using CFD. One of the well known commonly used atomizers is the externally heated quartz tube atomizer (EHQTA) which applies an electrical resistance device or an acetylene-air flame to heat the optical tube to a temperature in the range (700 – 1100 ^{o}C) *(Dedina, 2007).* In the current case study, the atomizer is assumed to be a heated quartz tube atomizer (L-shape HQTA) employing an internal central electrical resistance device to heat the tube bulk up to 1000 ^{o}K. The reason for proposing this design is to envisage the effect of the internal heating on the atomization mechanism and the distribution of the examined species along the tubular atomizer. The geometry is shown in **Figure (3-8)**, in which the gas channel internal diameter is assumed equal to (1 mm) and the arm tube that is utilized to supply the gases to the atomizer is connected from the left hand side.

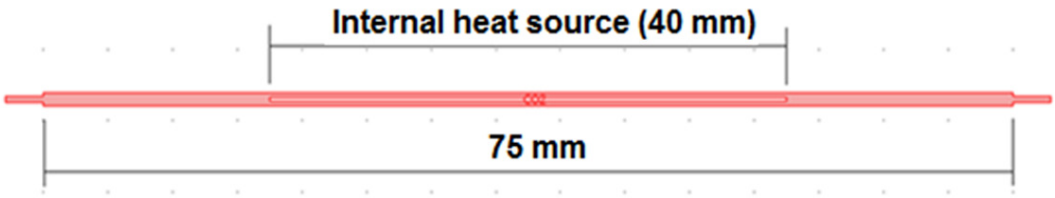

Figure 3-8 a schematic diagram illustrates top view of the rectangular L- shape HQTA; The illustrated section (75 mm length) represents the atomization channel. The center section (40 mm length) represents the electrical resistance device. AsH_3, helium gas and the accompanied hydrogen gas enters the atomizer from the arm tube that is connected to the atomization channel from beneath left hand side (not shown in the diagram).

(Dedina et al., 1998) divided the hydride atomization mechanism in a miniature diffusion flame quartz tube into physical processes and chemical reactions. The physical processes are attributed to macroscopic movements (e.g. convection, thermal expansion, and flow turbulances) and free atom diffusion. Chemical reactions are reported to occur with gaseous species transfers to the flame as well as the flame components itself. They concluded that the only feasible way for the hydride atomization is an interaction with a hydrogen radicals cloud which forms in the outer zone of the flame due to reactions between oxygen and hydrogen. *(Dedina, 2007)* reported that the cloud of hydrogen radicals that forms in the hot region of the heated quartz tubular atomizer is responsible for hydride atomization. The cloud position is dependant on the temperature profile and the gas flow rate inside the atomizer. It is also reported that the hydrogen entering the EHQTA atomizer from the gas-liquid separator, where it is generated due to the hydroborate decomposition, is enough to produce the required hydrogen radicals inside the atomization channel. However, a specific amount of oxygen, based on the total gas flow rate supplied to the atomizer and on the inner diameter of the atomizer, is required to intiate the H_2/O_2 reaction *(Dedina, 2007)*.

Accordingly, it is assumed that enough hydrogen radicals are available in the investigated L-shape HQTA atomizer and the current case study can concentrate on the distribution of AsH_3 species and the created free arsenic atoms along the atomizer.

According to *(Dedina, 2007)*, there are two reasons why free analyte atoms may be removed from the optical path of the atomizer; the first is the forced convection due to the gas flow inside the HQTA atomizer, while the second is the chemical reaction between the unstable free atoms outside the hydrogen radical cloud, which means the free atoms start to react after leaving the hydrogen radical cloud.

In practice, atomization is a simple first order removal of arsenic hydride from the gas phase and a later displacement of the arsenic atoms from the light path, represented by the following reaction pathway *(Van Wagenen et al., 1987).*

$$AsH_{3\,(g)} \overset{k_1}{\Rightarrow} As^o \overset{k_2}{\Rightarrow}$$

Where; $k_1 = 3.3\ sec^{-1}$ and $k_2 = 62\ sec^{-1}$

The change of species concentration with time is represented as follows:

$$\frac{dC_{AsH3(g)}}{dt} = -k_1\, C_{AsH3(g)} \qquad (3\text{-}51)$$

$$\frac{dC_{As^o}}{dt} = k_1\, C_{AsH3(g)} - k_2 C_{As^o} \qquad (3\text{-}52)$$

Three models are coupled simultaneously in Comsol 3.5a software to investigate the dissociation of the arsenic hydride into free arsenic atoms upon entering the atomization channel and being subjected to hydrogen radicals and thermal effects. The models included momentum, energy transfer (convection and conduction) and mass transfer (convection and diffusion). In the initial conditions, an inlet stream to the atomizer consists of helium gas accompanied by 2.66×10^{-4} mol/m^3 of arsenic hydride. Hydrogen from earlier stages is the source of the hydrogen radicals; however, it has not been included in the reaction mechanism to simplify the computations. The inlet stream velocity is assumed to be 0.084 m/sec. Hydride molecule dissociation into free atoms is an exothermic reaction (-189 kJ/mol) *(Ramesh Kumar and Riyazuddin, 2005)*. This value is used in this study in order to consider the effect of the generated heat.

Fluid flow is described using the incompressible Navier-Stokes equations, in which a laminar flow regime and constant fluid density are used to describe the system in a steady state condition according to equations (3-31 and 3-32). The boundary conditions are represented as follows: at the inlet of the atomization channel, the velocity vector is normal to the boundary, i.e. $u.n = u_0$; whereas the pressure at the outlet boundary is set ($p = p_0 = 0$). A no-slip boundary condition is selected at the interior surfaces of the atomization channel ($u = 0$).

Mass transfer in the studied domain occurs through a convection-diffusion scheme. The mass balance equation in a steady state condition is described by equation (3-33). At the

inlet section of the atomization channel, the boundary condition is assumed ($C_i = C_{i0}$) which equals the initial concentration. The outlet boundary conditions assume no mass flux occurs due to diffusion, hence they are dominated by convection; therefore the total flux is described as shown in equation (3-34). Zero mass transfer is imposed at the interior surfaces due to an assumption of insulated boundaries.

Heat transfer in the atomizer domain is considered through a convection-conduction scheme. The energy balance equation in a steady state condition is as follows:

$$\nabla.(-\mathrm{k}\,\nabla\mathrm{T}) + \rho\, C_p\, u\,.\nabla\mathrm{T} = \mathrm{Q} \qquad (3\text{-}53)$$

Here, C_p denotes the specific heat capacity (J/kg/K), k is the thermal conductivity (W/m/K), and Q is a sink or source term (W/m^3). At the inlet boundary, the temperature is assumed equal to ambient temperature ($T = T_0$); whereas a continuity boundary condition is assigned for the interior surfaces in touch with the atomization channel to assure heat transfer to and from the channel through these areas. Furthermore, thermal insulation boundary conditions are assigned for the outer surfaces. At the outlet section, a convective flux condition is assumed across the boundary, in which all energy transport is conducted through the convective flux, which indicates no heat flux occurs due to conduction. This assumption results in the following description for the total heat flux:

$$q\,.n = \rho\, C_p \mathrm{T\,u\,.n} \qquad (3\text{-}54)$$

All the equations described above and the boundary conditions are discretized according to the Galerkin finite element method with Lagrange second order elements except the pressure which has been treated by the hybrid P2 – P1 scheme. A numerical error estimation study was conducted to infer the appropriate grid size for higher solution accuracy. Eventually, a fine mesh with 50936 elements and 557246 degrees of freedom was applied to computations which produced a relative error less than 0.5 % for the arsenic free atom concentration at the end of the atomization channel. The results of the finest grid size, shown in **Figure (3-9)**, are adopted for discussion.

(A)

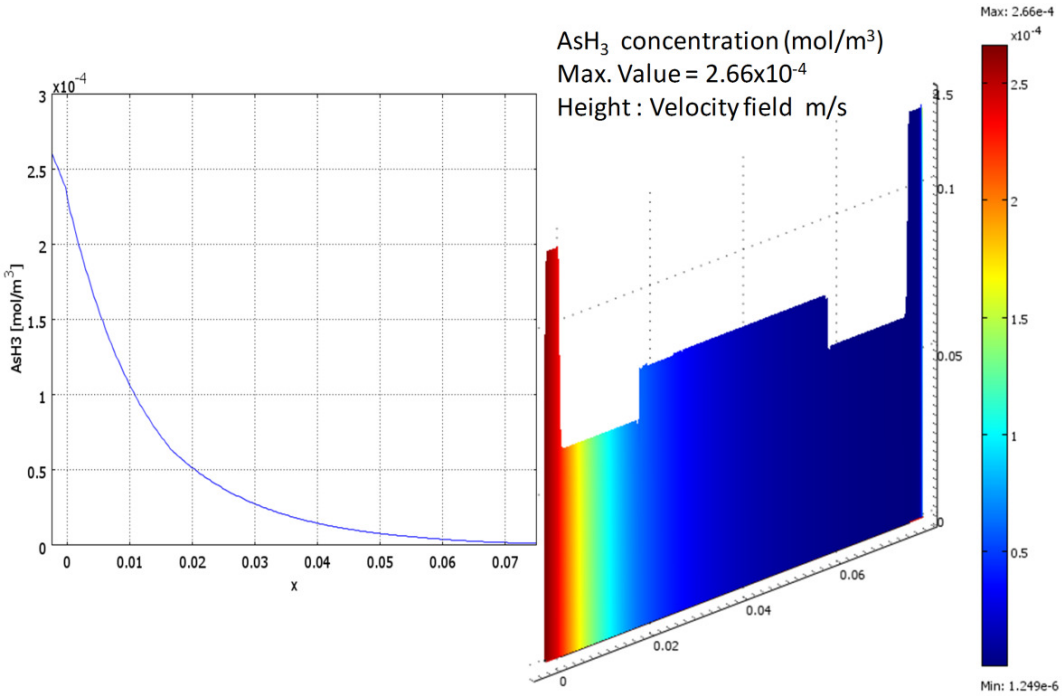
AsH3 [mol/m3]
x10-4
x
AsH3 concentration (mol/m3)
Max. Value = 2.66x10-4
Height : Velocity field m/s
Max: 2.66e-4
Min: 1.249e-6

(B)

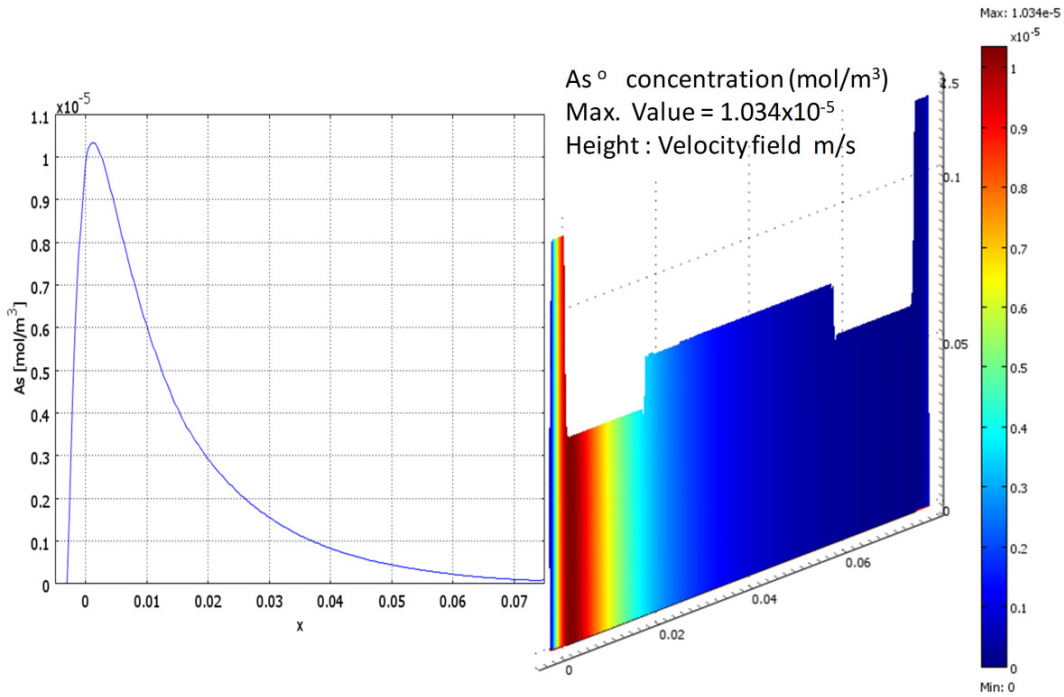
As [mol/m3]
x10-5
x
As ° concentration (mol/m3)
Max. Value = 1.034x10-5
Height : Velocity field m/s
Max: 1.034e-5
Min: 0

(C)

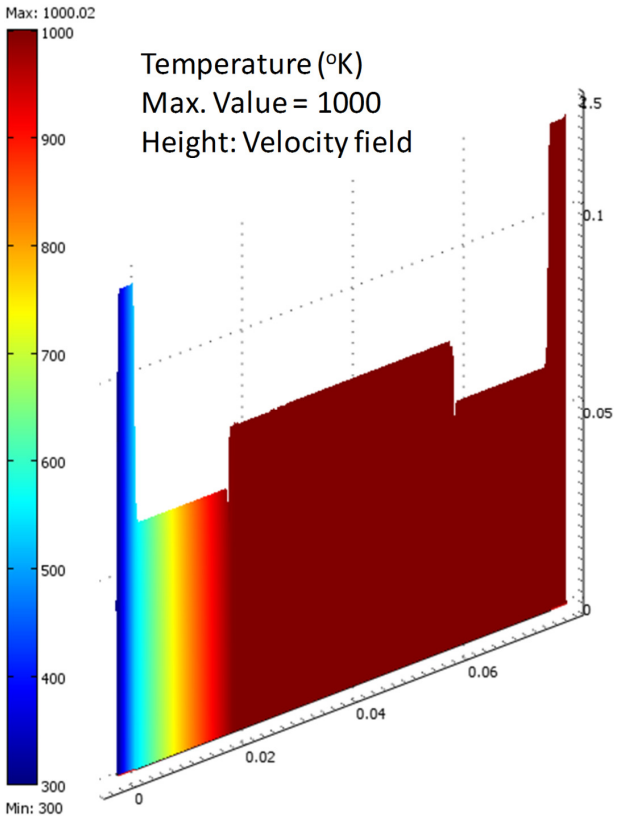

Figure 3-9 the simulation results of the internally heated quartz cell atomizer; *(A)* the concentration distribution of AsH_3 along the quartz cell at (y = 0.00125 mm), *(B)* the concentration distribution of the arsenic free atoms As^o along the quartz cell at (y = 0.00125 mm), *(C)* the temperature distribution along the atomization tube

The results show that the atomization process takes place within 0.4 sec in the first quarter of the atomization channel. A maximum of 1.5×10^{-5} mol/m^3 of arsenic free atoms is produced from 2.66×10^{-4} mol/m^3 arsenic hydride entering the atomization cell and this dissipates in a very short time when subjected to thermal energy from a heat source at 1000 ^{o}K in addition to the presumed collisions with a cloud of hydrogen radicals.

Although different concentrations of free arsenic atoms are found in the analytical and simulation studies, both cases show that the free arsenic atoms generate and dissipate before reaching the far end of the atomization channel.

These results are compatible with the findings of *(Dedina, 2007)* who reported that under typical conditions in a quartz tube atomizer, all free atoms disappear before

reaching the optical tube ends due to a series of recombination reactions outside the hydrogen radicals cloud. These results indicate that the centre of the atomization cell is the appropriate position for spectrometric data acquisition, which suggests that radial data acquisition will be reliable in the proposed design of HQTA.

3.6.2 Atomization of the volatile hydride in a dielectric barrier discharge atomizer

The application of 1000 ^{o}K in a quartz cell flame atomizer makes this equipment difficult to apply for miniaturization purposes. Alternatively, the DBD microplasma atomizer is reported to have low operating temperature and low power requirement.
A simulation study is conducted in this section to investigate the atomization of arsenic hydride in a DBD atomizer adopting the design shown in **Figure (3-10)**.

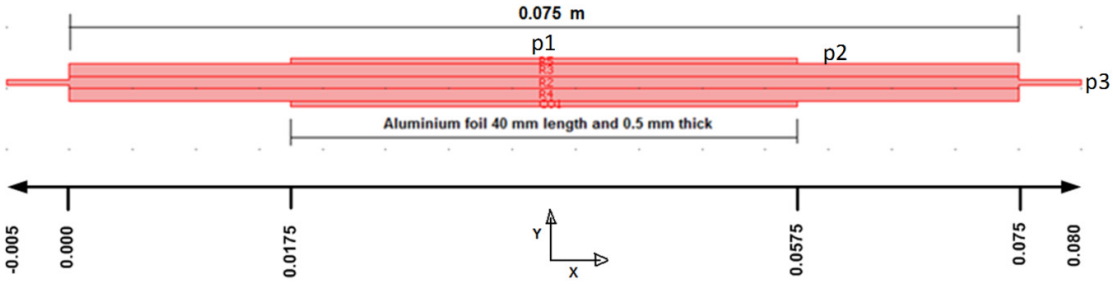

Figure 3-10 a schematic diagram shows the geometry of the adopted DBD atomizer; The values on X-coordinate are in meter. p1, p2, and p3 represent three positions selected for the spectral data acquisition, where p1 is at the channel centre, p2 at 1 cm after plasma generation section (radial data acquisition) whereas p3 refers to the axial position.

The central part (1mm thick) illustrates the rectangular gas channel which is bounded by two glass layers as dielectric barriers. The rectangular gas channel is connected with 0.5 mm ID tubes from both sides, which are used to connect the inlet stream from the left hand side and the fibre optic from the right hand side (axial viewing, x- coordinate). Two aluminium foils (0.5 mm thickness) are attached to the top and bottom surfaces of the atomization channel to represent the electrodes. Electron impact, where a hydrogen molecule in the excited state (H_2p) is considered to be generated due to collisions between the hydrogen molecule and electrons, is assumed for this scheme. Upon further

electrons collisions, the excited hydrogen molecules dissociate to form hydrogen atoms and excited hydrogen atoms. It is well known that hydrogen atoms in an excited state (H^*) are very reactive species and possibly recombine with other species or quench at the channel wall before getting a chance to collide with other species, which means that collisions of hydrogen atoms with arsenic hydride molecules is possible. However, in this study it was assumed that there were equivalent probabilities for hydrogen atoms and excited hydrogen atoms to collide with arsenic hydride molecules. Hence, the following mechanism is proposed assuming the collision occurs between hydride molecules and hydrogen atoms in an excited state to form intermediate species, which eventually lead to arsenic free atom formation:

$$H_2 + e \overset{K_1}{\rightarrow} H_2p + e \quad (3\text{-}55)$$

$$H_2p + e \overset{K_2}{\rightarrow} H^* + H + e \quad (3\text{-}56)$$

$$AsH_3 + H^* \overset{K_2}{\rightarrow} AsH_2 + H_2 \quad (3\text{-}57)$$

$$AsH_2 + H^* \overset{K_2}{\rightarrow} AsH + H_2 \quad (3\text{-}58)$$

$$AsH + H^* \overset{K_2}{\rightarrow} As^o + H_2 \quad (3\text{-}59)$$

$$As^o + As^o \overset{K_3}{\rightarrow} As_2 \quad (3\text{-}60)$$

The first reaction, equation 3-55, represents the dissociation of the hydrogen molecule due to collision with electrons in helium which is reported to occur with a rate coefficient (K_1= 4.54×10^{-11} cm^3/molecule/sec) *(Hagelaar et al., 2000)* at approximately 3 (eV) electron mean energy. The excited hydrogen atoms (H^*) collide with the arsenic hydride molecule and their intermediates in a series of three reactions, equations 3-57 to 3-59, which ultimately results in the formation of free arsenic atoms. The rate coefficients of these reactions are assumed equivalent to the rate coefficients of silicone hydride (SiH_4) molecule dissociation upon collision with hydrogen radicals (K_2 = 1×10^{-10} cm^3/molecule/sec) *(Moravej et al., 2004)*. The reaction represented by equation 3-60 has been included in order to demonstrate the effect of free arsenic atom recombination

on the total distribution of the atoms along the atomization channel. It is reported that recombination reactions of analyte free atoms play a fundamental role in depleting the free atom population in quartz tube atomizers. In the traditional quartz T-tube atomizer the hydrogen radical cloud is limited to a portion around the T-junction where the hydrogen gas and the hydride enter the atomizer. Outside the hydrogen radical cloud, the free atoms start to recombine causing: (1) curvature and rollover of calibration graphs *(Matousek and Dedina, 2000)*, (2) interferences due to recombination of analyte atoms among themselves and with different atoms which leads to double peak formations *(D'ulivo and Dedina, 1996, D'Ulivo and Dedina, 2002)*, and (3) re-atomization of the analyte solid deposits on the quartz tube atomizer walls due to the effect of hydrogen radicals. In order to prevent free atom recombination, *(Dedina et al., 1996)* utilized a multi flame quartz tube atomizer with the aim of filling the entire quartz tube with hydrogen radicals, thereby eliminating the free atom depletion. Since the DBD atomizer used in this work is homogeneously filled with hydrogen radicals due to continuous feeding of $NaBH_4$, it is expected that the effect of the recombination reaction will be limited. The recombination of atoms is well known to be a third order occurring at very low rate constant for different kind of atomic species (e.g. 9.26×10^{-34} cm^3/molecule/sec for the case of oxygen atoms, and 6.04×10^{-33} cm^3/molecule/sec for the case of hydrogen atoms *(Medodovic and Locke, 2009)*), therefore the reaction shown in equation 3-60 is expected to imply a very limited effect on the simulation. However, the rate constant for arsenic atom recombination (K_3) in the current study was considered equivalent to that for oxygen atoms (i.e. 9.26×10^{-34} cm^3/molecule/sec). Other possible recombination reactions are collision of excited hydrogen atoms with intermediate products already generated from recombination reactions (e.g. $As_2 + 4H^* \rightarrow 2AsH + H_2$). These reactions could be faster than the reaction described in equation 3-60 but will not significantly affect the whole mechanism, therefore it has not been considered in the current study to simplify the computations.

The DBD atomizer is simulated by using a finite element analysis in Comsol Multiphysics 3.5a software, in which a laminar flow model and three convection-diffusion models are applied in the computations to infer the distribution of species concentration along DBD atomization channel. Another two models (heat transfer convection-conduction model and AC power electromagnetic model) are added to predict the temperature distribution and the electrical field distribution throughout the

DBD atomizer. The fluid flow is described by using the incompressible Navier-Stokes equations, in which a laminar flow regime and constant fluid density is assumed to describe the system in a steady state condition according to the equations 3-31 and 3-32. The boundary conditions are assumed as follows: at the inlet of the atomization channel, the velocity vector is normal to the boundary, i.e. $u.n = u_0$; whereas the pressure at the outlet boundary is set to be ($p = p_0 = 0$). Moreover, a no-slip boundary condition is selected at the interior surfaces of the atomization channel ($u = 0$). The mass transfer in the studied domain is considered to occur through a convection-diffusion scheme. The mass balance equation in a stationary condition is described according to equation 3-33. At the inlet section of the atomization channel (at x = -0.005), the boundary condition is assumed ($C_i = C_{i0}$) which equals the initial concentration. The outlet boundary conditions assume no mass flux occurs due to diffusion, hence dominated by convection; therefore the total flux is described according to equation 3-34. Moreover, zero mass transfer is imposed at the interior surfaces due to the assumption of impermeable boundaries. The heat transfer in the atomizer domain is considered to occur through a convection-conduction scheme. The energy balance equation in a steady state condition is described according to equation 3-53. At the inlet boundary, the temperature is assumed equal to ambient temperature ($T = T_0$); whereas a continuity boundary condition is assigned for the interior surfaces in touch with the atomization channel to assure heat transfer to and from the channel through these areas. Furthermore, thermal insulation boundary conditions are assigned for the outer surfaces. At the outlet section, a convective flux condition is assumed across the boundary, in which all energy transport is conducted through the convective flux, which indicates no heat flux occurs due to conduction.

The AC power model was applied in the simulation by assuming the atomization channel is subject to both electrical and magnetic effects, with a potential difference of 3 kV across the atomization channel. Continuity boundary conditions were assigned for the interior surfaces in touch with the atomization channel, whereas all outer surfaces except the surfaces that represent the electrodes were assumed to be electrically insulated.

The flowing gas in the atomizer was applied in the simulation at 300 ^{o}K (inlet temperature) and 0.084 m/sec (gas velocity); two gases, helium and argon, are applied in the simulation in separate case studies. The initial concentration of the examined

arsenic hydride was 2.66×10^{-4} mol/m^3 whereas several concentrations of hydrogen gas that accompanying the arsenic hydride are adopted (3×10^{-6}, 3×10^{-5}, and 3×10^{-4} mol/m^3). It is worth noting that the generated hydrogen from the hydroborate decomposition is known to be higher than the examined values shown above. For instance, *(Pohl et al., 2007)* reported that 5.6 ± 0.3 ml/min hydrogen gas is generated from an aqueous stream flowing at 0.5 ml/min and contains 0.5 m/v $NaBH_4$. Nevertheless, applying higher hydrogen values than those shown above by one order of magnitude led to a significant reduction in the predicted free arsenic atoms concentration. The solution strategy was based on coupling the momentum transfer model with mass transfer models to estimate the distribution of the reactants, intermediates, and product concentrations along the atomization channel. Three mass transfer (convection – diffusion) models were utilized for the computations, the first model was used to simulate the reactions related to the collisions of the electrons with the hydrogen molecules (equations 3-55 & 3-56) which eventually produces hydrogen atoms and active species. The second convection – diffusion model was applied to treat the reactions of the hydrogen excited atom with the arsenic hydride and the intermediate products that formed and dissociated within a limited period. Moreover, the recombination reaction (equation 3-60) has been treated in the third convection – diffusion model. Ultimately, the heat transfer model and AC power model were coupled in the final stage to determine the temperature and electric field distributions throughout the whole atomizer. The equations and the boundary conditions are discretized according to the Galerkin finite element method with Lagrange second order elements except the pressure which has been treated by the hybrid P2 – P1 scheme. A numerical error estimation study was conducted to determine the appropriate grid size for the higher solution accuracy. Eventually, a fine mesh with 35314 elements and 128241 degrees of freedom was applied in the computations which produced less than 0.1 % relative error for the estimated free arsenic atom concentration at the end of the atomization channel. The simulation results are shown in **Figures (3-11 to 3- 13)**. The computations were accomplished in six stages, through which the free arsenic atom concentration is predicted at two positions; before the electrode overlapping section (EOS) and at the end of the atomization channel. In the first stage, helium was applied as a plasma gas and 2.66×10^{-4} mol/m^3 AsH_3 and 3×10^{-6} mol/m^3 hydrogen gas is to be entering the atomizer. In this stage, the recombination reaction (eq. 3-60) was not taken

into consideration; this is to deduce the difference in the prediction compared with stage 2. The results are shown in **Figures (3-11/A-E)** where the computed average velocity of the gas stream is found equal to 0.06 m/s in the centre of the atomization channel and higher values (approximately 0.12 m/s) found at the inlet and outlet sections of the gas channel due to the channel contraction at these sections.

(A)

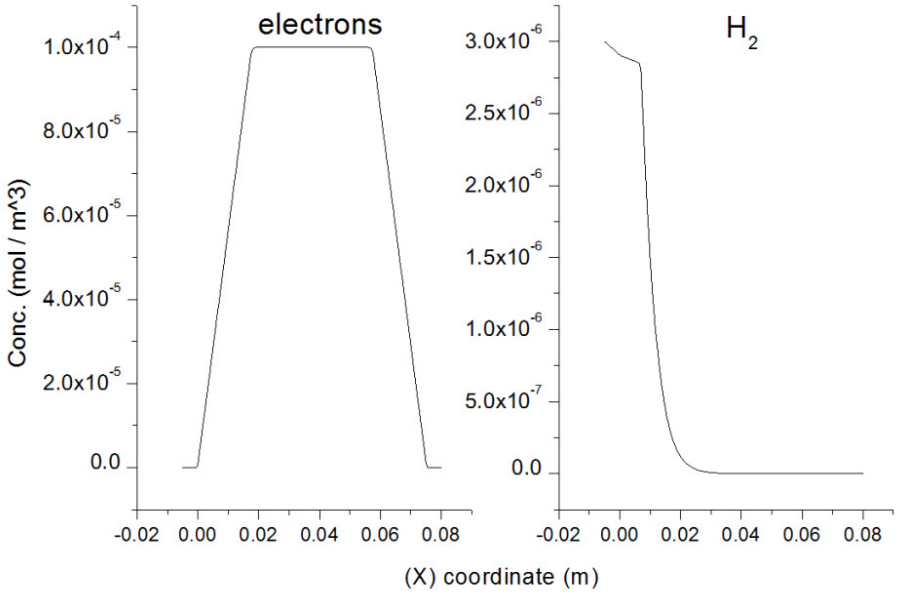

(B)

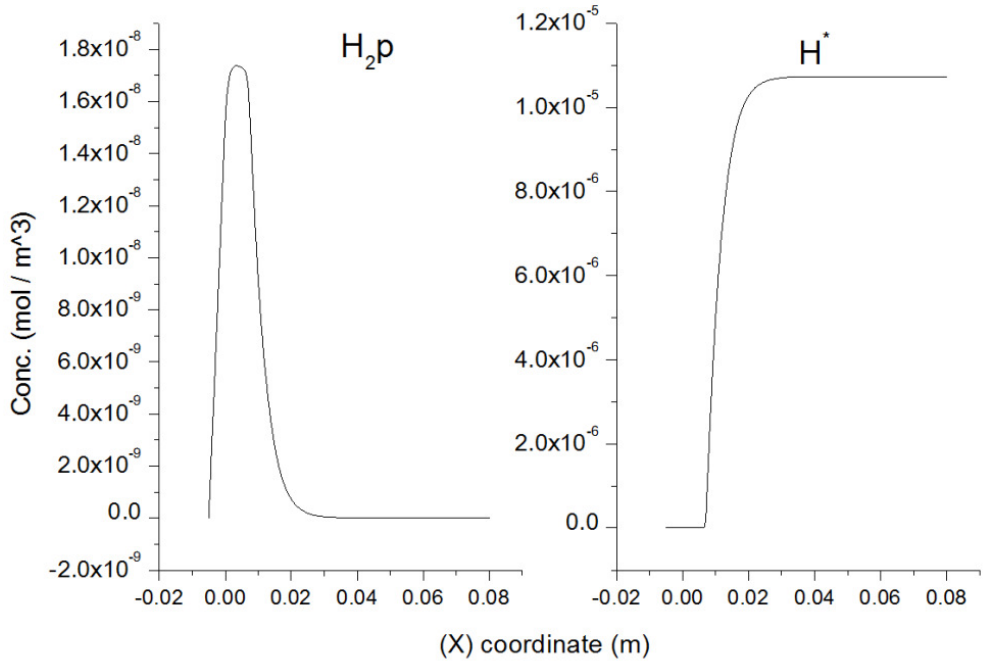

(C)

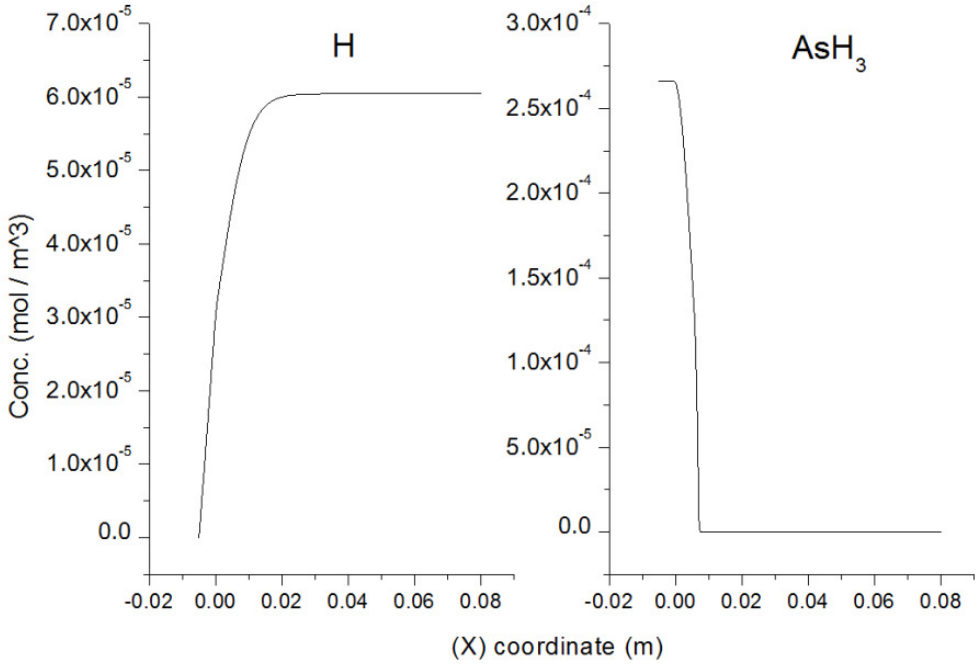
H
AsH3
Conc. (mol / m^3)
7.0x10-5
6.0x10-5
5.0x10-5
4.0x10-5
3.0x10-5
2.0x10-5
1.0x10-5
0.0
3.0x10-4
2.5x10-4
2.0x10-4
1.5x10-4
1.0x10-4
5.0x10-5
0.0
-0.02 0.00 0.02 0.04 0.06 0.08
(X) coordinate (m)

(D)

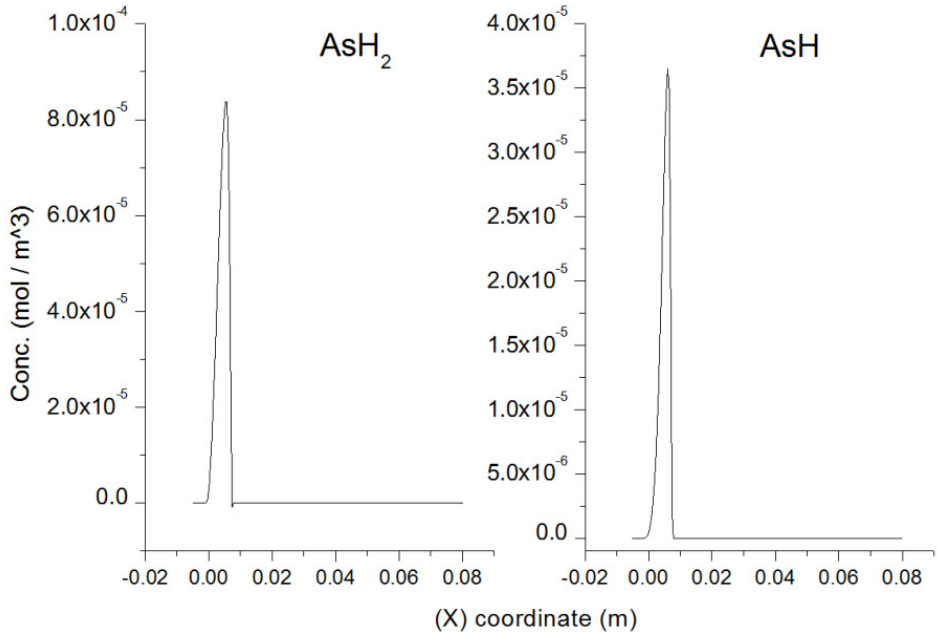
AsH2
AsH
Conc. (mol / m^3)
1.0x10-4
8.0x10-5
6.0x10-5
4.0x10-5
2.0x10-5
0.0
4.0x10-5
3.5x10-5
3.0x10-5
2.5x10-5
2.0x10-5
1.5x10-5
1.0x10-5
5.0x10-6
0.0
-0.02 0.00 0.02 0.04 0.06 0.08
(X) coordinate (m)

(E)

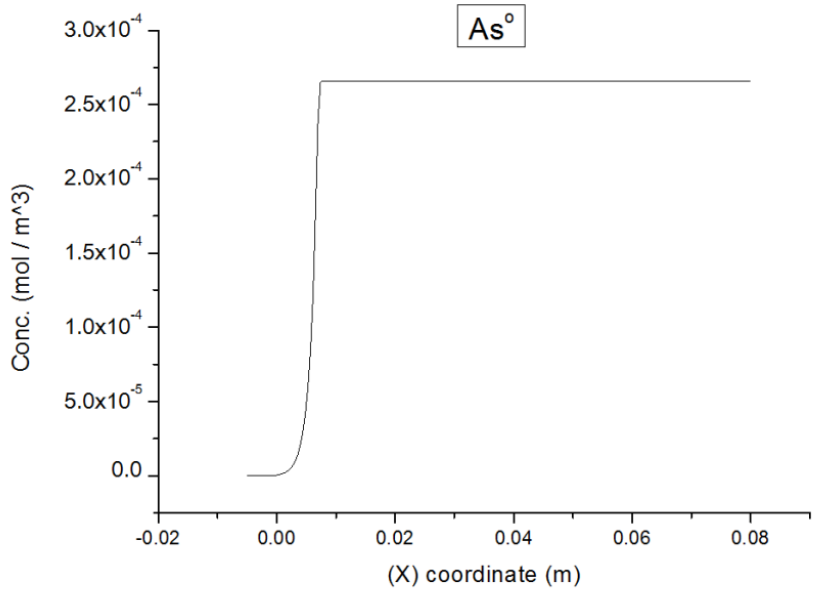

Figure 3-11 the simulation results – species concentration gradients along the DBD atomization channel.

From the computational model results, species concentration varies along the atomization channel in different ways. The electron concentrations builds up in the electrode overlapping section (EOS) which exists between the points 0.0175 and 0.0575 in **Figure (3-10)**, and this is attributed to the electrical field exerted in this specific area. Prior to EOS, it can be noticed, **Figure (3-11/A)**, that the hydrogen gas concentration reduces sharply in the first section of the gas channel and becomes zero within the first part of the electrode overlapping section, which indicates the initiation of the reaction series before entering EOS. This result is compatible with the current understanding of the atomization mechanism which is attributed by *(Dedina et al., 1998)* to the presence of hydrogen radicals in the diffusion flame outside the quartz tube. They reported that hydrogen selenide starts to atomize inside the tube (up to 4 mm inside) before reaching the flame due to the diffusion of hydrogen radicals. The velocity of the gases flowing in the DBD atomization channel is 0.06 (m/sec) then the total hydrogen gas consumption is expected to occur within 0.5 second. The results show a sharp increase is followed by a sharp decrease in the concentration of excited hydrogen molecules (H_2p), **Figure (3-11/B)**, in the first section of the gas channel. Consequently, the concentration of (H_2p) becomes negligible upon entering EOS within 0.5 second. The results also show that both the hydrogen gas atoms (H) and the excited species (H^*) are generated in the first

part of the gas channel, **Figure (3-11/B)** and **Figure (3-11/C)**, at a position before EOS, which is in agreement with *(Dedina et al., 1998).* These species build up very fast toward saturation within the first part of EOS. However, a higher concentration of atomic hydrogen (H) is predicted compared with (H^*). Most importantly is the conversion of arsenic hydride into intermediate species and the ultimate production of the free arsenic atoms. The computations show that total consumption of the arsenic hydride molecules occurs, approximately 0.16 second before entering EOS, probably due to the abundance of hydrogen radicals that collides with AsH_3.

A similar reaction scheme is deduced for the intermediate species (AsH_2) and (AsH), in which both species are shown to be generated in the first section of the gas channel. The results show that a sharp increase followed by a sharp decrease occurs in their concentrations within 0.016 seconds and consequently leads to a full depletion of the intermediate species before reaching EOS, as illustrated in **Figure (3-11/D)**. In consequence, the computations show that the arsenic free atoms (As^o) generates in the first section of the gas channel and saturate to a maximum (2.66×10^{-4} mol/m^3) within 0.014 second before reaching EOS. The computed time scale (14 milliseconds) actually represents the full time period for the whole reaction. This is in agreement with *(Kogelschatz et al., 1997)* who classify three time periods for the plasma reactions. Electrons collision reactions (excitation and dissociation) within 10 picoseconds. Free radicals reactions are in intermediate time scales (1 – 100 microseconds), whereas substantial displacement of species in convection and diffusion mechanisms in milliseconds. The computed concentration of (As^o) is found to be equivalent to the concentration assumed for the arsenic hydride, i.e. a 100% conversion. It can also be observed that (As^o) concentration has not been changed along the channel after reaching a maximum; this is due to the assumption made in the proposed mechanism (first stage) that no recombination reactions are expected to occur. A comparison between predicted free arsenic atom concentration from all the studied cases (stages 1-6) is shown in **Figure (3-12)**.

The computations in stage 2 were applied by including the recombination reaction described by (eq. 3-60) and considering the same operating conditions adopted in stage 1, i.e. helium is applied as a plasma gas, 2.66×10^{-4} mol/m^3 of AsH_3 and 3×10^{-6} mol/m^3 of hydrogen gas is assumed to be transported to the atomizer.

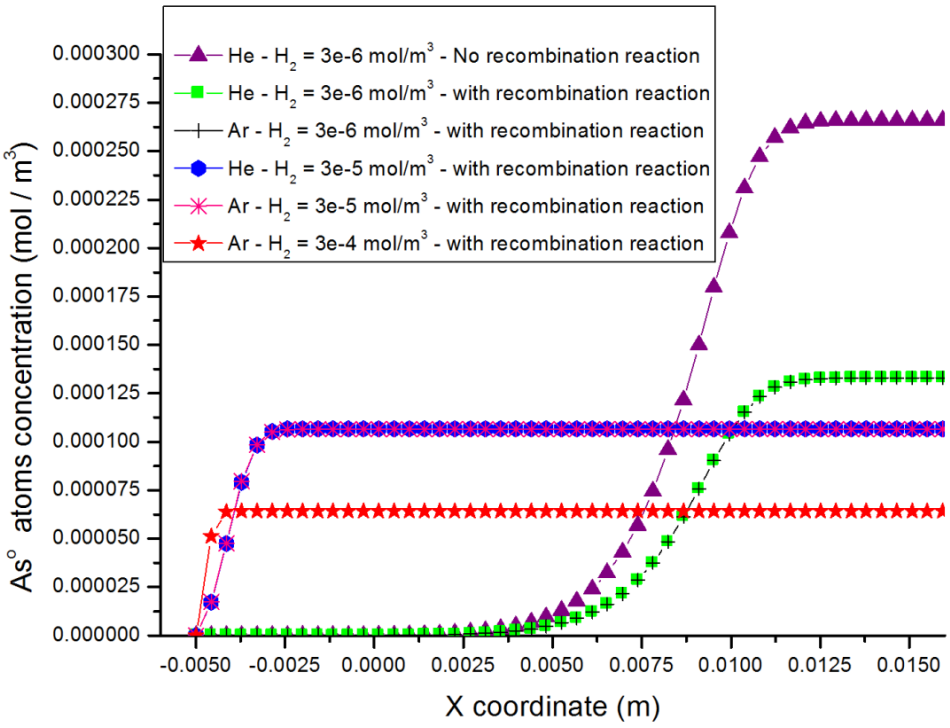

Figure 3-12 the simulation results – comparison between the predicted arsenic free atoms concentration from different case studies.

As expected, the inclusion of the recombination reaction results in slight differences in the predicted concentrations of all species. For instance, the free arsenic atom concentration at the atomization channel end is predicted to be 1.33×10^{-4} mol/m^3 which means a reduction by a half compared with stage 1, whereas the recombined As_2 molecules are predicted at very low concentration of 2.8×10^{-41} mol/m^3 which denotes the limited effects of recombination reactions. Recombination reactions do not lead to any significant effects concerning the reaction rate, (**Figure (3-12)**).

The computations in stage 3 were applied by considering argon as the plasma gas and applying the same concentrations of AsH_3 and hydrogen; this to deduce the effects of changing the physical properties of the gas on the whole mechanism. The results from stage 3 are similar to those from stage 2, which indicates that no effects occur on changing the plasma gas.

Computations in stages 4-6 were applied by using the same concentration of AsH_3 while increasing the hydrogen concentration gradually by one order of magnitude to determine the effects on the whole mechanism. In stage 4, a hydrogen concentration of 3×10^{-5} mol/m^3 has been applied while using helium as a plasma gas. The results show

a concentration of 1.06×10^{-4} mol/m^3 As^o atoms is predicted at the atomizer end, which is lower than that predicted in stage 3 (by 20%), whereas As_2 concentration is estimated at 2.1×10^{-41} mol/m^3. Most important is the increase in the free arsenic atoms generation rate. It can be observed in **Figure (3-12)** that the As^o creation on the abscissa is shifted back from 0.00375 m at the channel x- coordinate to the foremost point in the atomization channel, which indicates a significant increase in the reaction rate occurs due to an increase in the hydrogen concentration in the atomizer. This could be attributed to a higher hydrogen diffusion rate compared with other species. Hence, the formation of hydrogen radicals is proportional to the amount of hydrogen injected into the channel and consequently the speed of the whole reaction mechanism becomes dependent on the amount of hydrogen gas (**Figure (3-13)**).

The computations in stage 5 were applied using the same concentrations as mentioned in stage 4 while using argon as a plasma gas. Again, no differences were observed from changing the gas. In the last case study (stage 6), the computations were applied using argon as a plasma gas while applying a concentration 3×10^{-4} mol/m^3 of hydrogen. The free arsenic atom concentration at the atomizer end is estimated as 6.4×10^{-5} mol/m^3 which is lower than the concentration predicted from stage 5 by approximately 40%. This result emphasizes that higher hydrogen concentrations result in lower concentrations of free arsenic atoms and other intermediate species, **Figures (3-12 and 3-13)**, as well as a faster reaction mechanism.

One explanation for this result is related to the physical properties of hydrogen, where the hydrogen is known to have a high thermal conductivity and higher dissociation temperature compared to other gases *(Zhu et al., 2006b)*. The hydrogen is also capable of altering the electron energy and the electron distribution function; thereby changing the population density of the reactive species in the discharge *(Chaudhary et al., 2003)*. Thus, the presence of higher hydrogen concentrations in the DBD atomizer could result in the time required for the whole mechanism becomes shorter. The computations indicate the possibility of spectrometric data acquisition from any radial position along the channel section with the same efficiency. Since the computations show that all reactions are initiated in the section preceding EOS, which results in a constant free arsenic atom concentration along the atomization channel, it is possible to adopt a shorter atomization channel length eliminating any recombination reactions that may reduce the signal intensity of the analyte.

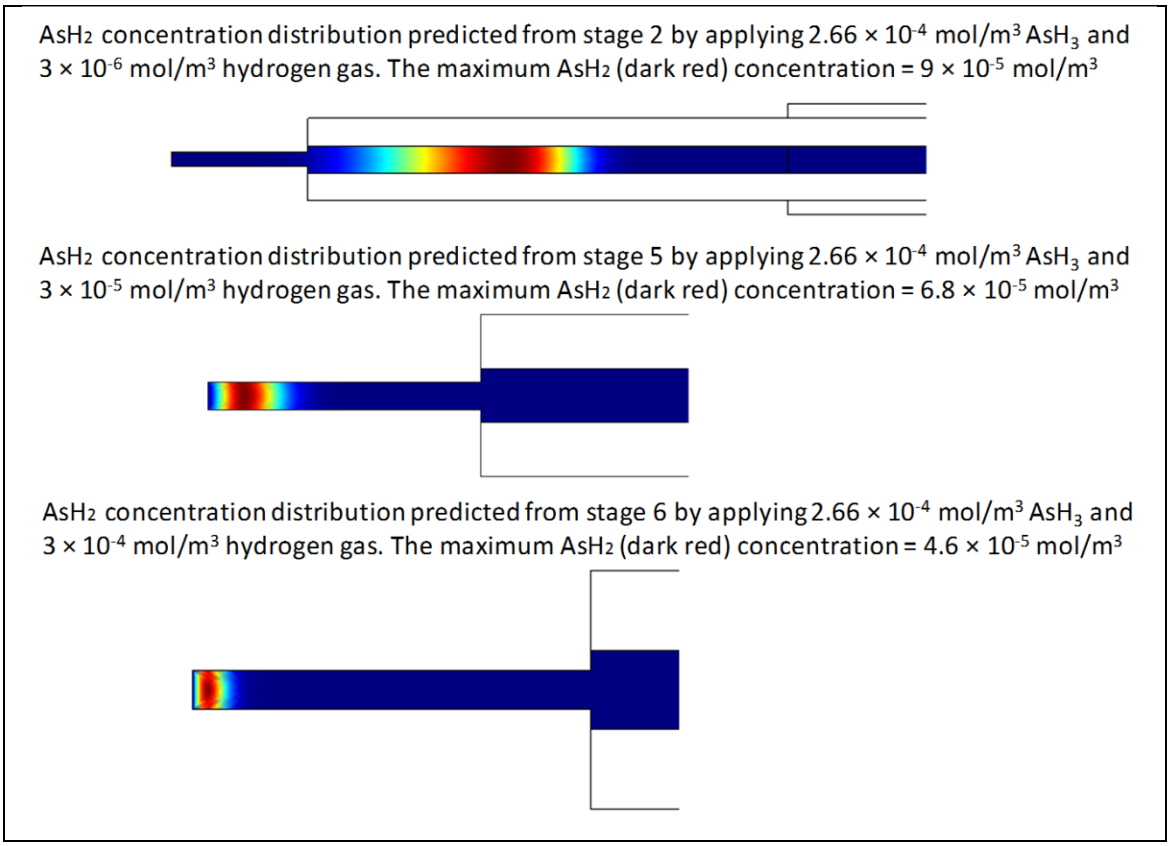

Figure 3-13 the simulation results - comparison between the predicted AsH_2 concentrations from different case studies;
The chosen segment represents the first part of the atomizer illustrated in **Figure (3-10)**.

Other computations were conducted by coupling the heat transfer model and the AC power model with the previous models (momentum and mass transfer) to interpret the temperature and the power distribution along the DBD atomizer. The results (**Figures 3-14 and 3-15**), illustrate a maximum temperature (approximately 900 ^{o}K) at the outlet section of the DBD atomizer, with a temperature in the range 820-840 ^{o}K in the channel section between the electrodes. The estimated temperature is approximately equivalent to 0.07 eV, which is higher than the gaseous temperature and could be related to the temperature of excited species in plasma bulk. **Figure (3-14)** shows that the total energy density approaches a maximum in the centre of the atomization channel, which is due to the exerted electrical power.

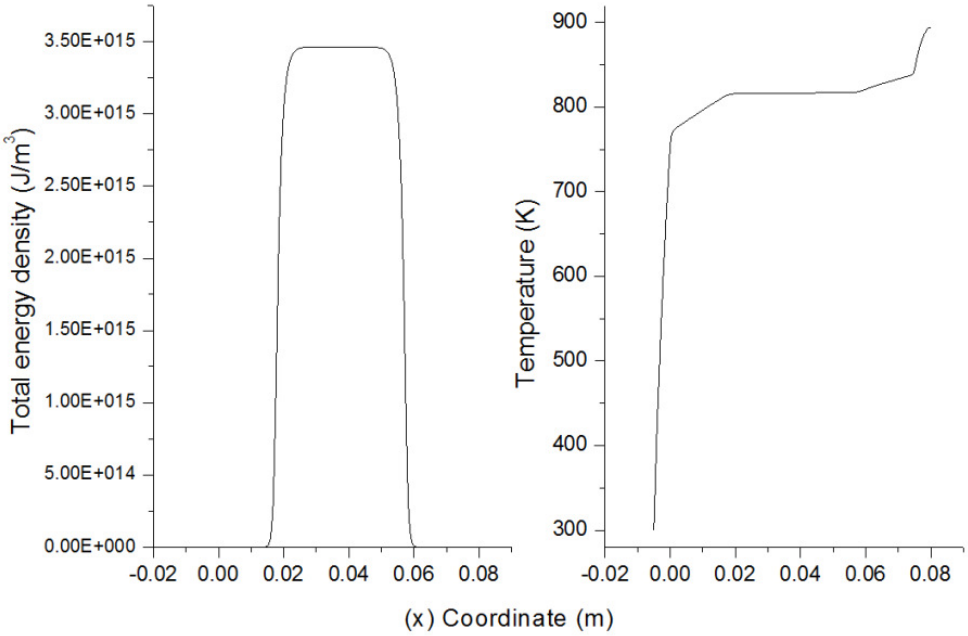

Figure 3-14 the simulation results – the temperature and the total energy distribution along the DBD atomization channel

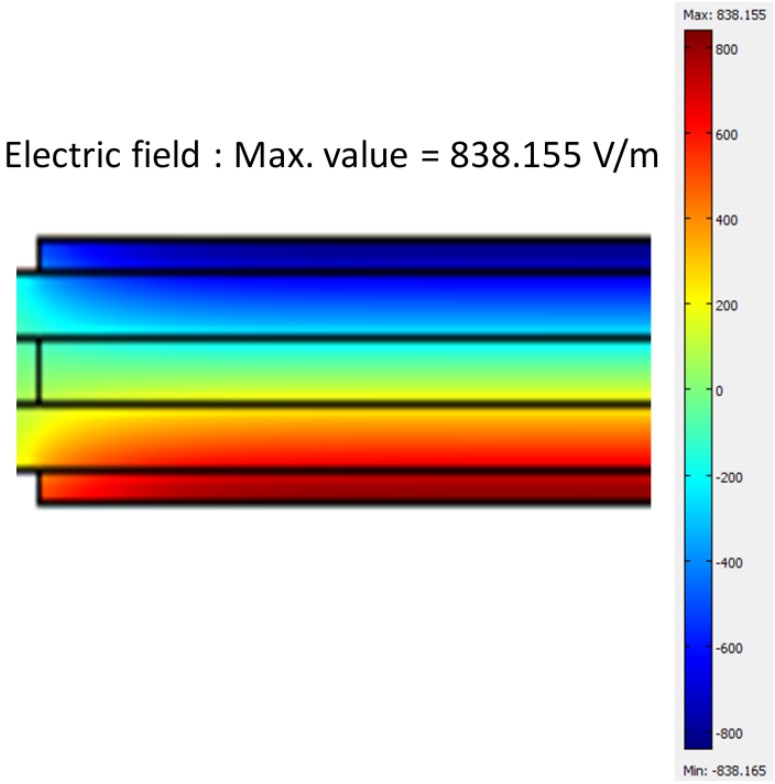

Figure 3-15 the electrical field distribution in the whole geometry;
The chosen segments represent the centre channel surrounded by glass barriers and two electrodes.

3.7 Summary of the findings from chapter three

Several analytical studies were carried out to investigate the process of the arsenic hydride generation and their coupling with a DBD atomizer. The outcomes can be summarized as follows:

1- Investigations of the reaction mechanisms based on two hypotheses indicate that the second hypothesis, hydroboron species formation, is more relevant for design purposes. The full reaction process is shown to occur within the first segment of the reaction coil which is approximately 5 cm length.

2- The simulation results from the helical tubular section show that a full separation of the vapour species from the liquid phase is achieved within the half of the tested section length (≈ 6.25 cm), which demonstrates that a total length of 11.25 cm (5 cm + 6.25 cm) is sufficient for the reaction and separation.

3- The simulation results of the nebulizer-gas liquid separator show that a significant reduction in hydrogen gas concentration is achieved upon injecting supporting streams of helium gas at 216 ml/min, which results in diluting the generated hydrogen by 7 orders of magnitude before entering the DBD atomizer. However, the computations show that a significant reduction in the arsenic hydride concentration also occurs which might attenuate the signal intensity of the targeted analyte. Therefore, an optimized flow rate of helium is required in order to utilize this kind of separator.

4- The analytical and simulation results of a quartz cell atomizer show high concentrations of free arsenic atoms form in the centre of the atomization cell and then dissipate totally at the walls of the cell. This result is attributed in the literature to the lack of hydrogen radicals in a flame type quartz cell atomizer. Accordingly, the best location for spectrometric data acquisition is the centre of the atomization cell giving that the heat source is centred in the atomization channel.

5- Simulation results of a rectangular DBD atomizer show that free arsenic atoms form and approach maximum concentration before reaching the electrode overlapping section (EOS). The results also indicates that the formed arsenic atom does not dissipate due to abundance of hydrogen radicals along the atomization channel, which is considered an advantage over the traditionally used quartz cell atomizer. In principle, this result indicates the possibility of achieving spectrometric data acquisition radially from any

position along the DBD atomization channel that follows the entrance part. It is also concluded that extra length of the atomization channel might result in undesirable recombination reactions which may lead to reduced signal intensity; therefore, it was decided to design and fabricate another DBD chip with a shorter spectral path length, as presented in chapter six.

The temperature distribution indicates that a value of 0.07 eV is reached at the atomizer centre and increases slightly at the outlet end of the gas channel. Actually, the estimated temperature is very close to the rotational temperature inside the plasma bulk determined experimentally, as shown in chapter four.

4. DESIGN, OPTIMIZATION, AND CHARACTERIZATION OF DBD PLASMA ATOMIZER

4.1 Preface

In this chapter, two designs for a DBD plasma atomizer are presented and tested for the purpose of selecting the optimum configuration. The tested models are fabricated from Perspex and glass materials and tungsten and aluminium alloys are used to form the electrodes. The optimum configuration is selected upon testing the models, taking into consideration that the highest signal intensity for the targeted species is the objective function. The optimal spectrometric parameters are inferred by conducting investigations based on a fixed experimental plan and optimization technique. The DBD plasma of the selected configuration has been characterized by applying spectrometric analysis and measuring other parameters.

4.2 Design and fabrication of a rectangular configuration DBD atomizer

As mentioned in the earlier sections, DBD discharge is generated in a discharge configuration with at least one insulation layer between the electrodes. In this sense, *(Pal and et al., 2010)* reported that several materials could be applied to form DBD dielectric layer such as glass and polymer coatings. Accordingly, poly methyl methacrylate (Perspex) and universal microscope glass slides are used in these experiments.

4.2.1 A Perspex DBD micro atomizer

A prototype DBD atomizer was designed and fabricated with minimum complexity as a first DBD model. A Perspex block (1.3 cm diameter × 3.5 cm length) micro reactor was made according to the following specifications: A centre channel (ID = 800 microns) is drilled to form the gas channel. Another channel with the same diameter is drilled in both sides of the gas channel to be used for residing the electrodes. The gap between each electrode and the gas channel is kept in the range (200-250 microns) in order to maintain the breakdown voltage to a minimum level. Tungsten alloy wires (750 microns) are used to form the electrodes, where the far end of each electrode is connected to the power source. The plasma is generated in the middle part of the channel which exists in the overlap between the electrodes (approximately 3 mm

length). Two cylindrical holes (ID = 3 mm) are drilled in the centre of the assembly, on the top and bottom of the generated plasma, and used for the optical sensor housing. **Figure (4-1)** shows a diagram and pictures for the Perspex DBD atomizer before and after operation.

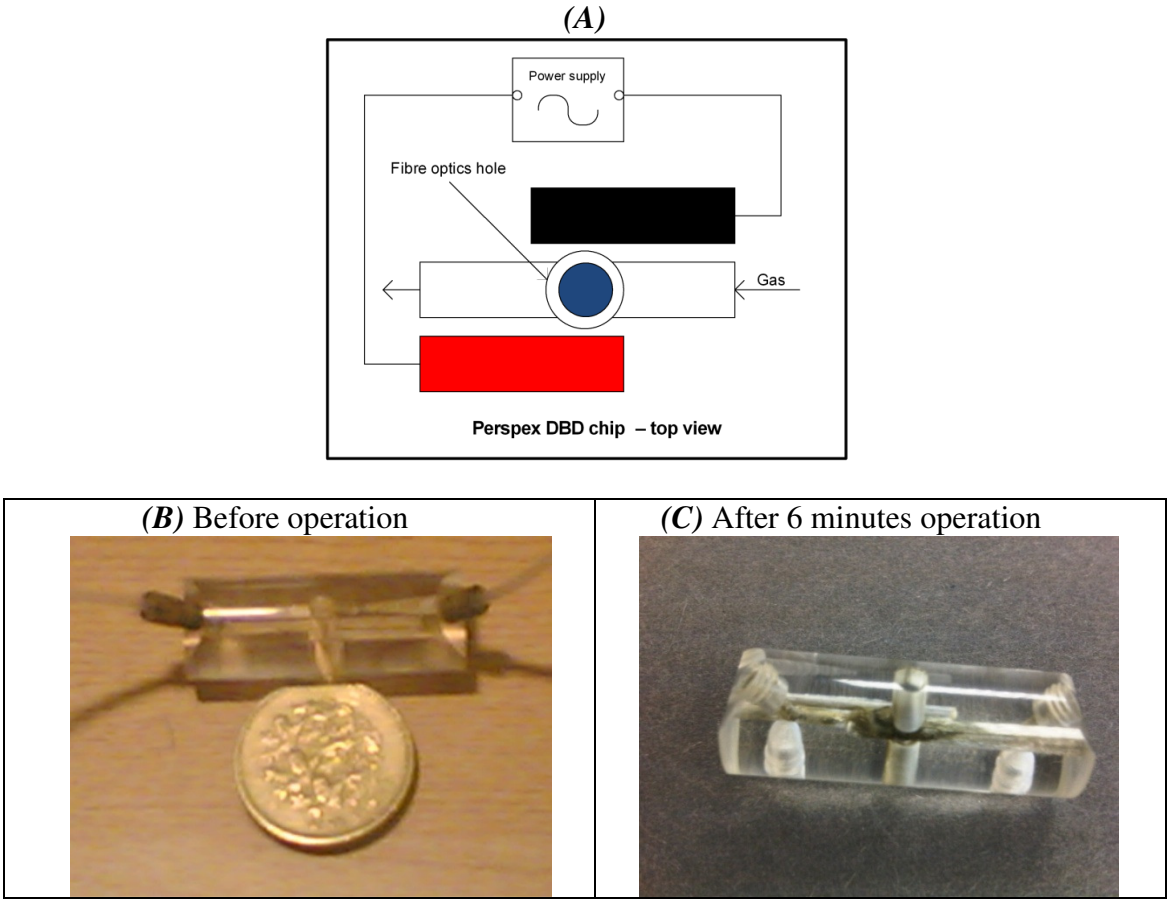

Figure 4-1 a Perspex DBD micro atomizer

The Perspex DBD atomizer was tested by using argon gas, in which approximately 3 kV AC at 30 kHz frequency was applied for few minutes. After approximately 6 minutes, a sudden arcing occurred inside the atomizer as a result of the Perspex layer between the channel and the electrodes collapsing, which smashed the interior body of the atomizer. One possible reason for this result is the temperature increase inside the atomizer which results in melting the thin layer of Perspex that separates the gas channel from the electrode channel. The abovementioned test has been repeated by applying 2 kV at 30 kHz using same configuration Perspex chip, obtaining the same result after approximately 9 minutes. This finding clearly indicates the Perspex material is not suitable for fabricating a DBD atomizer.

4.2.2 DBD atomizer fabricated from a combination of glass slides

A second atomizer based on glass was fabricated (**Figure (4-2)**). The chip is fabricated from commercial microscope glass slides (7.5 cm L x 2.5 cm W x 1 mm thick) which are aligned together using a Perspex chip holder to form a gas channel of 1 mm depth. 7.5 cm was adopted as the length for the atomization channel, whereas three values were tested for the gas channel width. The electrodes are formed from aluminium foil (0.5 mm thick), where the electrode width has been selected to be compatible with the channel width, (three values of the electrode length). The overlap between the electrodes is varied according to the electrodes length; eventually, three values of the overlapping section area were tested (**Table (4-1)**).

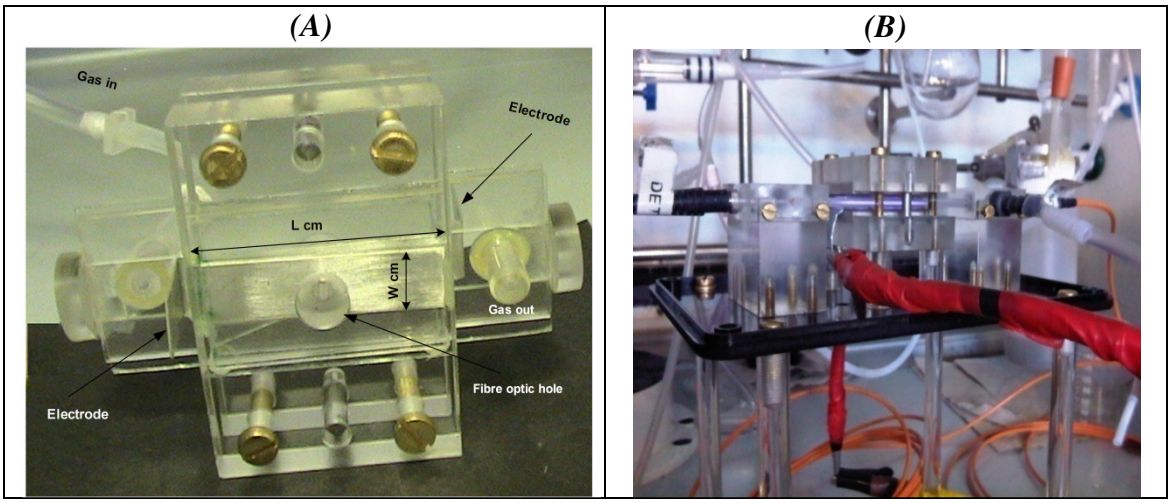

Figure 4-2 pictures for the fabricated glass DBD atomizer;
(A) a rectangular DBD atomizer, (B) the DBD atomizer in operation

Table 4-1 the details of the tested DBD configurations

	Gas channel dimensions	Electrode dimensions	Electrodes overlapping Section
1	7.5 cm (L) × 0.5 cm (W) × 1 mm (D)	3 cm (L) × 0.5 cm (W)	2 cm (L) × 0.5 cm (W) = 1.0 cm^2
2	7.5 cm (L) × 0.6 cm (W) × 1 mm (D)	3.9 cm (L) × 0.6 cm (W)	3.8 cm (L) × 0.6 cm (W) = 2.28 cm^2
3	7.5 cm (L) × 1.0 cm (W) × 1 mm (D)	4.0 cm (L) × 1.0 cm (W)	4 cm (L) × 1.0 cm (W) = 4.0 cm^2

The equivalent electrical circuit for the rectangular DBD chip is shown in **Figure (4-3)**.

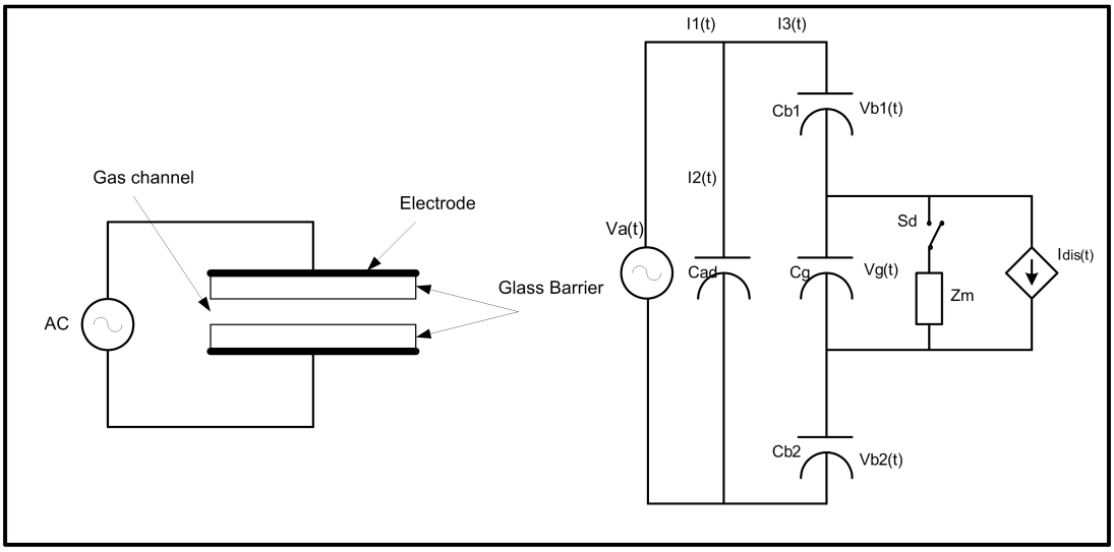

Figure 4-3 the equivalent electrical circuit for the DBD chip

The glass barriers form a dielectric barrier with capacitance Cb_1 and Cb_2, whereas the gas channel forms a capacitance C_g. The effects of the cables and the additional electrical circuit components are represented by the capacitance C_{ad} which is in parallel to the DBD layers. The microdischarge impedance is denoted by Z_m and the switch S_d is used to indicate the phenomenon of forming two discharges at a time interval during one complete cycle. The plasma discharge is interpreted by the current I_{dis} which is represented by equation (4-1) *(Pal and et al., 2010, Panousis et al., 2006)*.

$$I_{dis}(t) = (1 + \frac{C_g}{C_b}) I_3(t) - C_g \frac{dV_a(t)}{dt} \qquad (4\text{-}1)$$

Where, $$C_b = \frac{C_{b1}C_{b2}}{(C_{b1} + C_{b2})}, I_3(t) = C_b \frac{dV_b(t)}{dt}, V_b = V_{b1} + V_{b2}$$

4.3 The power source and the equipment used for the spectrometric and other data acquisition

A custom made high voltage power source (Entwicklung Leistungselectronic – Germany) was used in this work. The power source has been designed to supply high

voltage (up to 12 kV) with a frequency range (20 to 40 kHz).The device is provided with a manual control of voltage, current and frequency. It is also provided with two digital LCD's to monitor the voltage and current values. Due to a limited frequency range, no matching network was supplied with the device.

A fibre optics sensor is applied for the spectral data acquisition processed via an Ocean Optics USB 2000 spectrometer and analysed by using Spectra Suite software (Ocean Optics). The spectrometer specifications are: 0.3-1.5 nm FWHM resolution, 600 lines grating density blazed at 300 nm, and 25µm slit width. The spectrometric parameters (integration time and boxcar width) are optimized in **Section (4.4.2)** to obtain the highest signal to noise ratio at reasonable spectral resolution. The temperature of the discharge gas from the DBD chip was recorded via k-type thermocouple with digital temperature reader. The voltage supplied at the load is measured using a high voltage probe (Testec, HVP-15HF) and digital oscilloscope (Pico, ADC-212), whereas the current is measured using a digital current clamp meter (UNI-T, UT 201).

A high voltage capacitor (up to 10 kV and 200 µF) from (General Atomics electronic systems – USA) is integrated in the system to study the nature of the DBD discharge.

4.4 Optimization of DBD system parameters

4.4.1 DBD configuration

Three prototypes, described in **Table (4-1),** were tested to select the best configuration of the proposed DBD atomizer. The stability and homogeneity of the generated plasma are considered to be the main target that would result in highly accurate spectral data. As mentioned in **Section (2.6.3)**, the DBD discharge would be produced in either filamentary or homogeneous form. In order to implement the electrical characterization of the proposed DBD, the voltage – charge diagram (Lissajous figure) *(Pal et al., 2010)* gives an estimation of the energy consumed by the discharge per cycle of the applied voltage. In principle, the Lissajous figure illustrates the relation between the voltage and the charge waveform with respect to time. Since the capacitance of such a system measures the amount of electrical energy stored for a given electric potential, the voltage drop across a serial linked capacitor is actually the reason for the charge

delivered through the discharge cycle. On this basis, dissipation of the electrical energy in the discharge cycle is inferred by calculating the area of the characteristic shape produced via Lissajous figure. Hence, the mean dissipated power is deduced from the applied frequency and the estimated energy ($P = f \times E$) *(Kostov et al., 2009)*.
The experimental setup in the current work, to produce the Lissajous figure is illustrated in **Figure (4-4)**, where a high voltage capacitor (200 µF) is connected in series with the DBD atomizer *(Massines et al., 1998)*.

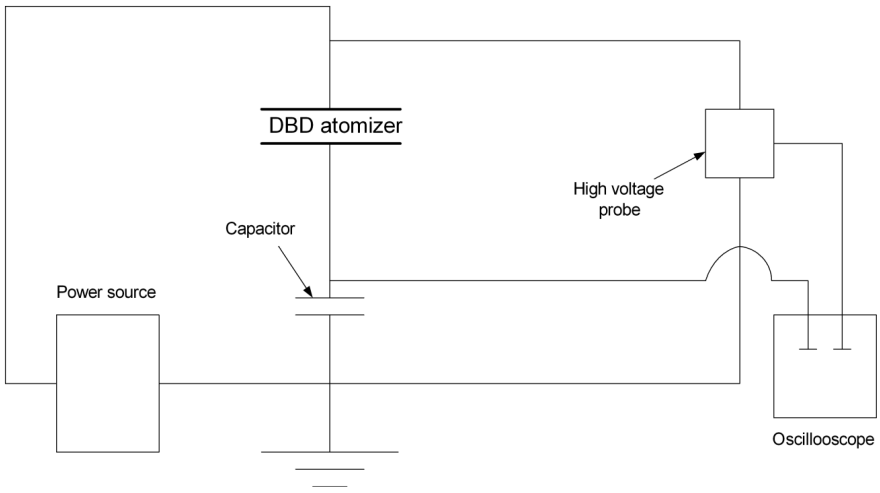

Figure 4-4 the circuit diagram used to generate Lissajous figure;
the charge is calculated by multiplying the voltage developed across the capacitor (in Volts) by its capacitance (in Farads).

The Lissajous figure produced for the DBD configuration (No.3) upon applying argon gas is shown in **Figure (4-5)**. The characteristic shape in the Lissajous figure resembles a parallelogram, which indicates a filamentary discharge in the tested DBD configuration *(Pal and et al., 2010, Massines et al., 1998)*. The energy consumed in the DBD atomizer each cycle is estimated by calculating the area of the voltage-charge diagram, using Origin 8 software, giving approximately 0.96 mJ. Accordingly, the mean power delivered to the atomizer in this experiment is estimated to be 36.5 Watt (= 0.96 mJ × 38 kHz) *(Takaki and Fujiwara, 2001)*. The estimated value through the Lissajous figure denotes the actual power dissipated in the atomizer, which is a clear indication of the level of power losses in the system.

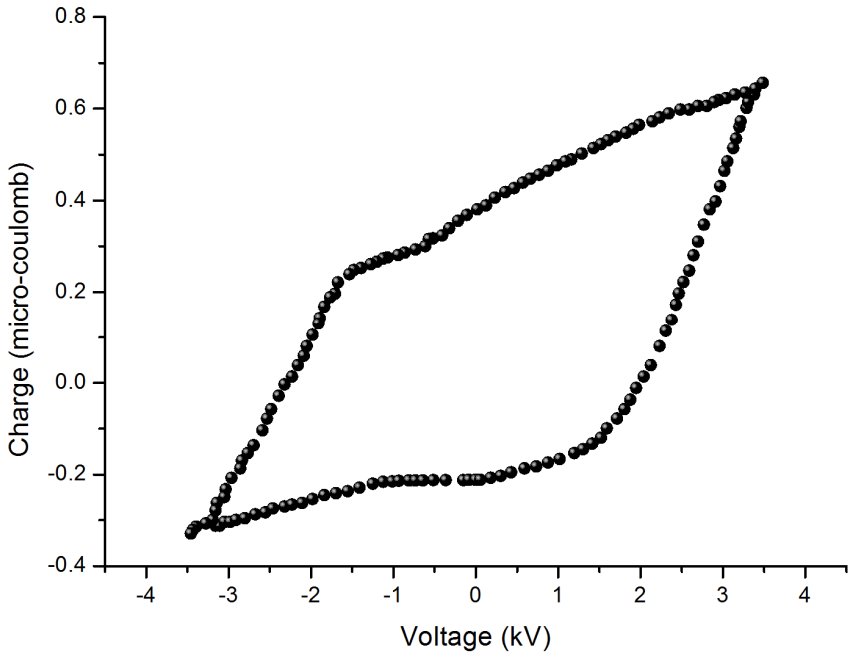

Figure 4-5 the Lissajous figure generated for the DBD / configuration (no.3) for one cycle when using argon gas and applying 38 kHz

It is worth noting that the produced characteristic shape in the current study is similar to that generated for a plane surface electrode as shown in the work of *(Takaki and Fujiwara, 2001)*. Upon generating Lissajous figures for the DBD configurations (1 and 2), similar parallelogram shapes are obtained, which indicate no effect of changing the area of the electrodes overlapping section.

Most importantly is the generated plasma in configuration (No.3) which is observed spectrometrically at relatively higher intensity compared with other configurations when applying the same power. Since similar frequency magnitudes are adopted for all tested configurations, increasing the area of the electrodes overlapping section in configuration (No.3) probably results in a slightly higher exerted power, compared with other configurations, which could not be detected on the power source LCDs. This increased power leads to the formation of more filaments in the discharge area, and consequently results in a higher glow discharge. It is believed that higher glow intensity is more advantageous for the spectrometric data analysis; thus, configuration (No.3) has been selected to conduct further studies in this research.

Pictures for plasmas obtained upon testing three gases via the DBD atomizer (configuration no. 3) are shown in **Figure (4-6)**.

(a) Argon discharge (whitish blue-violet), MBV ≈ 3.8 kV	(b) Helium discharge (violet), MBV ≈ 4.0 kV	(c) Nitrogen discharge, (blue-purple tendency), MBV ≈ 4.9 kV
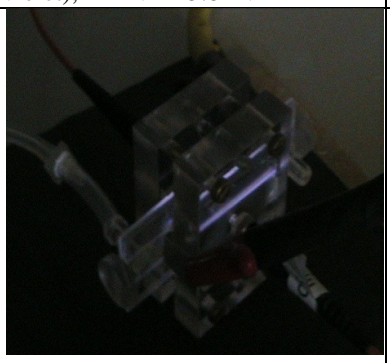	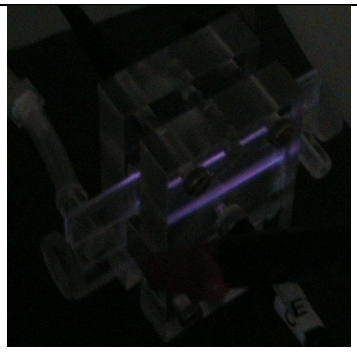	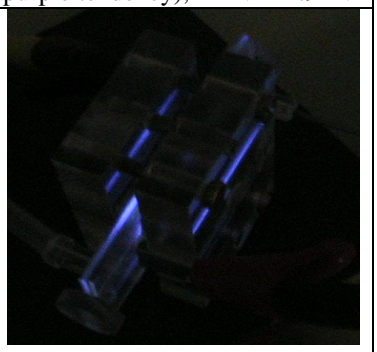

Figure 4-6 pictures for argon, helium and nitrogen DBD plasmas obtained upon applying (4 cm^2) electrodes overlapping section;
Where MBV represents the minimum breakdown voltage which has been obtained from the current - voltage characteristic diagram

4.4.2 Optimization of the spectrometric system parameters

The spectrometric parameters of the system are optimized by applying an experimental design plan according to the second order central composite rotatable design *(Cochran and Cox, 1992)*. Some details of the central composite design are shown in **Appendix 11.3**. Three parameters are treated in the optimization plan and tested in the following ranges:

- the integration time of the system: 300 – 1100 (ms)
- the boxcar width: 0 – 4
- the applied power: 75 – 175 (Watt) at constant frequency (≈ 38 kHz)

The values of the voltage and current displayed on the power source LCDs are calibrated using a high voltage probe and current clamp meter in order to be equivalent to the real values at the load (DBD atomizer). The tested power magnitudes are obtained by changing the voltage and current values making a priority to keep the current value at the load (DBD atomizer) within a defined range. The whole experiment is conducted at a constant gas flow rate (100 ml/min). Argon is selected to implement this study, in which the intensity of argon line at (314.64 nm) is recorded due to changes in the system parameters. The spectrometer software (SpectraSuite) is provided with a calibration criterion via the boxcar width function which acts as a tuner across multi

spectral data. For instance, a value of (boxcar width = 4.0) averages each data point with 4 points to its left and 4 points to its right; thus, a higher signal to noise ratio and smoother data is obtained when increasing the boxcar width. Hence, it was observed that the noise signal was reduced when the boxcar width increases to values more than zero, therefore it was decided to optimize the boxcar width value while considering the intensity of the selected emission line to be the objective function of the investigated system. The system has been tested according to the experimental plan shown in **Table (4-2)**, in which the real variables are converted into coded values. A quadratic multivariable model, equation (4-2), has been produced for the investigated system combining the single effect of the variables in addition to the effects resulted from interactions of the variables, (details given in **Appendix 11.3**).

$$Y = B_0x_0 + B_1x_1 + B_2x_2 + B_3x_3 + B_{11}x_1^2 + B_{22}x_2^2 + B_{33}x_3^2 + B_{12}x_1x_2 + B_{13}x_1x_3 + B_{23}x_2x_3 \quad (4\text{-}2)$$

A multiple stepwise regression analysis is performed to estimate the polynomial coefficients, (**Table (4-3)**). The average absolute error of the model is estimated to be 2.48 % (**Appendix 11.3**).

The optimal conditions for the highest intensity were obtained by performing non-linear constrained optimization using Matlab software (**Appendix 11.4**). The estimated optimal values are shown in **Table (4-4)**.

The optimal values of the integration time and the boxcar width are adopted in later experimental investigations in this research, whilst the estimated power conditions (≈ 5 kV × 25 mAmp ≈ 125 Watt) are applied in the assessment of the DBD plasma characteristics as presented in **Section (4-5)**.

Table 4-2 the experimental conditions according to the 2nd order central composite rotatable design and the recorded intensities for 314.64 nm emission line

Exp. No.	Integration time (ms)		Boxcar width		Power (Watt)		Intensity (*Y*) (a.u.)
	Real Value	Code (x_1)	Real Value	Code (x_2)	Real Value	Code (x_3)	
1	500	-1	1	-1	100	-1	823
2	900	+1	1	-1	100	-1	1361
3	500	-1	3	+1	100	-1	704
4	900	+1	3	+1	100	-1	1152
5	500	-1	1	-1	150	+1	703
6	900	+1	1	-1	150	+1	1189
7	500	-1	3	+1	150	+1	620
8	900	+1	3	+1	150	+1	1024
9	300	-1.682	2	0	125	0	526
10	1100	+1.682	2	0	125	0	1527
11	700	0	0	-1.682	125	0	1140
12	700	0	4	+1.682	125	0	852
13	700	0	2	0	75	-1.682	1050
14	700	0	2	0	175	+1.682	717
15	700	0	2	0	125	0	944
16	700	0	2	0	125	0	939
17	700	0	2	0	125	0	936
18	700	0	2	0	125	0	941
19	700	0	2	0	125	0	935
20	700	0	2	0	125	0	932

Table 4-3 the estimated polynomial coefficients

B_0	B_1	B_2	B_3	B_{11}	B_{22}
938.3643	260.6542	-77.6479	-77.9181	26.4792	15.6932
B_{33}	**B_{12}**	**B_{13}**	**B_{23}**		
-24.0914	-21.50	-12.0	10.0		

Table 4-4 the estimated optimal parameters for argon system

Integration time		Boxcar width		Applied power	
x_1	(ms)	x_2	Real value	x_3	(Watt)
-0.0359	≈700	0.1241	≈2.0	-0.114	≈120

4.4.3 Analysis of gases spectra

The discussion presented in this section is related to the spectrum shown in **Figure (4-7)**. The spectrum shown in **Figure (4-7/A)** is obtained in the current system for a stream of pure argon injected at 100 (ml/min); however, it shows species other than argon. The spectrum shows obvious argon lines, Ar (I), with considerable signal intensities in the visible range (696.54 nm) and infra-red region (794.81 nm), whereas other possible lines appeared with lower intensities (e.g. 706.87 nm). According to *(Bogaerts et al., 1998)*, the emission lines near the infra-red region are the most dominant in the argon spectrum, therefore the argon emission lines with higher intensities are selected in this study for plasma characterization.

Other peaks observed in the range (300 – 390 nm) and (390 – 480 nm) are attributed to the N_2 second positive system and ionized nitrogen molecules respectively *(Hong et al., 2008)*. *(Zhu et al., 2008a)* reported that molecular N_2 appears in the region 337-380 and ionized molecular N_2^+ at 391.4 and 427 nm. They also mentioned that the peaks at 777 and 844 nm are principally related to the reactive species of atomic oxygen, whereas the bands between 280-285 and 302-317 nm are characterized to be OH molecular emission lines *(Zhu et al., 2008a).*

Although pure argon was applied, the spectrum shown in **Figure (4-7/A)** shows that peaks other than argon are higher. This result directed the author to investigate the spectrum of other gases (Helium and Nitrogen). The recorded spectrum of pure nitrogen and helium, shown in **Figure (4-7/ B and C)**, give emission lines in the region (300-450 nm) that appear similar to the argon experiment. These lines denote possible interferences between the emission lines of pure nitrogen and other species. Practically, the appearance of similar lines in all the recorded spectrums is probably generated from air and other contaminant entrainment, as reported in the work of *(Zhu et al., 2008a)*. Since the examined system in the current case is well fastened, no chance for leak is expected and therefore this possibility is low. The other possible reason is surface reactions that could occur inside the plasma bulk. Since simple microscope glass slides are used to construct the atomization channel, there is the possibility for the formation of species from surface reactions with glass in contact with the plasma. The reason is apparently related to changes in glass properties, where the glass could be made hydrophilic upon being subjected to plasma effects *(Lim, 2004)*. It is mentioned in the

literature that a plasma effect leads to increasing the free radicals on the glass surface and the formation of polar compounds, which consequently causes considerable changes in the glass properties demonstrated by increases in the surface wettability. Other negative effects are also found on the dielectric properties of the glass laminate, whereas the surface resistivity increased *(Lim, 2004)*.

(A)

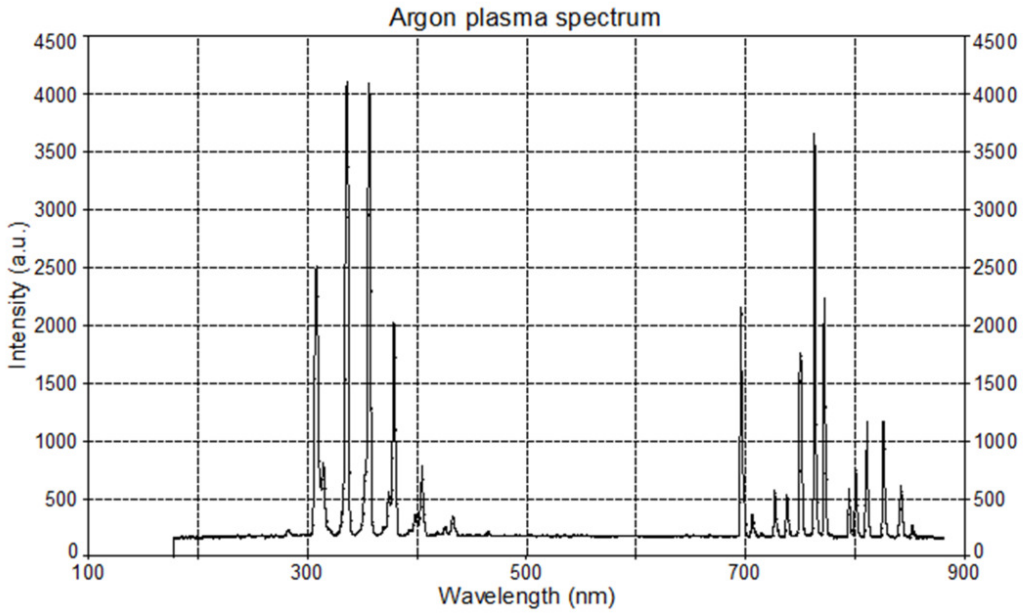

(B)

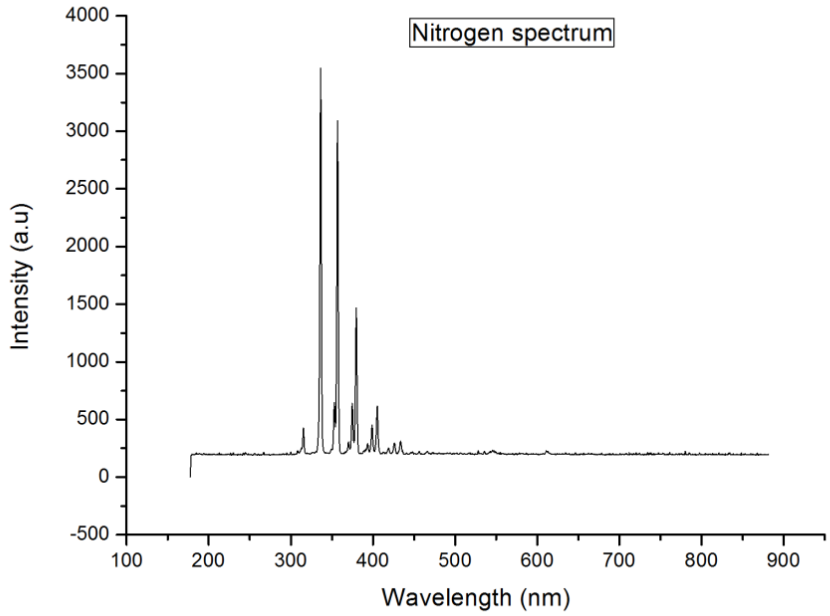

(C)

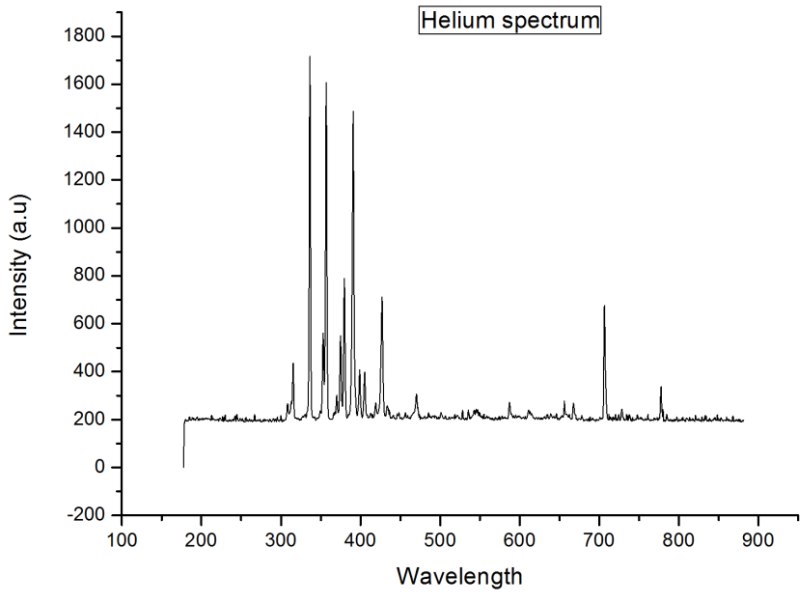

Figure 4-7 spectrum of high purity gases examined at 100 ml/min in the DBD atomizer; (A) argon with dominant lines at 696.54 and 794.81 nm, (B) nitrogen with dominant lines at 337.4 and 379.29 nm, (C) helium with dominant lines at 587.56 and 706.57 nm

The recorded spectrum of argon has been compared with the spectrum obtained from the work of *(Panakamol Deeyai and Dangtip, 2010)*. Their argon spectrum shows only one peak on the left hand side which is attributed to OH species at 309 nm, whereas the peaks to the right hand side resemble the peaks shown in the spectrum in the current study. The comparison is also made with the argon and helium spectra obtained by *(Zhu et al., 2008a)*, where similar left hand peaks with high intensity were observed in their argon spectrum, whereas obtained with low intensity in their helium plasma spectrum.
Looking at the similarities between this work and the abovementioned studies, the DBD atomizer was constructed of glass plates in the work of *(Zhu et al., 2008a)* and our study; accordingly, the left hand side peaks are observed in both cases. The only difference is between the argon spectrum is the peaks of *NO* which appeared in the region (215 – 272 nm) in the work of *(Zhu et al., 2008a)* but not observed in the spectra in this work. In contrast, no clear indication of glass material is mentioned in the work of *(Panakamol Deeyai and Dangtip, 2010)* which probably leads to different peaks shown to the left hand side of their spectrum.

These findings emphasize that an unknown species might be formed as a result of surface reactions on the glass layer. In order to explore the possible changes on the glass layer properties upon being subjected to plasma effects, the contact angle of a demineralized water droplet has been measured by using a one angstrom tensiometer and applying the sessile drop technique. The measurement applied for two glass slides; before and after being subjected to the plasma for few hours (not continuously). The results show that the contact angle for demineralized water droplet increases from 56,3^{o} to 103,35^{o} as shown in **Figure (4-8)**, which indicates significant alterations in the surface properties due to the plasma effect.

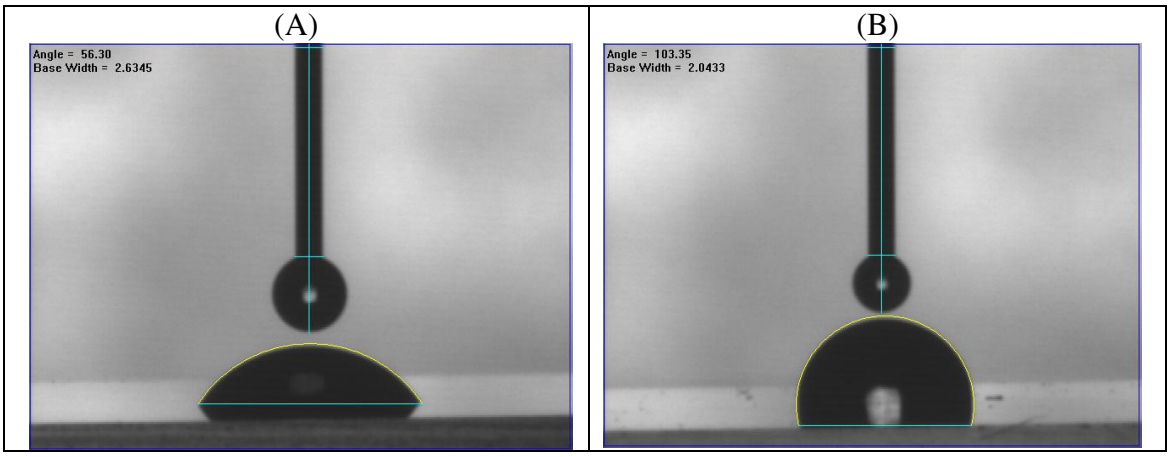

Figure 4-8 pictures show the results of the contact angle measured for two glass slides; (A) 56,3^{o} before being subjected to plasma effect, (B) 103,35^{o} after affected by plasma

It is also observed that the intensity of the peaks, to the left hand side of the spectrum, increases in accordance with the usage, i.e. higher intensity is proportional to the long use of the glass plates. This observation has been confirmed by replacing the glass slides with new ones; where the peaks of interest appear with a slightly lower intensity in the first use and increase with time; however, this interpretation should be supported with more investigations.

Further investigations were made to explore the effects of tubing material on the recorded spectra. The experiments were conducted using three kinds of tubing (Silicone, tygon, and poly ethylene) for connection between the gas cylinders and the DBD atomizer. It is observed that similar spectra were obtained in all cases, which indicates no effects due to changes in tubing material.

Although most of the peaks to the left hand side of the spectrum are attributed in the literature to the molecular and ionized nitrogen, other references show that peaks at 305, 336, 337, and 375 nm could be related to *NH* at an excited state upon several transitions *(Haak and Stuhl, 1984)*. In practice, the formation of *NH* species in the DBD atomizer is possible provided that a hydrophilic layer forms on the surface, which results in attracting the traces of water molecules and their deposition on the surface. Once the water molecules are deposited on the surface, a probability for *NH* formation, fragmentation, and excitation strongly exists since hydrogen has affinity to nitrogen that could be found in the inlet gas stream.

To sum up, it is difficult to elucidate a clear identification for the peaks shown to the left hand side of the spectra; however, the possibility for surface reactions and unknown species formation exists.

4.5 Investigations of DBD plasma characteristics

It is well known that the atmospheric DBD plasma consists of many separate microdischarges, also referred to as filaments, which result in transient plasma behaviour. The investigation of DBD plasma dynamics under atmospheric conditions requires spectral instruments with high resolution *(Wagner et al., 2005)*. Plasmas identities are normally inferred by determining the excitation and electron temperatures which can give an insight to their characteristics. Since the atmospheric DBD plasma is collision dominated, the most conventional way for measuring the temperature, a Langmuir probe, is difficult to apply for two reasons. The first is the high probability for electron and neutrals to collide before collecting the electrons by the probe *(Zhang et al., 2007)*. The second is the confined size of the plasma which makes the insertion of the probe into the plasma bulk difficult. An optical emission spectroscopy technique is used in this study for plasma characterization. The DBD configuration presumes a presence of an insulating layer between the two powered electrodes, which prevents the formation of a local thermodynamic equilibrium (LTE) *(Nehra et al., 2008)*, and consequently results in large differences between plasma temperatures ($T_e > T_{exc} > T_g$). Principally, the non thermal equilibrium condition occurs in a DBD atomizer because the primary and secondary electrons lose their energy and dissipate in a very short

period; therefore no energetic equilibrium is expected between electrons and heavy particles. Nonetheless, a large portion of the energy accumulates in meta-stable atoms and gradually releases to the discharge volume, which consequently maintains the discharge *(Stefecka et al., 2001)* .

The aforementioned details presume that there is no possibility for an LTE condition to hold within a DBD atomizer. Nevertheless, some researchers reported the existence of LTE conditions in a DBD plasma under special conditions.

The LTE condition assumes the population density of the species in the excited state follows the Boltzmann distribution function *(Gordillo-Vázquez et al., 2006).* In this case, the collision rate of depopulation from the excited state would be at least ten times greater than the radiative depopulation rate *(Faires et al., 1984).* Practically, the LTE condition is reported possible given the availability of high electron density. *(Alder et al., 1980)* measured the electron density for atmospheric DBD argon and found it in the order of 10^{16} cm^{-3}; accordingly, they report a probable LTE condition in their system. Further, *(Wagner et al., 2005)* measured the electron density for a N_2/O_2 mixture in a DBD plasma atomizer and found it to be in the order of 10^{20} m^{-3}; hence, they considered their system satisfies an LTE condition. Most controversial is the finding of *(Zhang et al., 2007)* who reported the existence of an LTE condition in their DBD argon system, provided that a high electron density N_e is available, according to the criteria shown in equation (4-3).

$$N_e \geq 1.7 \times 10^{20} \, (k \, T_e)^{1/2} \, X_{pq}^3 \qquad (4\text{-}3)$$

Where; k represents Boltzmann's constant, T_e is the electron temperature and X_{pq} is the energy level difference between upper state (q) and lower state (p).

In summary, the studies agree that the probability of LTE existence is directly related to the electron number density (10^{20} – 10^{22} m^{-3}) in a DBD plasma bulk, which has been adopted as a criterion to characterize the plasma generated in the current system.

For the DBD system adopted in this research, the aim is to characterize the plasma generated in the chip by measuring the electron number density and plasma temperatures (T_e , T_{exc} ,T_{rot} *and* T_g). As mentioned in **Section (2-4-2)**, applying the stark broadening technique or Thomson laser scattered method for estimating the electron

number density requires special preparation which is not applicable to the current case; thus, the electron number density in the system is calculated as a first step by applying the following fundamental principles:

$$n_e = \frac{J}{e.v_d} \quad (4\text{-}4)$$

Where;

n_e : the electron density (m^{-3}) , J : Plasma current density (Amp. m^{-2}) ,

e : electron charge = 1.602×10^{-19} (Amp.sec) , v_d = electron drift velocity (m. sec^{-1})

The electron drift velocity is estimated from the electron mobility and the applied electric field as follows:

$$v_d = \mu \times E \quad (4\text{-}5)$$

The mobility of the electron in atmospheric pressure argon plasma is estimated to be 0.01 m^2 V^{-1} sec^{-1} at 5000 ^oK *(Mili et al., 1987)*. As mentioned in **Section (4.4.2)**, a value of 5 (kV) is adopted as an optimum voltage which gives an electric field of 5×10^6 ($V.m^{-1}$) across 1 mm gap. Applying the estimated values of mobility and electrical field in equation (4-5) produces a drift velocity equal to 5×10^4 (m. sec^{-1}). The plasma current has been measured by using validated digital current clamp meter (UNI-T, UT 201) in a position very near to the load and found to be 25 mAmp when applying 5 kV. This value approximated the value shown on the LCD of the power supply. Current density is determined by dividing the current value by the cross sectional area of the atomization channel ($0.01\times0.001 = 1\times10^{-5}$ m^2), which produces a value of 25×10^2 Amp. m^{-2}. Applying the abovementioned values in equation (4-4) produces an electron number density equal to 3.1×10^{17} (m^{-3}) which is in agreement with the range reported in the literature *(Nehra et al., 2008)*. Since the estimated electron density is lower than the range (10^{20} – 10^{22} m^{-3}) that is required for LTE condition, it is concluded that the examined DBD system follows non thermodynamic equilibrium conditions (nLTE).

The spectral parameters of the peaks of the argon spectrum (**Figure (4-7/A)**), are obtained from the database of the national institute of standards and technology *(NIST-website, 2010)* (**Table 4-5**).

Table 4-5 Argon emission lines parameters and their recorded intensities (*)

λ_{ij}	A_{ij}	E_i	g_i	I_{ij}	$\ln\left(\frac{I_{ij}\lambda_{ij}}{g_i A_{ij}}\right)$
nm	sec^{-1}	cm^{-1}		a.u.	
696.54	6.39×10^6	93143.76	5.0	2081	-3.092
706.87	2.0×10^6	105617.27	5.0	171	-4.415
727.29	1.83×10^6	93750.59	3.0	560	-2.601
750.38	4.45×10^7	95399.82	3.0	1750	-4.621
794.81	1.86×10^7	94553.66	1.0	564	-3.725

Another important parameter discussed in the literature is the excitation temperature. This is found in most cases to be below 1 eV in a DBD plasma bulk. *(Alder et al., 1980)* reported an excitation temperature of 7000 ^{o}K in their atmospheric argon plasma system, while *(Zhang et al., 2007)* measured an excitation temperature in the range of 4200 to 4950 ^{o}K. *(Dong et al., 2005)* measured the excitation temperature in an atmospheric pressure argon DBD plasma and found it in the range 0.1-0.5 eV.

The conventional method to determine the excitation temperature is based on generating a Boltzmann plot by assuming an existence of LTE conditions, as illustrated in equation (4-6) *(Gordillo-Vázquez et al., 2006)*.

$$\ln\left(\frac{I_{ij}\lambda_{ij}}{g_i A_{ij}}\right) = -\frac{E_i}{k\,T_{exc}} + C \qquad (4\text{-}6)$$

T_{exc} is determined by applying the Fermi–Dirac distribution for the excited particles as described by *(Zhang et al., 2007)*.

$$\ln\left(\frac{I_{ij}\lambda_{ij}}{g_i A_{ij}}\right) = -\ln\left(\exp\left(\frac{E_i-\mu}{k\,T_{exc}}\right)+1\right) + C \qquad (4\text{-}7)$$

Where; μ represents the chemical potential (cm^{-1})

*: I_{ij} : the intensity of the emission line between the energy levels *i* and *j*, λ_{ij} : wavelength, g_i : the statistical weight of the emitting upper level *i* of the studied transition, A_{ij}: the transition probability for a spontaneous radiative emission from the level *i* to the lower level *j* , *Ei* : the excitation energy of level *i*.

Non linear curve fitting is conducted by applying a value (μ = 105000 cm^{-1}) and utilizing the non linear model fit tool in Wolfram Mathematica 7.0, to estimate the parameters in equation (4-7). This produced: T_{exc}= 6398 ^{o}K and C = -3.4689 with a standard error of 0.633. The calculated T_{exc} is very near to the value estimated by *(Alder et al., 1980)* but slightly higher than those estimated by *(Zhang et al., 2007, Dong et al., 2005)*, where the differences could be attributed to a different range of spectral lines used in these studies.

The electron temperature is calculated in a non thermodynamic equilibrium condition according to the following relation *(Gordillo-Vázquez et al., 2006)*:

$$\ln\left(\frac{I_{ij}\sum_{i>j} A_{ij}}{h\nu_{ij}\, A_{ij} b_i}\right) = \ln(R) = -\frac{E_i}{k\, T_e} + D \qquad (4\text{-}8)$$

Where;
D : constant, T_e : electron temperature, $h\nu_{ij}$: energy difference between levels i and j
$b_i = E_i^a \times P_i^b$, a *and* b are the fitting parameters obtained from *(Gordillo-Vázquez et al., 2006)*, (e.g. for line 750.38 nm , $a = -5.849$ *and* $b = -5.045$)

$$P_i = \sqrt{\frac{E_H}{\varphi - E_i}}$$

E_H : is the Rydberg constant (13.6 eV), φ and Ei are the ionization energy of argon species and the energy of the excited state *i* respectively.
Applying the sorted data in equation (4-8) produces the modified Boltzmann plot shown in **Figure (4-9)**.

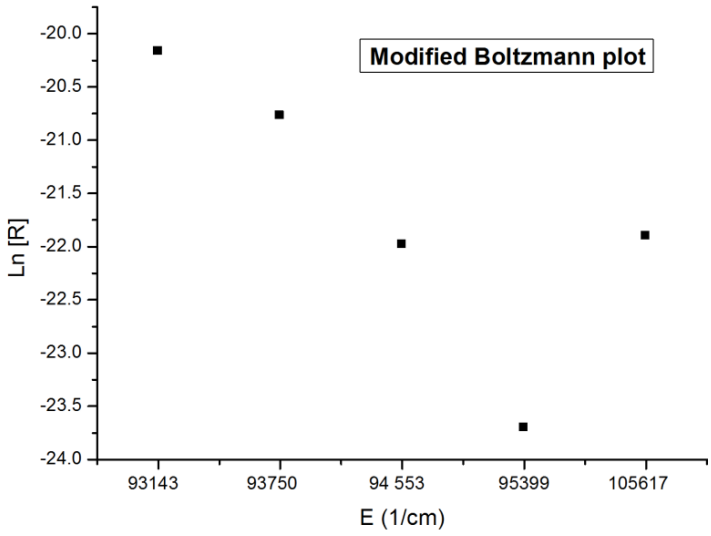

Figure 4-9 the modified Boltzmann plot

The data has been fitted by using the linear regression analysis tool through Wolfram Mathematica 7.0 software, producing the formula shown in equation (4-9) which has been applied to estimate the electron temperature:

$$\ln\left(\frac{I_{ij}\sum_{i>j} A_{ij}}{h\nu_{ij}\, A_{ij} b_i}\right) = \ln(R) = -\ 0.0000634\, E_i - 15.5832 \qquad (4\text{-}9)$$

The slope in equation (4-9) is equal to $\frac{-0.625}{T_e}$ and equivalent to (-0.0000634) which gives $T_e = 9858\ ^{o}\text{K} = 0.849$ eV

For an extra check, the electron number density (n_e) is re-estimated by applying the power balance criterion, shown in equation (4-10), assuming the plasma energy dissipates due to electron heating *(Park et al., 2001, Moravej et al., 2004)*:

$$P_{in} \approx P_{loss} \approx n_e \left(\frac{3}{2}kT_e - \frac{3}{2}kT_n\right) 2\frac{m_e}{m_{Argon}}\, \nu_{en} \qquad (4\text{-}10)$$

Where;
P_{in} : the applied power = 125 watt / 4×10^{-7} m^3 = 3.125×10^8 (watt. m^{-3}), m_e : mass of electron = 9.1×10^{-31} (kg), m_{Argon} : mass of argon atom = 6.6×10^{-27} (kg), k : Boltzmann constant = 1.38×10^{-23} (J . ^{o}K^{-1}) , ν_{en} : electron – neutral collision frequency ≈ $5.3\times10^{9}\times p$ *(Cook et al., 2010)*; for atmospheric pressure plasma, p = 760 Torr → ν_{en} = 4.02×10^{12} (sec^{-1}), T_n : gas temperature ≈ 359 ^{o}K, T_e : electron temperature = 9858 ^{o}K

Solving equation (4-10) for n_e produces $n_e = 1.45\times10^{18}$ (m^{-3}).

The calculated electron number density from equation (4-10) is higher than the value estimated experimentally from equation (4-4) by an order of magnitude; however, the difference is not large and could be attributed to the assumptions made in the criterion followed. Hence, the approximate values obtained from both applied methods indicate that the values of excitation and electron temperatures are estimated with reasonable accuracy.

The last part of plasma characterization is to measure the rotational temperature in the DBD atomizer. It is reported that if the pressure of the plasma bulk is sufficiently high, there is a strong correlation between the rotational temperature and the gas temperature. However, the former is a description for an excited state while the latter is a measure of the mean kinetic energy of the gas particles *(Ionascut-Nedelcescu et al., 2008)*. It is also

reported that the rotational temperature slightly exceeds the gas temperature. This observation is attributed to the species heating-up which occurs due to different types of collisions. Hence, the rotational temperature is normally estimated by utilising the N_2^+ electronic band as shown in the work of *(Ionascut-Nedelcescu et al., 2008)* and *(Motret et al., 2000)*. Accordingly, the rotational temperature has been estimated in this research by utilising the fine structure of N_2^+ electronic band (the first negative system). The intensity of such rotational line (for a transition (J' – J'')) can be expressed as a function of the oscillator strength S_j according to the following equation *(Hill, 2006)*:

$$ln\frac{I}{2(K''+1)} = w - \frac{B_v\, h\, c}{kT}(K''+1)(K''+2) \qquad (4\text{-}11)$$

Where;
S_j = the oscillator strength = $(K''+1)(K''+2)$, K'' = the quantum number (assigned for the lower state), $K' = K''$-1, T = the rotational temperature (^oK), c = speed of light = 3×10^{10} (cm sec^{-1}), h = Plank constant = 3.336×10^{-11} (sec cm^{-1}), k = Boltzmann constant = 0.695 (cm^{-1} $^oK^{-1}$), B_v = the rotational constant belonging to the vibrational quantum number = 2.07, w = constant

The slope $\frac{-B_v\, h\, c}{kT}$ in equation (4-11) equals $\frac{-2.983}{T}$

The intensities of the N_2^+ electronic band (R branch) are obtained from **Figure (4-10)**, which represents the nitrogen spectrum, and plotted versus the oscillator strength as shown in **Figure (4-11)**. The values of S_j proportional to the observed wavelengths are listed in **Table (4-6)**.

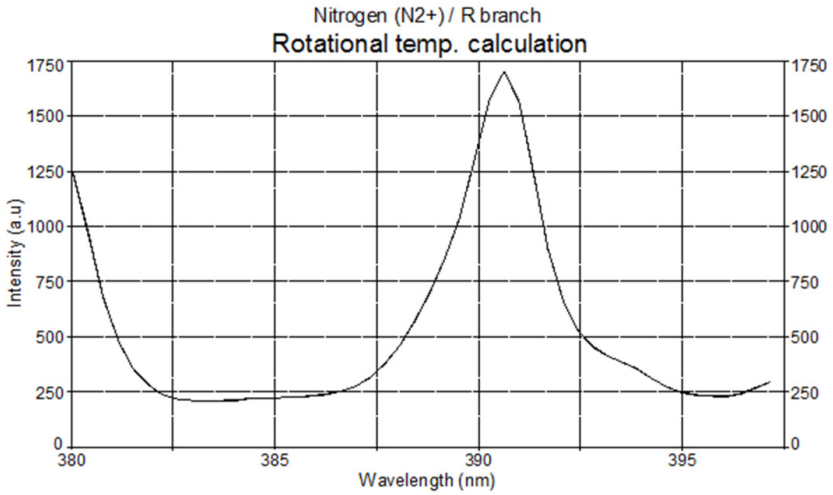

Figure 4-10 N_2^+ band (R branch)

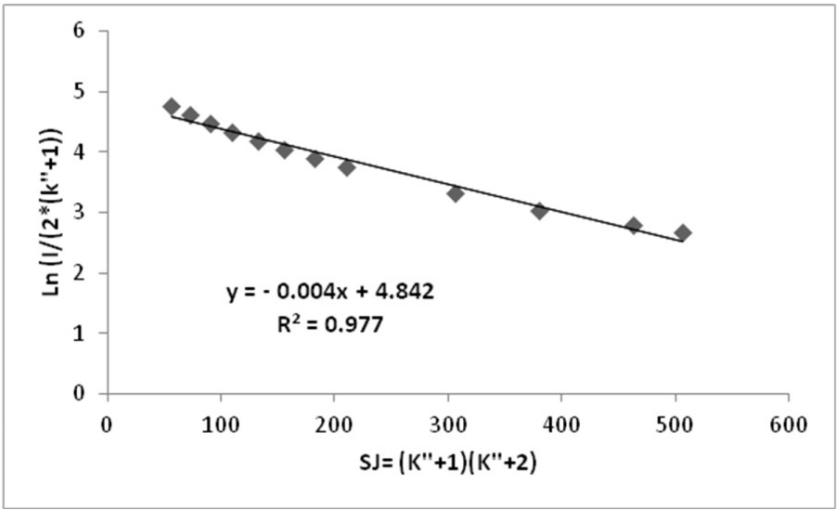

Figure 4-11 the estimation of the rotational temperature in the examined BDB atomizer

Table 4-6 Oscillator strength values according to the observed intensities of (N_2^+ band / R branch) *(Hill, 2006)*

Wavelength (nm)	Intensity (a.u)	$S_j = (K'' + 1)(K'' + 2)$	K''	$Ln\frac{I}{2(K''+1)}$
390.49	1656.4	56	6	4.77
390.4	1618.3	72	7	4.61
390.29	1594.1	90	8	4.48
390.19	1524.8	110	9	4.33
390.08	1448.5	132	10	4.18
389.97	1365.3	156	11	4.04
389.85	1285.6	182	12	3.90
389.73	1195.5	210	13	3.75
389.33	935.64	306	16	3.31
389.04	797.03	380	18	3.04
388.74	686.14	462	20	2.79
388.58	634.16	506	21	2.66

A slope equal to (-4×10^{-3}) is obtained from the graph, **Figure (4-11)**, which indicates a rotational temperature of 745 ^{o}K (= 0.064 eV) is estimated in the current system.

Since the aim of the current analysis is to characterize the DBD plasma for design purposes, local measurement of gas temperature is essential to indicate the highest temperature which would be reached during continuous operation of the chip. It is assumed in the current experiments that the measured value is equivalent to a temporal and spatial averaged gas temperature. The outlet gas temperatures for three investigated gases (argon, helium and nitrogen) were measured to study the limits of the chip heating

during the operation time. A thermocouple is placed in the outlet section of the gas channel, and the temperatures recorded manually with time. The temperature increase is found to be dependent on the gas flow rate, as illustrated in **Figure (4-12)**. The highest outlet gas temperature (86.4 ^{o}C) is for nitrogen, which is recorded after 15 minutes operation at 290 ml/min. This observation is found to be a slightly higher than the range (44-70 ^{o}C) reported in the work of *(Zhu et al., 2008c)* at 850 ml/min gas flow rate. The difference could be attributed to a higher gas flow rate, which might result in a higher cooling rate in the gas channel. The temperature range observed in the current research is considered reasonable, which allows the possibility of operating the DBD atomizer in proximity to other compartments, and consequently supports the device miniaturization.

In summary, the estimated electron temperature, excitation temperature, rotational temperature and the measured gas temperatures in the investigated system are demonstrated in the following order ($T_e > T_{exc} > T_{rot} > T_g$) which indicates a non thermal plasma is generated in the DBD atomizer. The temperature (0.07 eV) predicted from the computations in chapter 3 is found to be higher than the measured gas temperature (T_g) but in the same range as the estimated rotational temperature (T_{rot}). This shows that the computed temperature is related to the excited species in the bulk plasma.

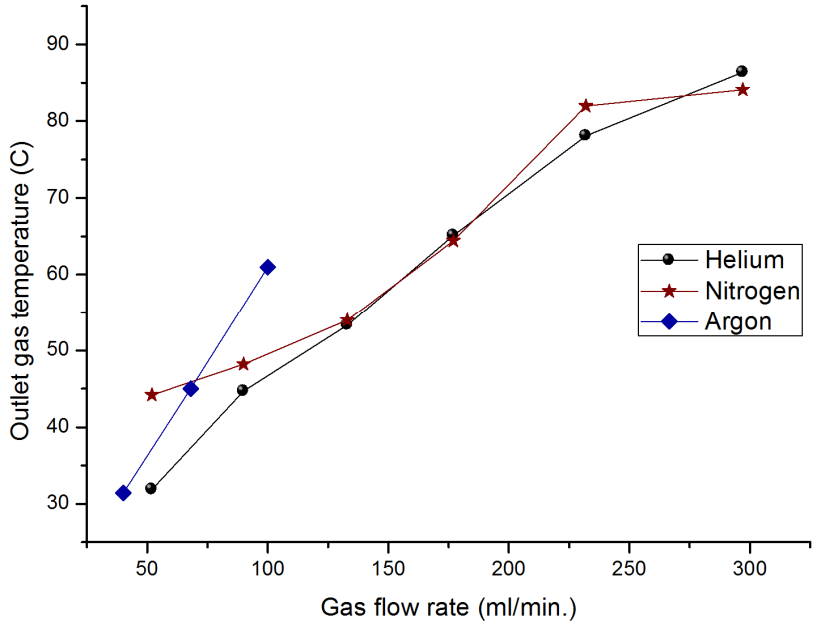

Figure 4-12 the variation of the outlet gases temperature with gas flow rate;
the temperatures were recorded after getting stable value (approximately 5 minutes) of the experiment start up. Higher flow rates for helium and nitrogen were examined due to a stable performance compared with argon

The argon plasma was found to be slightly different from helium and nitrogen plasmas. Shooting pulses (similar to arcing) from the plasma channel toward the thermocouple sensor occurs due to the gas flow rate increases from 40 to 60 ml/min. This becomes more obvious when a higher argon flow rate used, and consequently leads to sensor heating and deviation in the recorded outlet gas temperature. Although a different sensor position was applied to overcome the arcing, only three values of argon flow rate could be applied. This phenomenon was not observed for helium and nitrogen. Nonetheless, increasing the helium flow rate from 90 to 130 ml/min led to a plasma tail formation. The aforementioned observations are illustrated in **Figure (4-13)**. These different behaviours can be related to the gas first ionization potential, where argon gas has the lowest value (15.6 Volts) compared with nitrogen and helium (15.8 and 20.5 Volts respectively) *(Found, 1920)*. Other references show higher values for nitrogen and helium (16.3 and 24.5 Volts respectively).

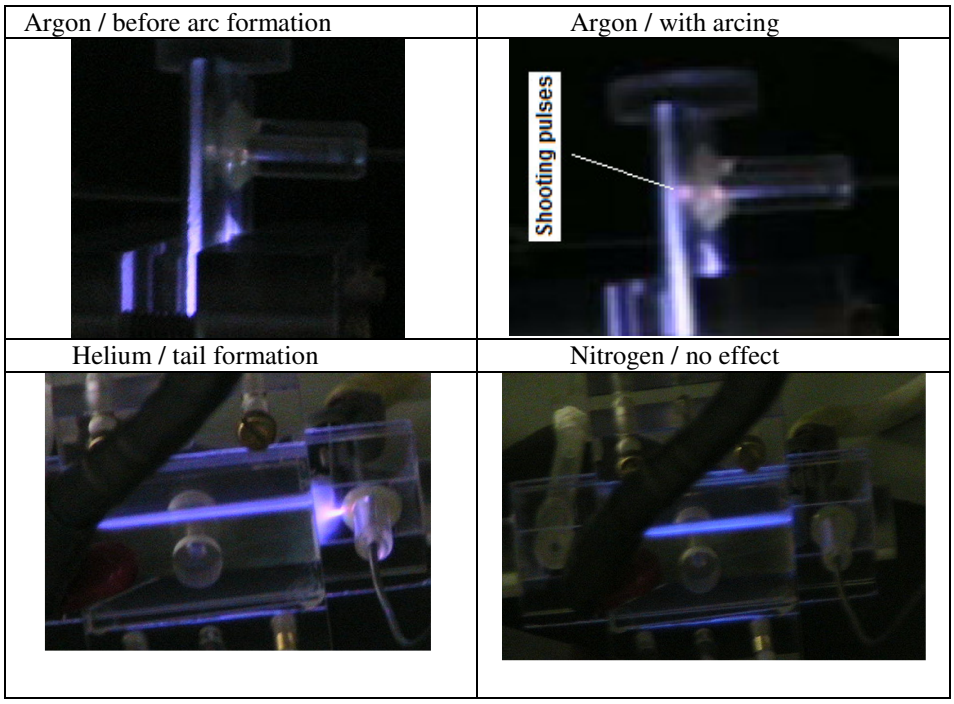

Figure 4-13 the effect of increasing the gas flow rate on plasmas behaviour

It is worth noting that the ionization potential refers to the voltage magnitude where a discontinuity in the linear dependency occurs in the ampere-voltage characteristic diagram caused by a rapid increase in current over voltage. The reason is the increase in

the positive ion density resulting from the applied potential that causes higher current to flow from the cathode to the anode. Therefore applying higher power is expected to increase the probability of gas breakdown and lead to a higher ionization rate for gases of low potential. Hence, the reason of arcing in the case of argon could be increased current in the bulk. It is also observed that the argon arcing becomes more intense at a higher gas flow rate. The nitrogen plasma is not affected even at maximum flow rate (290 ml/min) and appears more stable in the limits of the electrode overlapping section, whereas helium is found to be more sensitive to the flow increase and consequently a tail forms. The variation of signal intensity with a change in the argon flow rate is illustrated in **Figure (4-14)**.

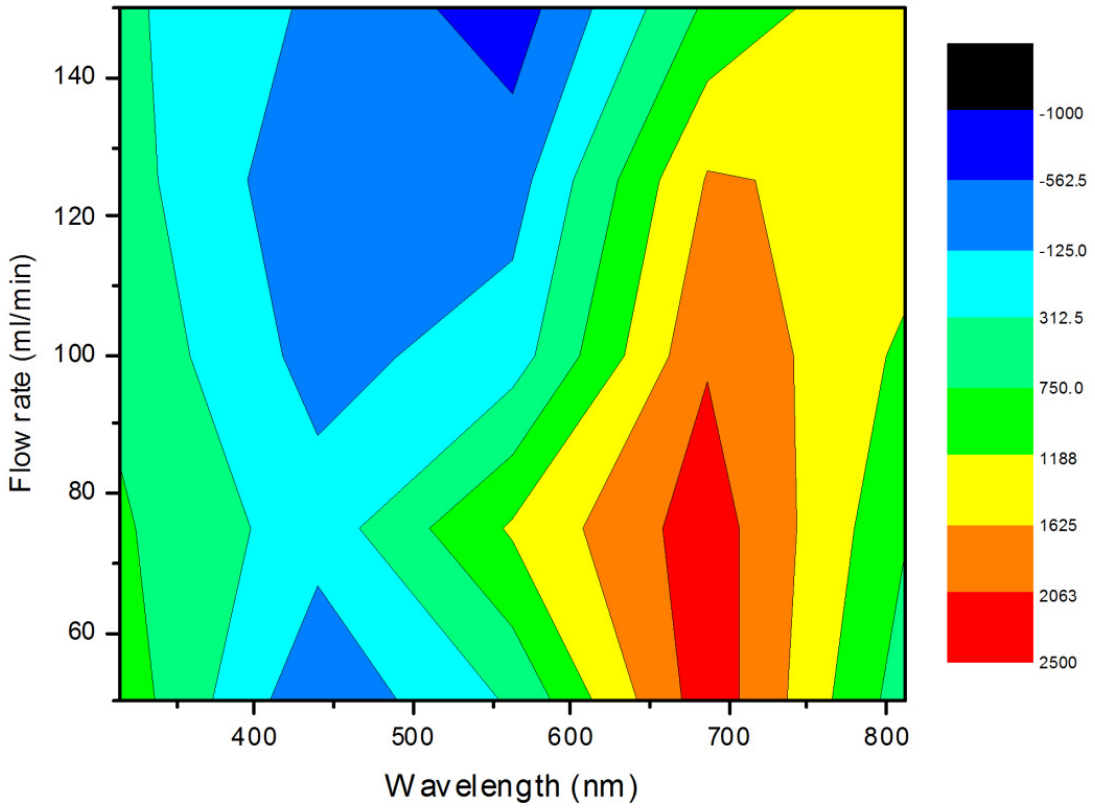

Figure 4-14 a contour diagram show the argon peaks intensity versus different argon flow rates

4.6 Summary of the findings from chapter four

1-The poly methyl methacrylate (Perspex) material is affected by plasma discharge and found inappropriate for constructing a DBD atomizer, whereas microscope glass slides proved useful for this application.

2-Three DBD configurations were tested; one of them with the largest electrode overlapping area, was selected to fabricate the final version of the DBD reactor due to a slightly higher observed intensity compared with other configurations.

3-The spectrometric parameters of the system are optimized by performing a non-linear constrained optimization. The optimized parameters are adopted for later studies in this research.

4-The performance of the DBD atomizer has been studied by applying three gases to explore the gas flow rate on the atomizer temperature. The maximum gas temperature, measured at the outlet end of the gas channel, is found to be 86 ^{o}C after 15 minutes operation. The temperature indicates the possibility of housing the DBD atomizer in proximity to other compartments for the purpose of miniaturization. The argon gas is observed to be more aggressive than helium and nitrogen gases. The gas flow rate is also shown to have a considerable effect on the recorded spectrum, in which the appearance of argon lines is significantly affected by higher gas flow rates.

5-The argon plasma has been characterized by applying spectrometric analysis, where the measured plasma temperatures ($T_e > T_{exc} > T_{rot} > T_g$) indicate that a non thermal plasma is generated in the examined DBD atomizer. The electron number density was measured experimentally and found to be in the order of 10^{17} m^{-3} which indicates a non thermal equilibrium in the examined system.

5. APPLICATION OF THE PROPOSED TECHNOLOGY FOR MERCURY DETERMINATION

5.1 Preface

This chapter is dedicated to study the application of the proposed technology for the detection and the quantitative determination of inorganic mercury in water samples. In the first section, the performance of the DBD atomizer is assessed when injecting a stream combining water vapour and argon gas. The later sections are extended to study the performance when applying an inlet stream containing vapour species generated from the reaction with reducing agents. Two derivatizing agents are examined; the first is tin chloride whereas sodium and potassium tetrahydroborate are applied in the later experiments. Three types of gas-liquid separator (GLS) are investigated to assess the efficiency of hydrogen dilution and separation on the recorded mercury signal. The experiments with tin chloride were planned and conducted according to a 2^{nd} order central composite rotatable design, in which four parameters are examined in the experimental range, whereas the recorded mercury signal is the objective function. The experimental data are fitted by applying multi variable regression analysis in order to obtain an empirical model describing the whole process. Furthermore, an optimization technique and two statistical approaches are utilized to analyse the data and to explore the individual and interaction effects of the variables on the objective function. The later section of this chapter is dedicated to the quantitative determination of mercury and achieving system automation. An automated version of the proposed analytical system is produced, thereby online – real time determination of inorganic mercury in a water sample is accomplished. Further experimental investigations were conducted to study the possibility of improving analytical performance by applying a physical effect, namely magnetization. This is believed to assist the release of vapour species and may be an alternative to expensive chemicals (e.g. surfactants) which are normally used to facilitate the analyte derivatization processes.

5.2 The effect of water vapour on DBD plasma consistency

It is mentioned in previous studies *(Motret et al., 2000, Zhu et al., 2008a)* that a DBD plasma could be operated with an inlet gas stream saturated with water vapour. In this regard, *(Zhu et al., 2008a)* found an advantageous effect for the water vapour on DBD plasma stability in terms of lowering the emission background from other molecular species. The above evidence denotes the possibility of injecting the DBD atomizer with

an inlet gas stream saturated with vapour. Since the aim of the research is to couple the DBD atomizer with a pre-chemical derivatization process that produces vapour species, it is essential to verify the applicability of the design for this specific operating condition.

Hence, a series of investigations were conducted applying two experimental sets; the first without removing the moisture content from the inlet stream to the examined DBD atomizer, whereas the moisture content has been reduced in the second by using a silica-gel trap. **Figure (5-1)** illustrates the methodology used.

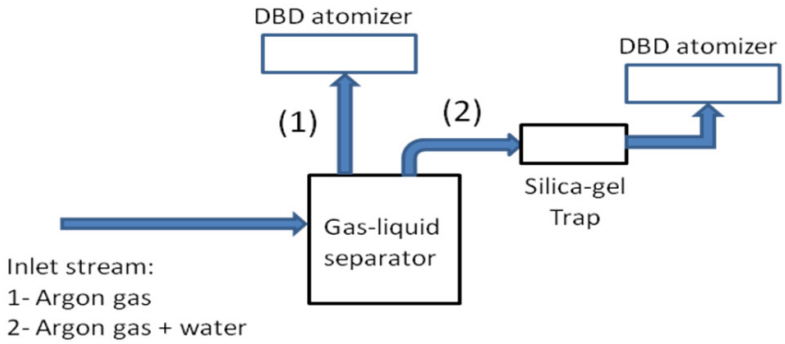

Figure 5-1 the methodology used to investigate the effect of moisture content on the DBD plasma consistency

A desiccant silica-gel (M_H value = 9) has been used to reduce the moisture content from the inlet stream to the DBD atomizer. Approximately 2 grams of silica-gel balls are packed in a plastic tube (6mm ID and 4 cm length) to form the trap as illustrated in **Figure (5-2)**. The function of the trap is aimed to remove 20% of the relative humidity of the stream that enters the trap at 100 ml/min.

Figure 5-2 a picture illustrates the silica-gel trap connected with a commercial gas – liquid separator

The results from all cases examined show that a significant change in the recorded spectrum occurs on introducing the water stream into the bulk of the gas-liquid separator. The intensity of most emission lines increased significantly after two minutes of the water introduction as shown in **Figure (5-3)**. *(Motret et al., 2000)* attributed this result to the collision of the argon excited species with OH radicals that form due to water molecule dissociation. The collisions lead to an efficient dissociative excitation of the water molecules, which consequently results in extra OH radicals as demonstrated by the increased intensity of OH emission lines (the band 302-317 nm). At the same time, the collision - radiative recombination of argon with energetic electrons results in forming argon atoms in various excited states, which is illustrated by the increased intensity of the argon emission line at 696.5 nm and other argon lines in the near IR region.

The introduction of the examined stream through the silica-gel trap before being introduced to the DBD atomizer results in negative effects. For instance, the intensities of the emission lines near IR region are significantly reduced; therefore all experiments in the later sections are conducted without using a silica-gel trap.

(A)

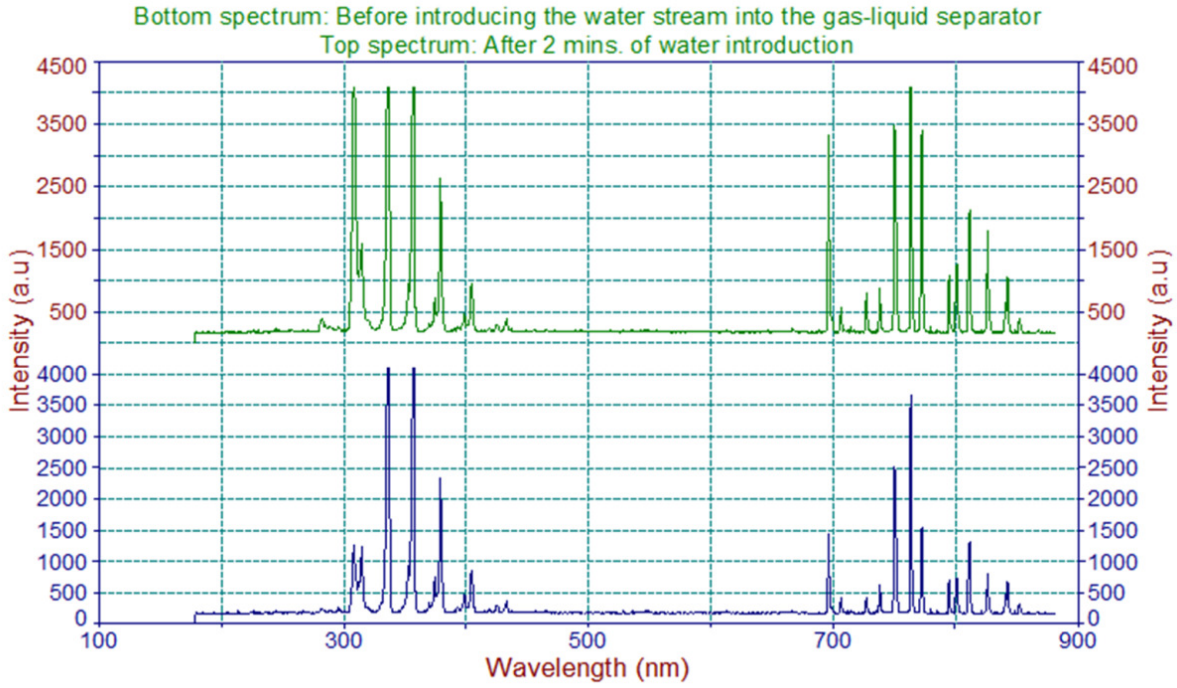

(B)

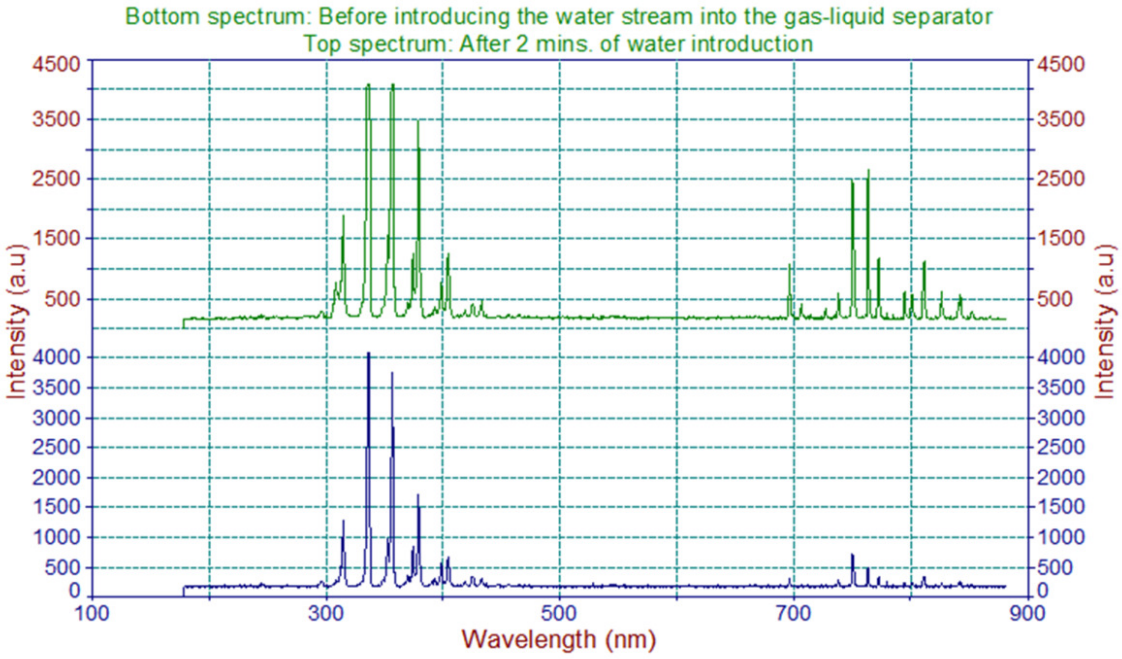

Figure 5-3 the effect of introducing gas stream saturated with water residues on the intensity of the emission lines;
(A) without using the silica-gel trap, **(B)** when the silica-gel trap is applied

5.3 Application of inorganic mercury cold vapour generation using $SnCl_2$ as a reducing agent

This section investigates the application of the DBD chip as a radiation source for the mercury vapour species generated from applying tin chloride ($SnCl_2$) as a reducing agent.

5.3.1 Experimental setup

The schematic diagram of the reaction system is shown in **Figure (5-4)**. Three single channel peristaltic pumps (Williamson pumps Ltd. – UK) were used for the water sample and other chemical feeding. One, fitted with 1.6 mm silicone tubing pumped the water sample at a rate of 2.8 ml/min, whereas 1.25 ml/min feeding rate pumps were used for HCl and $SnCl_2$ solutions. The water sample and the acidic solution were directed into a (20 cm length, 2.0 mm ID silicone tube) acting as a helical mixing coil. The mixed solutions (from the mixing coil) and the reducing agent $SnCl_2$ were directed

into a helical reaction coil (1 m length, 2.5 mm ID silicon tube). The reacted solutions are forwarded into a gas/liquid separator (GLS) where the influent stream is mixed with the carrier gas (4 mm ID plastic tube) through a tee junction placed ahead of the GLS entrance. The details of the traditional gas liquid separator (type A) used in this section are shown in **Figure (5-15)**. An additional argon line (30 ml/min) is introduced in the middle of the GLS to assist carrying the released vapour species from the influent stream into the DBD atomizer. The liquid residues are evacuated out of the GLS by using (2.8 ml/min) DC peristaltic pump, while the released volatile species are transported by the gas into the DBD chip. The carrier gas flow rate is controlled manually using gas flow meters purchased from (BOC special products – UK) and (Cole Parmer –USA).

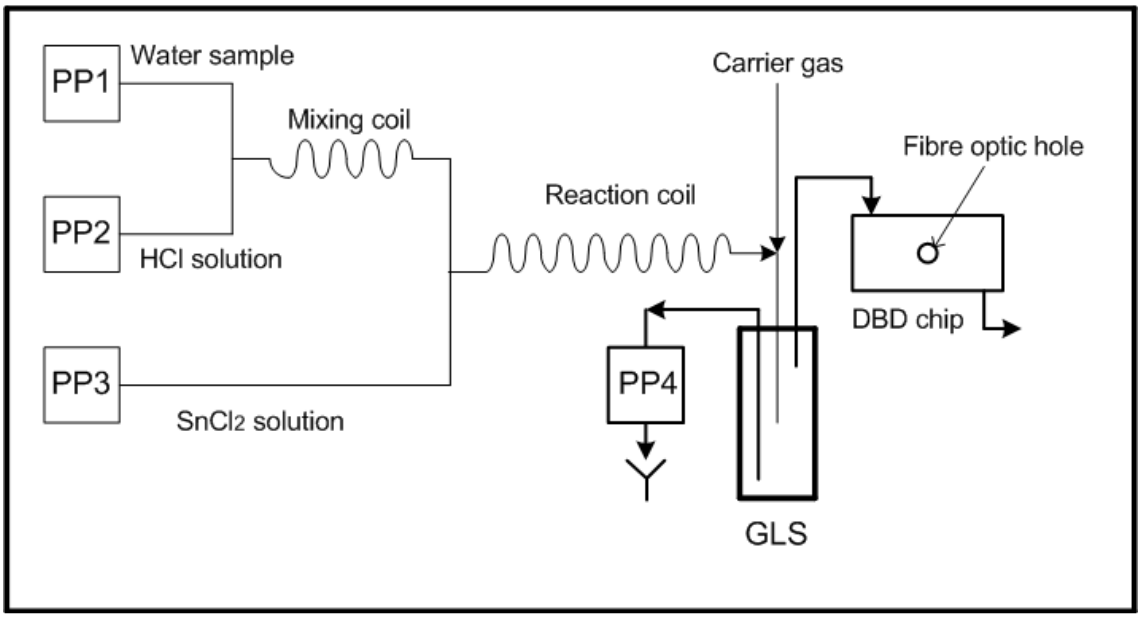

Figure 5-4 a process flow diagram for the system applied for the mercury cold vapour generation;
PP indicates peristaltic pump, GLS is a traditional self made gas liquid separator

5.3.2 Reagents

All chemicals used in this work were purchased from Sigma Aldrich (analytical reagent grades). A mercury atomic spectroscopy standard was applied to prepare 1 g/L stock solution. Specific amounts of the stock solution were diluted using distilled water to prepare the required working standards. HCl solutions (1-5% v/v) were prepared by diluting HCl concentrate (37 %) in distilled water, whereas the reductant solutions of tin

chloride (2-5% m/v) were prepared by dissolving suitable amounts of $SnCl_2$ in 1% v/v HCl. The background equivalent concentrations of mercury in the reagent solutions of $Sncl_2$ and HCl, which resulted from the impurities within the chemical reagents, were determined by using ICP-OES and found to be in the range 0.02-0.3 µg/L. High purity gases (99.999 % argon, helium, and nitrogen), purchased from (BOC-UK), are used in the experiments.

5.3.3 Optimization of the mercury cold vapour generation process

According to the literature, *(Zhu et al., 2008a, Yu et al., 2008a)* mercury cold vapour generation is affected by several factors; therefore this part of the study is devoted to investigate the effect of each factor on the response function (intensity of the mercury emission line at 253.65 nm). According to the calibration data given by Ocean Optics for the spectrometer (USB 2000), the emission line 253.65 (nm) appeared with 0.071 (nm) deviation, therefore the emission line at wavelength 253.58 (nm) has been adopted to monitor the mercury signal in all experiments; however it has been referred to as 253.65 (nm) in some illustrations. Four variables are selected as process parameters: the concentration of HCl solution (1-5% v/v), the concentration of the reducing agent ($SnCl_2$ 2-5% m/v), argon gas flow rate (40-180 ml/min), and the exerted electrical power (75 – 175 Watt at approximately 38 kHz). The power magnitudes are controlled as illustrated in **Section (4.4.2)**. The experiments are planned according to a 2^{nd} order central composite rotatable design *(Cochran and Cox, 1992)*, as illustrated in **Table (5-1)**. The experimental system is represented by a quadratic multivariable model combines the single effect of the variables in addition to the effects resulted from the interaction of the variables as shown in the following equation:

$$Y = B_0x_0 + B_1x_1 + B_2x_2 + B_3x_3 + B_4x_4 + B_{11}x_1^2 + B_{22}x_2^2 + B_{33}x_3^2 + B_{44}x_4^2 + B_{12}x_1x_2 + B_{13}x_1x_3 + B_{14}x_1x_4 + B_{23}x_2x_3 + B_{24}x_2x_4 + B_{34}x_3x_4 \quad (5\text{-}1)$$

The definitions of the parameters in equation (5-1) are described in **Appendix 11.3**.

Table 5-1 the experimental plan according to the central composite rotatable design and the recorded intensities for a water sample contains 100 µg/L mercury

Exp. No.	HCl (% v/v)		$SnCl_2$ (% m/v)		Argon (ml/min)		Power (watt)		Intensity (*Y*) (a.u.)
	Real Value	Code (x_1)	Real Value	Code (x_2)	Real Value	Code (x_3)	Real Value	Code (x_4)	
1	2	-1	2.75	-1	75	-1	100	-1	853
2	4	+1	2.75	-1	75	-1	100	-1	872
3	2	-1	4.25	+1	75	-1	100	-1	865
4	4	+1	4.25	+1	75	-1	100	-1	888
5	2	-1	2.75	-1	145	+1	100	-1	834
6	4	+1	2.75	-1	145	+1	100	-1	855
7	2	-1	4.25	+1	145	+1	100	-1	825
8	4	+1	4.25	+1	145	+1	100	-1	876
9	2	-1	2.75	-1	75	-1	150	+1	910
10	4	+1	2.75	-1	75	-1	150	+1	923
11	2	-1	4.25	+1	75	-1	150	+1	903
12	4	+1	4.25	+1	75	-1	150	+1	940
13	2	-1	2.75	-1	145	+1	150	+1	867
14	4	+1	2.75	-1	145	+1	150	+1	874
15	2	-1	4.25	+1	145	+1	150	+1	869
16	4	+1	4.25	+1	145	+1	150	+1	872
17	1	-2	3.5	0	110	0	125	0	854
18	5	+2	3.5	0	110	0	125	0	863
19	3	0	2	-2	110	0	125	0	876
20	3	0	5	+2	110	0	125	0	885
21	3	0	3.5	0	40	-2	125	0	874
22	3	0	3.5	0	180	+2	125	0	677
23	3	0	3.5	0	110	0	75	-2	798
24	3	0	3.5	0	110	0	175	+2	814
25	3	0	3.5	0	110	0	125	0	799
26	3	0	3.5	0	110	0	125	0	802
27	3	0	3.5	0	110	0	125	0	804
28	3	0	3.5	0	110	0	125	0	795
29	3	0	3.5	0	110	0	125	0	797
30	3	0	3.5	0	110	0	125	0	801
31	3	0	3.5	0	110	0	125	0	803

A multiple stepwise regression analysis was performed using the algorithm shown in (**Appendix 11.3**) to estimate the polynomial coefficients which are shown in **Table (5-2)**.

Table 5-2 the estimated polynomial coefficients

B_0	B_1	B_2	B_3	B_4	B_{11}
800.1627	8.0	2.8333	-28.1668	13.4167	22.3271
B_{22}	**B_{33}**	**B_{44}**	**B_{12}**	**B_{13}**	**B_{14}**
27.8271	1.5771	9.2021	3.375	-0.625	-3.375
B_{23}	**B_{24}**	**B_{34}**			
-1.625	-1.875	-6.625			

The standard error for the coefficients B_i, B_{ii} *and* B_{ij} is estimated to be 1.64, 1.48 and 2.01 respectively, whereas the average absolute error of the polynomial is 2.12%. The recorded peak for the mercury emission line is shown in **Figure (5-5).**

(A)

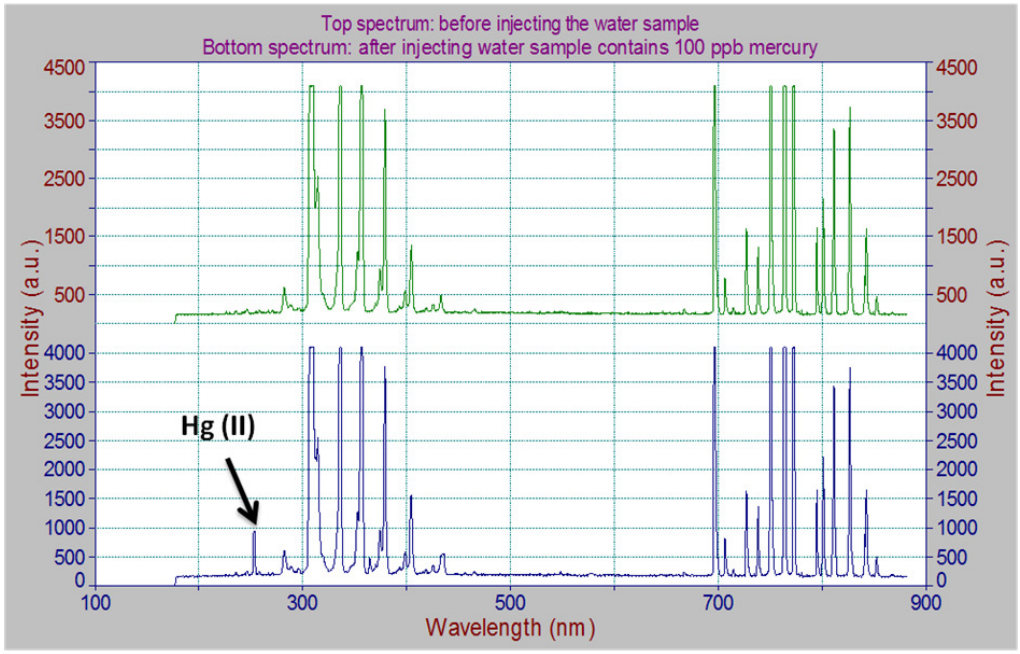

(B)

Figure 5-5 the signal recorded during mercury experiment;
(A) the recorded spectrum, (B) strip chart showing the signal versus time

Although the empirical model has 15 components which show various effects on the response function, not all of them are considered significant. The polynomial has been analysed statistically by applying the "Ridge technique" *(Hoerl, 1959)* to give an insight into the single effect of each variable on the objective function (intensity of 253.65 nm line) and to decide how stable the system is as well as to show the best compromise if unstable. The system of four variables has been derived as shown in (**Appendix 11.5**) and the following equations obtained and used for system analysis:

$$x_1(2B_{11} - 2B_{44} - \lambda) + B_{12}x_2 + B_{13}x_3 + B_{14}x_4 = -B_1 \quad (5\text{-}2)$$

$$B_{12}x_1 + x_2(2B_{22} - 2B_{44} - \lambda) + B_{23}x_3 + B_{24}x_4 = -B_2 \quad (5\text{-}3)$$

$$B_{13}x_1 + B_{23}x_2 + x_3(2B_{33} - 2B_{44} - \lambda) + B_{34}x_4 = -B_3 \quad (5\text{-}4)$$

$$B_{14}x_1 + B_{24}x_2 + B_{34}x_3 - \lambda x_4 = -B_4 \quad (5\text{-}5)$$

Where; the eigenvalue (λ) is defined to be:

$$\lambda = \frac{B_4 + B_{14}x_1 + B_{24}x_2 + B_{34}x_3}{x_4}$$

The system of linear equations (5-2 to 5-5) has an unique solution for any value of lambda except for the roots of the characteristic equation, but a choice outside this range leads to non-physical intensities. The choice of exactly the roots leads to an infinite number of solutions. Lambda close to the top of the physical range, however, leads to higher intensities which are desirable for greater sensitivity.

The solution strategy commences by determining the working limits of λ in the examined range. It should be mentioned that the examined eigenvalue (λ) is a value that makes the determinant equal to zero *(Hoerl, 1962)*. Therefore the limits were determined in the current analysis by arranging the coefficients in a matrix form, then extracting the equation of the determinant and equalizing it to zero. Hence, the following characteristic equation is satisfied by lambda:

$$\lambda^4 - 48.25\lambda^3 + 530.9\lambda^2 + 1224.59\lambda - 20323.38 = 0 \quad (5\text{-}6)$$

Equation (5-6) has 3 or 1 positive real roots and 1 negative real root according to the rule of signs. Four roots are produced upon solving equation (5-6); two of them are real values (-4.412 and 34.32) and adopted to be the limits of eigenvalues range. Since the aim of the analysis is to find the best conditions for the highest intensity, therefore the eigenvalues around the highest limit (34.32) are used to calculate the ridges as shown in **Table (5-3)**.

Table 5-3 the calculated ridges corresponding to the assumed values of $\boldsymbol{\lambda}$

λ	x_1	x_2	x_3	x_4	R_v
33.0	0.594	-0.799	0.5648	0.2778	1.1784
33.5	0.5289	-0.8466	0.5606	0.2837	1.179
34.32	0.424	-0.9591	0.5549	0.2945	1.2224
35.0	0.3314	-1.102	0.5517	0.306	1.313
35.5	0.2534	-1.256	0.5507	0.3174	1.4305
36.0	0.1584	-1.477	0.5514	0.3333	1.619
36.5	0.03042	-1.817	0.5552	0.3573	1.9342
36.66	-0.02244	-1.968	0.5575	0.3679	2.0787
36.675	-0.02781	-1.983	0.5577	0.369	2.0938

Several values of λ around 34.32 are selected and substituted in the equations (5-2 to 5-5); then the equations are solved to find the values of x_1 to x_4. The ridges corresponding to the calculated values of x_1 to x_4 are obtained from the following equation:

$$R_v = (x_1^2 + x_2^2 + x_3^2 + x_4^2)^{1/2} \qquad (5\text{-}7)$$

The ridge values are plotted versus the coded variables (x_1 to x_4) in **Figure (5-6)** for the aim of demonstrating the effect of each variable on the response function. **Figure (5-6)** indicates that for improving the intensity, major gains could be obtained by increasing the applied power (x_4) and decreasing the concentration of both HCl (x_1) and $SnCl_2$ (x_2) respectively, therefore (x_1, x_2 *and* x_4) are considered to be the key variables as they behave in a stable pattern. The values of (x_3) have shown unstable trends (decrease – increase) which may indicate that the argon flow rate is the most critical variable from the process control stand point.

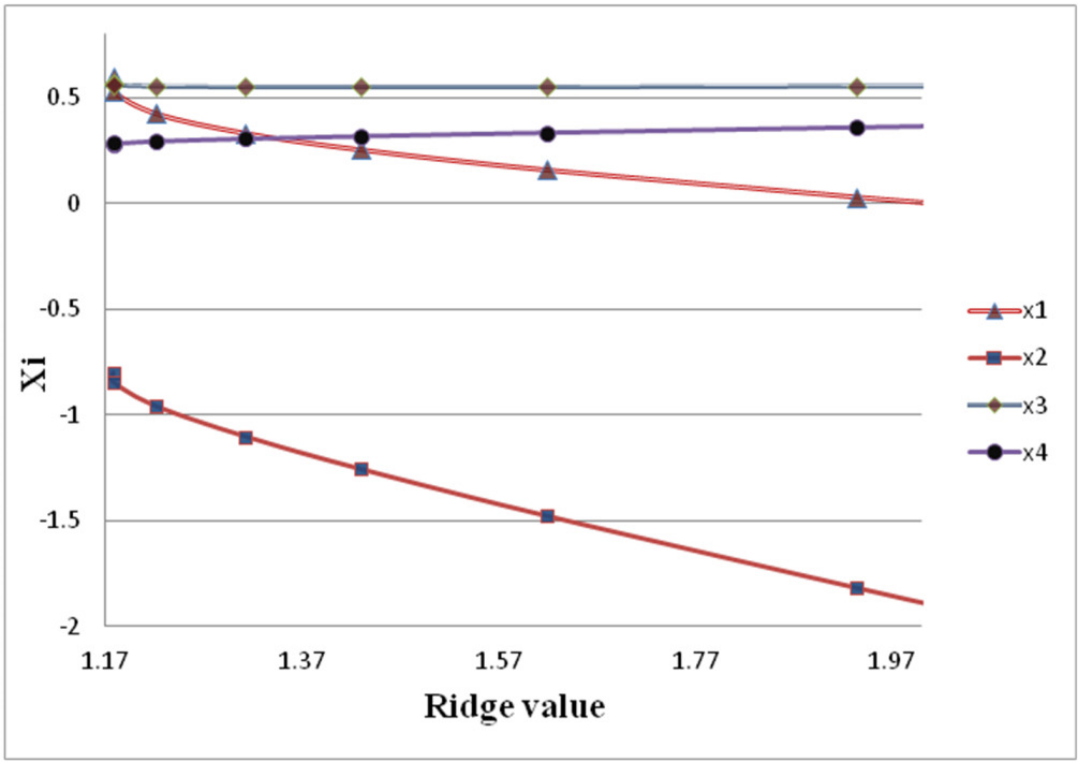

Figure 5-6 the calculated ridge values versus the coded values of the variables

It is necessary to quantify the relative effect of the variables interaction on the objective function. Traditionally, this is the role of F-factor analysis which is performed to analyse the present four variables system.

The calculations are achieved according to the analysis shown in **Appendix (11.6)**, whereas the estimated F-factor values are shown in **Table (5-4)**.

Table 5-4 the estimated F-factor values for the individual and interaction effects

Evaluated parameters	the estimated F-factor
x_1	1.1078E-06
x_2	1.11441E-06
x_3	1.12084E-06
x_4	1.14373E-06
x_1x_2	-0.04414013
x_1x_3	-0.04336648
x_1x_4	-0.03931418
x_2x_3	-0.04336999
x_2x_4	-0.03931778
x_3x_4	-0.04049423

Generally speaking, since the parameter (x_4 , the applied power) gained the highest F-factor value compared with other individual effects (x_1 , x_2 , x_3), it can be considered to be the most important factor during system operation. This result is compatible with the results of the ridge analysis technique which indicates x_4 as a key factor. It can also interpreted that the interactions of HCl concentration/exerted electrical power (x_1x_4), $SnCl_2$ concentration/exerted electrical power(x_2x_4), and gas flow rate/ exerted electrical power (x_3x_4) produce greater disturbances than other interactions. This indicates the significant role of x_4 on system stability. In conclusion, the abovementioned interactions are considered to be critical during system operation.

The optimal conditions for the highest mercury intensity are obtained by performing a non-linear constrained optimization. The details are shown in (**Appendix 11.4**) and the estimated optimum values are shown in **Table (5-5)**.

Table 5-5 the optimization results for the mercury cold vapour generation process

HCl concentration		$SnCl_2$ concentration		Argon flow rate		Power	
x_1	(% v/v)	x_2	(% m/v)	x_3	(ml/min)	x_4	(watt)
0.352	≈3.35	1.383	≈4.53	-0.686	≈86	0.14	≈128

Since the applied power is a key factor, which means that higher applied power results in higher intensity, a value of 150 Watt has been adopted in the later experiments.

Further investigations were carried out to explore the individual effects of each parameter on the objective function; the results are shown in **Figure (5-7)**. It can be seen that the trends are compatible with the results of the statistical approaches, in which the argon flow rate is a critical parameter affecting system performance. In contrast, other parameters show a stable effect on the system.

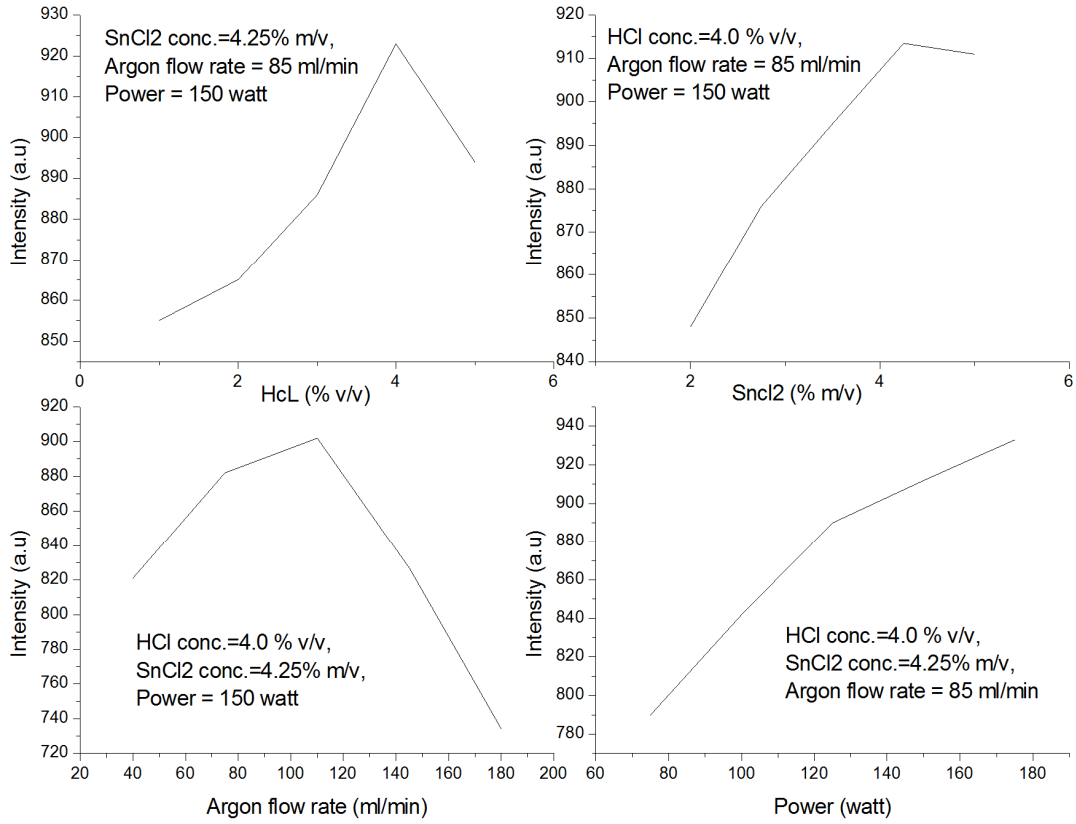

Figure 5-7 the effects of the individual parameters on the mercury signal intensity

The analytical performance of the system has been evaluated by measuring the detection limits. **Figure (5-8)** illustrates a calibration plot for the response of the system (the intensity of mercury line) versus different concentrations of mercury.

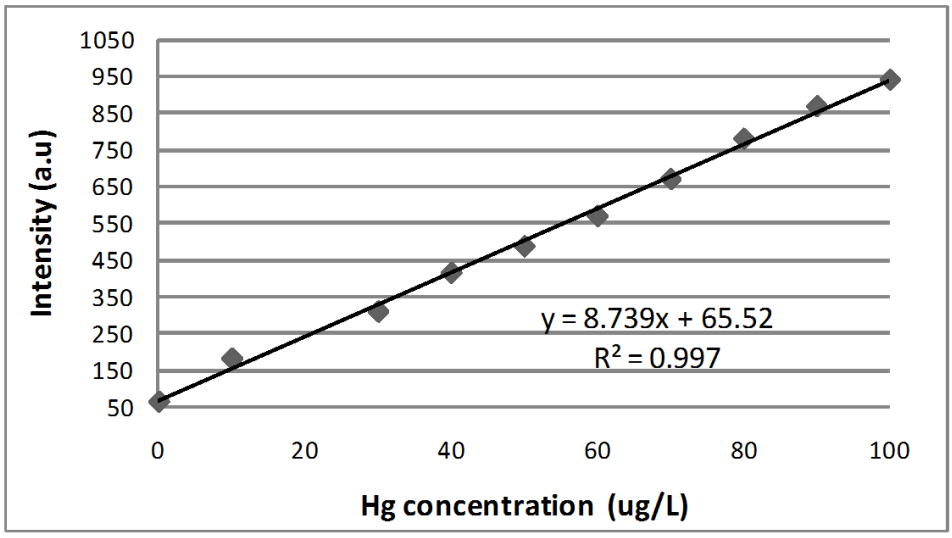

Figure 5-8 the recorded intensities versus several mercury concentrations;
at: 4% (v/v) HCl , 4.25% (m/v) $SnCl_2$, 85 (ml/min) argon and 150 (watt) power

The analytical figures of merit are estimated according to **Appendix 11.7**. The limits of detection (LOD) are calculated by spiking a blank solution into the system and measuring the intensity. The blank experiments repeated eight times and the standard deviation (*S*) calculated for the experimental set. The calculated figures of merit (LOD = 2.8 µg/L and RSD = 3.5%) shows a reasonable precision is achieved, which supports the adoption of the reaction system and the tested DBD chip for analytical purposes.

5.4 Implementing the mercury cold vapour generation process using hydroborates

In this section, the cold vapour generation technique is applied for mercury detection by using sodium and potassium hydroborates. The aim is to investigate the performance of the technique and its compatibility with a DBD atomizer. It is well known that the difference between applying $SnCl_2$ and hydroborates for mercury derivatization is the huge quantity of hydrogen gas which accompanies the decomposition of hydroborates in water. Stoichiometrically, four moles of hydrogen gas is produced upon decomposing one mole of sodium tetrahydroborate *(Agterdenbos and Bax, 1986)*:

$$BH_4^- + 3H_2O + H^+ \rightarrow H_3BO_3 + 4H_2 \qquad (5\text{-}8)$$

It is reported elsewhere that presence of hydrogen gas in a plasma reactor up affects the plasma reaction positively. *(Zhu et al., 2008b)* attributed this to the higher thermal conductivity of hydrogen compared to other gases (168 mW/m/^{o}K for H_2, 142.64 mW/m/^{o}K for He and 16.36 mW/m/^{o}K for Ar at 0 ^{o}C and 1 atm) and a relatively higher dissociation temperature. It should be noted that the generated hydrogen gas gives rise to an aerosol in the gas liquid separator which can disturb system performance *(Wickstrøm et al., 1996)*. Due to its lighter weight, the probability of hydrogen molecule transfer from the gas liquid separator to the atomizer is higher than for generated hydrides and other gases, which consequently leads to plasma instability. As mentioned in chapter 3, *(Chaudhary et al., 2003)* observed this behaviour in their atmospheric pressure cold plasma generator and reported that extra hydrogen leads to destabilization and completely extinguishes the plasma. A probable reason for the hydrogen effect on the plasma is the ability to alter the electron energy and the electron distribution function; thereby a significant change in the population density of the reactive species in

the discharge may occur. Moreover, *(Pohl et al., 2007)* observed a reduction in the excitation temperature (from 5800 to 5400 ^{o}K) and in the electron number density (from 1.76×10^{14} to 1.37×10^{14} cm^{-3}) of microwave argon plasma due to the hydrogen effect. A method to reduce hydrogen generation is to add sodium hydroxide to the hydroborate solution. This is to stabilize the solution and prevent the generation of excess hydrogen gas in the reaction coil; i.e. preserve the hydrogen content in the hydroborates. Therefore, the hydroborate solutions in all stages of this research were prepared using sodium hydroxide as a stabilizing agent.

The experiments are conducted by using the setup described in **Figure (5-4)** and applying axial viewing; i.e. connecting the fibre optics to the DBD atomizer in the axial position. Sample acidification is by injecting the sample to meet the acidic stream through a tee joint. The acidified stream is directed into a second tee joint to meet the stream of hydroborates. The mixed stream is forwarded into a gas liquid separator (GLS) through a helical shape reaction coil. A stream of argon gas is added to the beginning of the reaction coil to facilitate separation of the two phases. The gas stream from GLS is directed into the DBD atomizer, whereas the liquid residues from the GLS dispense to drain.

The first experiment was conducted by injecting only an acidified sample of water (with no mercury) in parallel with a stream containing 1% m/v $NaBH_4$, at 2.8 ml/min for both streams. The recorded spectra are shown in **Figure (5-9 A/B)**, in which the base level of the spectrum between (200- 500 nm) is disturbed (magnified) significantly upon injecting the hydroborate in the system. The reason can clearly be attributed to hydrogen generated in the system due to hydroborate decomposition or the alkaline mist accompanying the generated hydrogen (most likely composed of $NaBO_2$ and water vapour).

Since a large amount of hydrogen generates in the system accompanied by alkaline mist and water vapour, the author was expecting to observe some peaks for hydrogen ions, atoms, or excited species (e.g. H_γ at 434.04 nm, H_β at 486 nm or H_α at 656 nm). Nevertheless, none of these species appear in the spectrum except a very low signal for H_α at 656 nm when introducing a sample containing only water to the GLS, most likely from water vapour dissociation.

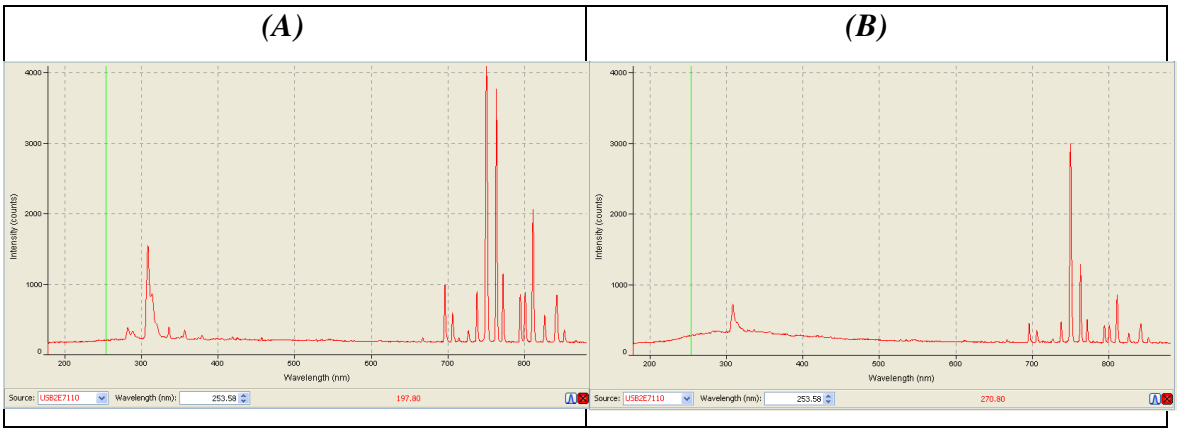

Figure 5-9 screen shots show the magnification effect of the hydrogen on the recorded spectrum;
(A) the recorded spectrum for a system injected with a sample of water, (B) the recorded spectrum after injecting an acidified sample of water in parallel with a stream contains 1% m/v $NaBH_4$.

This peak has totally disappeared when the hydroborate solution is injected, which indicates unknown reactions which eliminate the appearance of these species. These reactions probably occur with species such as (O, O^*, HO_2, O_2, H_2O, OH, OH^*, and H in the presence of the third body (M)), and produce unknown products which disturb the spectrum in the region 200 – 600 nm. The other reason for the magnification effect is hydrogen itself which is generated and transferred to the plasma. The application of higher concentration of $NaBH_4$ results in more discrepancy in the recorded spectra.

For further clarification, the spectra shown in **Figure (5-10)** were recorded for the plasma generated from an inlet stream composed of water vapour (steam from boiled water at low pressure) and argon gas. The application of this gas mixture aims to show the effect of generated hydrogen and accompanying residues on the spectral lines, specifically in the UV region. Since water vapour easily dissociates, it can be observed that a signal for OH with very high intensity appears for the band (302 – 317 nm) before introducing the $NaBH_4$ solution. Afterwards, all peaks are significantly reduced due to the large amount of hydrogen generated in the system; eventually the DBD plasma nearly extinguishes and takes some time to recover after hydrogen is totally removed from the system.

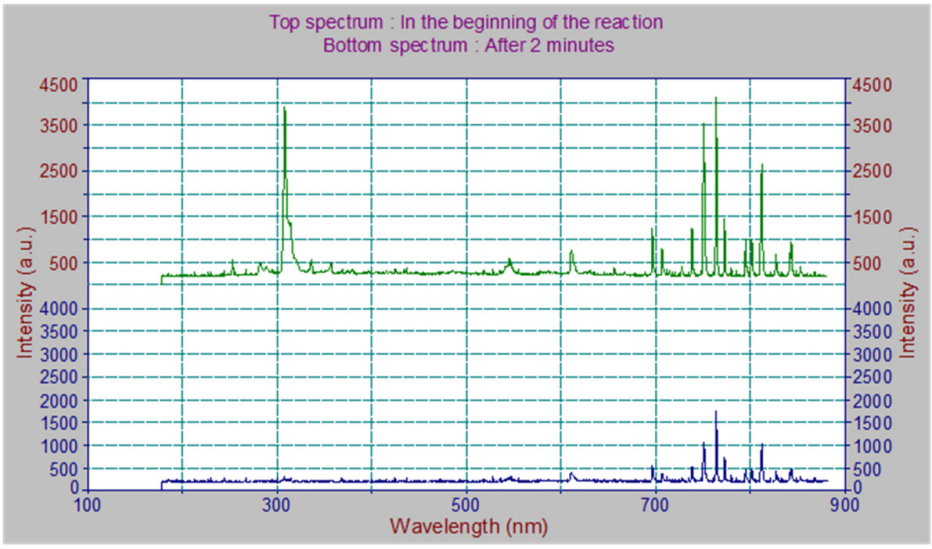

Figure 5-10 the recorded spectrum when using a mixture of steam and argon;
The signals recorded before and after injecting a (2 % m/v) $NaBH_4$ stabilized by using (0.5 % m/v) NaOH, whereas a gas stream (≈ 30 % water vapour + 70 % Ar) is introduced to the system.

As disruption occurred to the recorded spectrum, it was necessary to rectify the recorded signal. Accordingly, each experiment was conducted twice, once without spiking the water sample with mercury, and once with the targeted concentration of Hg (II). The difference between the two readings is the intensity relative to the spiked Hg (II) amount, as shown in **Figure (5-11)**.

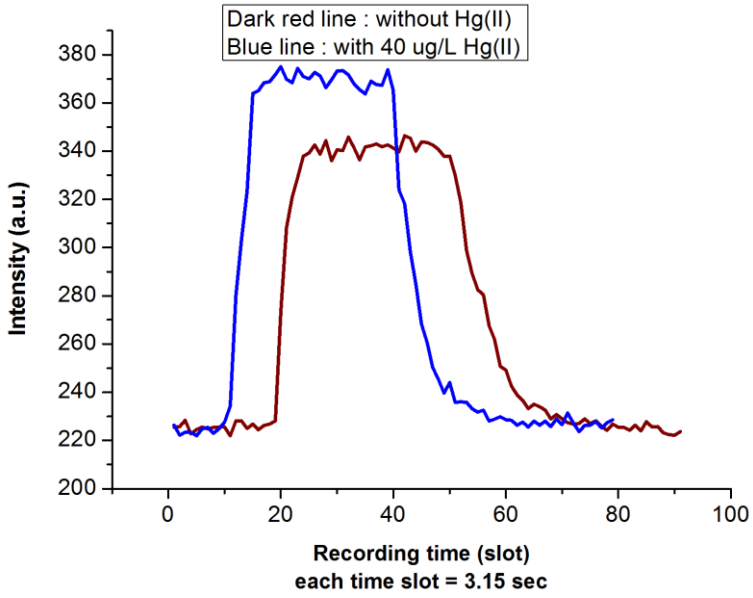

Figure 5-11 the signals recorded with and without 40 µg/L Hg (II);
by applying 1% m/v $NaBH_4$, 1 M HCl, 85 ml/min argon and 150 Watt

The dark red line in **Figure (5-11)** has been treated as a background signal; accordingly, the ratio of the signal obtained (due to the analyte effect) to the background signal (SBR) is adopted for later investigations in this case study.

Thus a strategy has been adopted in order to reduce the effect of hydrogen, where the mercury experiments are conducted using lower concentrations of $NaBH_4$ and KBH_4 (in the range 0.2 – 0.6 % m/v, and stabilized by using 0.2 % m/v NaOH).

The preliminary experiments were conducted by injecting 10 µg/L Hg (II) and applying different concentrations of $NaBH_4$ to explore whether the background signal deviates with an increase in $NaBH_4$. The results are shown in **Figure (5-12)**, which clearly indicates that the signal to background ratio (SBR) is affected by increasing $NaBH_4$ concentration.

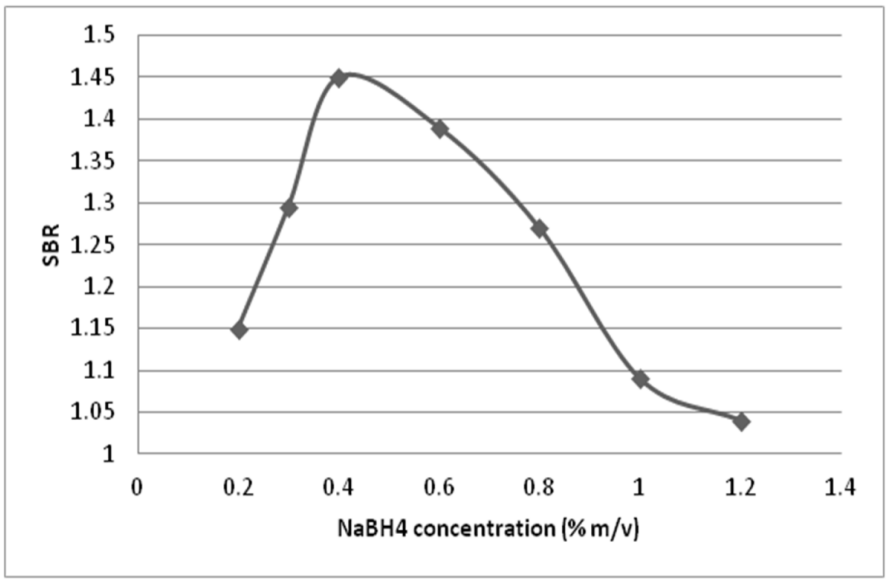

Figure 5-12 the recorded signal to the background ratio for a water sample spiked with 10 µg/L Hg (II) at 1M HCl, 85 ml/min argon flow, and 150 watt;
SBR represents the ratio of the mercury signal to the signal due to the hydrogen effect.

It can be observed that 0.4% m/v is the optimal $NaBH_4$ concentration for mercury derivatization; thus, other experiments are conducted to explore SBR variation with different concentrations of Hg (II) as illustrated in **Figure (5-13)**.

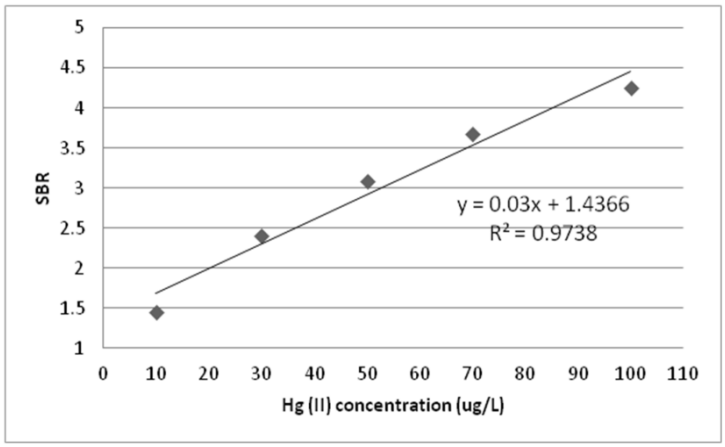

Figure 5-13 the recorded signal to the background ratio for a water sample spiked with different concentrations of Hg (II);
at 0.4% m/v $NaBH_4$,1M HCl, 85 ml/min argon flow, and 150 watt

It is worth noting that applying the sodium hydroborate results in better signal intensity compared with potassium hydroborate, (**Figure (5-14)**). The recorded signals actually include the combined effects from both Hg (II) and the hydrogen. No signal is differentiated from the background when using 0.2 % m/v KBH_4, whereas very clear signals are obtained when applying 0.2 – 0.6 % m/v $NaBH_4$. Signal intensity drops when applying (0.5 % m/v $NaBH_4$) and higher, which can be attributed to a larger quantity of hydrogen generated.

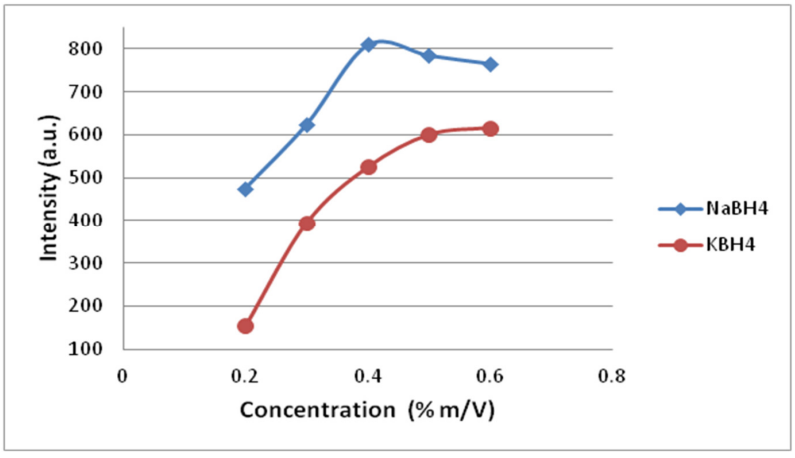

Figure 5-14 the recorded intensities for a water sample contains 100 (µg/L) Hg (II) upon applying different concentrations of the hydroborates;
at: 1M HCl, 85 (ml/min) argon and 150 (Watt) applied power.

It can be deduced from the abovementioned observations that the presence of hydrogen gas in a DBD plasma bulk up to certain limits enhances the atomization processes;

however, greater amounts disturb the plasma and disrupts the appearance of the spectral lines, which clearly denotes hydrogen concentration as a critical parameter affecting the whole process. This is considered a barrier against the coupling of the hydride generation technique with a DBD plasma atomizer for analytical purposes. The concentration of hydrogen gas required to be reduced before entering the DBD atomizer can be achieved by using the lowest possible $NaBH_4$ concentration. However, applying low concentrations of hydroborates is not a solution when the hydride generation process is required for multi analyte determination that may require higher concentrations of hydroborates. It has been reported that the generated hydrogen in a system applying 0.4% m/v $NaBH_4$ at a flow rate of 0.5 ml/min is equal to 4.2 ± 0.2 ml/min *(Pohl et al., 2007)*. Since the stream flow rate in the current study is set to 2.8 ml/min, the generated hydrogen in the system would be higher than the abovementioned value due to higher flow rate. In consequence, the plasma would be significantly affected and therefore it is required to dilute the generated hydrogen to an acceptable extent. An alternative method to reduce the hydrogen concentration is to dilute the gaseous bulk with an inert gas. This method has been applied in this research by inserting a second gas stream in a suitable position in the gas liquid separator. Three gas-liquid separators were tested to explore their performance; their details are shown in **Figure (5-15)**. Two of the GLS's were fabricated by the author, whereas the third GLS is a commercial separator. The separator shown in **Figure (5-15/A)** is a simple plastic container provided with a glass section used for injecting the combined gas-liquid stream and extracting the separated gases. The separated volatile species are transported to the DBD atomizer with aid of a carrier gas, whereas the water residues are disposed out of the separator by either a peristaltic pump or gravity. The separator shown in **Figure (5-15/C)** is a self made nebulizer-GLS separator, in which a combination of an ICP torch, central nebulisation tube and an expanded glass section are utilized to conduct the separation process. The proposed design of the nebulizer - GLS is simulated earlier in **Section (3.5)**, where the simulation results indicate a significant reduction in hydrogen concentration obtained when introducing 216 (ml/min) helium gas from the supporting lines (3 and 4). The experimental results obtained from testing the examined gas – liquid separators are shown in **Figure (5-16)**.

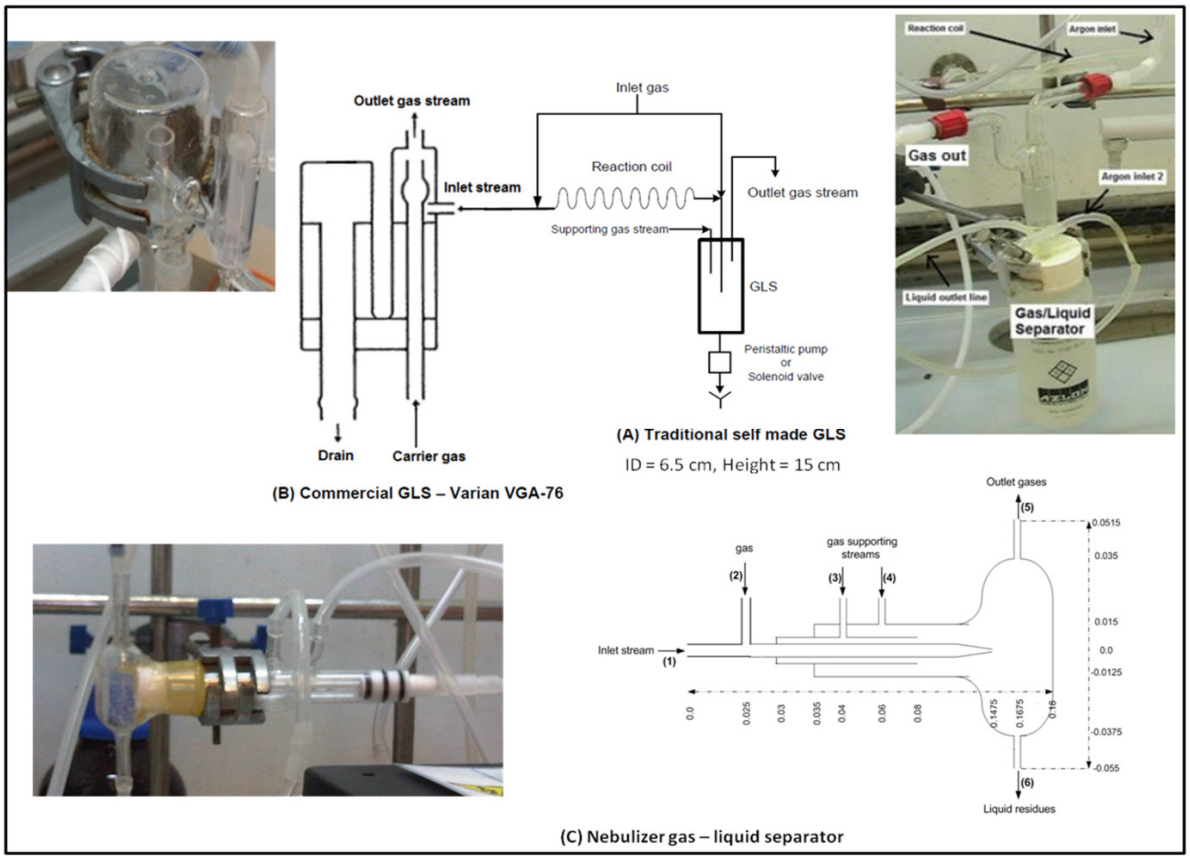

Figure 5-15 three types of a gas liquid separator used for Hg (II) determination by applying $NaBH_4$ scheme;
(A) 500 ml container provided with a supporting carrier gas stream at 30 ml/min, (B) a commercial separator provided with a 30 ml/min supporting gas, (C) self made separator fabricated from a consumed ICP torch, the full details are provided in **Figure (3-4)** shown in chapter three.

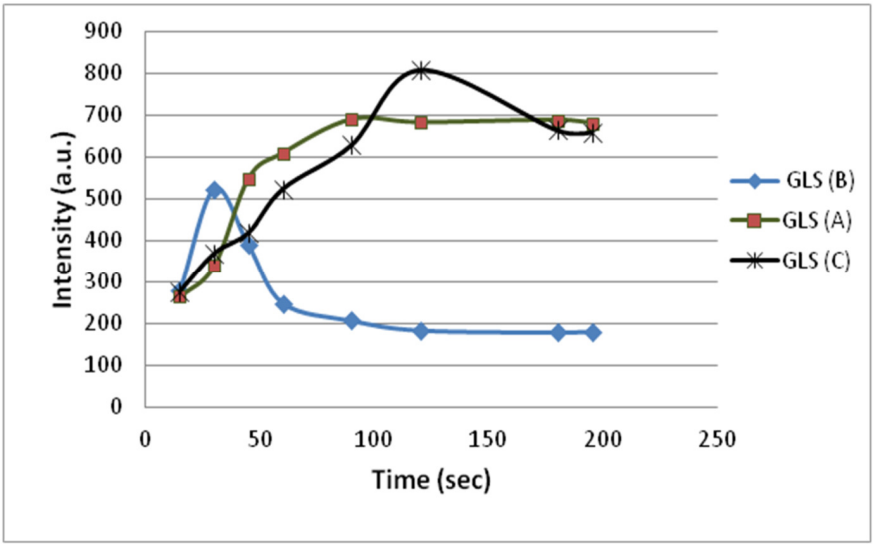

Figure 5-16 the recorded mercury signal intensities obtained upon testing three GLSs;

The signals (including the hydrogen magnification effect) are recorded for 100 (µg/L) Hg (II) spiked in the examined sample and reduced at 1M HCl , 0.3% (m/v) $NaBH_4$, 150 (Watt) applied power, 105 (ml/min) argon for GLS (A) and (B) while approximately 250 (ml/min) helium is applied for GLS (C).

The performance of GLS (A) is enhanced by controlling the flow of the supporting gas through a solenoid valve, where gas pulses are injected to the GLS instead of applying a continuous flow. The details of the proposed control techniques are described in **Section (5.5)**. This methodology has improved the performance of GLS (A) even when using (0.5 % m/v $NaBH_4$). The performance of GLS (A) becomes more reliable during the operation time. The reasons could be a spacious bulk for separation as well as the advantageous effect of applying a supporting gas stream and gas pulses which results in a dilution ratio ≈ 4.2 H_2/105 Ar, assuming 4.2 ml/min hydrogen is generated in the system. The supporting gas stream attenuates the hydrogen and probably the mist concentration in the plasma; thereby producing a consistent discharge. However, the application of a higher carrier gas flow rate could lead to analyte signal attenuation; and should be estimated precisely. Although higher signal intensities are recorded when applying GLS (C) (dilution ratio ≈ 4.2 H_2/ 250 He), the performance of GLS (C) is less stable compared with GLS (A). The fluctuations in signal intensity refer to an interaction effect most probably caused by turbulent flow in addition to attenuation in the mercury concentration which occurs due to higher gas flow rate. GLS (B) was the weakest performer. Thus, GLS (A) was used in later experimental investigations.

In order to determine the reason behind the enhanced performance of GLS (A), the parameters that lead to disturbances in the separation bulk should be taken into consideration. Aerosol and foam formation is reported highly possible in different types of GLS, especially when a large amount of hydrogen releases into the GLS bulk. Some researchers consider foam formation to be detrimental to GLS performance; thus, they used anti-foam agents to reduce this tendency *(Karadjova et al., 2005)*. In practice, the application of anti foam chemicals is impractical and could lead to signal interferences especially in the case of conducting simultaneous detection of multi metals. Another limiting parameter, is the possible generation of extra hydrogen from waste residues at the base of the GLS. In this regard, *(Sturgeon et al., 1996)* reported that overall H_2 production from waste could be reduced by adopting a fast evacuation system or by adding a stream of NaOH (e.g. 1 M) to quench further liberation of H_2.

A reason for the enhanced performance of GLS (A) could be a lower tendency of hydrogen release from the surface interface of liquid residues at the base of GLS. Extra hydrogen could be released to the bulk of the gas-liquid separator due to instability of the settled liquid residues. If a forced continuous stream of argon gas is injected toward the liquid surface at the base of the GLS, then the stripping of the hydrogen from the gas – liquid interface becomes easier. Hence, pulses of argon gas possibly result in a gentle argon flow as well as more stability inside the GLS, and consequently facilitates the transportation of the generated vapour species from the GLS to the DBD atomizer without further hydrogen generation.

The calibration plot of mercury system when applying the hydride generation scheme is illustrated in **Figure (5-17)**. Better precision and performance is obtained when using $NaBH_4$ as a reducing agent compared to $SnCl_2$ (LOD = 2.19 µg/L and RSD = 2.19%) but with operational difficulties.

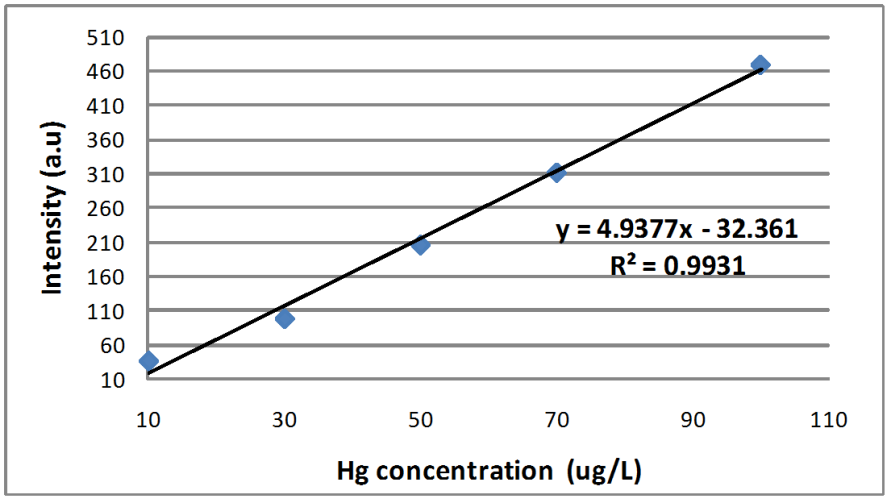

Figure 5-17 the recorded intensities (rectified from the hydrogen magnification effect) versus several mercury concentration values;
at: 1M HCl , 0.4% (m/v) $NaBH_4$, 105 (ml/min) argon and 150 (watt) power.

5.5 Quantitative determination of inorganic mercury by applying a fully automated cold vapour generation process

The main objective of the current research is to determine metal concentrations with high accuracy. The most important stage that controls the performance of the whole process is the gas-liquid separator (GLS) especially when applying the hydride generation technique. The role of the GLS is to separate the gaseous phase from the

liquid matrix upon completion of the reduction reaction. The design of the GLS should provide optimal separation of the aerosol droplets, created by the bubbling action of the evolved gases, which might result in signal disruption in the case of poor separation. We have adopted GLS (A), shown in **Figure (5-18)**, to implement the gas liquid separation process.

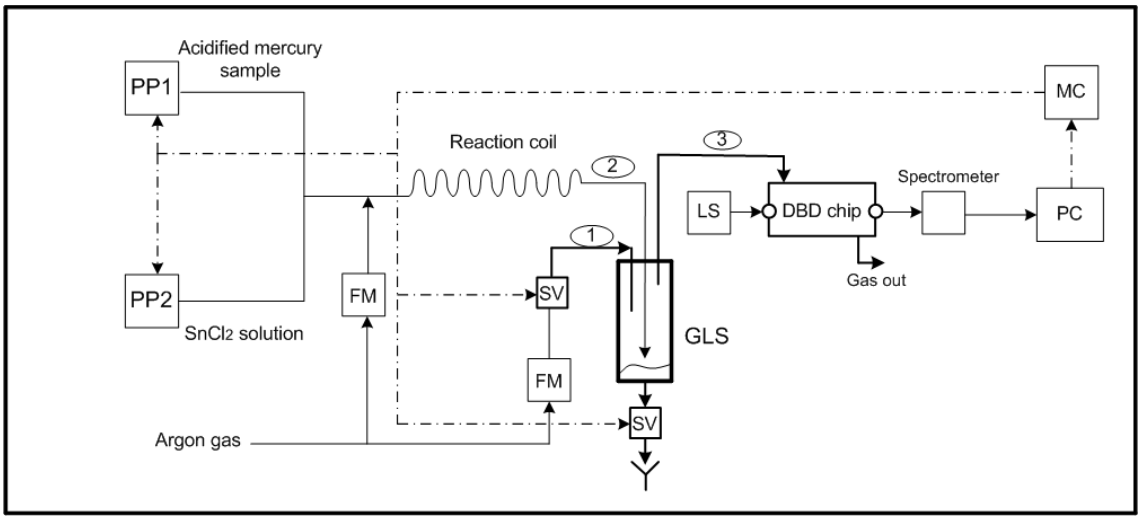

Figure 5-18 a schematic diagram shows the automated system used for the quantitative determination of Hg (II);
PP: peristaltic pump, FM: flow meter, SV: solenoid valve, LS: light source, PC: Computer, MC: microcontroller interface, the dotted line refers to the electronic signal transfer path

The available volume (≈500 ml) is suitable to achieve aerosol separation and carry the generated vapour species out of the separator. According to the statistical analysis (**Section 5.3.3**) the gas flow rate should be controlled precisely in order to prevent signal disruption. It is believed that the release of the generated vapour species and their transfer to the DBD atomizer could be implemented with high efficiency when utilizing a gentle flow of the carrier gas rather than a forced flow, and this is clearly required to prevent carrying aerosol droplets in the vapour. It is also expected that the forced flow of any other supporting gases may lead to eddies and foam formation which is undesirable in the gas-liquid separator due to highly sensitive processes and critical vapour species. Practically, the limiting factor that controls the performance of the GLS is the necessity to work below or at the minimum gas velocity in the separator. Since many reasons might lead to disturb the GLS performance, the author selected the

minimum superficial gas velocity for onset of foaming (j_m) to be the limiting factor. According to *(Pilon and Viskanta, 2004)*, j_m is equal to 10 (mm/sec) for argon and a steady state foam thickness of about 2.5 (mm), which is considered applicable to this study. Thus, a mass balance has been applied to determine the required quantity of the injected argon gas (1).

argon in stream (1) + argon in stream (2) = argon in stream (3)

Where;
argon in stream (2) = 35 (ml/min), a continuous feeding with the liquid phase.
argon in stream (3) is calculated based on 10 (mm/sec) as a minimum superficial velocity and 1.5 (cm) diameter for the concentric outlet section from the separator which gives a flow rate equal to 105.6 (ml/min). Therefore, a flow rate of 70.6 (ml/min) is determined for stream (1) as a maximum, albeit better performance is expected to achieve when applying lower injection rate.

The control strategy of the gas liquid separator utilizes a solenoid valve to control the injection of the supporting gas (stream 1) into GLS (A). The concept is to supply pulses of the supporting gas through stream (1) which prevents the build-up of a high pressure inside the separator and consequently limits the formation of disturbing factors and facilitates the release of the vapour species without disrupting the bulk. A solenoid valve (Takasago – Japan) with 2 (mm) bore size powered by 12 volt DC has been used to control the injection of the supporting gas pulses. The control strategy is accomplished using a microcontroller (Arduino – Mega) interface which is operated by PC software. The control strategy for the whole system is shown in **Figure (5-18)** and the code used to operate the microcontroller is written using Arduino microcontroller software language, which is similar to C++, (**Appendix 11.8**). In the adopted control strategy, pulses of the supporting argon gas at 70 (ml/min) are injected into GLS (A) in a sequence form. For instance, the supporting argon gas is injected for 4 seconds and then stopped for 3 seconds, to be re-injected again for 4 seconds and re-stopped for 3 seconds and so on. Since an argon flow rate of (70/60 =1.16 ml/sec) is applied, a total quantity of 4.66 (ml) argon gas is injected to the separator through stream (1) in a 4 seconds period, which assists transfer of the generated vapour species in a stabilized sequence. Accordingly, 15 pulses with 4.66 ml argon are actually supplied through stream (1) in 1 minute. These time slots are selected by applying an optimization study with the results shown in **Figure (5-19)**.

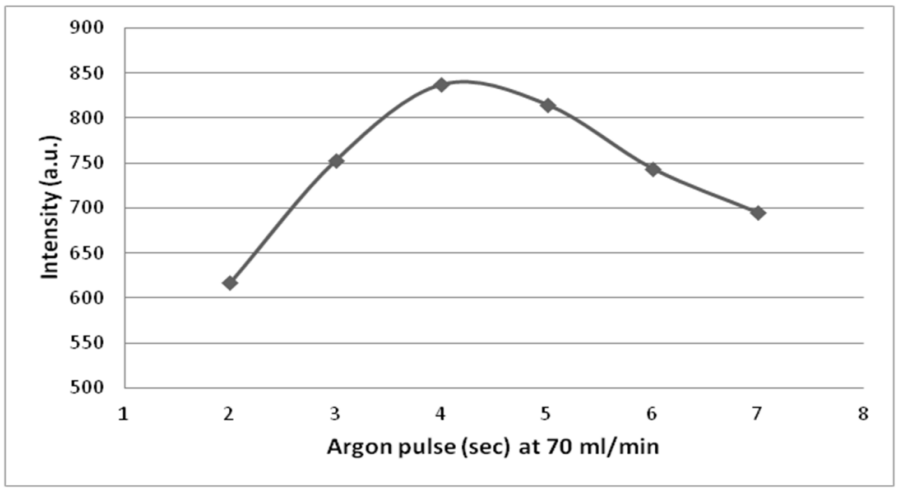

Figure 5-19 the effect of changing the gas pulse length on the signal intensity; a 50 (µg/L) Hg (II) is spiked in the examined sample and reduced by applying 4% (v/v) HCl, 4.25% (m/v) $SnCl_2$ and 150 (watt) applied power

The peristaltic pumps are actually running for 3 minutes and 15 seconds which is the time required to inject 10 (ml) of both the acidified analyte solution and the reducing agent. After stopping the pumps, an extra period of 45 seconds is given to make sure that all vapour species entered the atomizer. As soon as 4 minutes of the full process time passes, the readings shown on the computer screen in (mol/L) are recorded for 15 seconds. 2-3 different values appear on the screen and the average of these values is the measured concentration of the analyte. At 4:15 minutes, the solenoid valve at the bottom section of GLS (A) opens to dispose the liquid residues from the separator. 1 minute is given to load argon gas into the separator bulk for purging purposes. This is necessary to make sure that the rest of the gas residuals release from the separator before starting a new analytical run; thereby reducing memory effect.

The length of the tube sections of streams (1, 2, 3) inside GLS (A), (**Figure (5-18)**) is found to be another critical parameter affecting system performance. An optimization study was conducted to determine the optimum lengths of these sections. The results show that the most critical section length is stream (2), which led to considerable changes in the intensity of the collected signal. For instance, the signal intensity increased upon increasing the length of stream (2) tubing into a position near the liquid surface inside GLS (A). The reason could be related to a limited opportunity for carrying aerosols out of the separator as well as limited foam formation. A higher potential for foaming occurs inside the bulk of GLS due to higher possibility of contact between the content of stream (2) and the gas injected through stream (1). A lower

tendency for foam formation occurs when stream (2) releases at a point near the liquid surface and consequently leads to more stability in the whole process performance. In contrast, performance is reduced when shorter lengths of stream (2) are used. **Figure (5-20)** shows the mercury signal intensity obtained upon applying different section lengths of stream 2 while applying tube lengths of 4 and 1 cm for streams (1) and (3) respectively.

Further experimental investigations are conducted to explore the effect of changing the volume of the gas liquid separator. In addition to the aforementioned GLS (A) (500 ml), two gas liquid separators with the same design but with different volumes (350 ml and 1000 ml) are adopted for this study.

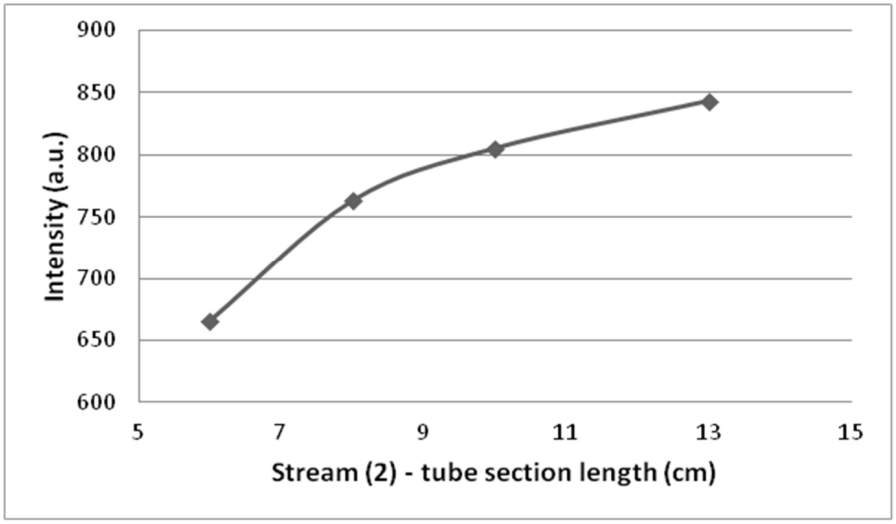

Figure 5-20 the effect of increasing the tube section length of stream (2) inside GLS (A);
Hg (II) signals are recorded upon injecting 50 (µg/L) and applying 4% (v/v) HCl, 4.25% (m/v) $SnCl_2$, 105 (ml/min) argon and 150 (watt) power and adopting a length of 4 (cm) and 1(cm) for streams (1) and (3) respectively.

The mercury signal is recorded in accordance with changes in the GLS characteristic volume and the gas injection period (i.e. the gas pulse). The change in these parameters is represented by the Strouhal number, which is a dimensionless group that combines the measured characteristic length, considered to be the effective height of the container, **Table (5-6)**, with the applied frequency (inverse of the pulse period).

Table 5-6 the details of GLS type (A) with different characteristic volumes

Approximate volume cm^3	Inside diameter cm	Height cm	Real volume cm^3
350	5.7	14	357
500	6.5	15	497.5
1000	8.7	17	1010

The Strouhal number is described as follows:

$$St = \frac{f\,L}{V} \qquad (5\text{-}9)$$

Where;

f : oscillation frequency (sec^{-1}) = $\frac{1}{pulse\ length\ (\sec)}$

V : characteristic velocity (cm/sec) = $\frac{\mu}{\rho L}$, μ is the gas dynamic viscosity, ρ is the gas density, and L is the characteristic length (represent the effective height of the GLS type A).

Substituting the characteristic velocity in equation (5-9) produces a description for Strouhal number as follows:

$$St = \frac{f\,L^2}{\mu/\rho} \qquad (5\text{-}10)$$

For argon gas at 20 ^{o}C and 1.35 bar, the density and viscosity are considered to be 2.12×10^{-3} $g.cm^{-3}$ and 2.22×10^{-4} $g.cm^{-1}.s^{-1}$ respectively.

A range of argon pulse lengths (2-7 seconds) was tested with the three gas-liquid separators. The intensity of the mercury signal relative to the estimated Strouhal number is shown in **Figure (5-21)**.

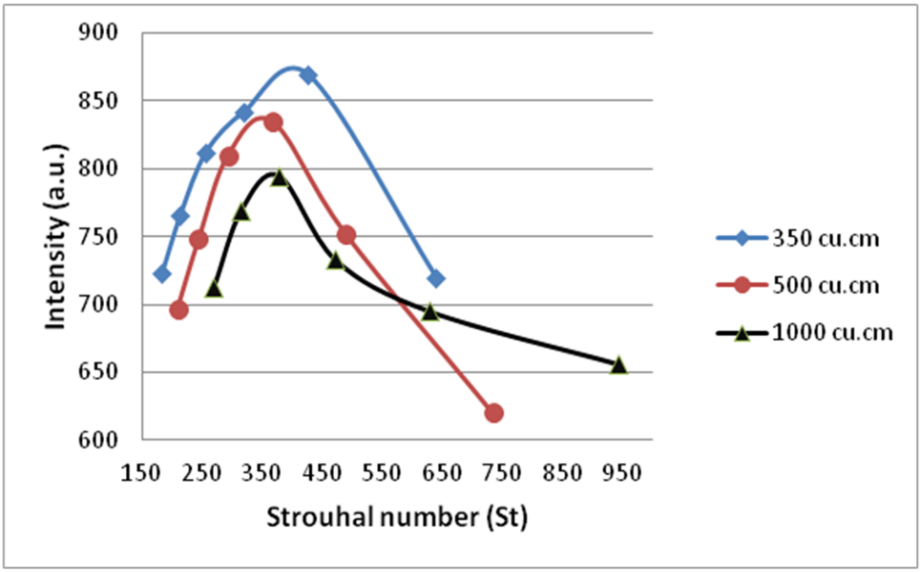

Figure 5-21 the recorded mercury signal intensities relative to the change in Strouhal number for different characteristic volumes of GLS (A);
The signals recorded upon injecting 50 (µg/L) and applying 4% (v/v) HCl , 4.25% (m/v) $SnCl_2$, 105 (ml/min) argon,150 (Watt) power, and adopting 4 cm and 1cm for the lengths of streams 1and 3 respectively, whereas the length of stream (2) inside GLS is kept approximately 1 cm over the liquid surface.

It is observed that higher intensities are recorded for the smallest characteristic volume of GLS (350 cm^3), which indicates that the characteristic volume of the gas liquid separator is an important parameter affecting the system performance. Hence, GLS (A) of 350 cm^3 volume has been adopted in later experiments.

In the quantitative determination of mercury an absorption spectrometric technique, using mercury hollow cathode light source (F-O-Lite, from World precision company – UK) was used. The fibre optics are placed for axial viewing at the ends of the gas channel. Two positions were chosen along the atomization channel to conduct radial data acquisition, as illustrated in **Figure (5-22)**. The results show a 40% increase in the signal intensity occurs when applying axial, compared to radial, data acquisition. The signal intensity collected from positions (1 & 2) is found to be similar. This is probably due to the action of hydrogen radicals that present in abundance along the atomization channel on the analyte dimers, which consequently prevent their dissipation. This finding is considered logical based on knowledge on the quartz tube atomizer, where low concentrations of hydrogen radicals result in free atom recombination out of the hydrogen radical cloud leading to free atoms dissipation *(Matousek and Dedina, 2000)*.

This observation is consistent with the findings from the simulation results, **Section (3.6.2)**, that indicate the free atom concentration is not expected to change after passing the centre of the gas channel.

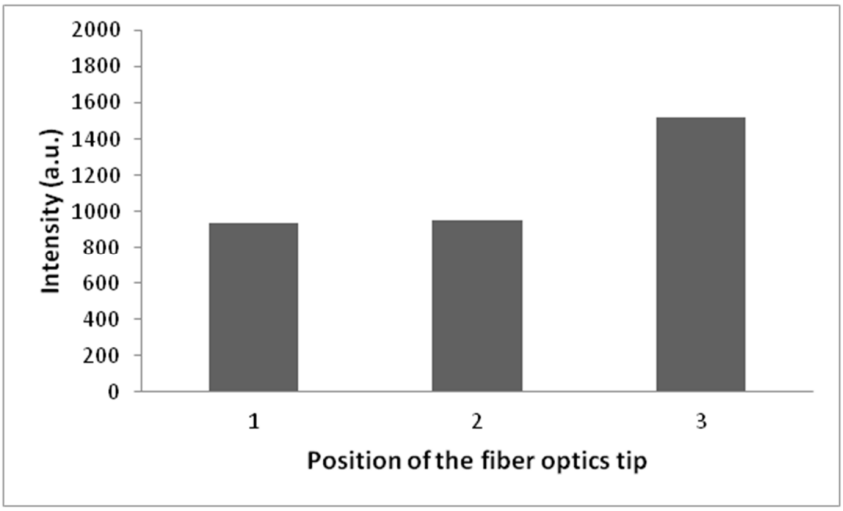

Figure 5-22 the effect of applying different fibre optic positions on the mercury signal intensity;
a 100 (µg/L) Hg (II) is determined by applying 4% (v/v) HCl , 4.25% (m/v) $SnCl_2$, 105 (ml/min) argon and 150 (watt) power; position (1) at the centre of the atomization channel, position (2) 10 mm after passing the electrodes overlapping section, and position (3) the end of the gas channel (axial viewing).

As mentioned in **Section (2.6.2.2/a)**, the quantitative determination of analyte based on absorption spectroscopy is usually interpreted according to Lambert-Beers' law, in which the amount of light emitted from a defined light source and absorbed due to the presence of the analyte is utilized to infer the concentration of the analyte. In this study, the author utilized SpectraSuite software which is compatible with the spectrometer (USB-2000) to conduct absorption measurements and to infer the concentrations according to equation (5-11), which is extracted from equation (2-45):

$$C = \frac{A}{\varepsilon\, l} \qquad (5\text{-}11)$$

Where;
A: The absorbance, also called molar absorptivity (dimensionless)
ε: the molar absorption coefficient (L/mol/cm) at a specific wavelength
l: optical path length of the absorption (cm)
C: molar concentration (mol/L)

The absorbance (A) is evaluated through SpectraSuite software by applying the following formula *(OceanOptics, 2010)*:

$$A_\lambda = -log_{10}\left(\frac{S_\lambda - D_\lambda}{R_\lambda - D_\lambda}\right) \quad (5\text{-}12)$$

Where;
S = Sample intensity at wavelength λ
D = Dark intensity at wavelength λ
R = Reference intensity at wavelength λ

The molar absorption coefficient for Hg(II) is estimated by utilizing the criteria of linear dependence of absorbance on species concentration as described in the work of *(Deshpande and Zimmerman, 2005)*. Absorbance is measured for several injected mercury concentrations which results in linear dependency, as shown in **Figure (5-23)**. The linear dependence indicates that the slope of the fitted line is equal to ($\varepsilon\, l$). 8 cm was adopted for the spectral path length taking into consideration the gas channel length (7.5 cm) and (0.25 cm) extension from both sides to place the fibre optics sensors. The slope in **Figure (5-23)**, gives a molar absorption coefficient of 12.5 $\times 10^4$ (L/mol/cm) for Hg (II) in the current system.

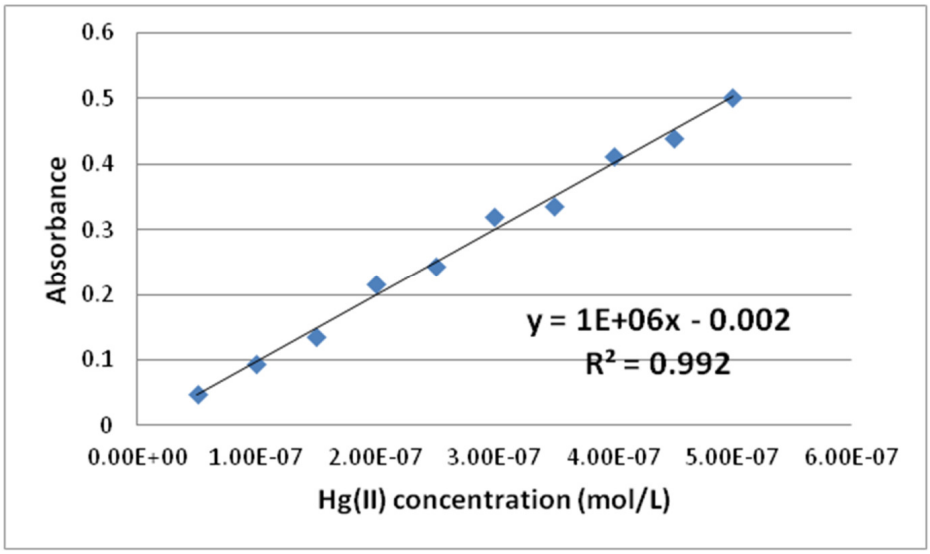

Figure 5-23 the measured absorbance relative to the spiked Hg(II) concentrations; when applying 4% (v/v) HCl , 4.25% (m/v) $SnCl_2$, 105 (ml/min) argon and 150 (watt) power

This result is slightly higher but in the same order of magnitude as the value (5.02×10^4 L/mol/cm) reported in the work of *(Khan et al., 2005)*, who utilized a commercial mercury analyzer based on the HG technique.

Quantitative determination of mercury was investigated using $SnCl_2$, $NaBH_4$, and KBH_4 schemes and applying a 3 second pulse length by the same procedures described earlier in this section. In all the experimental sets, the mercury signal begins to appear after approximately 2 minutes from the sample injection. The measured concentrations increased gradually and reach a maximum after approximately 4 minutes of the experiment start up.

The recorded absorbance throughout the sample injection period is monitored via a strip chart, and the estimated mercury concentration shown in a separate screen, as illustrated in **Figure (5-24)**.

(A)

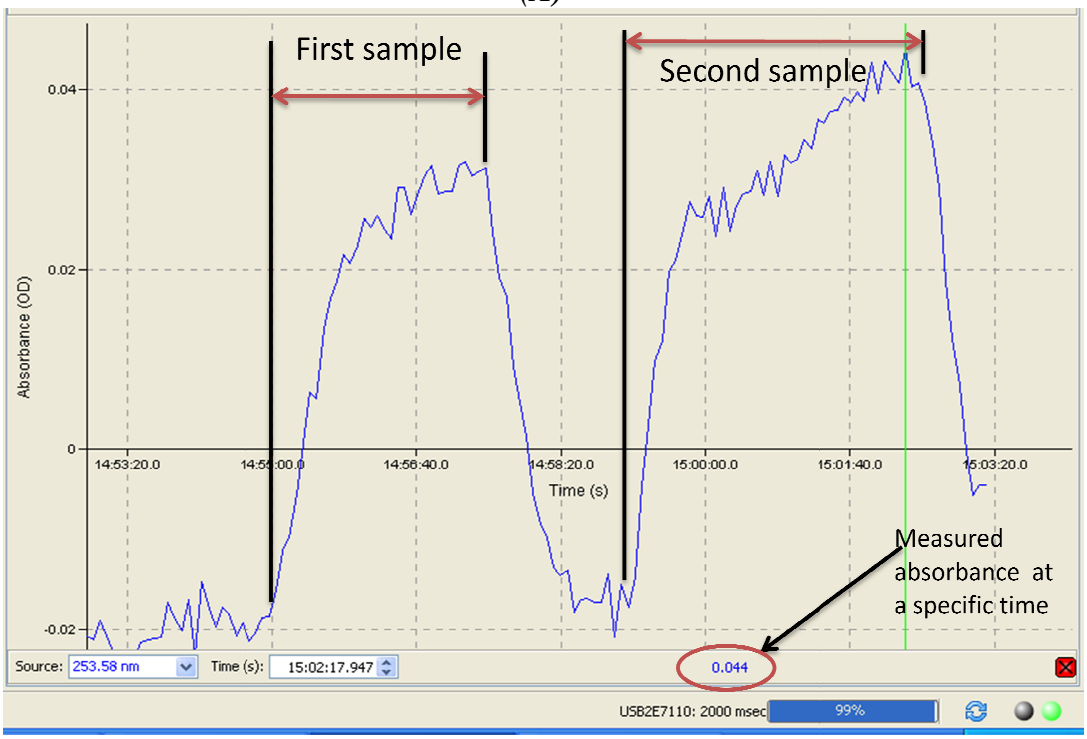

(B)

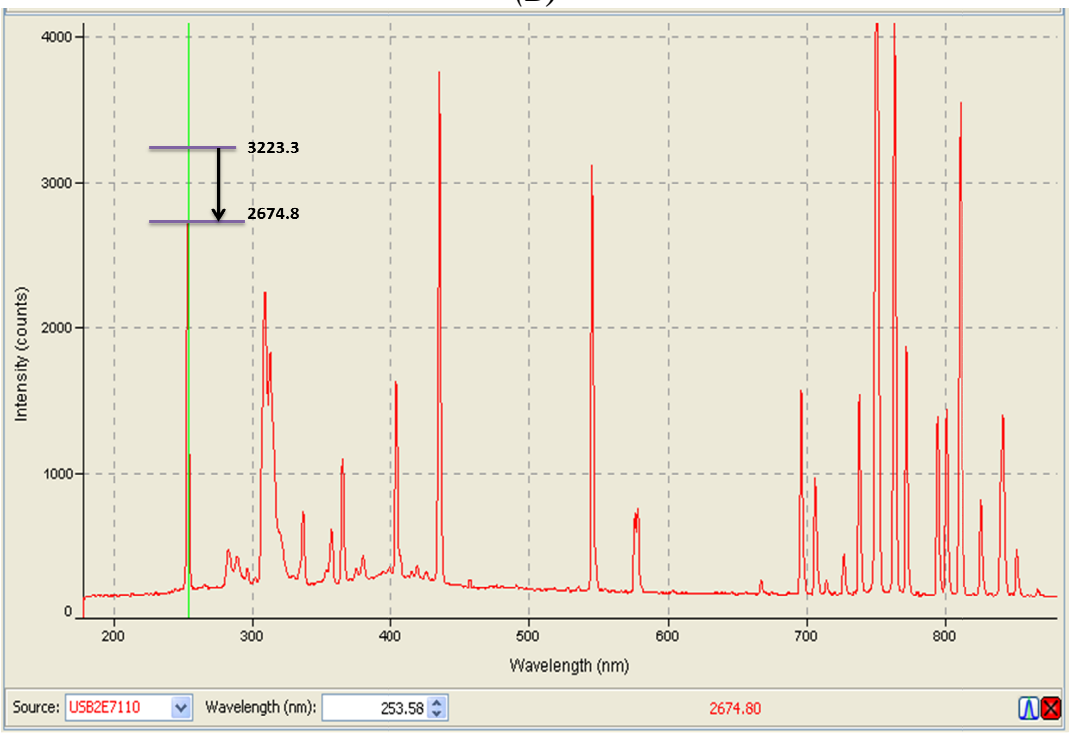

(C)

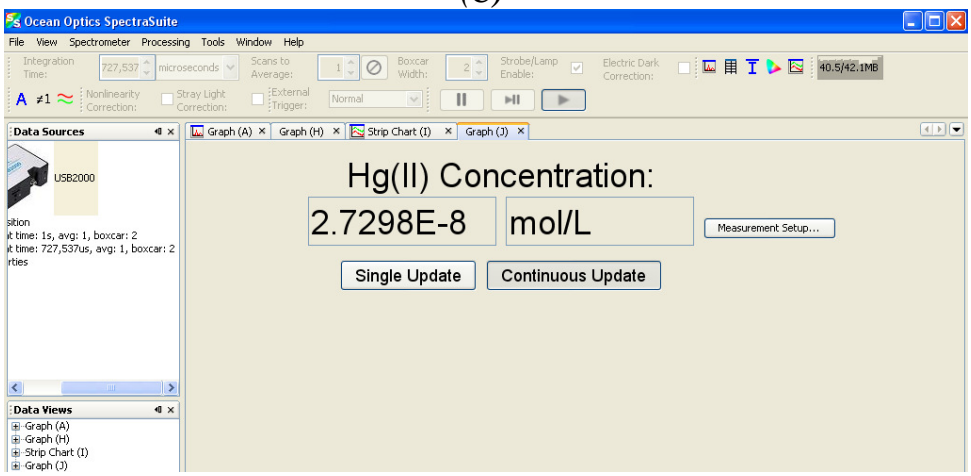

Figure 5-24 screen shots for the results of Hg (II) quantitative determination; by applying 4% (v/v) HCl, 4.25% (m/v) $SnCl_2$, 105 (ml/min) argon and 150 (Watt) applied power; (A) represents a strip chart for the absorbance measurement with time for a sample containing10 (µg/L), (B) the recorded intensities before and after injecting the mercury sample, (C) a screen shot showing the estimated concentration based on $\varepsilon = 12.5\times10^4$ L/mol/cm (note that the concentration is updated with time according to the measured absorbance),

Figure (5-25) shows calibration graphs for mercury relative to injected values.

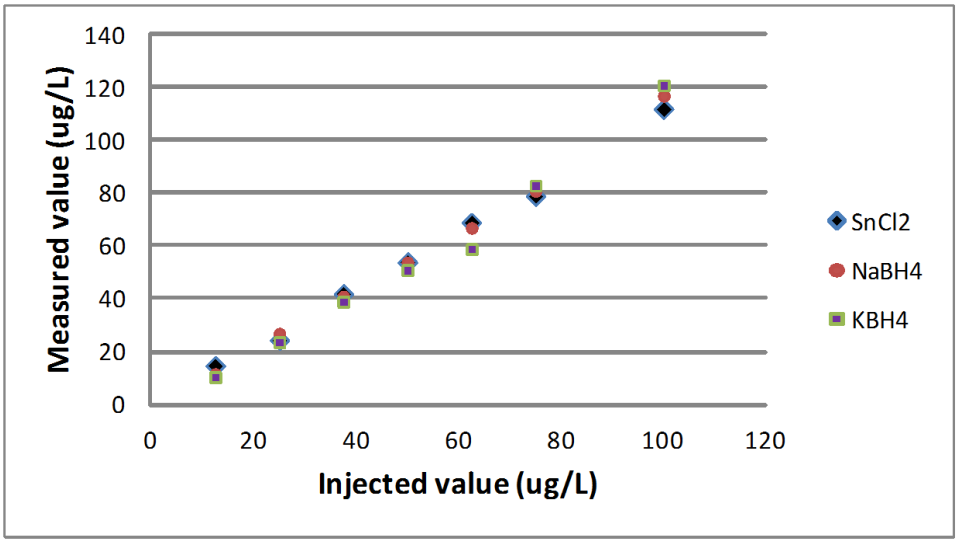

Figure 5-25 Calibration graphs show the measured Hg (II) corresponding to the real injected values;
105 (ml/min) argon and 150 (watt) are applied in all experiments; the signals are recorded upon applying 4% (v/v) HCl and 4.25% (m/v) $SnCl_2$, 1M HCl and 0.4% (m/v) of $NaBH_4$ and KBH_4.

The injected samples are evaluated with an expected error of (± 5%) and this is attributed to the error due to sample preparation by applying stepwise dilution as well as the error due to mercury residues found in the chemicals. The average absolute error, determined according to **Appendix 11.3**, is found to be 9.73% , 9.13% , and 9.2% for $SnCl_2$, $NaBH_4$, and KBH_4 schemes respectively, which indicates that all the tested systems act with similar efficiency. This error (≈ 10%) is considered reasonable. However, larger error values result for high mercury concentrations compared with low mercury concentrations. This indicates that better detection limits can be obtained when testing low mercury concentrations, which is the objective of the proposed system.

5.6 The study of the impact of mercury sample magnetization prior to detection by emission spectroscopy

The effect of the physical factors (e.g. periodic oscillation of external electric field, temperature fields, ultrasounds, UV radiation, and magnetization effect) has been studied and utilized in the environmental sectors since they can provide simple and economically justifiable performance with low ecological impact. Among those

physical factors, the magnetic treatment phenomenon has been applied recently in the water treatment sectors and the environmental fields. It is reported that water magnetization could lead to several effects such as lowering surface tension and viscosity as well as increasing permeability, which accounts for valuable effects. In this regard, researchers have reported beneficial results due to water magnetization such as saving in the quantity of water required for irrigation as well as enhancing the productivity of plants in the agriculture field *(Maheshwari and Grewal, 2009)*. Good results were also reported in the fields of water and waste water treatment such as scale reduction in the hot water reservoirs *(Smith et al., 2004)*, an increase in the efficiency of water clarification *(Hattori et al., 2001)*, a COD reduction (by 35 %), a P-PO4 reduction (by 90 %), an N-NH_4 reduction (by 50 %) and odour reduction *(Krzemieniewski et al., 2004)*. Moreover, recent studies reported an enhancement in the efficiency of heavy metals removal from water and waste water due to the magnetic field effects. Different kinds of supportive materials such as polymer resin and glass wool were mixed with magnetite (iron ferrite) as a seeding material to form an adsorbent matrix. The adsorption efficiencies for metal ions, metal colloids and nanoparticles are reported to increase when applying a suitable magnetic field *(Navratil and Shing, 2003)*, leading to better separation. On the other hand, the magnetic nanoparticle based materials such as Fe_3O_4 coated with decanoic acid *(Faraji et al., 2010)***,** and Fe_3O_4 coated with silica and modified with trimethoxysilane *(Huang and Hu, 2008)* were recently used for heavy metals determination by ICP-MS and ICP-OES respectively. The nanoparticles were also used in the solid phase extraction as an adsorbent for metal species in the aqueous samples (e.g. cadmium, copper, mercury, nickel, lead, chromium and zinc). Those applications are based on the fact that the magnetic nanoparticles are able to adhere to the target elements and removed readily from the matrix by applying the magnetic field, without any agglomeration after the magnetic field removal.

Hence, it is expected that the magnetic field is able to create advantageous effects on the sample pre-treatment before being analysed by any of the known techniques. The emergent environmental effect by magnetization could be utilized to assist analyte derivatization, and may act in a similar way to expensive chemicals that are normally injected in the analytical processes (e.g. surfactants).

The following work is to assess the impact of pre water sample magnetization on the results of mercury detection. Two experimental sets were conducted to analyse multi water samples, spiked with different mercury concentrations, without and with sample

pre magnetization respectively. The results are compared based on the recorded intensities. A custom-made tubular section (8 mm ID, 10 cm length) was used (**Figure (5-26)**), where 0.3 Tesla magnetic field was applied to magnetize the water fed through a closed loop cycle (3 L/min).

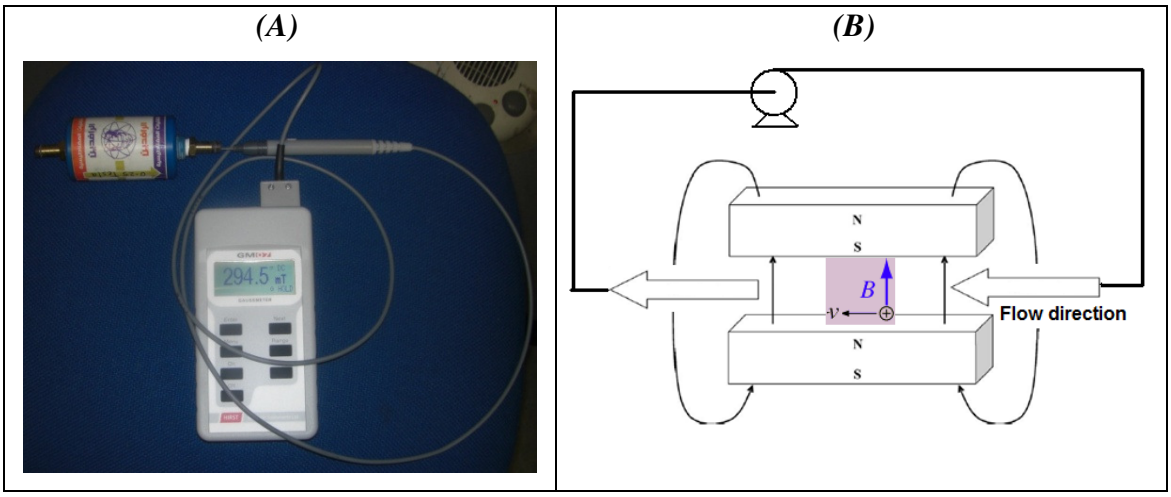

Figure 5-26 the setup used to implement the sample magnetization;
(A) a picture for the magnetization unit, the probe of measuring device is inserted temporarily to measure the magnetic field, (B) the magnetization system; *B* and *v* represents the magnetic field and velocity of charge respectively

5.6.1 Effect of magnetization on the properties of tap water

In the first experiment, the impact of magnetization on the change in water properties is studied. Several magnetization periods were applied and pH and electrical conductivity measured using an integrated device (Mettler Toledo). The water surface tension is determined by using a (First ten angstrom) tensiometer and applying the pendant drop hanging method. The magnetic field was measured by a (Hirst) gauss meter. Closed cycle tap water magnetization is implemented continuously for 14 hours. During the magnetization period, samples of the treated water are collected while pH, conductivity, and the interfacial tension are recorded instantaneously and after six days at 21 ^{o}C to determine the consistency of magnetization effect. Results are shown in **Figure (5-27)**, which indicates a permanent effect of magnetization on the tested samples.

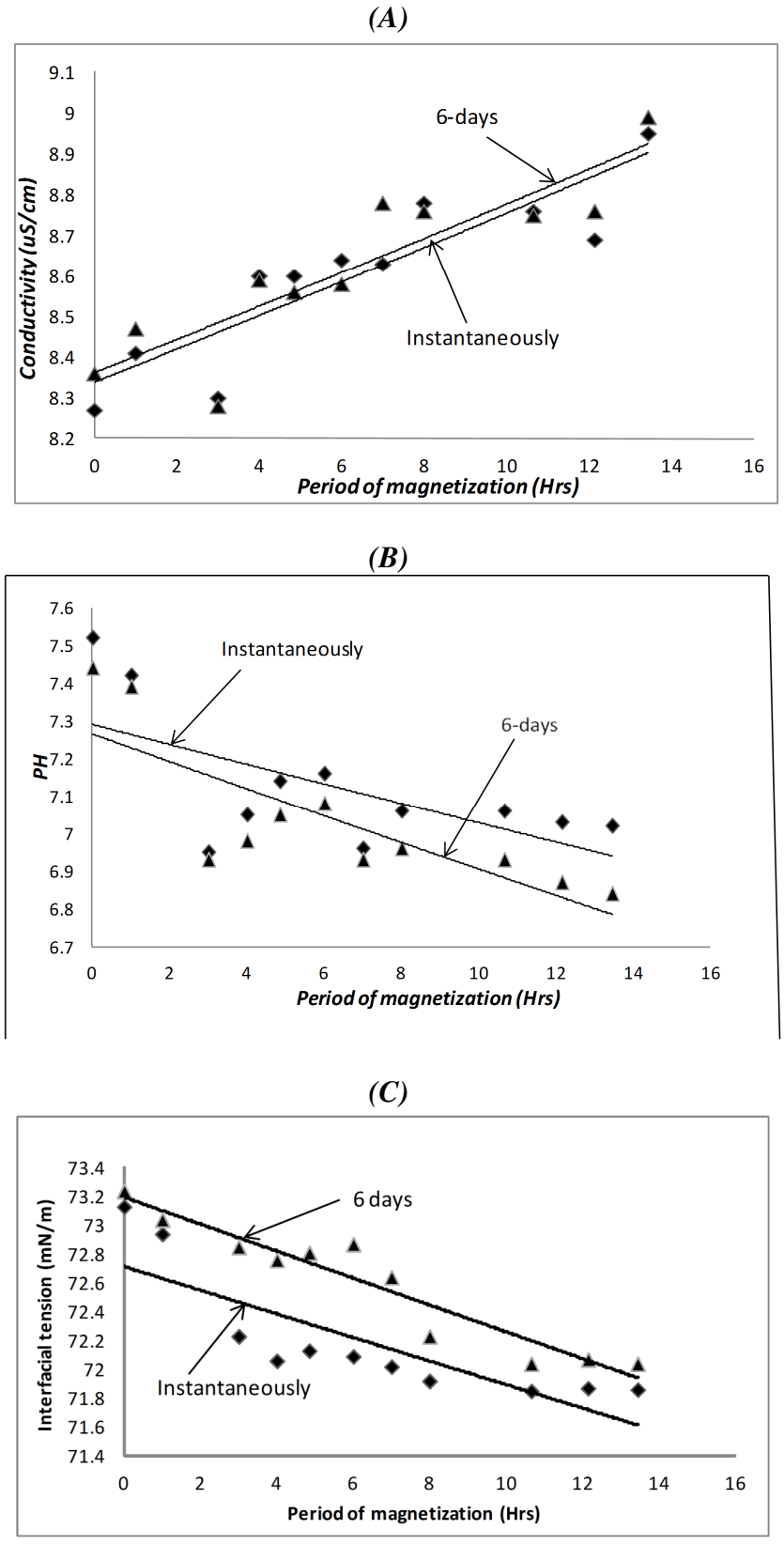

Figure 5-27 the effect of magnetization on tap water properties;
(A) The impact on tap water electrical conductivity, (B) The impact on tap water pH, (C) The impact on tap water interfacial tension; the applied pendant droplet volume = 15 µL. all data in the figures are fitted exponentially.

The results show a 7% and 0.2% reduction in the values of pH and interfacial tension respectively, whereas electrical conductivity increased 8% after being magnetized for 14 hours. Readings after six days show the same trend; however, the values for the electrical conductivity and the interfacial tension increased slightly after six days, which most likely occurred due to contact with atmosphere. Values of pH decreased slightly after six days which could be attributed to CO_2 gas dissolving in the water causing an increase in water acidity due to H_2CO_3 formation. Although the difference between the values is small in the case of interfacial tension, the impact of magnetization could be increased by optimising parameters such as magnetic field strength and magnetization period. In contrast, the impact of magnetization on electrical conductivity is considered valuable and could affect in later processes positively.

5.6.2 The impact of magnetization on mercury detection and determination

Two experiments were conducted to verify the impact of magnetization on mercury detection and determination by using the proposed analytical method. In the first set of experiments, a mercury standard solution (1 g L^{-1}) was prepared using normal distilled water, followed by stepwise dilution to prepare the target mercury solutions. In the second set, the mercury standard solution (1 g L^{-1}) was prepared using distilled water treated by applying a magnetization cycle for 14 hours. HCl and $SnCl_2$ solutions are prepared by using the specified water type accordingly. The results are shown in **Figure (5-28)**, which shows a slight increase (3.5 – 7.5%) in the intensities of the samples treated by magnetization.

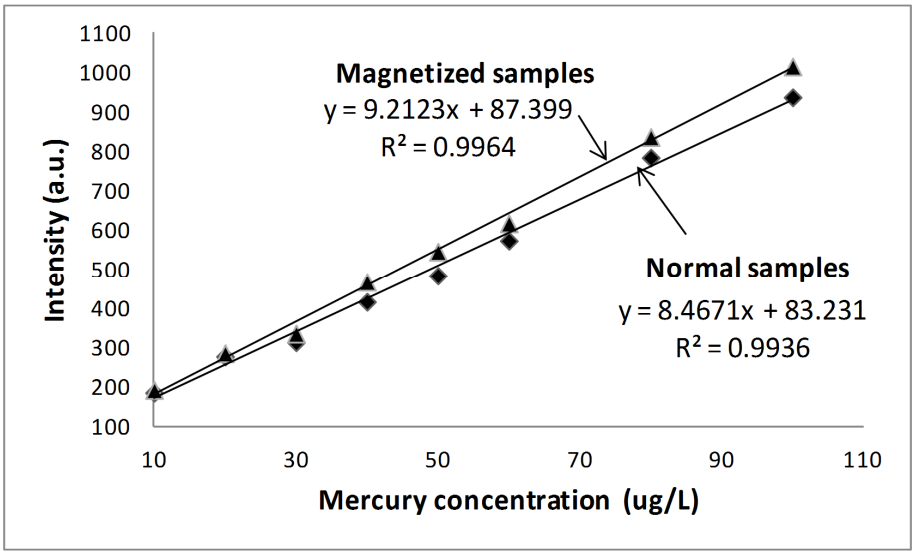

Figure 5-28 the effect of magnetization on Hg (II) detection;
the mercury signals are recorded upon applying 4% (v/v) HCl , 4.25% (m/v) $SnCl_2$, 105 (ml/min) argon and 150 (watt).

A possible interpretation for the increase in signal intensity is the reduction in interfacial tension due to magnetization. The diminished interfacial tension facilitates the adsorption of paramagnetic particles of oxygen increasing the oxygen concentration in the water samples. This results in removing gases of high atomic weight such as mercury. Another reason could be a modification of water structure due to magnetization. Such a change simplifies the release of all gases proportionally, regardless their atomic weight. It is mentioned in the literature *(Krzemieniewski et al., 2004)* that imposing a magnetic field on a flowing liquid might lead to changes in electrical potential. These changes integrate with an increase in electrical conductivity and causes a disturbed liquid surface. The disturbance would eventually facilitate the release of the species that exist in the boundary layer, and most likely include the mercury vapour species. On the other hand, *(Moor et al., 2000)* reported that increased acidity is advantageous for the reduction of the analyte and suppression of the signal from other metals. Therefore the reduction in pH due to magnetization might also contribute to improved signal intensity.

There is a clear effect of sample magnetization on the time required for mercury signal to appear. The signals begin to appear after approximately 1.5 minutes compared to 2 minutes for non-magnetized samples.

In conclusion, the physical effect of the magnetization process has proved useful for mercury detection and determination, and could be extended further for better results by optimizing the operating parameters such as the magnetic field strength and magnetization period. This effect would be more advantageous when the analyte is difficult to reduce and requires assisting chemicals (e.g. surfactants).

5.7 Summary of the findings from chapter five

1- The intensity of argon and other emissions lines increased significantly when a water stream was introduced into the bulk of the gas liquid separator. This result is attributed to: (1) the collision of the excited species with OH radicals, (2) the collision - radiative recombination of argon with the energetic electrons. These collisions generate extra OH and other radicals and consequently increase the intensity of the OH emission line and other argon lines in the near IR region.

2- The removal of 20% moisture content from the stream entering the DBD atomizer affects the argon lines near IR region negatively, which supports the findings mentioned in 1.

3- The experimental investigations and the statistical analysis for the mercury cold vapour generation process show that chemical concentration and power are key factors in enhancing the system performance. In contrast, the argon flow rate is found to be a critical factor and should be controlled accurately to keep a stable system performance. Other reasons for unstable system performance can be attributed to the interactions of parameters.

4- The mercury derivatization process is conducted by applying three schemes: $Sncl_2$, $NaBH_4$ and KBH_4. Results show that lower detection limits are found when using $NaBH_4$.

5- One problem addressed through the application of HG technique is the disturbance in the DBD plasma due to the presence of hydrogen. The hydrogen gas leads to a magnification on the recorded spectrum in the region 200 – 600 nm and ultimately misleads the interpretation of the recorded signals. The problem was solved by applying two experiments, with and without spiking mercury. The difference between the recorded signals is considered proportional to mercury. Even with the presence of

hydrogen in the DBD atomizer, no clear signals obtained for hydrogen excited species (H_γ , H_β or H_α) which may indicate a consumption of these radicals in unknown reactions.

6- Three types of gas liquid separator were evaluated experimentally; two of them constructed by the author and a commercial separator. Best performance is obtained when using GLS (A) and injecting the supporting gas in pulses. The performance of the commercial separator is found the weakest compared to the custom made separators.

7- The quantitative determination of mercury is similar when applying any of the three schemes. However, $NaBH_4$ is slightly more effective based on the calculated average absolute error.

8- The application of magnetization for sample pre-treatment proved advantageous for the determination of mercury.

6. APPLICATION OF THE PROPOSED TECHNOLOGY FOR MULTI HEAVY METALS DETERMINATION

6.1 Preface

The aim of this chapter is to investigate the applicability of the proposed analytical technique for heavy metals other than inorganic mercury. Arsenic, Tin, Cadmium and Lead as well as other transition metals (Chromium, Copper, Nickel, and Zinc) were selected. Although cadmium is known to be a transition metal, most literature characterizes cadmium as a hydride forming element. According to the literature, the selected analytes show a variety of reduction conditions, which provides the opportunity to explore a wide range of derivatization conditions. The first experimental sets are devoted to analysis of the selected analytes individually by using the hydroborates scheme and other assisting oxidizing and pre-reducing agents. The second experimental set is to investigate the simultaneous determination of a mixture of analytes.

Preliminary experiments were conducted for all the analytes to identify the wavelengths of the applied standards, shown in **Table (6-1)**. It is also important to note that most of the wavelengths reported in literature and shown in **Table (6-1)** could not be detected because of limited resolution offered by the spectrometer used (USB 2000).

Table 6-1 Summary of the detected wavelengths for the applied spectroscopic standards

Examined element	Wavelengths reported in the literature *(Grotti et al., 2005, Pohl and Zyrnicki, 2001) (Zhu et al., 2006b, y Temprano et al., 1993) (Heisterkamp and Adams, 1999, Chen et al., 1995)*	Observed wavelength range integrated through USB 2000
As	188.98, 193.696, 228.812	228.65 - 229.03
Sn	189.927, 283.998, 326.233, 286.3	326.03 - 326.40
Cd	226.50, 214.44	226.38 - 226.76
Pb	405.783, 261.418, 220.353, 217.0	220.31 - 220.69
Cu	324.75	324.55 - 324.92
Ni	231.60	231.30 – 231.68
Zn	213.86	213.86
Cr	267.72	267.49 – 267.87

Atomic absorption spectroscopy standards (1 g/L), purchased from Sigma Aldrich, were used to prepare the standard solutions and then to prepare the working solutions by applying stepwise dilution with distilled water. In the process of wavelength

identification for the standards, a 2% m/v $NaBH_4$ stabilized by using 0.5% m/v NaOH solution is used to implement the hydride generation reaction. The examined analyte (100 µg/L) was acidified with 0.8 (M) HCl solution.

Operating concentrations are adopted from the work of *(Grotti et al., 2005)* who applied them for multi elements simultaneous determination. HCl concentrations higher than 2 M are reported to be a critical condition may extinguish the plasma due to H_2 load *(Sturgeon et al., 1996)*. Therefore all experimental sets in this chapter and later experiments undertaken in this research were conducted by using HCl concentration lower than 2 M.

A similar reaction system to that shown in **Figure (5-18)** was used. A traditional gas-liquid separator GLS (A) with 350 ml volume utilized and controlled by the strategy as described in **Section (5-5)**. Since higher concentrations of hydroborates (up to 2% m/v) are applied, an extra amount of hydrogen is released to the GLS (A) which puts a burden on the whole process.

In order to reduce the tendency for extra hydrogen generation, plastic beads (with different sizes) are placed at the GLS base, acting as a filter. The liquid residues are disposed out of the separator through the beads filter; thereby hydrogen generation from liquid residues is prevented. The solenoid valve connected to the GLS base is left open during operation in order to release all the liquid residues on time. This operational technique is adopted for all the elements when a concentration higher than 0.5% m/v of $NaBH_4$ is applied.

6.2 Individual studies applied for qualitative determination

6.2.1 Arsenic determination

An optimization study is conducted to explore the best derivatization conditions for arsenic determination through the hydride generation scheme. As stated in chapter five, the key parameters that control analyte derivatization are the applied power, argon flow rate, sample acidity and the concentration of the reducing agent. The values of 105 (ml/min) and 150 (watt) are adopted to be the optimum for argon flow rate and the applied power in all experiments undertaken from this stage of research. Therefore only two parameters (sample acidity and the reducing agent concentration) are investigated

in the current optimization study. An experimental plan based on the second order central composite rotatable design *(Cochran and Cox, 1992)* was conducted by considering the concentration of HCl and hydroborates as the system variable parameters and the intensity of emission line in the range (228.65 – 229.03 nm) as the objective function, (**Table (6-2)**).

Table 6-2 the arsenic experiments according to the 2nd order central composite rotatable design plan;
The table shows the recorded intensities (rectified for hydrogen effect) for 100 (µg/L) arsenic observed in the range (228.65 – 229.03 nm)

Exp. No.	HCl (M)		$NaBH_4$ (% m/v)		Intensity	KBH_4 (% m/v)		Intensity
	Real Value	Code (x_1)	Real Value	Code (x_2)	(a.u.)	Real Value	Code (x_2)	(a.u.)
1	0.75	-1	0.875	-1	323	0.875	-1	306
2	1.25	+1	0.875	-1	349	0.875	-1	328
3	0.75	-1	1.625	+1	364	1.625	+1	339
4	1.25	+1	1.625	+1	373	1.625	+1	365
5	0.5	-1.414	1.25	0	297	1.25	0	267
6	1.5	+1.414	1.25	0	338	1.25	0	298
7	1	0	0.5	-1.414	278	0.5	-1.414	257
8	1	0	2.0	+1.414	305	2.0	+1.414	319
9	1	0	1.25	0	316	1.25	0	323
10	1	0	1.25	0	319	1.25	0	327
11	1	0	1.25	0	308	1.25	0	319
12	1	0	1.25	0	311	1.25	0	321
13	1	0	1.25	0	312	1.25	0	325

Table (6-2) illustrates the adopted plan and the recorded signal intensities upon injecting 100 (µg/L) arsenic samples and applying two reducing agents in two separate experimental sets. 10 ml of the acidified sample and the reducing agents are injected in all experiments in the set. The experiments repeated two times, with and without the examined analyte. The difference between the signals intensities is considered proportional to the concentration of the analyte.
The experimental system is represented by a quadratic multivariable model combining the single effect of the variables and the effects resulting from interactions:

$$Y = B_0x_0 + B_1x_1 + B_2x_2 + B_{11}x_1^2 + B_{22}x_2^2 + B_{12}x_1x_2 \qquad (6\text{-}1)$$

A multiple stepwise regression analysis (**Appendix 11.3**) was performed to estimate the polynomial coefficients which are shown in **Table (6-3)**. The average absolute error is estimated at 4.93% and 5.26% for $NaBH_4$ and KBH_4 respectively.

Table 6-3 the estimated polynomial coefficients for arsenic reduction by using hydroborates reducing agents

$NaBH_4$					
B_0	B_1	B_2	B_{11}	B_{22}	B_{12}
313.273	11.621	12.897	14.025	1.029	-4.25
KBH_4					
B_0	B_1	B_2	B_{11}	B_{22}	B_{12}
323.068	11.479	19.708	-7.993	-5.243	1.000

Optimal conditions for the highest arsenic intensity are obtained by performing a non-linear constrained optimization (**Appendix 11.4**) and the optimal values are shown in **Table (6-4)**.

Table 6-4 the optimal reduction conditions for the arsenic hydride generation

$NaBH_4$				KBH_4			
HCl concentration		$NaBH_4$ concentration		HCl concentration		KBH_4 concentration	
x_1	M	x_2	(% m/v)	x_1	M	x_2	(% m/v)
0.693	≈1.4	-0.626	≈1.5	-0.474	≈1.2	0.039	≈1.6

The application of the statistical optimization technique is useful for systems that consist of more than two variables. Since the current investigation has only two variables, the statistical optimization can be readily tested. Further experiments were carried out to check the optimization of conditions that were estimated statistically. Accordingly, the effect of changing the hydroborate and HCl concentrations on the signal intensity was studied and the results, rectified for the hydrogen effect, are shown in **Figures (6-1)** and **(6-2)**.

The results show that increasing the hydroborate concentration increases the signal up to a limit, after which the signal intensity reduces due to the increased hydrogen generation. In a similar way to mercury cold vapour generation, $NaBH_4$ gives a better arsenic signal intensity compared to KBH_4, therefore it was decided to adopt $NaBH_4$ in later hydroborate experiments. Increasing HCl concentration also increases signal intensity up to 1.3 M after which the signal intensity is reduced. Thus, the optimal HCl concentration of 1.3 M is applied in further experiments.

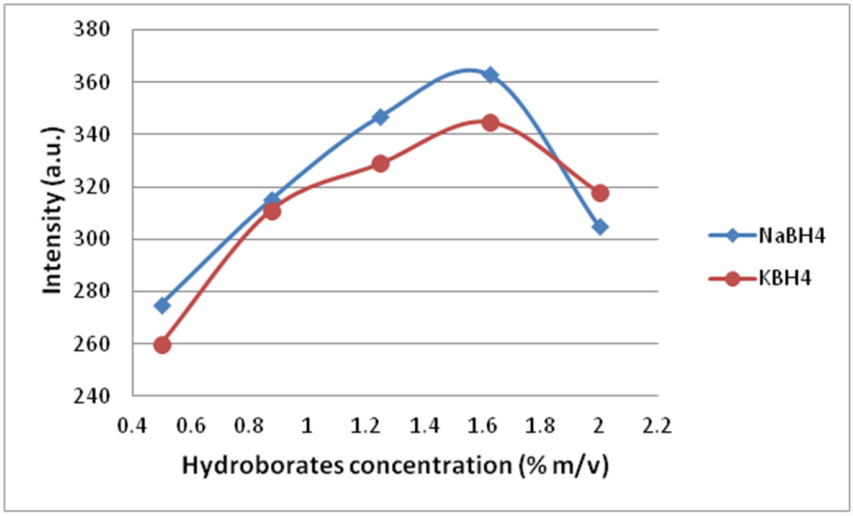

Figure 6-1 the recorded signals (rectified for hydrogen effect) for arsenic;
The signals obtained upon spiking 100 (µg/L) and applying several hydroborates concentrations while keeping constant HCl concentration at (1.4 M).

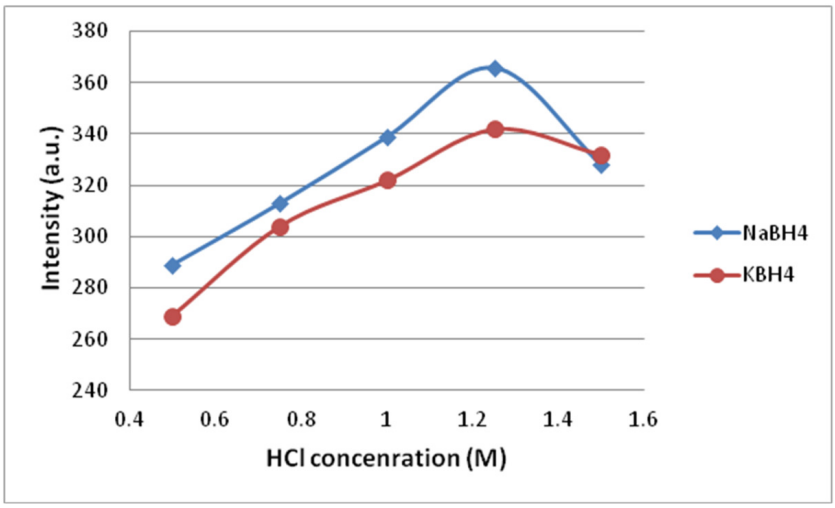

Figure 6-2 the arsenic signals (rectified for hydrogen effect);
The signals obtained upon spiking 100 (µg/L) and applying several HCl concentrations while keeping constant hydroborates concentration at (1.5% m/v).

The analytical figures of merit are estimated for the arsenic system by spiking a blank solution into the system and measuring the intensity. The blank experiments were repeated eight times and the standard deviation (*S*) calculated. The calibration graph of the arsenic signal intensities versus different concentrations of arsenic is shown in **Figure (6-3)**. The figures show that 3.7 (µg/L) LOD and 1.82% RSD are achieved for arsenic by adopting the proposed system. As mentioned in **Table (1-2)**, the acceptable limit of arsenic in drinking water is about 10 (µg/L), which indicates a reasonable precision could be obtained for arsenic detection by the proposed system.

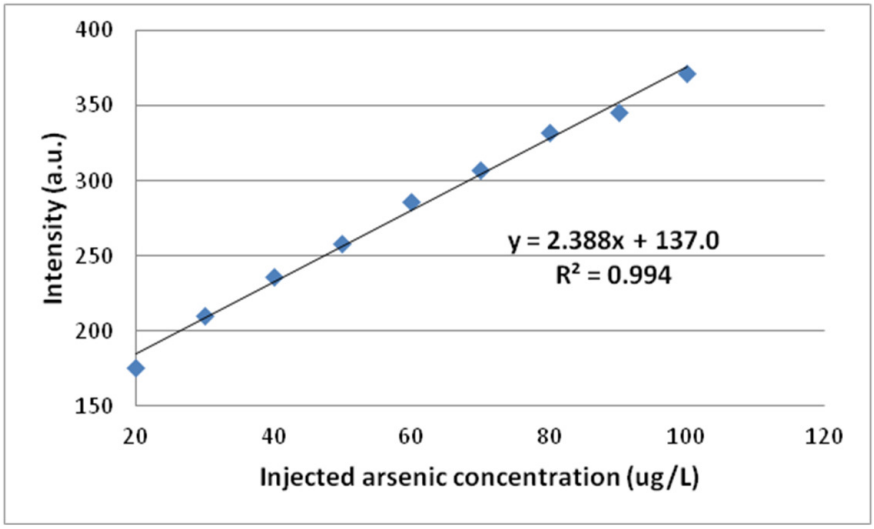

Figure 6-3 a calibration graph generated for arsenic;
The signals (rectified for hydrogen effect) recorded upon spiking several arsenic concentrations at 1.3 (M) HCl and 1.5% (m/v) $NaBH_4$.

It is reported in the literature that efficient hydride generation from arsenic species at relatively low HCl levels can be achieved by using a pre-derivatization step with compounds containing thiol groups such as L-cysteine, ascorbic acid, thiourea, or thiolglycolic acid *(Tsalev et al., 1996, Howard and Salou, 1996, Musil and Matousek, 2008)*. For instance, an intermediate compounds (e.g. an arsinothiol derivate) forms due to the reaction between $NaBH_4$ and the SH group of L-cysteine, which is more effective than $NaBH_4$, and consequently leads to enhanced signal intensity.

It is also reported that not all of the abovementioned pre-reducing agents are suitable for online derivatization; for example, pre-reduction reaction with L-cysteine occurs within one hour and requires higher bulk temperature than room temperature *(Matousek et al., 2008)*. In contrast, a (1% m/v) concentration of thioglycolic acid TGA will accomplish a pre-reduction of arsenic within two minutes, which makes TGA a good agent for the online pre-reduction process. In order to investigate the effect of applying a pre-reducing agent, an experimental set was conducted using several concentrations of TGA. A concentrate of TGA (98%) purchased from Sigma Aldrich was used to prepare dilutions with distilled water. 1 ml TGA was added directly to the examined sample and injected through the sampling pump (PP 1), shown in **Figure (5-18)**. The recorded arsenic signals upon applying different concentrations of TGA are illustrated in **Figure (6-4)**.

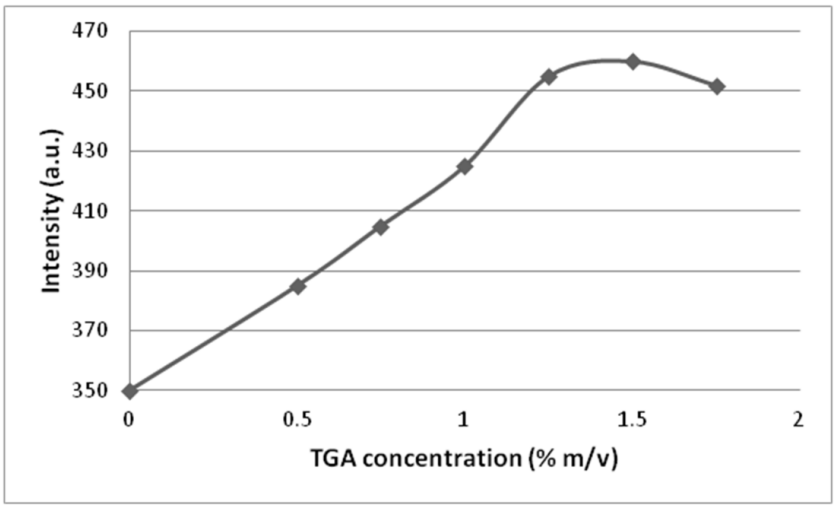

Figure 6-4 the recorded arsenic signals (rectified for hydrogen effect) corresponding to the added pre-reducing agent;
Several concentrations of thioglycolic acid (TGA) added upon spiking 100 (µg/L), while applying concentrations of 1.3 (M) HCl and1.5% (m/v) $NaBH_4$.

The signal intensity increased in linear pattern when applying TGA up to 1% m/v. As similar intensities were obtained when using concentrations more than 1.25% m/v, a value of 1.25% m/v TGA was adopted as an optimal. The signal intensity achieved is shown in **Figure (6-5)**.

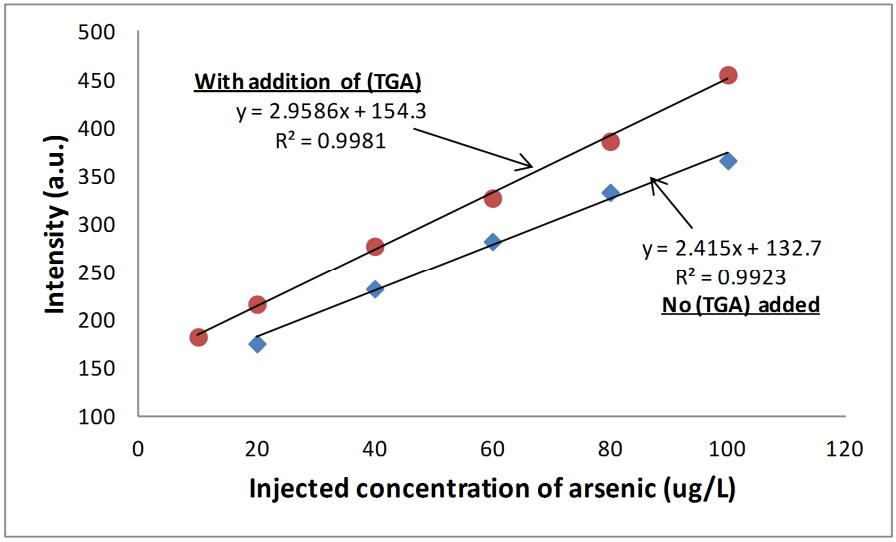

Figure 6-5 comparison between the arsenic signals recorded with and without adding TGA;
The signals recorded upon applying several concentrations of arsenic before and after injecting (1.25% m/v) thioglycolic acid while using 1.3 (M) HCl and 1.5% (m/v) $NaBH_4$.

The signal intensities increased by approximately 20% for all concentrations of arsenic. It was also observed that the signal of 10 (µg/L) could be differentiated from the background (i.e. the signal due to the hydrogen magnification effect) when TGA was added to the sample, which was not observed without TGA application.

Further investigations explored the beneficial effect of magnetizing the sample before applying the derivatization stage, which is mentioned earlier in **Section (5-6)**. Several arsenic samples are prepared using two types of distilled water; the first is the normal distilled water, the second distilled water subjected to a magnetization cycle for 14 hours. Both sample sets were derivitized using $NaBH_4$ as a reducing agent, followed by an atomization stage in the DBD atomizer. No clear differences were observed in the recorded arsenic signal when comparing the results from both categories; nevertheless, an increase in signal intensity up to 6% was observed for samples prepared from the magnetized distilled water and stimulated by injecting 1.25% m/v TGA, as shown in **Figure (6-6)**. Hence, it is expected that better signal intensities could be obtained when applying optimized sample magnetization conditions.

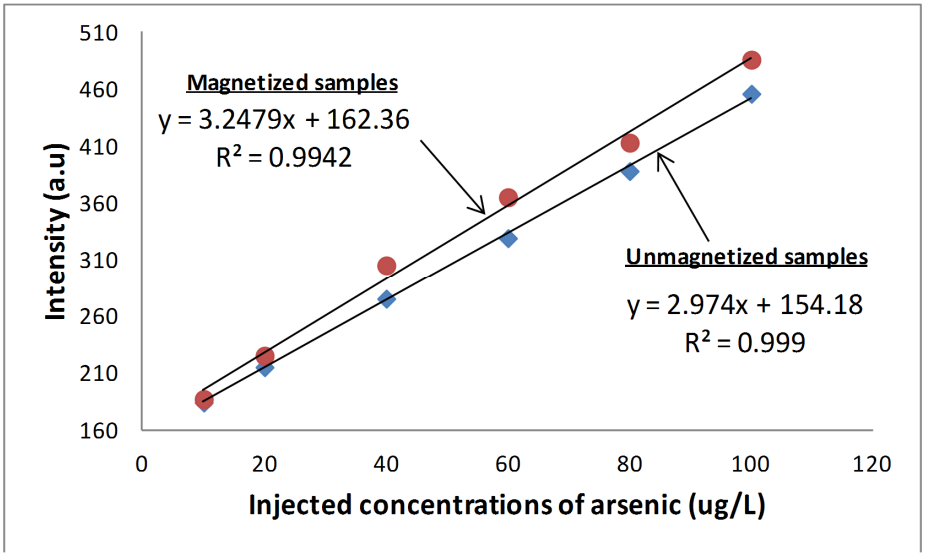

Figure 6-6 the effect of sample magnetization on the recorded arsenic signals;
The signals (rectified for hydrogen effect) are recorded upon injecting several concentrations of arsenic with addition of (1.25% m/v) thioglycolic acid while using 1.3 (M) HCl and1.5% (m/v) $NaBH_4$.

6.2.2 Tin determination

A study was conducted to explore the optimum derivatization conditions ($NaBH_4$ and HCl concentrations) for Sn hydride generation using 105 ml/min argon and 150 Watt power in all experiments. **Table (6-5)** shows the experiments to conduct the optimization study according to a second order central composite rotatable design, in which 100 µg/L tin was in the examined sample. Concentrations are confined in the ranges 0.5-2% m/v for $NaBH_4$ and 0.5-1.5 M for HCl. 10 ml of both the acidified sample and the reducing agent are injected in all experiments. The experimental system was represented by a quadratic multivariable model; hence, a multiple stepwise regression analysis was performed by using the algorithm shown in **Appendix 11.3** to estimate the polynomial coefficients. The following empirical model is produced for the Tin system with an estimated average absolute error of 5.9 %:

$$Y = 400.693x_0 + 19.54x_1 + 22.871x_2 + 18.872x_1^2 + 6.125x_2^2 - 7.25x_1x_2 \quad (6\text{-}2)$$

Table 6-5 the tin experiments according to the 2nd order central composite rotatable design plan;
The table shows the recorded intensities (rectified for hydrogen effect) for 100 (µg/L) tin observed in the range (326.03 – 326.4 nm)

Exp. No.	HCl (M)		$NaBH_4$ (% m/v)		Intensity
	Real Value	Code (x_1)	Real Value	Code (x_2)	(a.u.)
1	0.75	-1	0.875	-1	410
2	1.25	+1	0.875	-1	456
3	0.75	-1	1.625	+1	487
4	1.25	+1	1.625	+1	504
5	0.5	-1.414	1.25	0	367
6	1.5	+1.414	1.25	0	433
7	1	0	0.5	-1.414	354
8	1	0	2.0	+1.414	395
9	1	0	1.25	0	402
10	1	0	1.25	0	396
11	1	0	1.25	0	407
12	1	0	1.25	0	400
13	1	0	1.25	0	398

The optimal conditions giving the highest Sn signal, obtained by performing a non-linear constrained optimization (**Appendix 11.4**) are found to be (x_1 = +0.669 & x_2 = -0.5285) 1.42 M HCl and 1.45% m/v $NaBH_4$ respectively.

The effect of changing the concentrations of $NaBH_4$ and HCl on the signal intensity was studied individually for the examined ranges; the results are shown in **Figures (6-7)** and **(6-8)**.

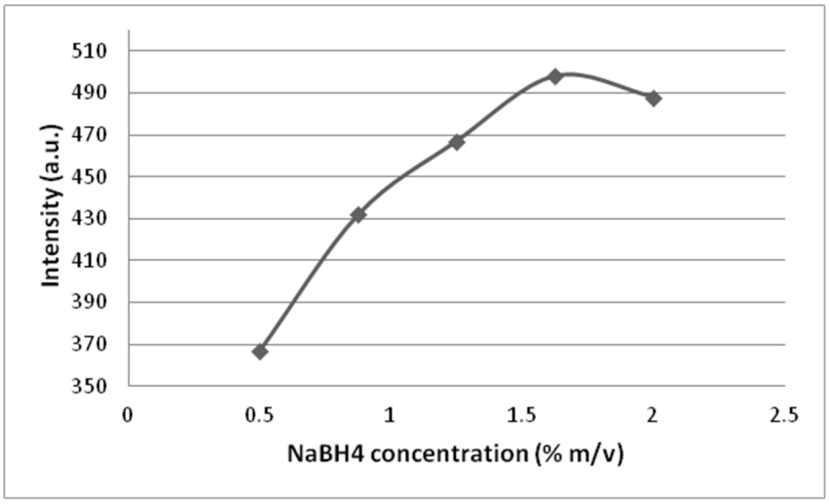

Figure 6-7 tin signals recorded when applying different $NaBH_4$ concentrations;
The signals (rectified for hydrogen effect) are for 100 (µg/L) tin and constant HCl concentration (1.4 M).

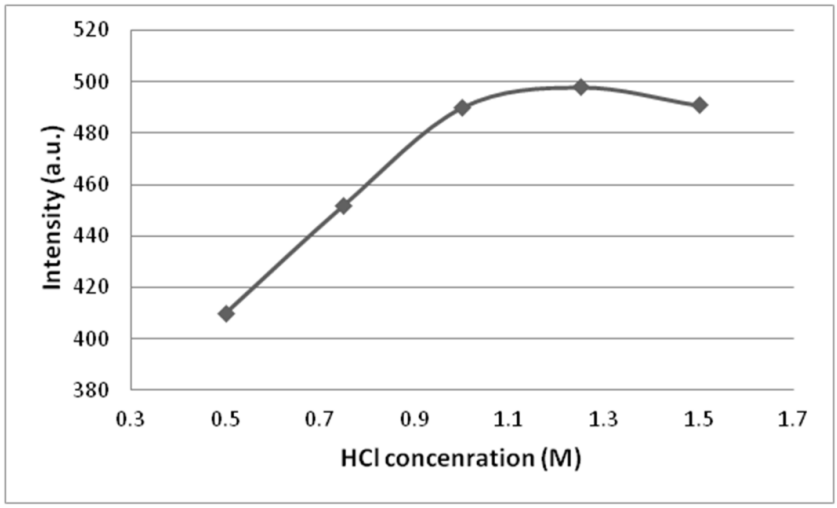

Figure 6-8 tin signals recorded when applying different HCl concentrations;
The signals (rectified for hydrogen effect) are for 100 (µg/L) tin and constant $NaBH_4$ concentration (1.5% m/v).

Increasing the concentration of $NaBH_4$ above 1.6% m/v reduces the signal intensity, (attributed to the increase hydrogen generation). Increasing HCl concentration is also advantageous up to 1.3 M, after which there is a decrease in the signal. Accordingly, the

optimal derivatization conditions were corrected to 1.3 M HCl and 1.5% m/v $NaBH_4$ respectively. These optimized conditions resemble the derivatization conditions found for arsenic, which is advantageous for achieving simultaneous detection.

The analytical figures of merit are estimated for the tin system by spiking a blank solution into the system and measuring the intensity. The blank experiments were repeated eight times and the standard deviation calculated. The calibration plot thus constructed is shown in **Figure (6-9)**.

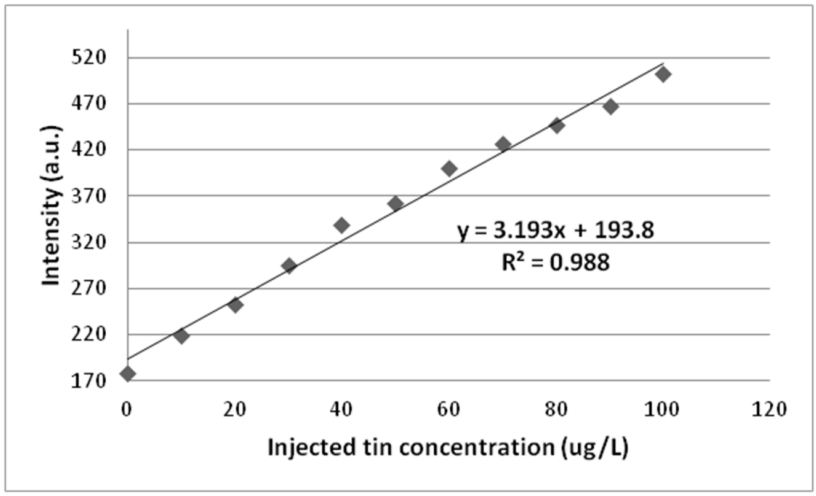

Figure 6-9 a calibration graph generated for tin experimentation;
The signals (rectified for hydrogen effect) recorded upon spiking several tin concentrations applying 1.3 (M) HCl and 1.5% (m/v) $NaBH_4$.

The estimated figures of merit show that 2.13 (µg/L) LOD and 1.29 % RSD are achieved by adopting the proposed analytical system. No clear standard limits shown in the literature for inorganic tin; however the main adverse effects of tin on humans occurs if the absorbed limit exceeds 150 mg/Kg *(WHO, 2008)*. Thus the achieved detection limits are quite reasonable. As mentioned in chapter two, inorganic tin was derivitized in previous studies without a pre-reducing agent. Thioglycolic acid (TGA 1.25% m/v) was investigated in this study as a pre-reducing agent to explore the effect on signal intensity. The results show 11% higher signal intensities are obtained for tin when applying TGA (**Figure (6-10)**).

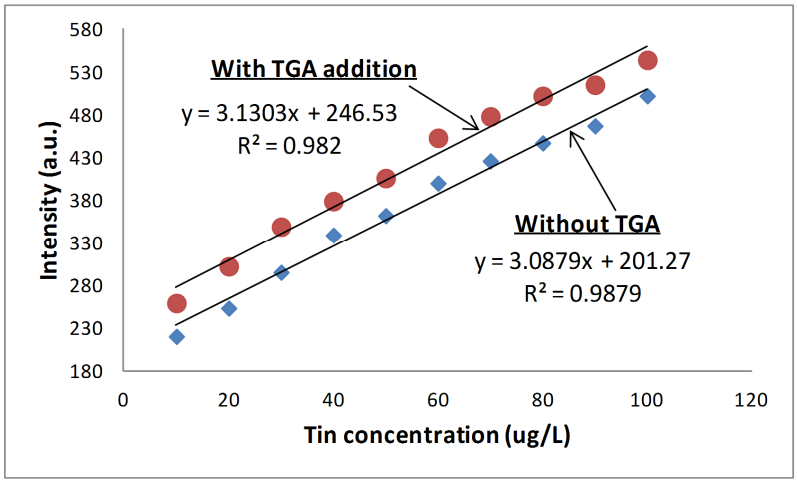

Figure 6-10 the recorded signals for tin with and without applying TGA (1.25% m/v); The signals (rectified for hydrogen effect) recorded upon spiking several concentrations of tin and applying 1.3 (M) HCl and1.5% (m/v) $NaBH_4$.

6.2.3 Cadmium determination

As reported in **Section (2.5.2)**, no certain mechanisms are given in the literature for the generation of cadmium volatile species. Most likely, the reaction of cadmium with hydroborates in acidic medium results in the formation of cadmium hydride (CdH_2), which rapidly decomposes to a free cadmium atom (Cd^0) at room temperature *(Li et al., 2004)*.

Since cadmium derivatization by applying $Sncl_2$ scheme failed, as reported elsewhere, $NaBH_4$ was selected for Cd reduction in this research. It is worth noting that the literature shows various derivatization conditions for cadmium represented by higher hydroborate concentrations and lower concentrations of HCl compared with other analytes (e.g. 3.5% m/v hydroborates and 0.6 M HCl *(Li et al., 2004)*, 4.0% m/v and 0.4 M HCl *(y Temprano et al., 1993)*).

In order to determine the optimal derivatization conditions, an optimization study based on a second order central composite rotatable design plan was conducted, through which the concentrations of $NaBH_4$ and HCl are investigated while applying 105 ml/min argon and 150 W power in all experiments. The experimental plan is shown in **Table (6-6).**

Table 6-6 the cadmium experiments according to the 2nd order central composite rotatable design plan;
The table shows the recorded intensities (rectified for hydrogen effect) for 100 (µg/L) cadmium observed in the range (226.38 – 226.76 nm)

Exp. No.	HCl (M)		$NaBH_4$ (% m/v)		Intensity
	Real Value	Code (x_1)	Real Value	Code (x_2)	(a.u.)
1	0.75	-1	0.875	-1	322
2	1.25	+1	0.875	-1	309
3	0.75	-1	1.625	+1	367
4	1.25	+1	1.625	+1	353
5	0.5	-1.414	1.25	0	358
6	1.5	+1.414	1.25	0	341
7	1	0	0.5	-1.414	276
8	1	0	2.0	+1.414	317
9	1	0	1.25	0	327
10	1	0	1.25	0	331
11	1	0	1.25	0	325
12	1	0	1.25	0	330
13	1	0	1.25	0	326

The experimental system is represented by a multiple quadratic multivariable model and the following empirical model is generated for the examined cadmium system with an estimated average absolute error of 1.6%.

$$Y = 327.878x_0 - 6.379x_1 + 18.371x_2 + 14.47x_1^2 - 12.021x_2^2 - 0.25x_1x_2 \quad (6\text{-}3)$$

The optimal conditions for cadmium derivatization are estimated by applying a non-linear constrained optimization. The optimal values are found to be (x_1 = -0.7751 & x_2 = -0.5013) 1.2 M HCl and 1.44 % m/v $NaBH_4$.
Further investigations explored the effect of $NaBH_4$ and HCl concentrations on the cadmium signal. An increase of $NaBH_4$ concentration up to 1.6% m/v increases the signal intensity while higher concentrations (2%) of $NaBH_4$ results in a decrease, (**Figure (6-11)**). In a similar pattern, increases in the value of HCl concentrations over 1.2 M leads to a decrease in the signal intensity, (**Figure (6-12)**).

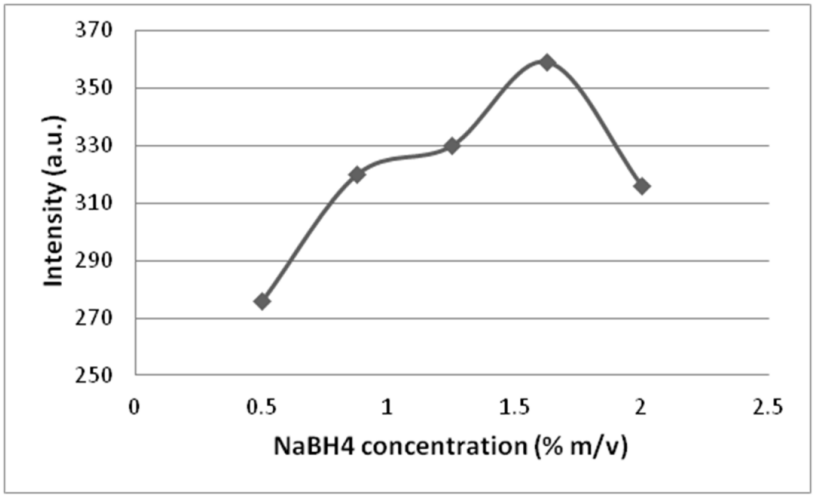

Figure 6-11 the recorded cadmium signals when applying different $NaBH_4$ concentrations;
The signals (rectified for hydrogen effect) recorded upon spiking 100 (µg/L) cadmium at several $NaBH_4$ concentrations while keeping constant HCl (1.2 M).

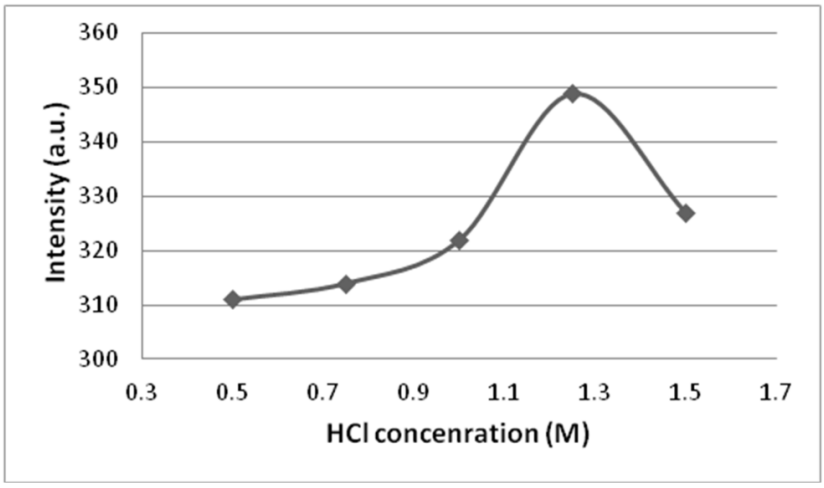

Figure 6-12 the recorded cadmium signals when applying different HCl concentrations;
The signals (rectified for hydrogen effect) recorded upon spiking 100 (µg/L) cadmium at several HCl concentrations while keeping constant $NaBH_4$ (1.5 % m/v).

The analytical figures of merit are estimated for the cadmium system by spiking a blank solution into the system and measuring the intensity. The blank experiments were repeated eight times and the standard deviation calculated. **Figure (6-13)** illustrates the calibration plot for different concentrations of cadmium.

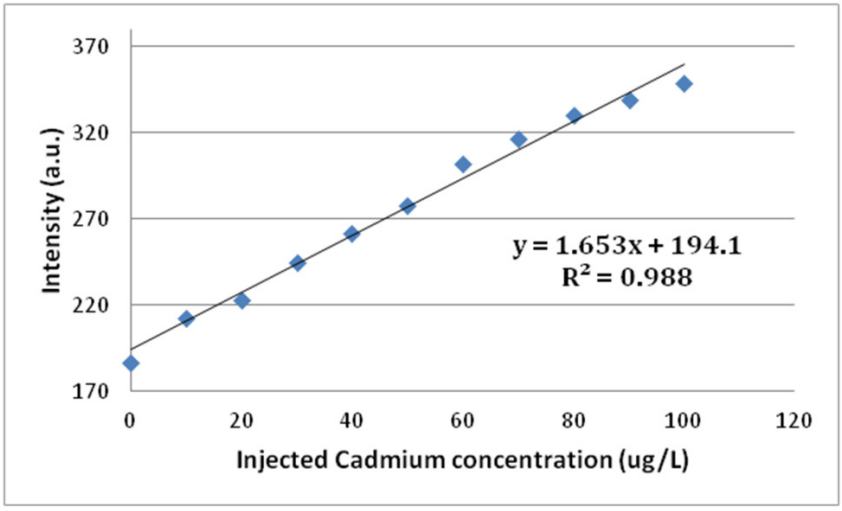

Figure 6-13 a calibration graph generated for cadmium;
The signals (rectified for hydrogen effect) recorded upon spiking several cadmium concentrations and applying 1.2 (M) HCl and 1.5% (m/v) $NaBH_4$.

The estimated figures of merit are 4.56 (µg/L) LOD and 1.37% RSD. The estimated LOD for cadmium is higher than the acceptable limit of cadmium in drinking water, (3 µg/L) shown in **Table (1-2)**; therefore an attempt was made to improve the detection limits by applying further assisting agents as described below.

Practically, the kinetics of cadmium vapour species generation is developed by applying supporting agents such as organized surfactants (e.g. didodecyldimethylammonium bromide (DDAB) vesicles) which is reported capable of creating a special microenvironment for reactions at the molecular level and altering the chemical equilibrium, the reaction rates and other important chemical features *(y Temprano et al., 1993)*. Sodium iodate ($NaIO_3$), applied in the work of *(Li et al., 2004)*, enhanced the efficiency of cadmium vapour species generation. $NaIO_3$ acts as a consumer for a part of the hydroborates present in the system, which results in lowering the hydrogen generation rate. Moreover, $NaIO_3$ assists the reaction between the generated cadmium hydride CdH_2 and ionic or atomic halogen to form stable and volatile multi halogen complexes of cadmium.

Thus, another experimental set was conducted to examine the effect of adding $NaIO_3$ to the cadmium sample. A solution of 5% m/v $NaIO_3$ was prepared by dissolving suitable amount of sodium iodate in distilled water. The selected concentration is based on the work of *(Li et al., 2004)* who reported a massive enhancement in detection limits

because of $NaIO_3$. **Figure (6-14)** shows an increase (10.5 – 16.5%) in the cadmium signal intensity upon adding 1 ml $NaIO_3$ to the sample.

The LOD with $NaIO_3$ is estimated to be 3.8 (µg/L), which is slightly higher than the accepted limit in drinking water; however, a lower detection limits is expected when using an optimized concentration of sodium iodate.

Other experiments were conducted to explore the combined effect of thioglycolic acid and sodium iodate. 100 µg/L Cd was stimulated by the addition of 0.5 ml each of TGA (1.25% m/v) and $NaIO_3$ (5% m/v). The increase in signal intensity is about 14%. This indicates that both agents react together without any side effects or interferences. This finding emphasizes the possibility of mixing two assisting agents which is essential for simultaneous detection of multi elements.

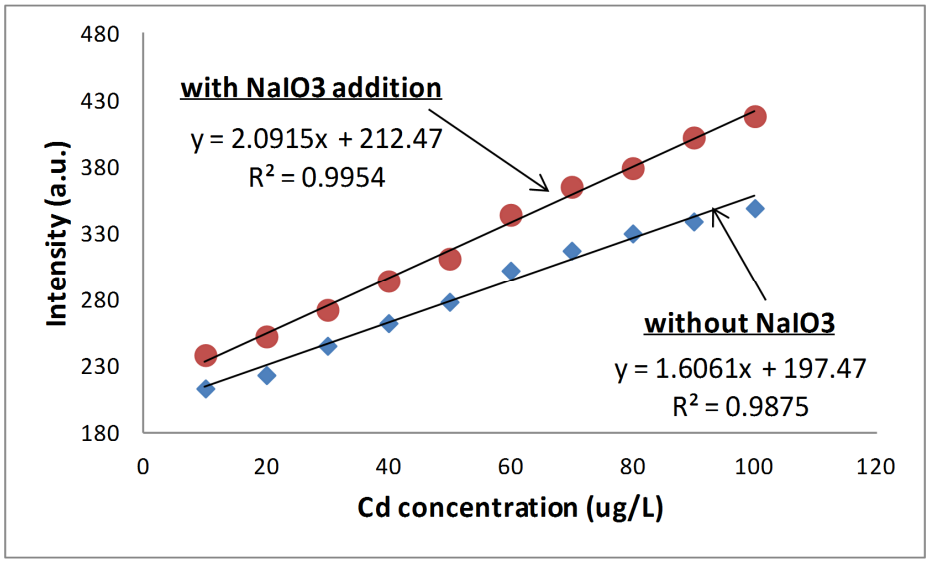

Figure 6-14 the recorded signals of cadmium with and without applying $NaIO_3$; The signals (rectified for hydrogen effect) recorded upon spiking several concentrations of cadmium while applying 1.2 (M) HCl and1.5% (m/v) $NaBH_4$

6.2.4 Lead determination

It is reported that the Lead hydride PbH_4 (Plumbane), is difficult to generate. Thus, Plumbane has been rarely studied due to the low yield and stability. PbH_4 is known to be generated from the (IV) oxidation state (i.e. Pb (IV)), therefore Lead that exists in a lower oxidation state (e.g. Pb (II)) must be oxidized before applying the reduction stage

to form the hydride. Many researchers report that Pb (II) can be oxidized by several oxidizing agents; potassium ferricyanide (K_3 Fe $(CN)_6$) being the most efficient.

The first step is to find the applicable wavelength for the standard solution. A Lead atomic absorption standard (1 g/L) was used to prepare the Lead standard and other working solutions using distilled water and stepwise dilution. The Lead emission lines are observed at 405.783 and 261.418 nm in the work of *(Heisterkamp and Adams, 1999)* and at 220.35 and 217.0 nm *(Chen et al., 1995)* and *(Rapsomanikis et al., 1986)* respectively.

In this study, only one emission line, in the range 220.31- 220.69 nm was observed; however, with low intensity. Accordingly, 5% m/v (K_3 Fe $(CN)_6$) was applied as an oxidizing agent to enhance the signal intensity. No information could be found in the literature regarding the reaction rate, therefore the oxidizing agent was added to the sample 15 minutes before applying the derivatization reaction to give enough time. Using the oxidizing agent resulted in 20% increase in the Lead signal intensity as well as the appearance of another signal at 217 nm, but with low intensity, which was not taken into consideration for Lead identification in later experiments. Based on the above results, the emission line in the range (220.31- 220.69 nm) has been adopted to identify Lead in all related experiments in this research.

An optimization study was conducted using an argon flow rate of 105 ml/min and applied power of 150 Watt throughout the experiments, while applying different $NaBH_4$ and HCl concentrations. The experimental plan is illustrated in **Table (6-7)**, in which 10 ml of acidified sample and reducing agent as well as 0.25 ml of the oxidizing agent (at 5% m/v) are applied in all the experiments.

The experimental system is represented by a multiple quadratic multivariable model and the following empirical model is generated to describe the Lead system with an estimated average absolute error of 0.88%.

$$Y = 280.47x_0 + 5.246x_1 + 28.855x_2 + 4.118x_1^2 + 9.86x_2^2 + 3.25x_1x_2 \quad (6\text{-}4)$$

The optimal conditions for Pb reduction are estimated by applying non-linear constrained optimization; the optimal coded values are found to be (x_1 = -0.5886 and x_2 = -0.7793) 1.15 M HCl and 1.54 % m/v $NaBH_4$ respectively.

In order to validate the estimated optimized values, a parallel study was conducted to investigate the effect of increasing $NaBH_4$ and HCl concentrations on the Lead signal intensity. The results are shown in **Figures (6-15)** and **(6-16)** and indicate that both parameters act positively to enhance the Lead signal intensity.

Table 6-7 the Lead experiments according to the 2nd order central composite rotatable design plan;
The table shows the recorded intensities (rectified for hydrogen effect) for 100 (µg/L) Lead observed in the range (220.31 – 220.69 nm)

Exp. No.	HCl (M)		$NaBH_4$ (% m/v)		Intensity
	Real Value	Code (x_1)	Real Value	Code (x_2)	(a.u.)
1	0.75	-1	0.875	-1	267
2	1.25	+1	0.875	-1	273
3	0.75	-1	1.625	+1	313
4	1.25	+1	1.625	+1	332
5	0.5	-1.414	1.25	0	281
6	1.5	+1.414	1.25	0	293
7	1	0	0.5	-1.414	254
8	1	0	2.0	+1.414	243
9	1	0	1.25	0	284
10	1	0	1.25	0	282
11	1	0	1.25	0	279
12	1	0	1.25	0	277
13	1	0	1.25	0	280

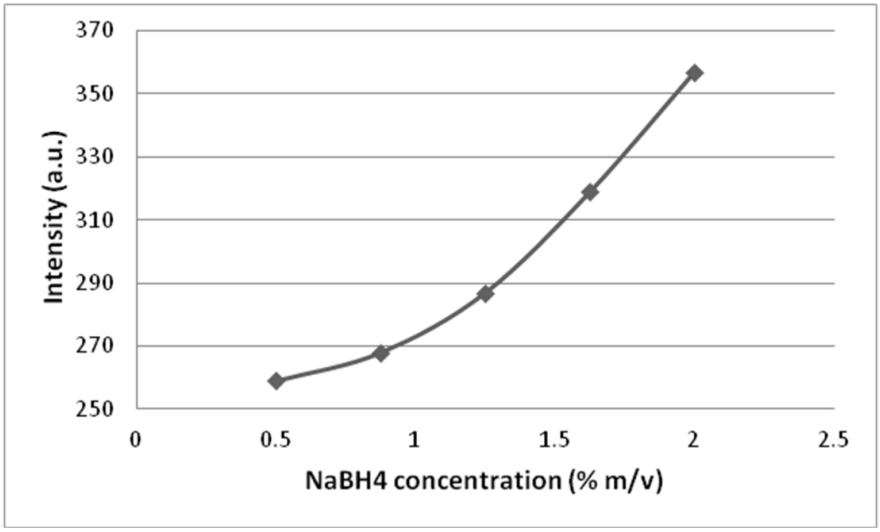

Figure 6-15 the recorded Lead signals when applying different $NaBH_4$ concentrations;
The signals (rectified for hydrogen effect) recorded upon spiking 100 (µg/L) Lead at several $NaBH_4$ concentrations while keeping constant HCl (1.15 M).

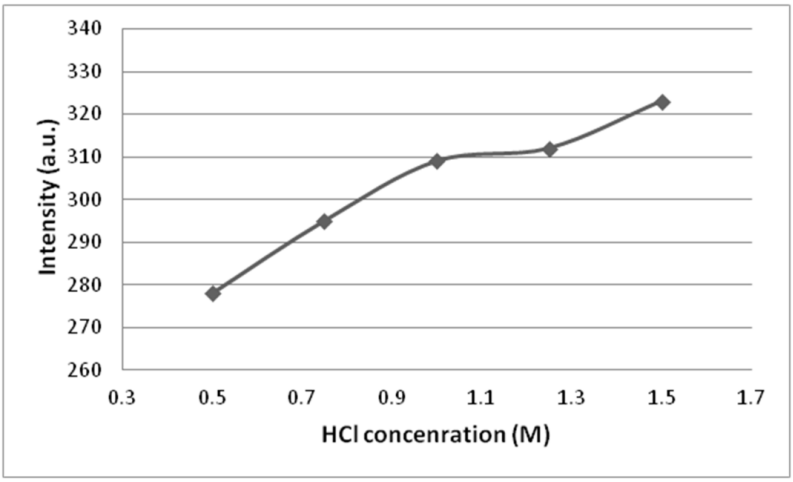

Figure 6-16 the recorded Lead signals when applying different HCl concentrations;
The signals (rectified for hydrogen effect) recorded upon spiking 100 (µg/L) Lead at several HCl concentrations while keeping constant $NaBH_4$ (1.54% m/v).

The analytical figures of merit were estimated for the Lead system by spiking a blank solution into the system and measuring the intensity. The experiments were repeated eight times and the standard deviation calculated. The calibration plot for different concentrations of Lead is shown in **Figure (6-17)**. The LOD and RSD for the Lead system are found to be 2.67 (µg/L) and 1.0 % respectively. In **Table (1-2)**, the accepted limit of Lead in drinking water is 10 (µg/L), which indicates a reasonable precision for inorganic Lead detection is achieved by using the proposed technology.

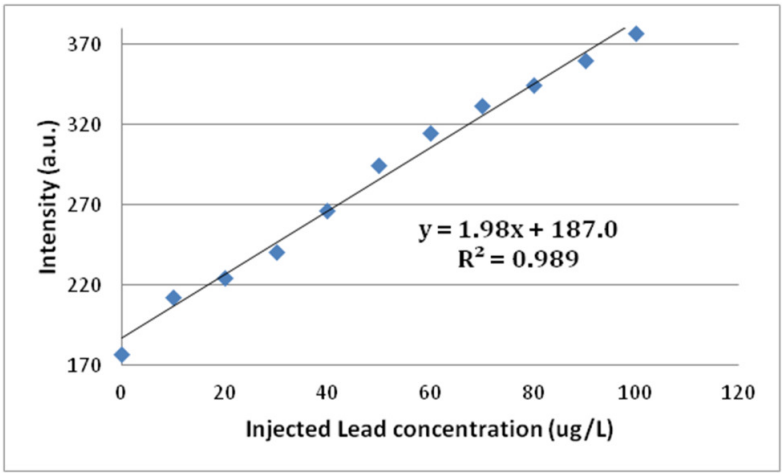

Figure 6-17 calibration graph generated for Lead;
The signals (rectified for hydrogen effect) recorded upon spiking several Lead concentrations and applying 1.15 (M) HCl and 1.54 % (m/v) $NaBH_4$

6.2.5 Determination of transition metals

A transition metal is defined as an element having atoms with an incomplete *D-sub-shell*. It is well known that analysis using the hydride generation technique suffers interferences due to the presence of transition metals in the examined sample. This interference is either after the transition metals are reduced to metals or after being converted to metal borides *(Sturgeon et al., 1996)*. In both cases this leads to scavenging of the analyte or effects on decomposition before phase separation. The effect from transition metals on suppressing the signal of the targeted analyte is more significant than that from other metals. For example, *(Pohl and Zyrnicki, 2001)* reported that a disturbance in the arsenic signal occurs due to cadmium interference if the Cd to As concentration ratio is higher than 100. The interferences can mislead spectrometric analysis especially when close spectral lines are used for discrimination (e.g. As (I) at 228.812 nm and Cd (I) at 228.802 nm).

This section is dedicated to the detection of some transition metals (Cr, Cu, Ni, and Zn) by applying the proposed system and using $NaBH_4$ as a reducing agent.

General derivatization conditions (0.8 M HCl, 2% m/v $NaBH_4$, 105 ml/min argon and 150 watt power) were applied to determine the emission lines applicable for the tested elements. Atomic absorption standards (1 g/L) of each (Cu, Ni, Zn, and Cr), purchased from Sigma Aldrich, were used to prepare standard solutions and working solutions using distilled water and stepwise dilution. The emission lines are shown in **Table (6-1)**. All signals appeared without using assisting chemicals; i.e. oxidizing or pre-reducing agents.

Further individual optimization studies were conducted to explore the effect of varying the concentrations of $NaBH_4$ and HCl on the signals. The parameters are examined in the ranges 0.5 to 1.5 M HCL and 0.5 to 2% m/v $NaBH_4$. The experimental plans, **Table (6-8)**, were designed according to a second order central composite rotatable design, in which a 100 (µg/L) of the examined analytes are spiked into acidified samples. 10 ml of both the acidified sample and the reducing agent were injected in all experiments.

Table 6-8 transition element experiments according to the 2nd order central composite rotatable design plan;
The table shows the recorded intensities (rectified for hydrogen effect) upon spiking 100 (µg/L) of each Cu, Ni, Zn, and Cr

Exp. No.	HCl (M)		$NaBH_4$ (% m/v)		Recorded intensities (a.u.) for the exam. analytes			
	Real Value	Code (x_1)	Real Value	Code (x_2)	Cu	Ni	Zn	Cr
1	0.75	-1	0.875	-1	385	314	304	319
2	1.25	+1	0.875	-1	397	327	325	332
3	0.75	-1	1.625	+1	427	364	372	394
4	1.25	+1	1.625	+1	442	388	398	419
5	0.5	-1.414	1.25	0	403	329	348	373
6	1.5	+1.414	1.25	0	413	338	362	388
7	1	0	0.5	-1.414	367	296	286	297
8	1	0	2.0	+1.414	431	368	377	407
9	1	0	1.25	0	422	319	325	348
10	1	0	1.25	0	426	322	321	345
11	1	0	1.25	0	421	326	318	352
12	1	0	1.25	0	427	315	323	341
13	1	0	1.25	0	423	320	320	343

The experimental systems are represented by quadratic multivariable models. The following empirical models are generated for the examined systems (Cu, Ni, Zn, and Cr respectively). The average absolute errors of the models are estimated to be 0.89 %, 1.73 %, 0.94 %, and 0.72 % for Cu, Ni, Zn, and Cr respectively.

$$Y = 423.897x_0 + 5.142x_1 + 22.187x_2 - 5.667x_1^2 - 10.166x_2^2 + 0.75x_1x_2 \quad (6\text{-}5)$$

$$Y = 320.480x_0 + 6.215x_1 + 26.601x_2 + 10.359x_1^2 + 9.609x_2^2 + 2.75x_1x_2 \quad (6\text{-}6)$$

$$Y = 321.482x_0 + 8.349x_1 + 33.709x_2 + 18.355x_1^2 + 6.609x_2^2 + 1.25x_1x_2 \quad (6\text{-}7)$$

$$Y = 345.888x_0 + 7.401x_1 + 39.692x_2 + 17.213x_1^2 + 2.967x_2^2 + 3.0x_1x_2 \quad (6\text{-}8)$$

The optimal derivatization parameters of the examined systems were estimated statistically to be in the range 1.21 – 1.39 M HCl and 1.47 – 1.71% m/v $NaBH_4$. Hence,

1.25 M HCl and 1.625% m/v $NaBH_4$ were selected to calculate the analytical figures of merit. The procedure was accomplished by spiking a blank solution into the system and measuring the intensity. The blank experiments were repeated eight times and the standard deviation calculated.

The following equations are obtained for the calibration plots of the examined analytes (Cu, Ni, Zn, Cr) respectively:

$$Y = 2.642\,x + 209.9,\ R^2 = 0.937 \quad (6\text{-}9)$$

$$Y = 1.948\,x + 190.9,\ R^2 = 0.995 \quad (6\text{-}10)$$

$$Y = 2.052\,x + 191.7,\ R^2 = 0.994 \quad (6\text{-}11)$$

$$Y = 2.242\,x + 195.5,\ R^2 = 0.993 \quad (6\text{-}12)$$

The estimated coefficient of determination (R^2) for copper is found to be slightly lower than the other transition metals. The reason could be a slight deviation from linearity after injecting 70 µg/L.

The figures of merit are 3.03 µg/L LOD and 1.55% RSD for copper, 6.04 µg/L LOD and 2.19% RSD for nickel, 4.08 µg/L LOD and 1.54% RSD for zinc, as well as 6.02 µg/L LOD and 2.52% RSD for chromium. According to the standard acceptable limits in drinking water, shown in **Table (1-2)**, the estimated detection limits for all the examined transition metals indicate very reasonable precision is achieved by using the proposed technology.

Figures (6-18) and **(6-19)** show the recorded signals with different concentrations of HCl and $NaBH_4$. The results show that all transition metals are positively affected by increasing the reducing agent concentration up to 1.625% m/v. Further increases lead to a reduction in signal intensity, probably because of larger amounts of hydrogen generated in the system and the accompanying alkaline mist. On the other hand, signal intensities increased with increasing acidity of the sample even when using the top value in the range (1.5 M HCl).

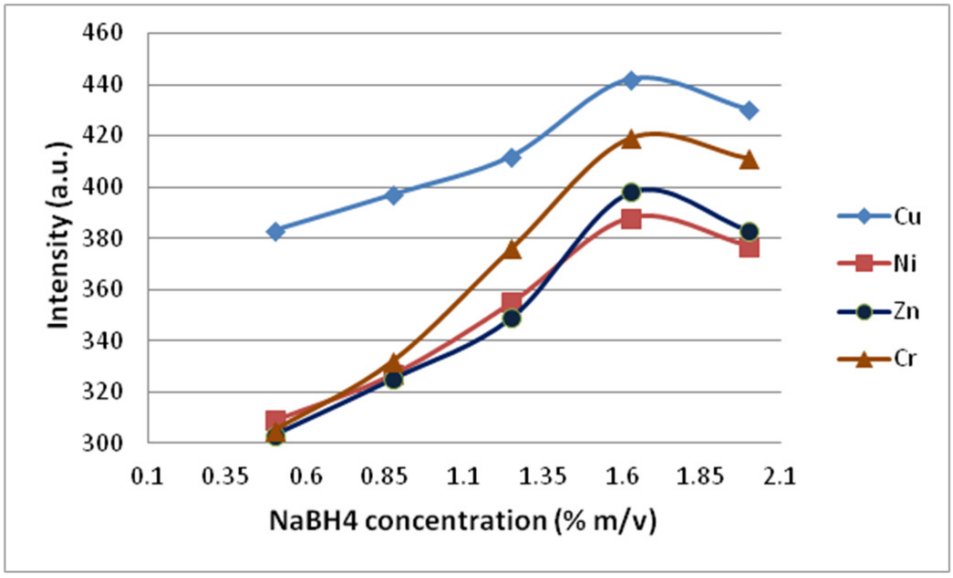

Figure 6-18 the recorded signals for the examined transition metals when applying different $NaBH_4$ concentrations;
The signals (rectified for hydrogen effect) recorded upon spiking 100 (µg/L) of each of the examined elements at several $NaBH_4$ concentrations while keeping constant HCl concentration (1.25 M).

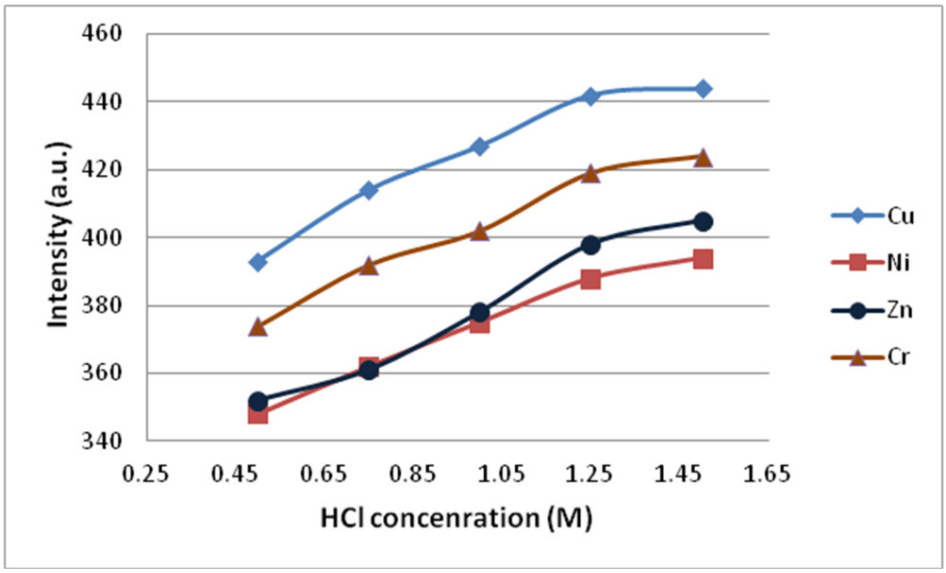

Figure 6-19 the recorded signals for transition metals when applying different HCl concentrations;
The signals (rectified for hydrogen effect) recorded upon spiking 100 (µg/L) of each of the examined elements at several HCl concentrations while keeping constant $NaBH_4$ concentration (1.625% m/v).

Further experimental investigations were conducted to explore interference effects of transition metals on other elements. Separate experiments were conducted for each of

the examined analytes. A mixture of the transition metals (Cu, Ni, Zn, and Cr), (200 µg/L of each), was spiked with 100 (µg/L) of each of the tested elements (Hg, As, Sn, Cd, and Pb). A solution was prepared by adding (1ml) of this mixture to (5 ml) acidified solution (1.25 M HCl) followed by the addition of extra distilled water to form a 10 (ml) solution. The prepared solutions were injected in individual experiments with 10 (ml) of reducing agent (1.625% m/v $NaBH_4$) and the signals monitored.

The results of all examined elements (Hg, As, Sn, Cd, and Pb), (**Figure (6-20)**), show no more than 5% signal suppression due to interferences from the transition metals. This indicates the possibility of conducting simultaneous detection without significant disturbances.

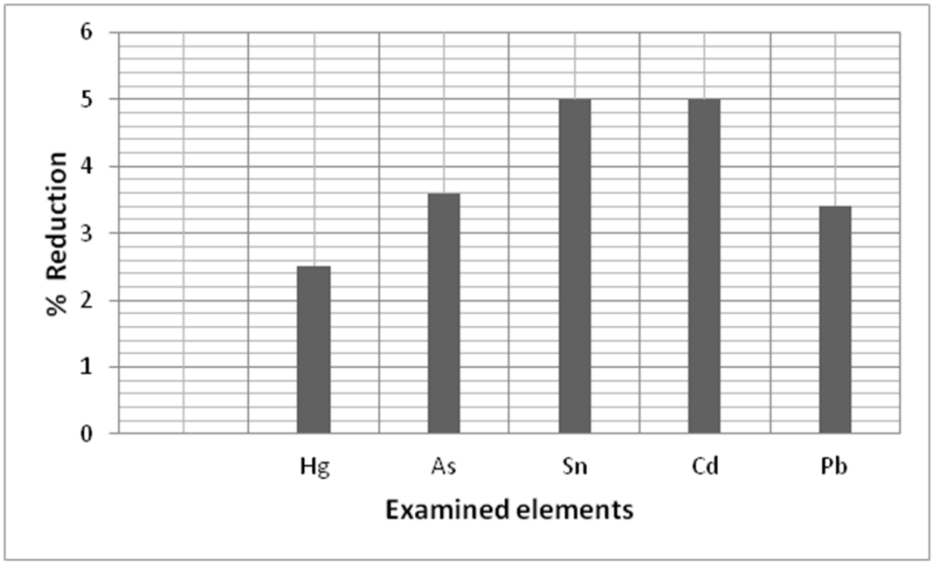

Figure 6-20 the effect of interferences from transition metals on the recorded signals of the hydride forming elements;
The signals are recorded upon spiking 100 (µg/L) of the examined element into the transition metal mixture and applying 1.625% m/v $NaBH_4$ and 1.25 M HCl.

6.3 The simultaneous detection of multi heavy metals

This section is dedicated to investigate the simultaneous detection of the examined group of heavy metals. The aim is to find the optimal derivatization conditions for the highest signals intensities. Particularly, the efficiency of the chemical vapour generation (CVG) process is reported to be very sensitive to variations in experimental conditions. *(Matoušek, 2007)* reported a 1% change in experimental conditions could lead to a 10% change in signal intensity if the CVG efficiency does not exceed 10%. According to

this, the chemical vapour generation process for a mixture containing multi heavy metals is expected to be a non-uniform process, which requires a lot of care to decide the optimal conditions. Although the general derivatization conditions (0.8 M HCl and 2.0% m/v $NaBH_4$) produces signals for all the examined elements; the intensities vary. Hence, it is important to match optimal derivatization conditions to the individual studies for each examined element. **Table (6-9)** shows the optimal values for the reduction of the examined elements, at an argon flow rate at 105 ml/min and power of 150 Watt.

Table 6-9 summary of the optimal derivatization conditions – individual studies

Examined element	Wavelength (nm)	HCl (M)	$NaBH_4$(% m/v)
Hg	253.58	0.12	0.4
As	228.65-229.03	1.3	1.5
Sn	326.03-326.40	1.3	1.5
Cd	226.38-226.76	1.2	1.44
Pb	220.31-220.69	1.15	1.54
Cu	324.55-324.92	1.28	1.46
Ni	231.30-231.68	1.39	1.54
Zn	213.86	1.22	1.71
Cr	267.49-267.87	1.25	1.63

Preliminary experiments for detecting the elements simultaneously were conducted for a mixture of three elements (cadmium, copper, and tin), selected because of various derivatization conditions, **Table (6-9)**, and to examine the possibility of detecting two hydride forming elements in presence of a transition element. The elements were examined at three levels (100, 50, 10 µg/L) using pre-reducing agents (0.25 ml TGA, and 0.25 ml $NaIO_3$) and applying 1.2 M HCl and 1.5% m/v $NaBH_4$. The recorded signal to background (i.e. the signal due to the hydrogen magnification) ratios are shown in **Figure (6-21)**.

Practically, the simultaneous detection of the full group of nine elements is not an easy task due to the difficulty of selecting the optimum derivatization conditions that covers the ranges (0.12 – 1.39 M HCl and 0.4 – 1.71% m/v $NaBH_4$). Hence, another experimental plan was applied according to the details shown in **Table (6-10)**. The examined samples in all experiments consisted of a mixture of nine analytes, (100 µg/L of each). The data set composed 13 experiments and for each the signal to the

background (i.e. the signal due to the hydrogen effect) ratio (SBR) for all analytes was determined.

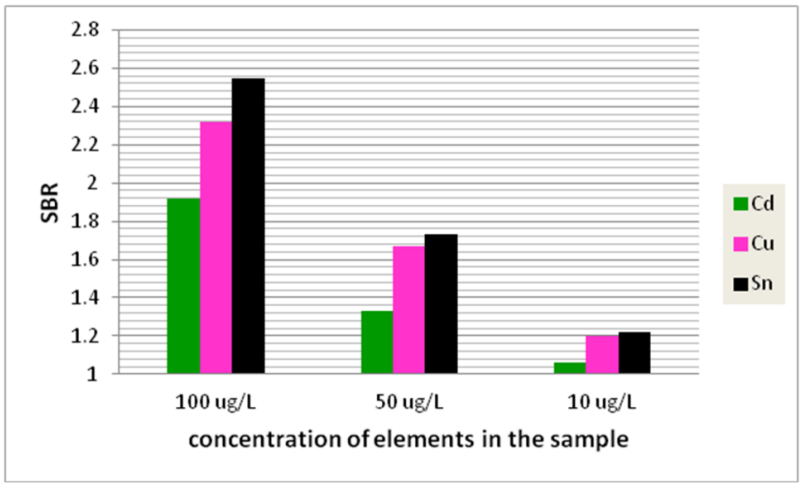

Figure 6-21 the recorded signal to the background ratio for three analytes examined simultaneously;
Different concentrations of the examined analytes (Cd, Cu, and Sn) were examined by applying 1.2 M HCl and 1.5% m/v $NaBH_4$

Although clear signals were recorded for all the examined analytes, no clear interpretation can be drawn due to large variations in the recorded intensities. Thus, a principal component analysis (PCA) technique, **Appendix 11.9**, was applied in order to classify the responses of the analytes with changes in the derivatization conditions.
The results of the PCA analysis (**Figure (6-22)**) indicate two groups and an outlier (Hg).

(A)

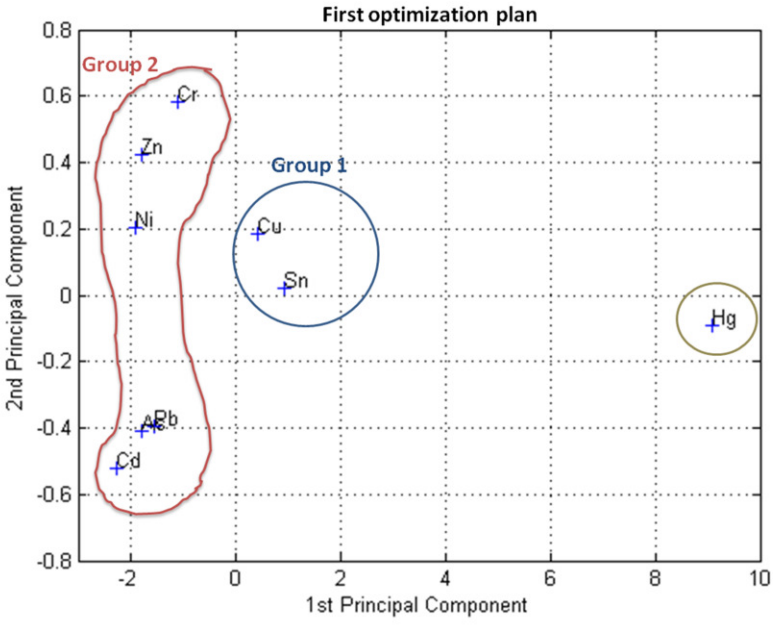

(B)

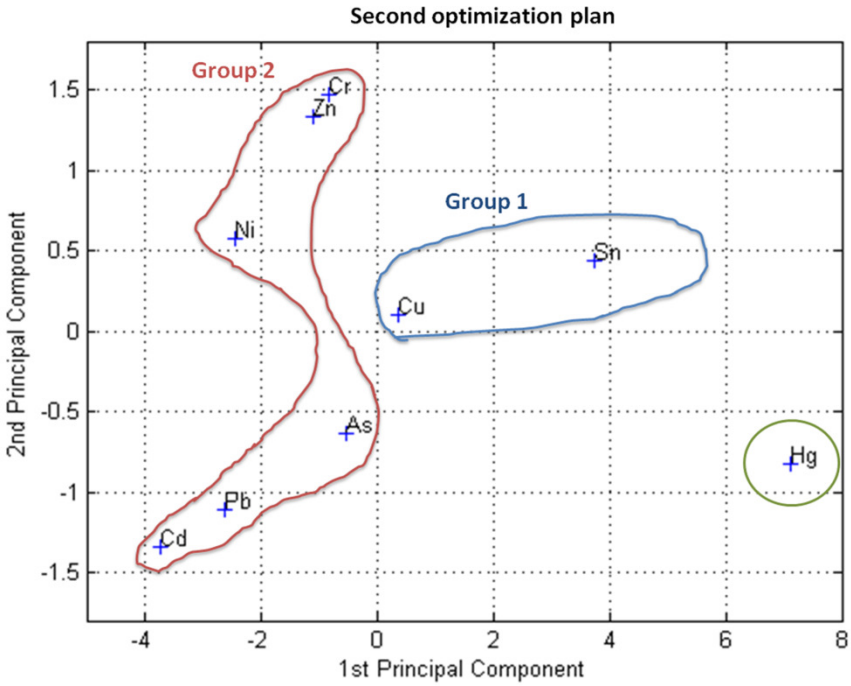

Figure 6-22 the loading plots produced upon applying PCA analysis;
(A) is the loading plot obtained upon applying the plan shown in **Table (6-10)**, (B) is the loading plot obtained upon applying the plan shown in **Table (6-11)**

PCA1 (an eigenvector with highest eigenvalue) was selected to compare the results from this analysis because it represents more than 90% of the total variance. It can be observed in **Figure (6-22/A)** that the responses of group 2 highly correlates to changes in the derivatizations conditions with respect to PCA1 values lower than zero. It is also clear that the analytes in group 1 are correlated with regard to PCA1 values greater than zero.

Although sensible correlations and small differences between the scores of group 1 and 2 are observed, the score of the outlier (Hg) is uncorrelated to the groups. Hence, the tested experimental ranges are concluded to be invalid to cover the examined elements for simultaneous detection.

Better performance of the system can be achieved if the differences in the scores of all examined elements are lower. Therefore another experimental plan with compressed ranges, (1 – 1.4 M HCl and 1.2 – 1.7% m/v $NaBH_4$), was performed. The plan with the recorded SBR is illustrated in **Table (6-11)**, while the loading plot is shown in **Figure (6-22/B)**.

Table 6-10 the simultaneous detection of nine elements injected at 100 µg/L – the first optimization plan

Exp. No.	HCl		$NaBH_4$		SBR								
	Real value (M)	Code value (x_1)	Real value (% m/v)	Code value (x_2)	Hg	As	Sn	Cd	Pb	Cu	Ni	Zn	Cr
1	0.44	-1	0.73	-1	3.956	1.810	2.378	1.745	1.854	2.081	1.697	1.643	1.724
2	1.1	+1	0.73	-1	4.048	1.837	2.410	1.767	1.875	2.145	1.767	1.756	1.794
3	0.44	-1	1.4	+1	3.632	1.875	2.454	1.789	1.897	2.308	1.967	2.010	2.129
4	1.1	+1	1.4	+1	3.745	1.935	2.518	1.816	1.929	2.389	2.097	2.151	2.264
5	0.12	-1.414	1.05	0	4.140	1.816	2.291	1.670	1.854	2.178	1.778	1.881	2.016
6	1.39	+1.414	1.05	0	3.972	1.875	2.475	1.762	1.875	2.232	1.827	1.956	2.097
7	0.75	0	0.4	-1.414	4.102	1.816	2.162	1.713	1.843	1.983	1.600	1.545	1.605
8	0.75	0	1.71	+1.414	3.572	1.805	2.216	1.691	1.864	2.329	1.989	2.037	2.200
9	0.75	0	1.05	0	4.010	1.827	2.270	1.751	1.875	2.281	1.724	1.756	1.881
10	0.75	0	1.05	0	3.935	1.848	2.302	1.735	1.864	2.302	1.740	1.735	1.864
11	0.75	0	1.05	0	3.989	1.859	2.259	1.756	1.875	2.275	1.762	1.718	1.902
12	0.75	0	1.05	0	3.913	1.816	2.313	1.713	1.886	2.308	1.702	1.745	1.843
13	0.75	0	1.05	0	3.951	1.827	2.281	1.745	1.864	2.286	1.729	1.729	1.854

Table 6-11 the simultaneous detection of nine elements injected at 100 µg/L – the second optimization plan

Exp. No.	HCl		$NaBH_4$		SBR								
	Real value (M)	Code value (x_1)	Real value (% m/v)	Code value (x_2)	Hg	As	Sn	Cd	Pb	Cu	Ni	Zn	Cr
1	1.1	-1	1.33	-1	2.661	2.171	2.640	1.930	2.005	2.122	1.917	1.939	1.931
2	1.3	+1	1.33	-1	2.725	2.206	2.676	1.950	2.028	2.188	1.997	2.072	2.009
3	1.1	-1	1.6	+1	2.445	2.253	2.724	1.979	2.050	2.354	2.223	2.372	2.385
4	1.3	+1	1.6	+1	2.521	2.323	2.796	2.012	2.084	2.436	2.369	2.538	2.536
5	1.0	-1.414	1.46	0	2.790	2.183	2.544	1.847	2.005	2.221	2.009	2.219	2.258
6	1.4	+1.414	1.46	0	2.640	2.253	2.748	1.946	2.028	2.277	2.064	2.308	2.348
7	1.2	0	1.2	-1.414	2.760	2.183	2.400	1.897	1.994	2.023	1.808	1.824	1.798
8	1.2	0	1.71	+1.414	2.400	2.171	2.460	1.872	2.016	2.376	2.247	2.404	2.464
9	1.2	0	1.46	0	2.700	2.195	2.520	1.938	2.028	2.326	1.948	2.072	2.106
10	1.2	0	1.46	0	2.640	2.218	2.556	1.921	2.016	2.348	1.966	2.047	2.088
11	1.2	0	1.46	0	2.680	2.230	2.508	1.946	2.028	2.321	1.991	2.028	2.131
12	1.2	0	1.46	0	2.630	2.183	2.568	1.897	2.039	2.354	1.924	2.060	2.064
13	1.2	0	1.46	0	2.661	2.195	2.532	1.930	2.016	2.332	1.954	2.040	2.076

The (Hg) score in the second optimization plan is 20% lower, whilst As and Sn increased by the same percentage (20%). Other analytes show lower responses to the modified optimization plan.

In conclusion, the second optimization plan, conducted with compressed experimental ranges, resulted in higher SBR for all analytes except Hg; nonetheless, the system performance becomes better as a general outcome.

When detecting nine elements simultaneously, the recorded SBR for some elements reduces to significant levels. This is obvious when applying low concentrations of the examined elements, and could be attributed to interferences leading to masking the signal from some elements. **Figure (6-23)** illustrates the recorded SBR for nine elements examined at three levels (100, 50, and 10 µg/L).

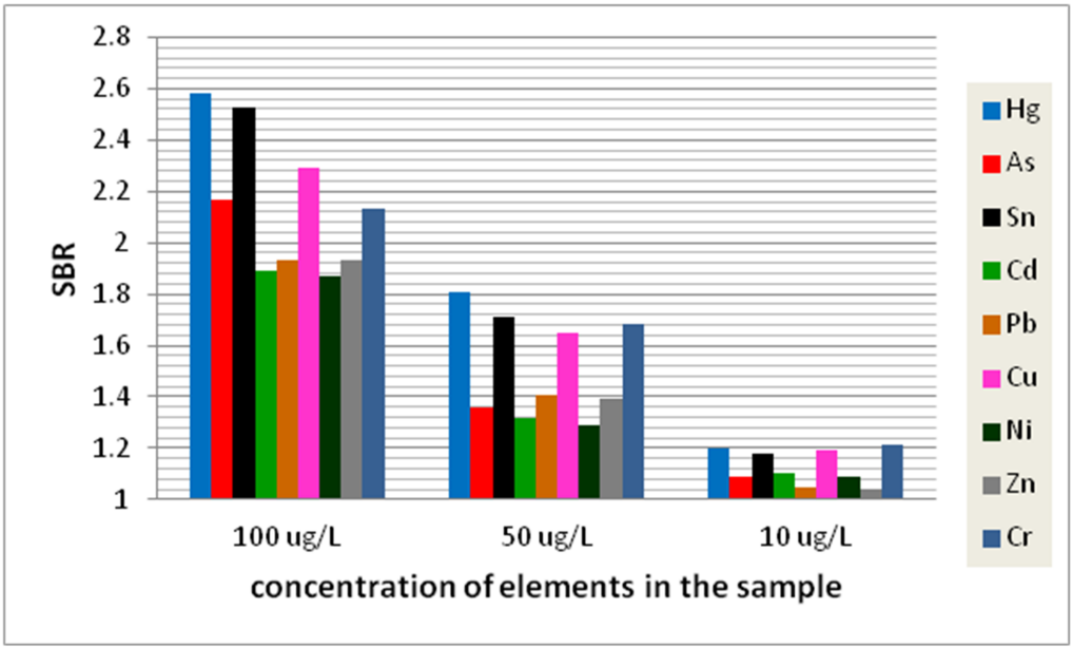

Figure 6-23 the signal to background ratios (SBR) recorded for nine elements examined simultaneously;
The elements examined at three concentration levels by applying (1.2 M HCl) and (1.46 % m/v $NaBH_4$)

Figure (6-24) shows a strip chart of the nine elements detected simultaneously at 10 (µg/L) with aid of oxidizing and pre-reducing agents (a mixture composed 0f 0.25 ml of $K_3Fe(CN)_6$, 0.25 ml TGA, and 0.25 ml $NaIO_3$).

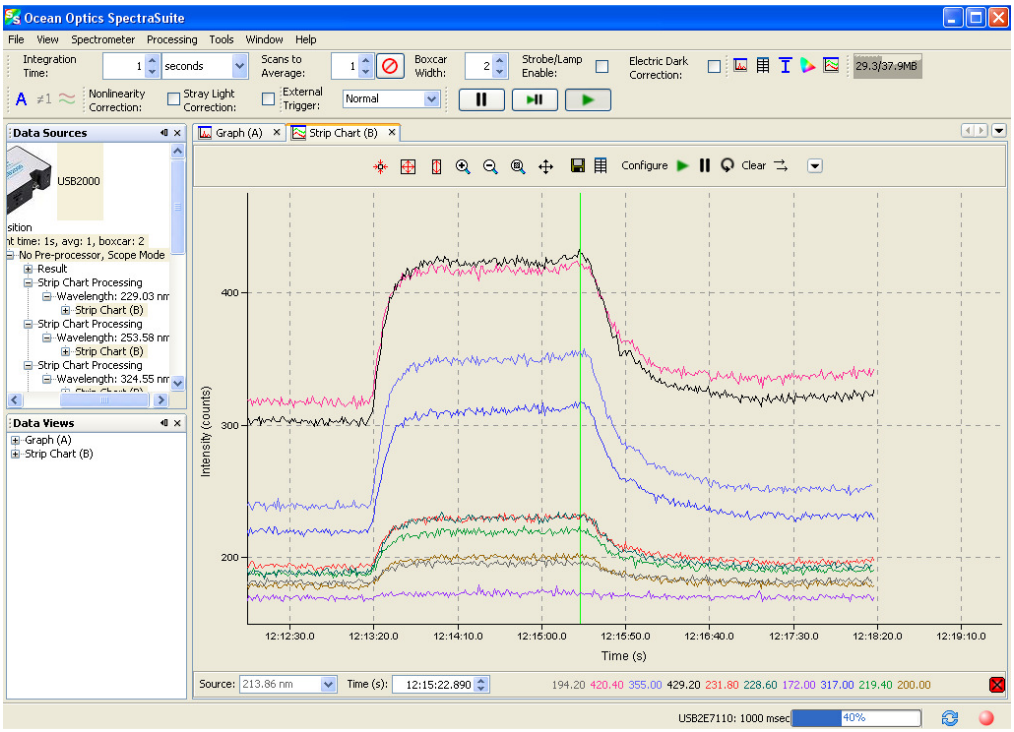

Figure 6-24 a strip chart for nine elements examined simultaneously;
The elements were injected at 10 (µg/L) and reduced by applying (1.2 M HCl) and (1.46 % m/v $NaBH_4$); from the top: black, Sn; pink, Cu; blue, Cr; dark blue, Hg; red, As; olive, Ni; green, Cd; brown, Pb; grey, Zn; violet, reference line

6.4 The quantitative determination of some heavy metals

The aim of this section is to determine some of the examined metals quantitatively via the absorption spectrometry technique. A conclusion drawn from the simulation results (**Section (3.6.2)**) is that there is no necessity to apply the full spectral length (8 cm) especially when recombination reactions could occur and lead to a reduction in the signal intensity. Hence, a new miniaturized DBD atomizer, illustrated in **Figure (6-25)**, was designed and fabricated with the same basis but with a 2 cm length for the electrode overlapping section and a shorter spectral path length (3.5 cm) to conduct quantitative determination of selected elements. In order to conduct multi element quantitative determination, the application of a general light source in the range of UV/Visible region is more practical for miniaturization purposes compared to using a hollow cathode light source for each element. As a first try, a deuterium light source (D2-World precision company) with a spectral range (185-400 nm) was tested in the new miniaturized DBD chip.

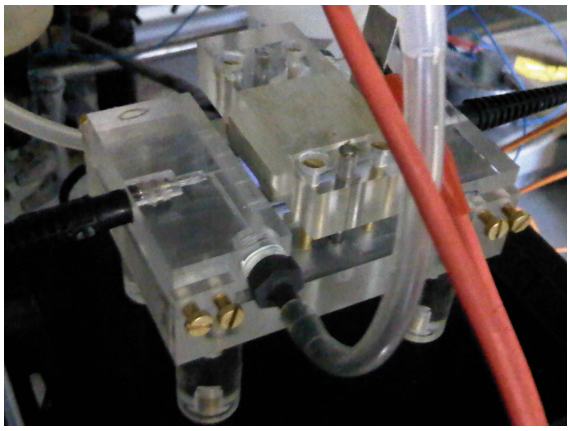

Figure 6-25 a picture shows the miniaturized DBD chip (spectral path length = 3.5 cm)

Even with 3.5 cm spectral path length, the light source intensity was found to be insufficient. It was observed that reduction occurs especially in the UV region, as illustrated in **Figure (6-26)**. This indicates that the D2 light source is not appropriate. A high power UV/visible light source (model number L10290, Hamamatsu photonics K. K. – Japan) with a spectral range 200 – 1600 nm was tested in the new chip. It can be observed in **Figure (6-27)** that the light intensity increased considerably in the region > 300 nm when applying only 100 msec integration time. Although a lower intensity is observed in the region < 300 nm, it was concluded that the high power light source is suitable for the quantitative analysis since the integration time is set at 700 msec, as concluded in **Section (4.4.2)**.

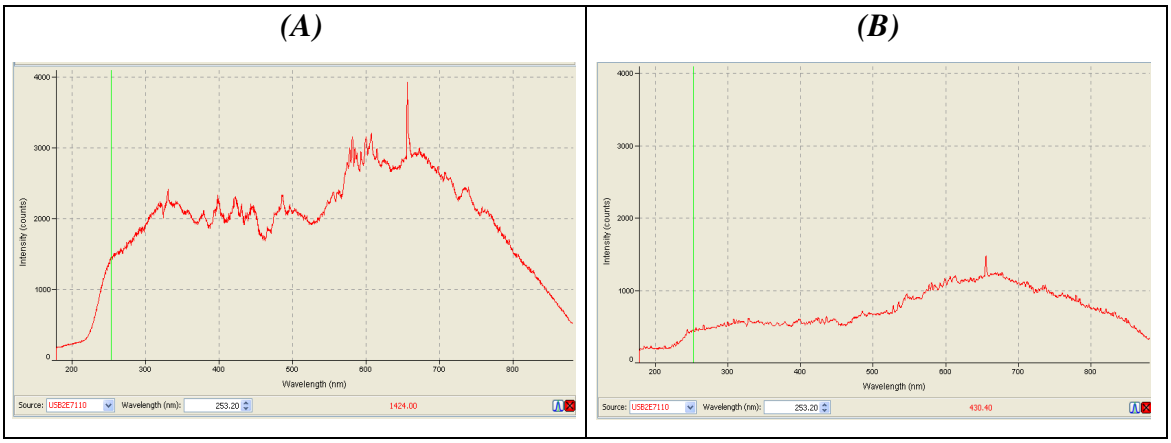

Figure 6-26 the recorded spectrum of D2 light source before and after passing the atomization channel;
(A) the spectrum recorded at zero path length with 310 msec integration time and zero Boxcar width, (B) the spectrum recorded at the end of the atomization channel (path length = 3.5 cm) with 5000 msec integration time and a value of 2 for the Boxcar width.

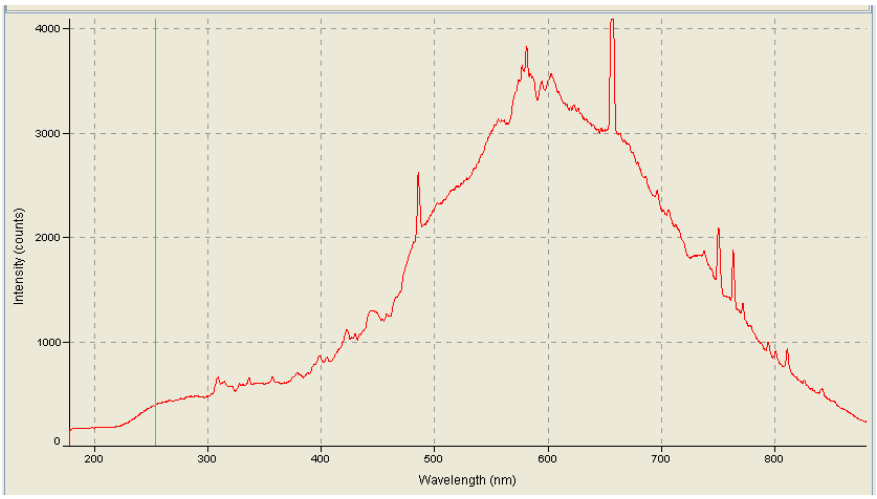

Figure 6-27 the spectrum recorded when applying a high power UV/visible light source through the spectral path in the new DBD atomizer;
It should be noted that only the deuterium lamp is switched on and the applied integration time was 100 msec.

Preliminary experiments, were conducted with the new DBD atomizer to characterize the recorded spectrum and to check whether the performance is similar to the previous DBD atomizer. Similar derivatization conditions (1.2 M HCl and 1.46 % m/v $NaBH_4$) were adopted. The recorded signals are shown in **Figure (6-28)**.

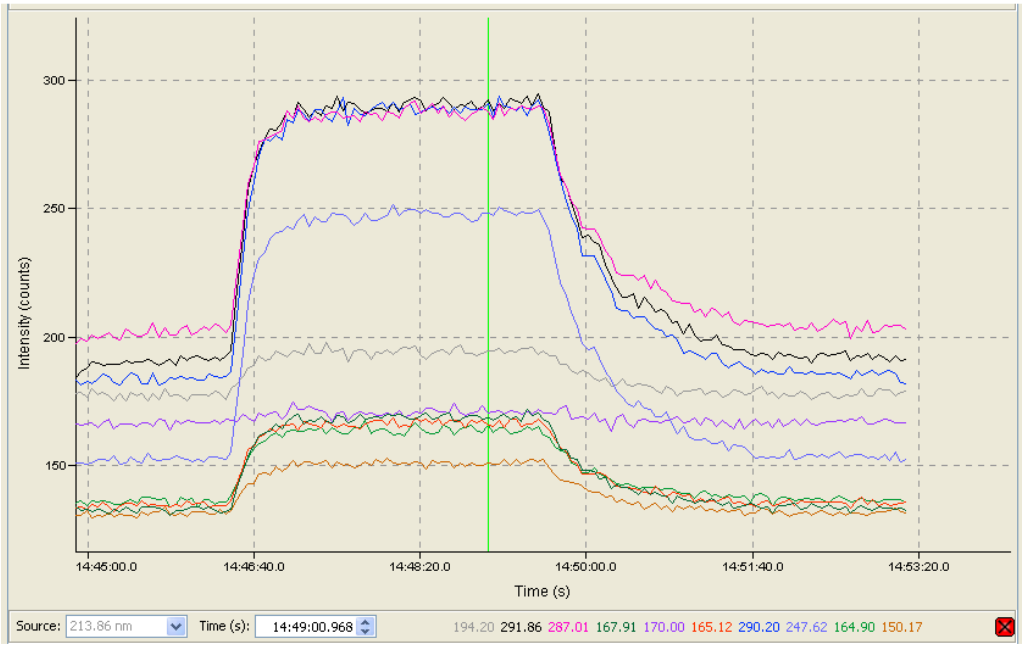

Figure 6-28 a strip chart recorded for nine elements examined simultaneously in the miniaturized DBD chip with 3.5 cm spectral path length;
The elements injected at 10 (µg/L) and examined by applying (1.2 M HCl) and (1.46 % m/v $NaBH_4$); from the top: pink, Cu; black, Sn; dark blue, Hg; blue, Cr; grey, Zn; violet, reference; olive, Ni; red, As; green, Cd; brown, Pb

As can be observed in **Figures (6-24)** and **(6-28)**, slight changes in the signal intensities are recorded for some elements in the new chip. The shorter atomization channel and spectral path length of the new chip probably eliminates or reduces the opportunity for recombination reactions; and the signals are produced with slight increases in intensity. This result is compatible with **Section (3.6.2)**.

The higher signal intensity may lead to better discrimination between signals when conducting quantitative analysis. Accordingly, all the experiments in this section and later experiments undertaken in this research were conducted using the new miniaturized DBD atomizer.

The molecular absorption coefficient was re-assessed for the elements tested by the miniaturized new chip. The first experiment was conducted by injecting 100 (µg/L) Hg (II) through the hydroborate scheme. The absorbance is 0.588, as shown in **Figure (6-29).**

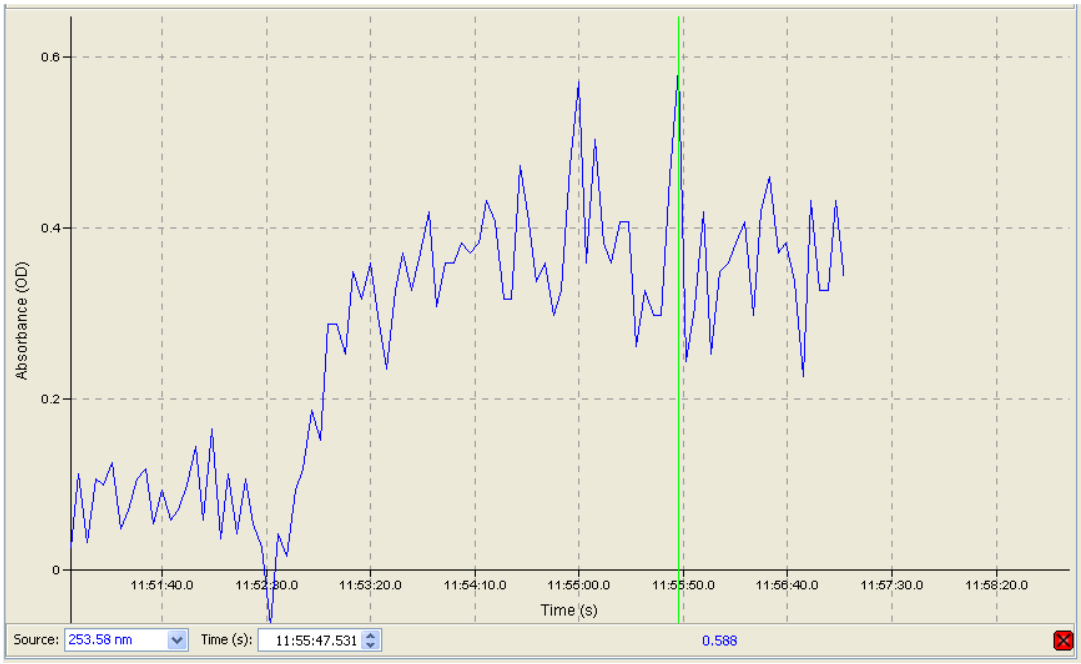

Figure 6-29 a strip chart shows the recorded absorbance for mercury sample;
A water sample containing 100 (µg/L) Hg (II) is reduced by applying 0.12 M HCl, 0.4 % m/v $NaBH_4$ and examined using the miniaturized DBD atomizer/Hollow cathode mercury light source.

The linear dependency obtained in **Figure (6-30)** enables the estimation of the molar absorption coefficient from the slope ($\varepsilon \times l$), and is found equal to 28.5×10^4 L/mol/cm.

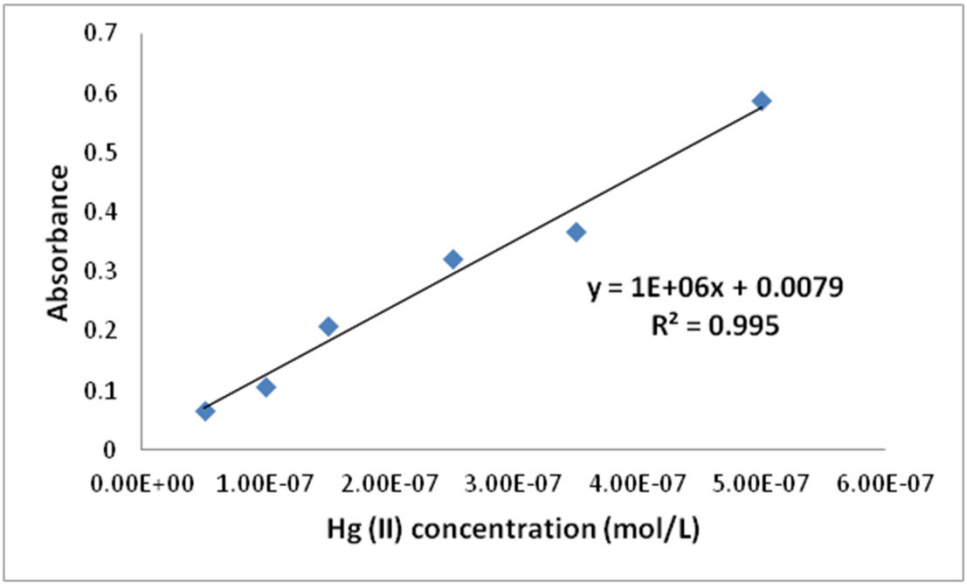

Figure 6-30 measured absorbance corresponding to the injected Hg (II) concentrations; The samples were examined by using the miniaturized new DBD atomizer (3.5 cm spectral path length) and applying 0.12 M HCl, 0.4 % m/v $NaBH_4$ for mercury reduction.

The developed system was used to conduct quantitative determination of As, Sn, and Cu individually by applying HG scheme and utilizing the high power UV/visible light source. These elements were selected as they include hydride forming elements as well as a transition element. Due to the existence of a considerable amount of hydrogen and alkaline mist in the system as well as the nature of the light source, a negative absorbance was produced, which is found to be anomalous. The reason is the criteria applied through SpectraSuite software, represented by equation (5-12) - **Section (5.5)**. As previously described, the hydrogen magnifies the signal into values larger than the reference. In consequence, a negative sign is produced for the estimated absorbance; however, if the negative sign in equation (5-12) is removed then a positive absorbance should be produced.

Following the same procedures applied for the qualitative analysis, the absorbance for the examined analyte was determined in two steps. In the first step, an acidified water sample, spiked with the examined analyte is injected, whereas only acidified water (with no analyte) is injected in the second step, or vice versa. The aforementioned steps are conducted in parallel with injection of a $NaBH_4$ stream. The difference between the recorded absorbance is proportional to the examined analyte. The recorded signals are stored as data files to conduct data analysis. The absorbance of 10 µg/L arsenic is 0.013 as illustrated in **Figure (6-31)**.

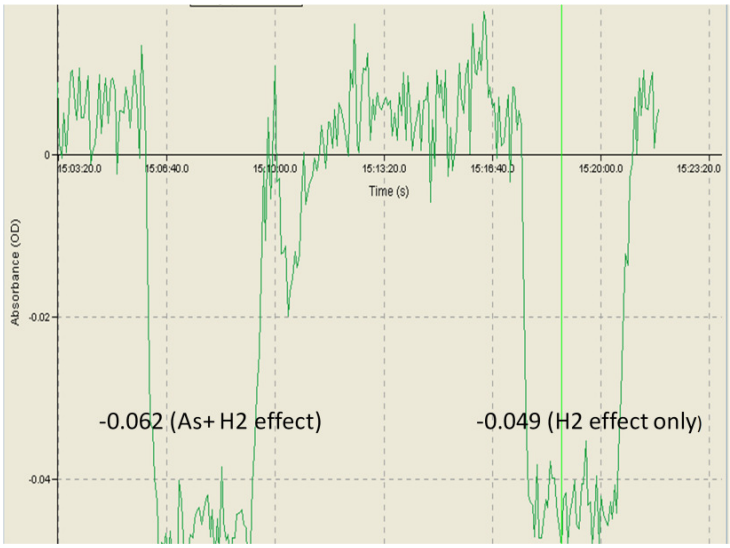

Figure 6-31 a strip chart recorded for the arsenic absorbance signal;
The signal recorded upon injecting 10 µg/L arsenic at 1.3 M HCl and 1.5% m/v $NaBH_4$. The difference between the recorded signals (0.013) is proportional to the amount of analyte injected.

Calibration graphs for the analytes are produced by conducting the same experimental procedures described earlier for mercury determination. The graphs are shown in **Figure (6-32)**, and accordingly the molar absorption coefficients are estimated to be 5.9 $\times 10^4$, 18.9 $\times 10^4$, and 9.8 $\times 10^4$ (L/mol/cm) for As, Sn, and Cu respectively.

The measured concentrations through the examined system are compared with the real injected values; hence, the average absolute error of the estimate is found to be 11.81%, 9.51%, and 10.38 % for As, Sn, and Cu respectively. The estimated errors are in the same order as that determined for the Hg (II) system, and can be attributed to the accuracy of the step wise dilution procedures.

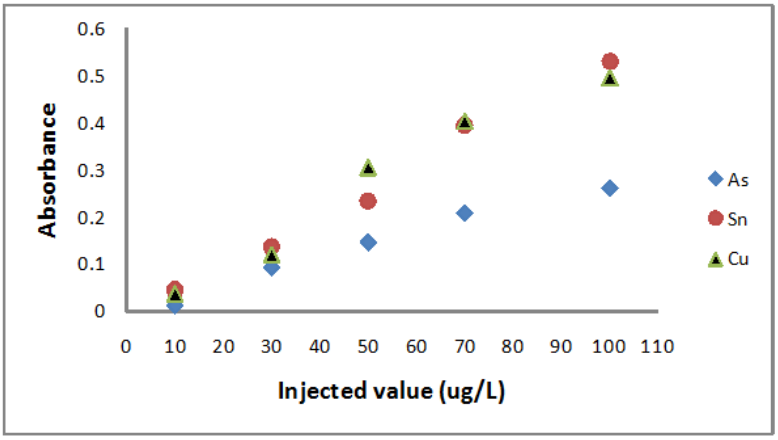

Figure 6-32 the calibration graphs of As, Sn, and Cu generated upon applying 1.3 M HCl and 1.5% m/v $NaBH_4$.

6.5 Summary of the findings from chapter six

1- Individual studies were conducted to examine eight elements using the hydride generation scheme, in which a second order central composite rotatable design plan composed of 13 experiments was accomplished for each of the examined analytes. Empirical models were produced for the examined systems and the coefficients estimated by applying a multiple regression analysis. Optimal derivatization conditions (concentrations of $NaBH_4$ and HCl) were determined by applying constrained optimization technique.

2- As stated in chapter five, hydrogen generation in the system results in disruption of the recorded signals. Therefore extra work was applied to rectify the signals for the hydrogen magnification effect.

3- Nine elements could be detected simultaneously with the highest signal intensities obtained by applying an extended optimization plan based on a principal component analysis (PCA). The results of PCA analysis identify the best derivatization conditions that apply for all the examined elements.

4- In order to overcome the recombination reactions that may occur in a DBD atomizer, a miniaturized chip with a shorter atomization channel and spectral path length (3.5 cm) was tested. Consequently, a quantitative determination of three elements was accomplished with an average error of 10%.

7. A FULLY INTEGRATED SYSTEM BASED ON MULTI DBD STAGES

7.1 Preface

In this chapter, a miniaturized fully integrated system is designed and tested for heavy metals detection and determination based on applying several DBD atomization stages. The proposed system aims to implement the full analysis procedures, starting from the sample pre-treatment in the first DBD atomization stage and ending with spectrometric analysis in the last DBD atomizer. Other stages based on plasma effects (e.g. UV radiation) or other effects such as subjecting the sample to ultrasound irradiation or a combination of these effects are utilized. The aim is to facilitate the fragmentation of the examined compounds and release their vapour species especially when the sample contains complex forms (e.g. biological). Considerable work has been accomplished to study the pre-treatment of samples containing biological and organic species. Finally, real samples of mineralized natural water and digested sludge taken from a wastewater treatment plant are examined to assess the system performance.

7.2 Analytical system based on multi DBD atomization stages

It is well known that electron kinetic energy can be effectively converted to an ultraviolet irradiation in a DBD cell, which can be utilized to achieve analyte reduction through a photochemical vapour generation (PVG) process. In principle, the mechanism of PVG assumes that analyte ions convert to their volatile species with the aid of strong reducing radicals (e.g. H^* or CO^*). These radicals, considered to be very reactive species, could be generated from the photochemical-decomposition of low molecular weight (LMW) organic compounds (e.g. formic or acetic acid). The unique features of DBD plasma has been recently utilized in the field of analyte photochemical reduction, as reported by *(Wu et al., 2011, Liu et al., 2011)* who generated the vapour species of inorganic and organic mercury by applying LMW organic acids and recently *(Wu et al., 2012)* who determine thiomersal in vaccines. Photo-chemical vapour generation is also applicable to other hydride forming elements and transition elements by applying different UV light sources *(Bendl et al., 2006, Zheng et al., 2010a, Zheng et al., 2009).* Practically, PVG retains most advantages of traditional cold vapour generation techniques as well as extra features such as lower cost, simpler reaction mechanisms and greener method with non-toxic disposals. Generally speaking, the efficiency of the

PVG technique is found to be lower than other techniques (e.g. Hydride generation) *(Zheng et al., 2010a)*; nonetheless, some elements (e.g. Pb, Cd) were critically reduced with better results when applying PVG compared with the traditional HG. The responses of different examined analytes to PVG reduction are found to be widely dependent on parameters such as the type and concentration of the organic acid as well as the irradiation period. Basically, the reduction of the elemental ions into their corresponding volatile species occurs when radicals are created in the reaction bulk. Hence, a sufficient concentration of organic acid leads to sufficient radical formation; however, excessive organic acid might reduce efficiency, probably, due to radical recombination reactions which consequently lead to the formation of new organic compounds.

The main objective of this part of the research is to produce a customized version of a fully integrated system based on utilizing the DBD plasma effect in multiple stages for pre-treating the sample as well as conducting spectrometric analysis. Other objectives are to examine the photo-chemical reduction promoted with ultrasound irradiation as an alternative to the hydroborate scheme.

In principle, it is reported that at least three steps are involved in the mechanism of the PVG process: (1) a reduction of the examined analyte into a lower oxidation state, which occurs with simultaneous generation of and attack by organic radicals, (2) formation of volatile compounds, (3) subsequent decomposition into various forms *(Zheng et al., 2010a, Zheng et al., 2010c).*

A hypothesis is proposed in this research to show that the PVG mechanism may involve an initial decomposition of water or organic compounds to form reducing radicals in the examined sample solution with aid of both DBD discharge thermal and chemical effects as well as the effect from UV irradiation. The radicals react with the complex species in the sample to generate species with less complexity (molecules or atoms), which are dissociated in a later atomization stage to produce free atoms of the examined analyte. In the proposed technique, a water sample taken from a high level contamination source containing different complex species (inorganic and organic) is forwarded to the first atomization stages, where the complex species are dissociated into fragments. The stream from the first atomizer is forwarded into a gas liquid separator, in which the gaseous species are separated and transported into another atomizer with aid of a carrier gas (e.g. Argon). The gaseous molecule dissociates and atomizes in a second stage DBD atomizer to produce free atoms that can be detected by atomic spectroscopy. The

geometry of the first stage DBD atomizers consist of an annular section formed between two glass cylinders kept in concentric configuration. The annular space between the two cylinders is utilized as a channel for the aqueous sample flow with spontaneous plasma generation. The interior cylinder is the inner dielectric barrier, which holds the inner electrode. The outer cylinder is the second dielectric layer, where the second electrode (ground) covers the outer surface. The second DBD atomizer is a rectangular configuration (3.5 cm spectral path length) which is already described and used in previous sections.

7.3 Design of a cascade annular DBD atomizer

A cascade annular DBD atomizer has been designed as illustrated in **Figure (7-1)**.

(A)

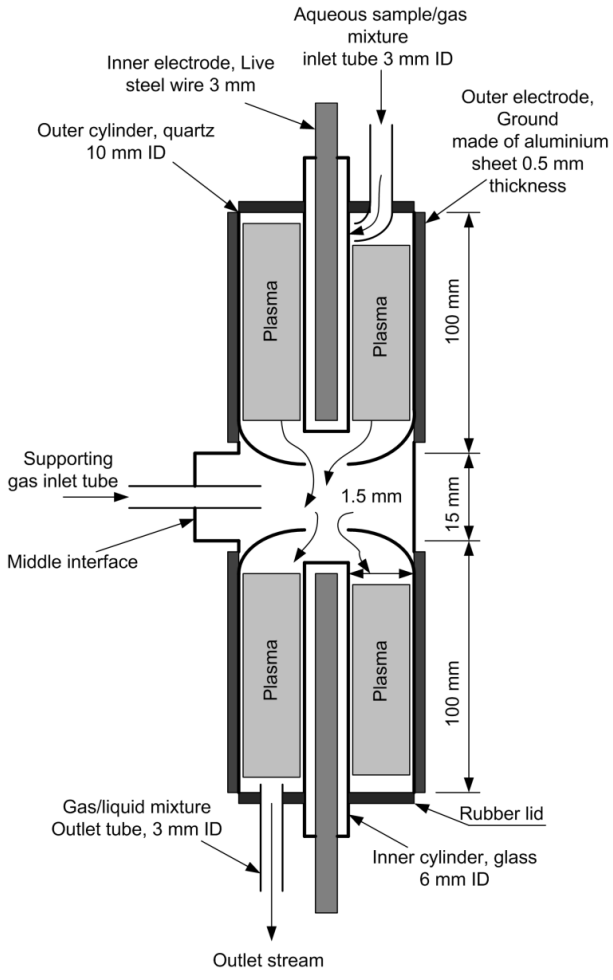

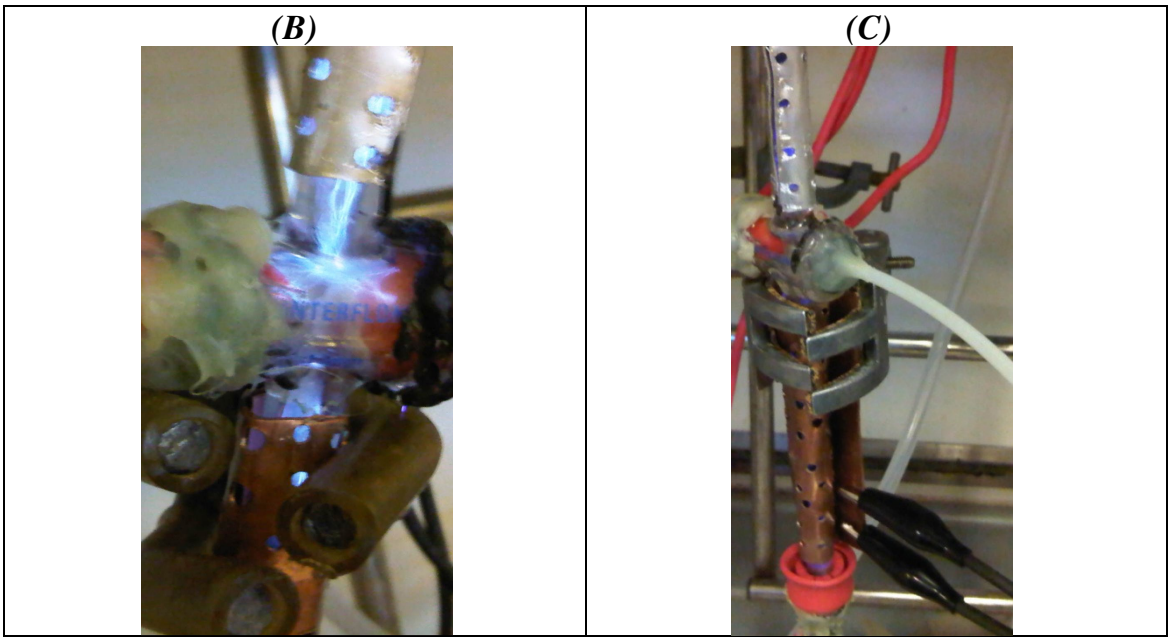

Figure 7-1 the details of a cascade annular DBD atomizer;
(A) a schematic diagram illustrate the atomizer details, (B) a picture for the streamers formed before introducing the liquid sample, (C) a picture shows the plasma formed in presence of the liquid sample (notice the reduction in the glow intensity)

The main concept of this design is to utilize two atomization stages combined in series and separated by an interface in the centre, which is used to insert supporting gas. The application of the interface between the two atomization stages aims to avoid temperature increase which is an unfavourable effect, especially after long operation times *(Zheng et al., 2010c)*. The temperature increase in the atomizer may lead to elevated water vapour pressure and consequently results in poor separation of the analyte vapour species from the accompanying water residues in the gas-liquid separator. The outer shell cylinder (10 mm ID, 12 mm OD) has been made of quartz glass to enable the spectrometric data acquisition in the UV region, whereas the inner cylinder is a simple glass test tube (6 mm ID, 7 mm OD). It is worth noting that the inner glass tube, which houses the live electrode, has been wrapped with a metal strip (very fine diameter) to form a corrugated screw shape on the outer surface. The aim is to generate a thin film of the falling liquid along the electrode, which would result in several advantageous effects such as a rapid release of any generated species and efficient contact between the falling film and the UV irradiation; thereby minimizing the residence time required inside the atomizer and enhancing the separation of the generated vapour species. The outlet stream from the annular atomizer is connected to a

gas/liquid separator; from which the separated vapour species is transported with aid of a carrier gas into a rectangular DBD atomizer (with a 3.5 cm spectral path length), illustrated in **Figure (6-25)**, to achieve species atomization and their spectrometric data acquisition.

Preliminary experiments were conducted to produce the current-voltage characteristic diagram of the examined annular DBD atomizer described in **Figure (7-1)**. Steam plasma in which the voltage is increased gradually and the corresponding increase in current is recorded, generating the characteristic diagram shown in **Figure (7-2)**. A sharp increase in voltage occurs in the first region (a) accompanied by a limited increase in the current, which resembles a Townsend regime that occurs prior to spark ignition. In the second region (b), a transition regime produced where a decrease in voltage is accompanied by a limited increase in current similar to the regime described in **Figure (2-9)**. The parallel increase in the current and voltage in the third region (c) indicates disappearance of the normal glow discharge region and the direct appearance of abnormal glow discharge which has ended at the point (≈ 17 mA and 4kV). Further increase in the voltage might lead to arc formation; therefore it has been discontinued at the aforementioned value. It can be deduced that a minimum breakdown voltage of 3.5 kV is required for steam plasma, which is lower than the MBV required for argon (3.8 kV) in a rectangular configuration.

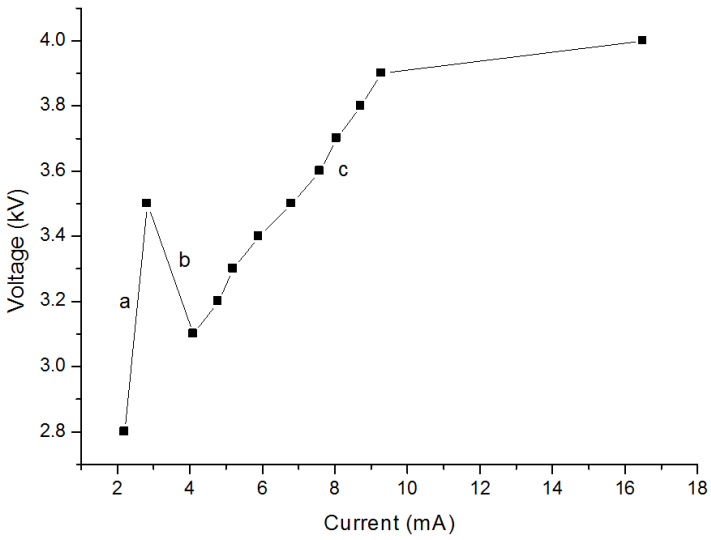

Figure 7-2 the current voltage characteristics diagram of steam plasma generated in annular DBD atomizer.

7.4 Application of the annular cascade atomizers for the sample pre-treatment

Since the main objective of the whole system is to analyse real samples collected from different water sources, it is essential to pre-treat the sample to remove any possible biological or other contaminants. In this section, the feasibility of utilizing DBD plasma for sample pre-treatment through the cascade annular atomizers prior detection by atomic spectroscopy is investigated. The aim is to explore the pre-treatment efficiency for two possible contaminants, biological and organic. Accordingly, two types of artificial water samples were prepared individually by spiking specific concentrations of E.coli bacteria as a biological contaminant and acetic acid, phenol, and isopropyl alcohol as organic contaminants in distilled water. The details of preparing the examined samples are described in **Appendix 11.10**. Two experimental sets were conducted, the first applying one cascade atomizer whereas two cascade atomizers linked in series are adopted in the second experimental set to attain longer irradiation times for the sample (**Figure (7-3)**). A peristaltic pump with a feed rate (2.8 ml/min) was used to inject the liquid sample into a tee junction (3 mm ID). A supporting gas (dried air at 20 ml/min) is also injected through the T-junction in order to generate air/water plasma in the top section of the cascade atomizer, which gives rise to active species and radical formation in the system. In other experiments, argon (35 ml/min) is also injected into the system from the centre interface in addition to the main air stream. The resulting liquid/gas mixture is directed from the T-junction through Tygon tubing (3 mm ID, 30 cm length) into the first cascade atomizer, in which there is approximately 5 seconds for the sample irradiation. In the case of two cascade atomizers, the outlet stream from the first atomizer is directed into the top section of the second atomizer, and the total irradiation period in both atomizers is estimated to be approximately 15 seconds. Some experiments were conducted by re-circulating the sample through a single and two DBD atomization stages for different periods; this is to deduce the enhancement in treatment efficiency. The air and argon gas flow rates are controlled manually by using gas flow meters purchased from (BOC special products – UK). A high voltage power source from (Entwicklung Leistungselectronic – Germany) and USB 2000 spectrometer integrated with Spectra Suite software from Ocean Optics are were used.

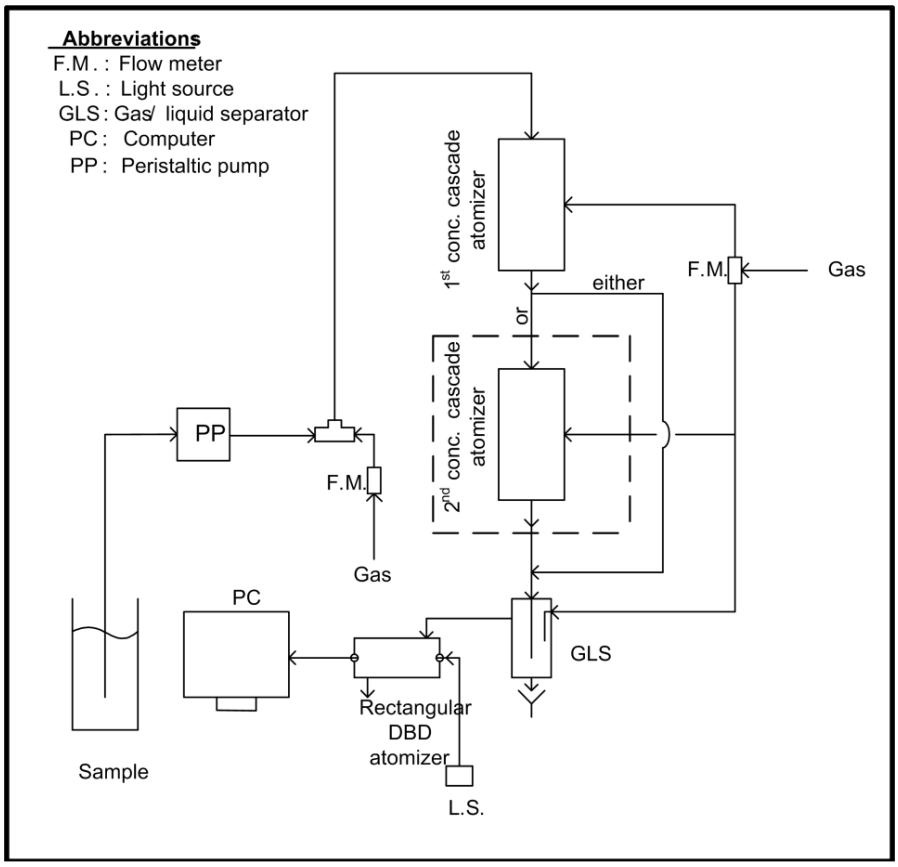

Figure 7-3 a process flow diagram illustrates three DBD atomization stages utilized for the sample treatment and the analyte species vapour generation

7.4.1 Treatment of biological samples - *Ecoli*

The effect of the treatment strategy on the biological components of the wastewater is tested by subjecting pure cultures of *E. coli* grown in nutrient-rich medium, Luria broth, to viability tests after the treatment process. A semi-quantitative approach to viability testing based on batch growth curves, is undertaken in this study. As outlined in **Appendix 11.10**, the relative number of viable cells in the treated samples is defined by the length of the lag phase in a typical batch growth curve of *E. coli* , which means the length of the lag phase increases proportionally with the decrease in the concentration of viable cells. As a proof of concept, different starting concentrations of *E. coli* are subjected to batch growth. The results, **Figure (7-4/A)**, demonstrate the increase in the lag phase with a decrease in the initial concentration, represented by the number of viable cells of *E. coli*. The effect of treatment time on the reduction in the number of viable cells is then determined. *E.coli* diluted to a starting concentration of 0.5 OD_{595} is

treated for different time intervals then subjected to batch growth. The increase in the length of the lag phase in the treated samples when compared to the untreated control (UTC) suggests a reduction in the viability of the cells after treatment; **Figure (7-4/B)**.

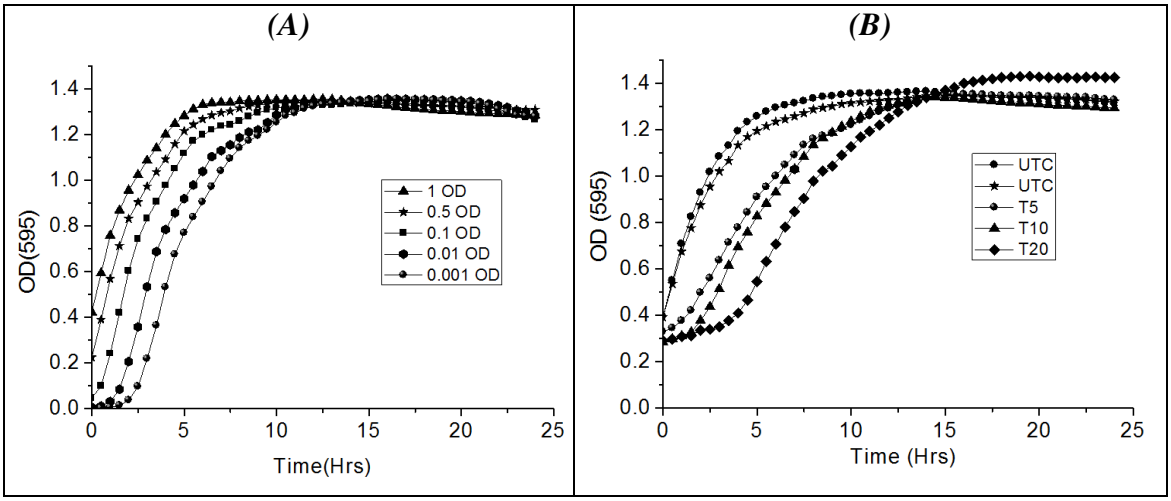

Figure 7-4 growth curves generated for *E. coli* grown in LB media;
(A) several concentrations of *E. coli* (1, 0.5, 0.1, 0.01, and 0.001 OD_{595}) grown at normal conditions (37 ^{o}C for 24 hours), (B) UTC (two samples) indicates untreated *E. coli* samples (at 0.5 OD_{595} concentration) grown at normal conditions, while T5, T10, and T20 refers to a 0.5 OD_{595} *E. coli* samples treated for 5, 10, and 20 minutes respectively and then grown at normal conditions

The results shown in **Figure (7-4/B)** suggest that the efficiency of the treatment, demonstrated by the reduction of viable cells number, increases in a time dependent manner with 20 minutes resulting in the greatest reduction of viable cells. Two separate replicates from different starting cultures (biological replicates) were setup for the UTC to determine the magnitude of biological variation in the batch growth of *E. coli*. Although the viability of *E. coli* reduces significantly after plasma treatment, it was questionable whether the reduction occurs due to the effects on the live cells or nutrient deterioration (e.g. Peptone in the culture medium). In this sense, two separate experiments were conducted, in which the effect of treatment conditions on the nutrients in the culture medium was investigated by monitoring the growth of *E. coli* in LB subject to different treatment times, the results are shown in **Figure (7-5)**.

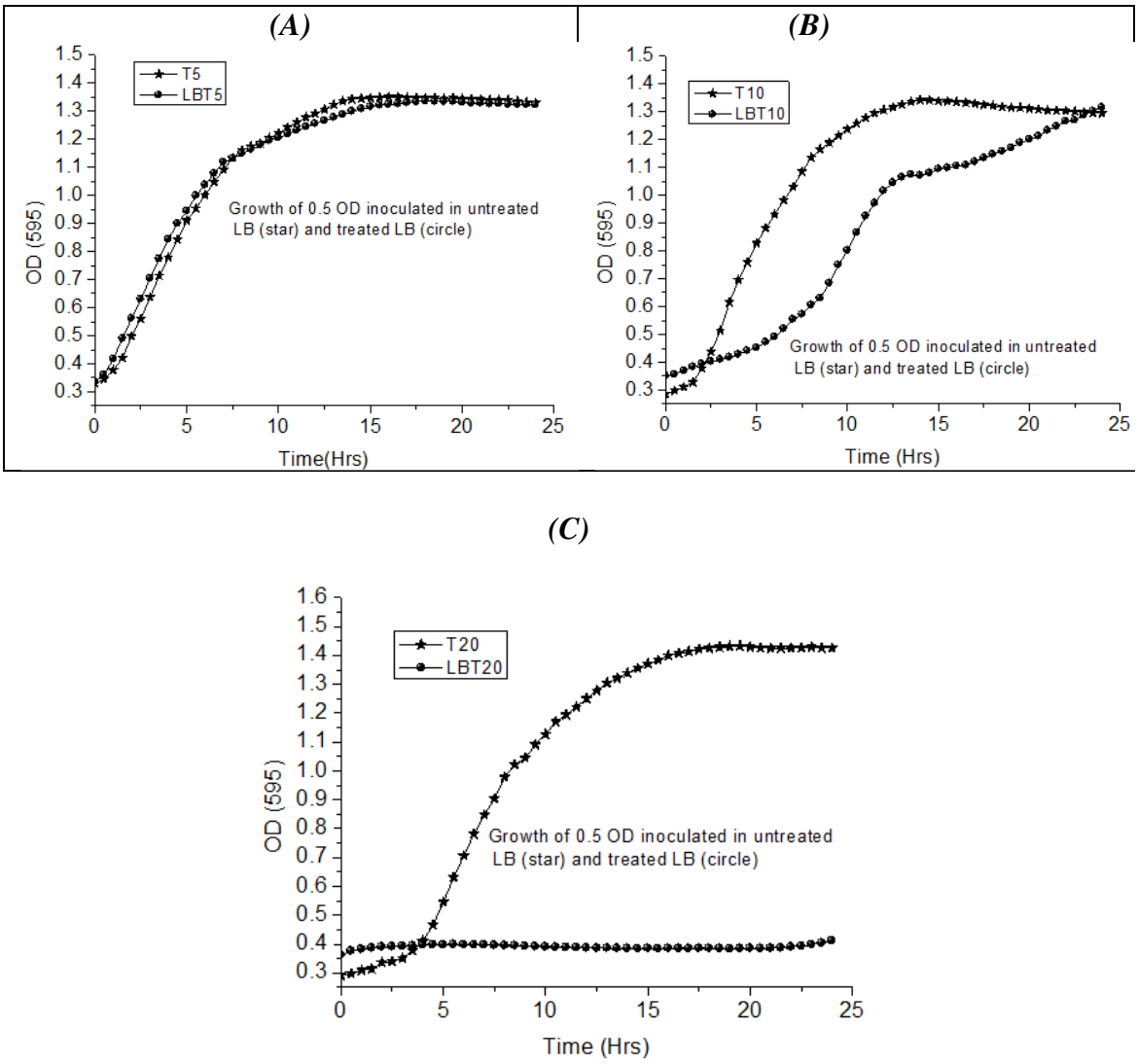

Figure 7-5 growth curves 0.5 OD_{595} *E. coli* inoculated in untreated and treated LB medias;
(A) 5 minutes, (B) 10 minutes, and (C) 20 minutes

The progressive reduction in the ability of *E. coli* to grow in LB medium treated for increasing periods of time suggest that the treatment indeed targeted the nutrients in the culture medium. Therefore, the effect of the treatment conditions on the viability of *E. coli* was further investigated by using a viable plate count assay. As outlined in **Appendix 11.10**, a 0.5OD_{595} suspension of *E. coli* in sterile distilled water is subjected to treatment for different periods. Viable plate counts were made of the treated samples and compared to that of the untreated control. The results show that the treatment is effective against *E. coli* and significantly reduces the number of viable cells, from approximately 5×10^7 cells in the untreated control to approximately 5×10^4 cells (3 orders of magnitude) after only 5 minutes of treatment, as shown in **Figure (7-6)**.

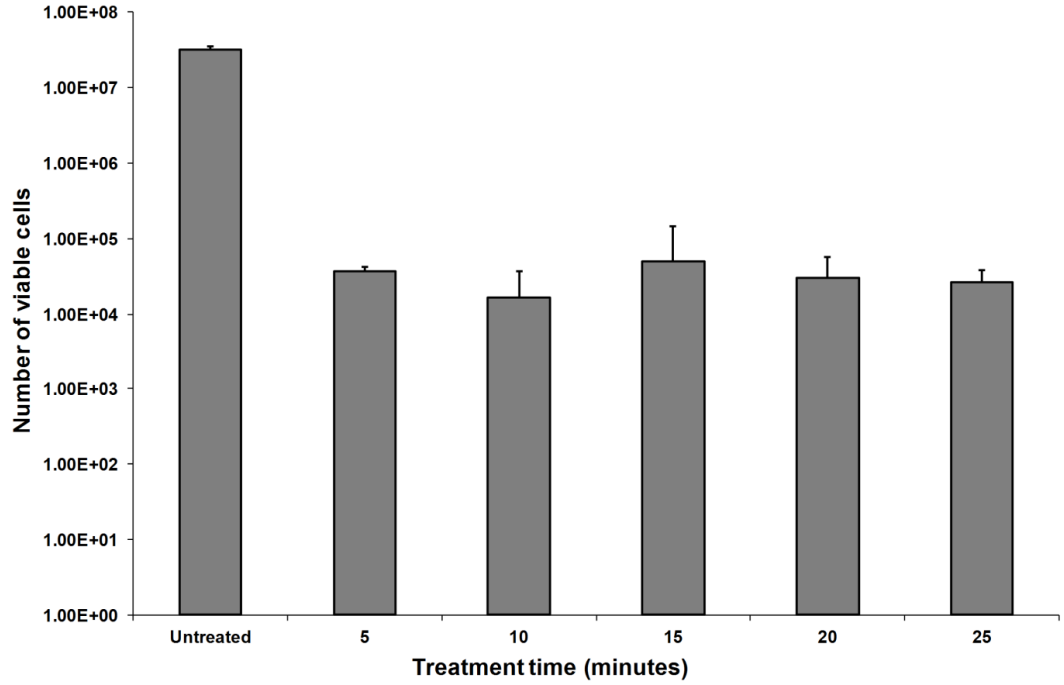

Figure 7-6 the number of viable cells counted before and after treatment for samples contain (0.5 OD_{595}) *E.coli*

The treated samples are visualised under a light microscope, where an extensive lysis of cells was seen (irregular shapes) with no change in the structure of the intact cells, **Figure (7-7)**.

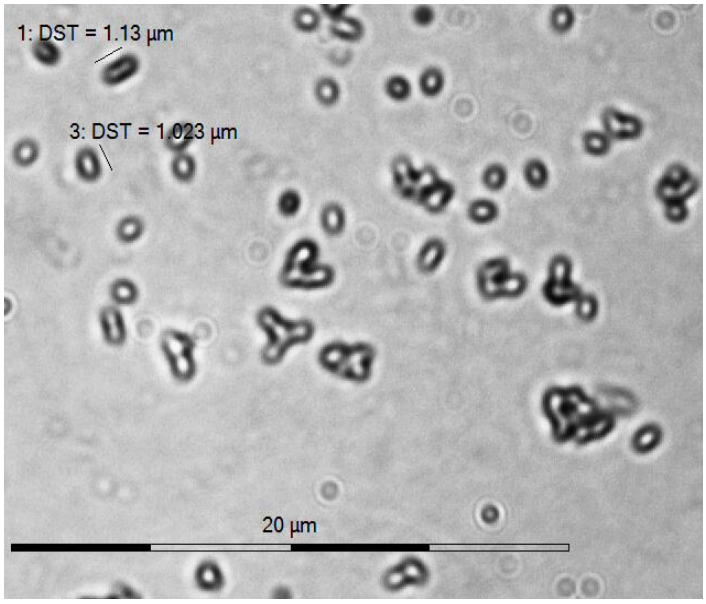

Figure 7-7 a picture shows *E. coli* after treatment for 25 minutes;
the unaffected cells appears either circular or cylindrical, while the lysed cells form irregular shapes

It can be observed that a further reduction in the number of viable cells occurs after 10 minutes but not below the order of 10^4, obtaining approximately same results for other treatment periods (15, 20, and 25 minutes). Hence, 10 minutes has been selected as an optimal time period for treating real water samples, as described in **Section (7.7)**.

Taken together, the results of the above experiments demonstrate the efficiency of the DBD plasma treatment not only in reducing the number of viable *E. coli* in the samples but also in the treatment of organic components in the nutrient medium. Generally speaking, applying streamer discharges in the liquid phase results in several effects such as inducing highly energetic electrons and producing chemically active species as well as UV radiation and shock waves. These effects are able to decompose practically any kind of compound and result in water disinfection. Plasma discharge may cause direct effects from electron collisions or other effects caused by molecular, ionic or radical species such as the pyrolysis and photolysis reactions. On the other hand, the mechanism of biological cell degradation due to application of an electrical field is attributed to the phenomenon called electromechanical compression. Applying a sufficient electrical field could result in creation of pores in the membrane, which consequently causes a disruption of its biological structure. If the ratio of the total pores to the total membrane area becomes significant, the membrane will not be able to repair the disruption and such effects (e.g. electroporation or electrofusion) might be formed. Other studies report that an electrical field could result in either local action due to the chemical reactions in plasma bulk or non local action due to the UV radiation and shock waves *(Locke et al., 2006).* It is worth noting that UV radiation in the range of (200-400 nm) may induce organism mutation (i.e. mutagenic effects), whereas the shock waves in the range (5 – 20 kBar) could lead to deform the structure of the cell. The shock waves could be formed due to the effect of electrohydraulic discharge when a plasma channel is rapidly expanded leading to different radical reactions. In this regard, two kinds of radical reactions are distinguished in the literature and attributed to the electrohydraulic cavitations phenomenon; namely pyrolytic reactions and indirect free radicals reactions. The interaction between the aforementioned effects consequently leads to deactivate the microorganisms and dissociate the organic compounds in the contaminated sample of water. Thus, the reduction in bacteria activity could be attributed to well known treatment mechanisms such as live cell destruction which occurs due to the electrical field (electroporation), the species produced in the plasma bulk (e.g. O_3, H_2O_2, OH^*, H^*), the thermal effects as well as UV radiation.

The temperature of the re-circulated solution through the DBD atomizer is measured outside the plasma bulk and found to be about 40 ^{o}C after 20 minutes circulation, which indicates limited thermal effects.

OH species are clearly observed in the spectrum collected from the annular DBD atomizer, (**Figure (7-8)**), especially in the band (302 to 317 nm) which is characterized as *OH* molecular emission lines *(Zhu et al., 2008a)*.

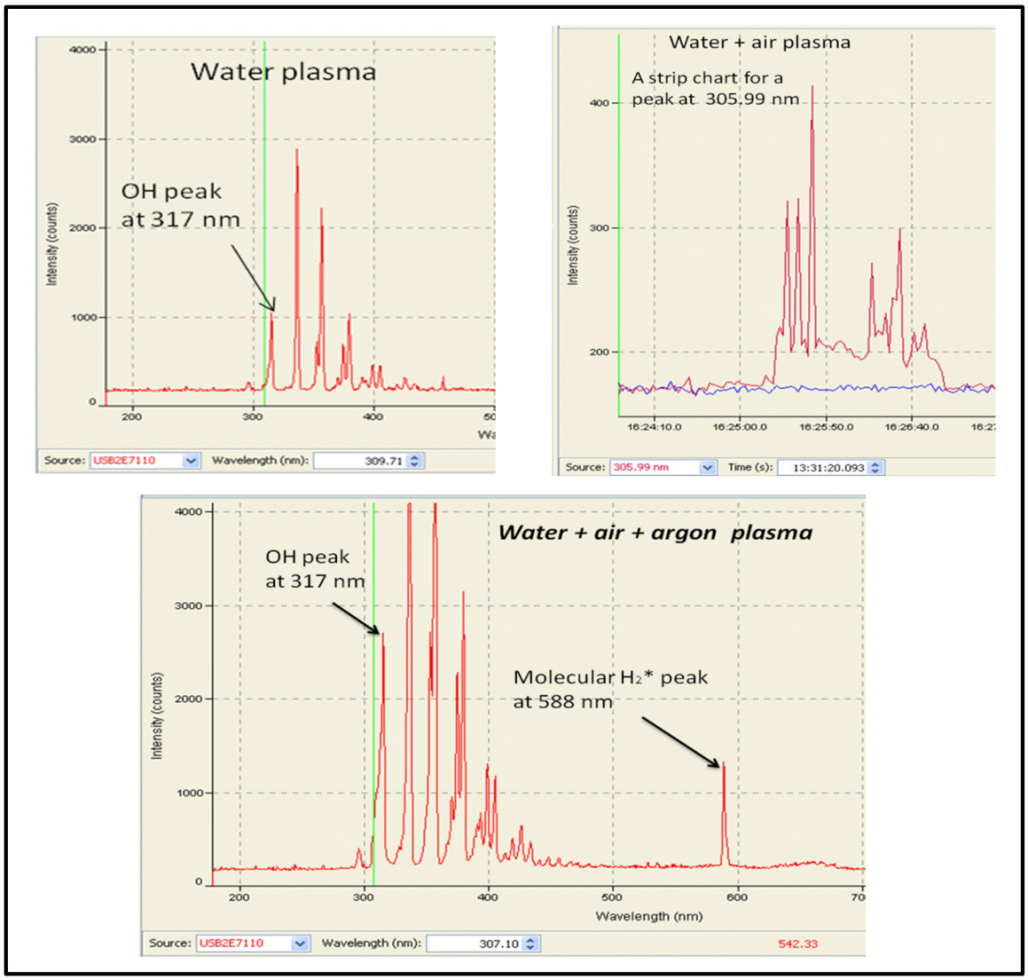

Figure 7-8 the recorded signals for *OH* species (302 to 317 nm) in the first cascade annular atomizer when applying water plasma, (water + air) plasma and (water + air + argon) plasma**;**

The *OH* signal becomes more intense when argon gas is injected with water and air; moreover, molecular H_2 at 588 nm is also observed when combining water, air and argon.

The signal at 309 nm has been attributed to *OH* in the relaxation state ($A^2\,\Sigma^+\,(v=0) \rightarrow x^2\Pi\,(v=0)$ *(Shih and Locke, 2010)*, whereas the signal at 317 nm is related to *OH* in the excited state. The *OH* species could result from: 1) a dissociative recombination of

hydronium ions (H_3O^+) with electrons in plasma bulk to form OH. The hydronium ion is normally formed when an abundance of hydrogen is available in the bulk of water, 2) another perspective postulates that a high voltage electrical discharge in the gas phase above the water surface or in the water itself, also known as electrohydraulic discharge, is able to produce many species such as molecular oxygen and hydrogen, hydrogen peroxide, hydroperoxyl, hydroxyl, and other radicals *(Locke et al., 2006)*. In presence of air or oxygen, ozone could be produced in the bulk of water that subjected to high voltage discharge; however, we could not detect any ozone species in the current system.

A mechanism is postulated for the plasma reactions in the annular DBD atomizer, shown as follows *(Fridman, 2008, Aleksandrov et al., 2007, Avtaeva et al., 2010)*:

$$H_2O + e \xrightarrow{Dissociation\ reaction} H + OH + e$$

$$H_2O + e \xrightarrow{Vibrational\ excitation} H_2O^* + e$$

$$H_2O + e \xrightarrow{Dissociative\ attachment\ of\ electrons} H^- + OH$$

$$H_2O + e \xrightarrow{Dissociative\ attachment\ of\ electrons} H + OH^-$$

$$H_2O + e \xrightarrow{Dissociative\ attachment\ of\ electrons} H + O^- + H^+ + e$$

$$H_2O + e \xrightarrow{Dissociative\ attachment\ of\ electrons} H^- + O^+ + H + e$$

$$O^+ + H_2O \rightarrow H_2O^+ + O$$

$$H^+ + H_2O \rightarrow H_2O^+ + H$$

$$H_2O^+ + e \rightarrow H + OH$$

$$H_2^+ + H_2O \rightarrow H_3O^+ + H$$

$$H + H + M \rightarrow H_2 + M$$ (M is the third body)

$$H_2O^+ + H_2 \rightarrow H_3O^+ + H$$

$$H_2O^+ + H_2O \rightarrow H_3O^+ + OH$$

$$H_3O^+ + e \rightarrow H + H_2O$$

$$H_3O^+ + e \rightarrow H_2 + OH$$

7.4.2 Treatment of artificial organic samples

The mechanism for organic contaminant degradation in wastewater is attributed to hydroxyl radical attack on the organic molecules which results in fragmenting the double bond long chain molecules, forming single bond molecules or even dissociating the molecules. Some investigations on phenol degradation by electrohydraulic discharge show that the mechanism to be hydroxyl radical and ozone under oxygen or argon environments. It is reported that phenol degradation by hydroxyl radicals produces primary products (e.g. catechol and hydroquinone) which react with other hydroxyl radicals to form high molecular weight organic acids (e.g. fumuric acid). The organic acids are then oxidized in the same reaction series to form lower molecular weight organic acids (e.g. formic acid).

A general illustration for the degradation of organics in presence of electrohydraulic discharge is described as follows *(Locke et al., 2006)*:

- Radical formation: $H_2O \rightarrow H + OH$
- Radical – molecule reaction: $OH + organic \rightarrow products$
- Photochemical reactions: $O_2 + organic \rightarrow products$
- Electron – molecule: $e_{aq}^- + H_2O_2 \rightarrow OH + OH^-$
- Fenton's reaction: $Fe^{2+} + H_2O_2 \rightarrow OH + OH^- + Fe^{3+}$
- Ozone – molecule: $O_3 + organic \rightarrow products$
- Aqueous electron reactions: $e_{aq}^- + organic \rightarrow products$

The experimental investigations on organic fragmentation, using annular cascade DBD atomizers were for samples of phenol and isopropyl alcohol whose absorbance was measured at 283 nm and 204 nm. The wavelengths are selected based on a wave scan method, where the wavelength with highest intensity is adopted for the examined sample. The treatment of the solutions results in great differences in the measured absorbance before and after treatment; for instance the measured absorbance reduced from 0.038 to 0.003 for a solution composed of 1.0 portion of alcohol / 11.0 portion of water after 10 minutes treatment. The concentration/absorbance calibration graph could not be produced for the examined chemicals due to non-sensible changes in the measured absorbance. Therefore the results related for those chemicals (phenol and

isopropyl alcohol) are excluded from the discussion. As an alternative samples with different concentrations of acetic acid have been used. The samples are treated by applying one and two annular cascade DBD atomizers. The samples before and after treatment are assessed using three methods: 1) titration with 0.1 M *NaOH*, 2) interfacial tension measurement, and 3) absorbance measuremed at 241.0 nm. The results are shown in **Figure (7-9)** which shows a proportional reduction in the quantity of *NaOH* equivalent volume from that required for titration, in accordance with treatment time. The result in **Figure (7-9/A)** shows a 50% reduction in acetic acid concentration (for a sample contains 0.57 acetic acid / 1.0 water) after 10 minutes treatment. Other proof of acetic acid dissociation is the increase in the interfacial tension, up to 14%, which occurs after treating the sample containing 1.2 acetic acid / 1.0 water, (**Figure (7-9/B)**). Only one result, considered anomalous, is related to the increase of sample absorbance after treatment, (**Figure (7-9/C)**). This result could be attributed to the formation of other species due to acetic acid dissociation, which has increased by up to 14% for a sample containing 0.57 acetic acid / 1.0 water.

(A)

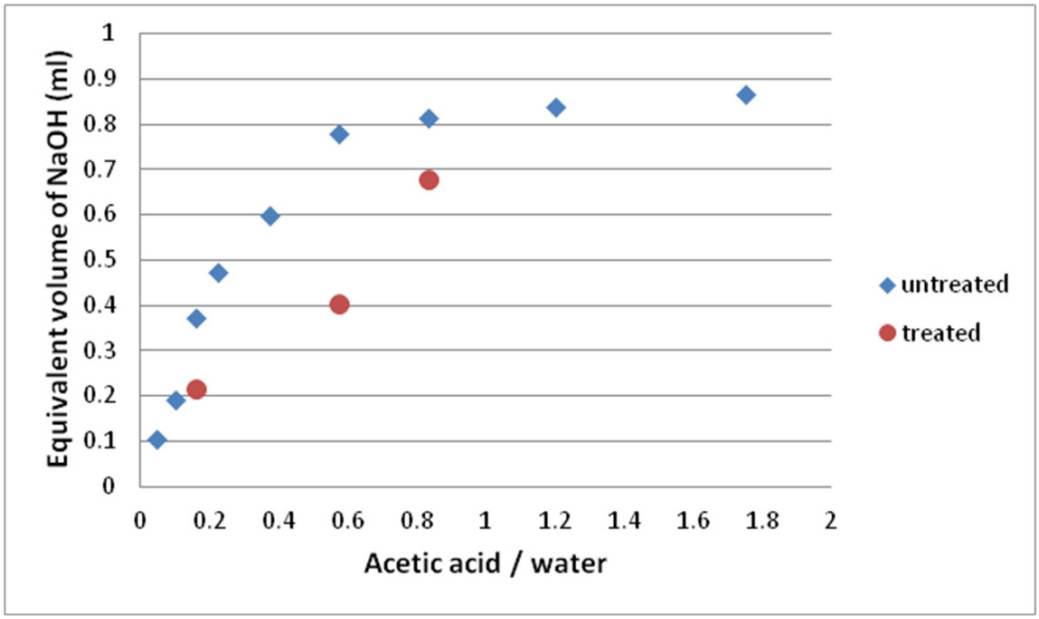

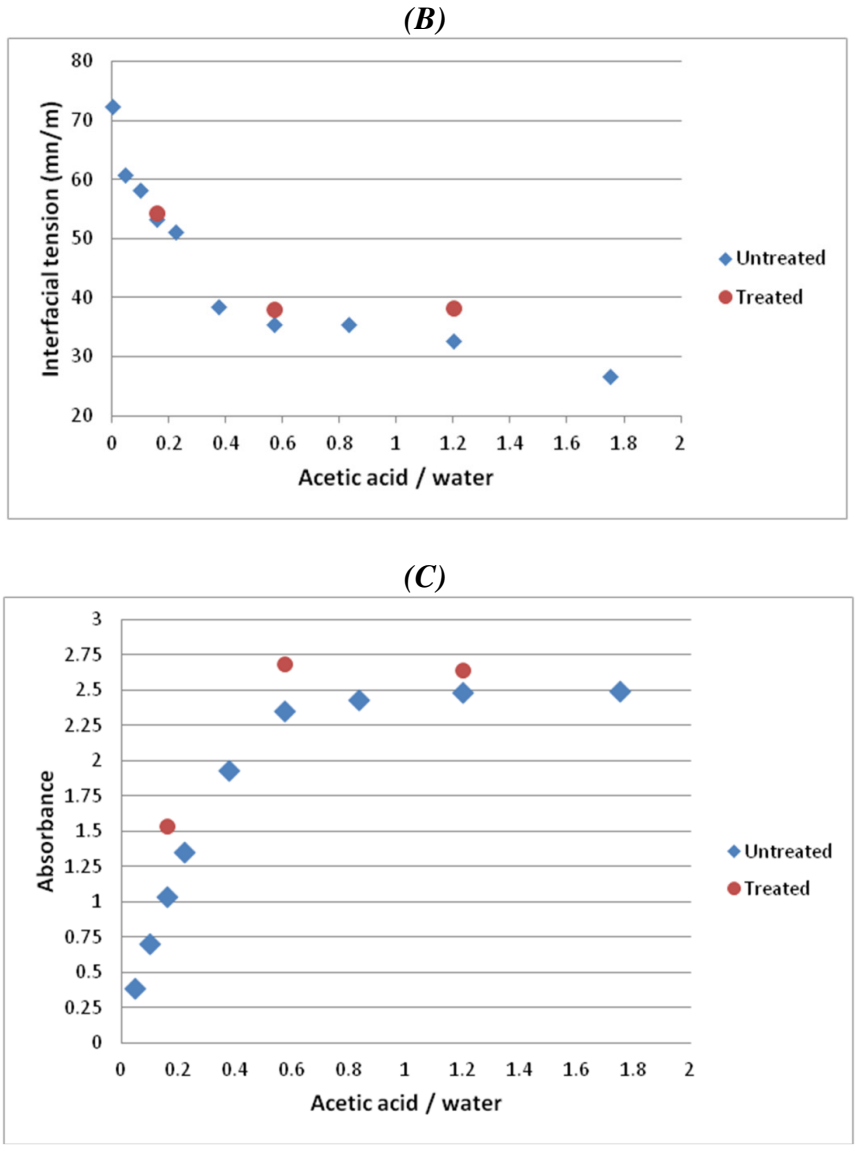

Figure 7-9 treatment of different concentrations of acetic acid by using one cascade DBD atomizer;
(A) the titration results by using 0.1 M *NaOH*, (B) the measured interfacial tension before and after treatment, (C) the measured absorbance at 241 nm before and after treatment

An increase in the absorbance after treatment by DBD plasma was observed by *(Chen et al. 2009)* and *(Ognier et al. 2009)*, who attributed this to an increase in the derivative concentration that formed due to the dissociation of compound bonds (organic dye and enzymatic assay respectively).

In the current research the efficiency of treatment increases with an increase in the applied power and treating period. Increased efficiency is proportional to an increase in the sample absorbance; therefore sample absorbance has been used for comparison between the examined cases (**Figure (7-10)**). The absorbance in case number 5 slightly

increased over the absorbance measured when treating the sample for 10 minutes in one atomizer, (**Figure (7-9/C)**). The results show that power and irradiation time are key factors for better acetic acid determination through the cascade atomizers. Comparing the increase in absorbance, obtained from cases 5 and 6 in **Figure (7-10)**, it can be seen that two cascade atomizers result in better treatment efficiency even than when applying a higher power rate with a single atomizer. Although the treatment scheme has combined many factors, it could be interpreted that longer contact time with UV radiation is more effective than other parameters.

The decomposition in case number 2 is in agreement with the results of *(Ognier et al. 2009)* who achieved 5% acetic acid decomposition by applying higher energy density (5.6×10^6 J/L) in a falling film gas – liquid DBD reactor. The removal efficiencies reported were in the order (1-heptanol > ethanol > phenol > acetic acid).

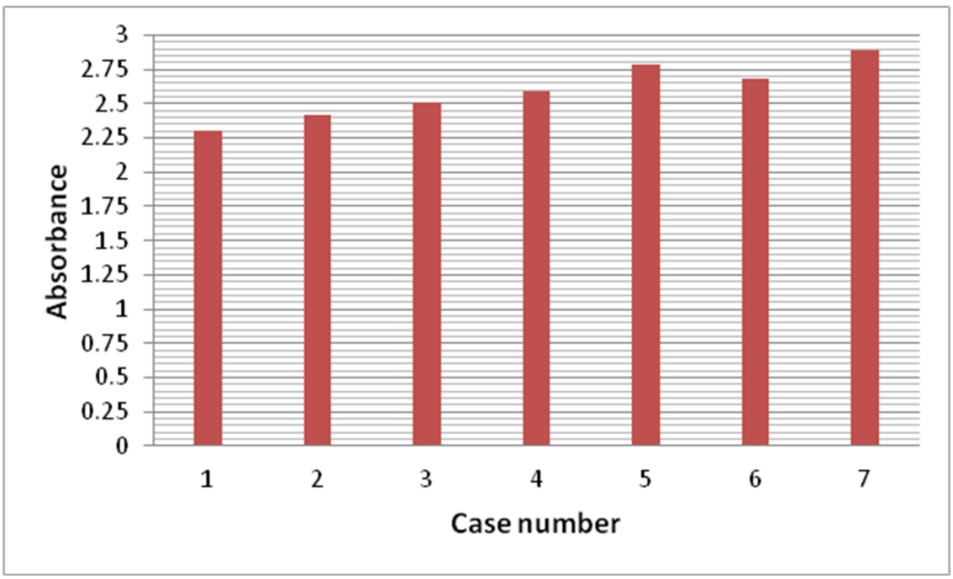

Figure 7-10 the measured absorbance before and after treatment by applying one and two cascade DBD atomizers for samples contain (0.57 acetic acid / 1.0 water);
Case number and description, the value given (%) refers to the decomposition occurred in the acetic acid:
(1) before treatment
(2) passing through one atomizer at 150 Watt (30 mA × 5 kV) → input energy density in one pass (power/sample flow rate) = 3.2×10^6 J/L which led to 4.1%.
(3) passing through two atomizers at 150 Watt which led to 8.0%.
(4) circulation for 5 minutes through one atomizer at 150 Watt which led to 11.5%.
(5) circulation for 5 minutes through two atomizers at 150 Watt which led to 17.8%.
(6) circulation for 5 minutes through one atomizer at 175 Watt (35 mA × 5 kV) → input energy density in one pass = 3.8×10^6 J/L which led to 14.8%.
(7) circulation for 5 minutes through two atomizers at 175 Watt which led to 20.6%.

7.5 Application of the annular cascade atomizers for analyte photo-chemical reduction

This section is devoted to the performance of annular cascade DBD atomizers for carrying out photo chemical reduction as alternative to traditional derivatization techniques used in previous chapters. Two analytical grade organic acids, acetic acid (CH_3COOH, 99.8% - from BDH) and formic acid (HCOOH, 88% - from Fisher Biotech) were used to prepare several concentrations (10%, 20%, 30%, 40% and 50% v/v) of acidic solution using distilled water. Preliminary experiments were conducted for mercury photo-chemical vapour generation, in which a range of Hg (II) (10 – 100 µg/L) was tested using both acid solutions and applying one and two cascade atomization stages. The annular atomizers are integrated with a rectangular DBD atomizer, **Figure (6-25)**, for species atomization and spectrometric data acquisition. The quantitative determination of mercury is conducted according to the same procedures described earlier, using a mercury hollow cathode light source (F-O-Lite) and a gas-liquid separator (GLS-A) of 350 ml volume. The results are shown in **Figure (7-11).**

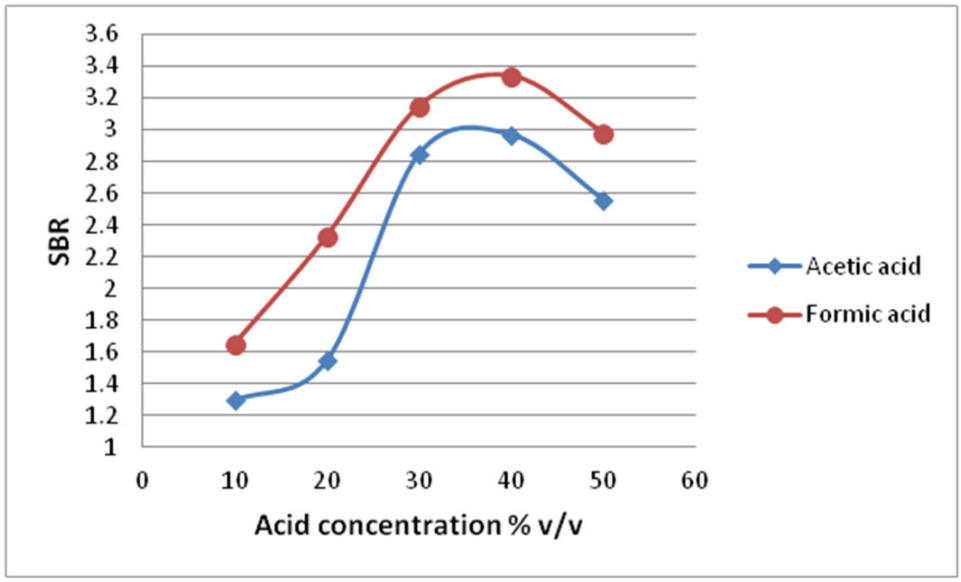

Figure 7-11 the effect of increasing the acidic concentration on the recorded signal to background ratio at 150 watt applied power.

No significant signals for mercury were obtained when using 10% of either organic acid and 20% of acetic acid, whereas clear signals were observed when using 30% of either organic acid. An increase to 40% does not show any increase in the recorded mercury signal, whereas a reduction in signal intensity was observed when using 50%

concentration of either organic acid. This reduction in the intensity could be attributed to a re-oxidation of mercury species, which consequently results in reduced generation efficiency *(Zheng et al., 2010b)*.

It is concluded that 30% of either organic acid is the optimal concentration. Formic acid results in better signal intensity. This result has also been reported in the work of *(Wu et al., 2011)* and is attributed to a decrease in the dissociation efficiency of the organic compound, in DBD plasma bulk, with increase in the length of the carbon chain.

A concentration of acetic acid over 30% v/v results in a disruption in the recorded spectrum as shown in **Figure (7-12)**, whereas spectral stability is observed for all examined concentrations of formic acid.

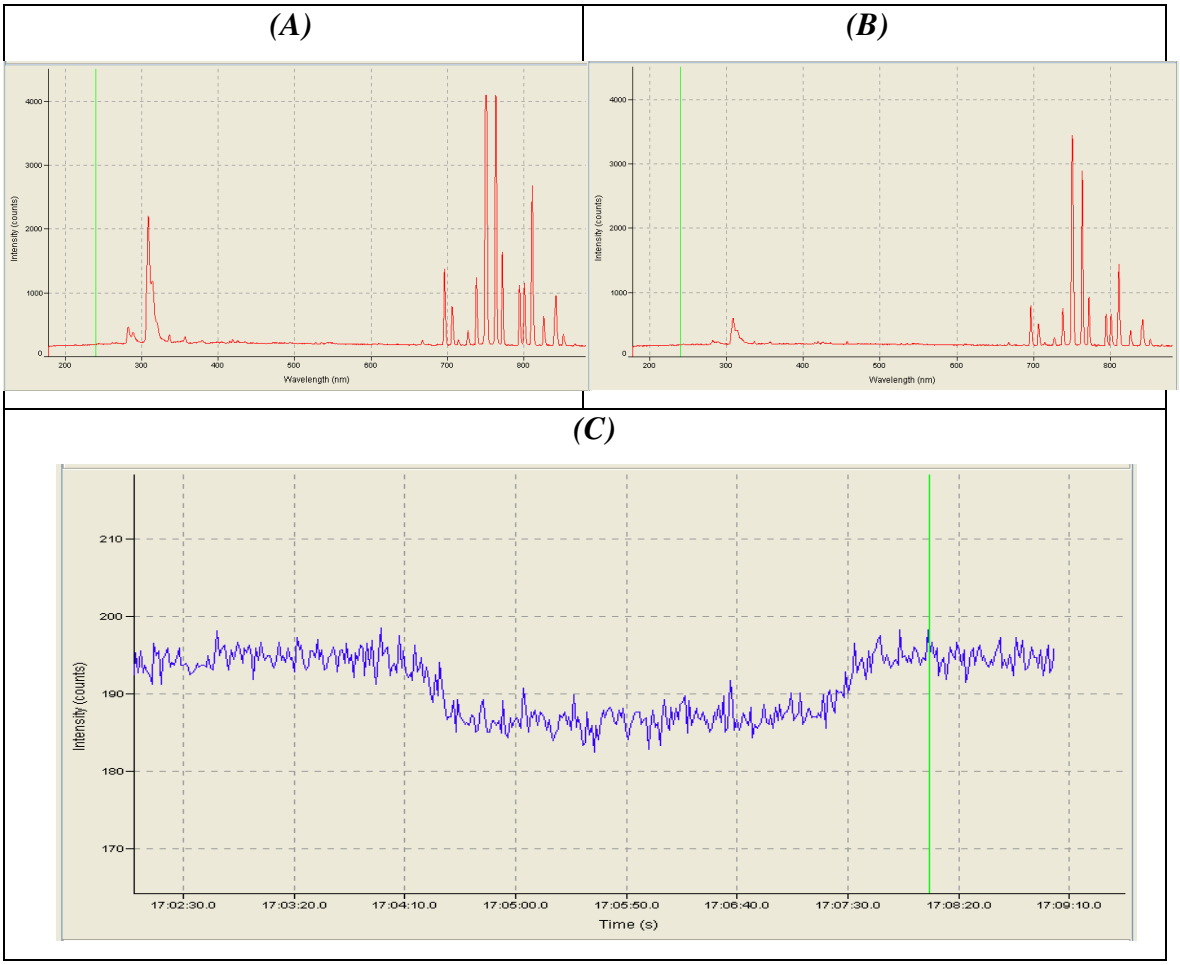

Figure 7-12 strip charts illustrate the effect of acetic acid on the recorded spectrums without applying light source;
(A) the recorded spectrum upon injecting a sample of water, (B) the recorded spectrum upon injecting a sample of water spiked with 50% v/v acetic acid, (C) a strip chart recorded for 253.58 nm line (no mercury injected) illustrates the signal depression due to the effect of 50% v/v acetic acid.

The disturbance occurring due to acetic acid does not resemble the disturbance observed due to the hydrogen and alkaline mist effects in the case of HG scheme. It can be observed, in **Figure (7-12/ B-C)**, that all peaks were significantly disturbed and some peaks totally disappeared. This effect could result from an unknown species generated due to the degradation of acetic acid. The unknown species depressed the signal of nitrogen and other species in the spectral range (280-400 nm) and affected the signal intensity in the NIR spectral region. Consequently, the sensitivity study directed the author to apply PVG for As, Sn, and Cu by using only formic acid.

The molar absorption coefficient of mercury in this experimental set is re-assessed taking into consideration a shorter spectral path length, 3.5 cm. The linear dependency of the recorded absorbance on the mercury concentration, **Figure (7-13)**, justified the estimation of the molar absorption coefficient from the slope ($\varepsilon \times l$), which is found equal to 23.8×10^4 L/mol/cm.

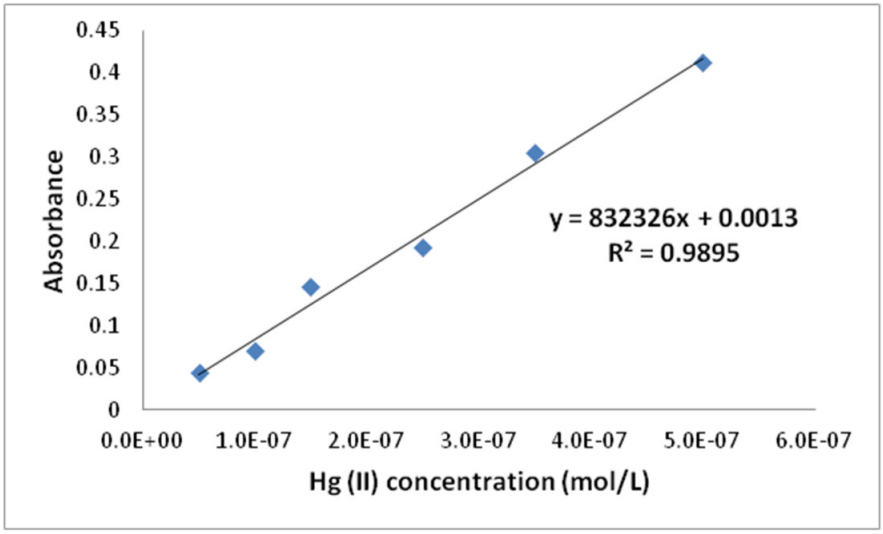

Figure 7-13 the measured absorbance relative to the injected concentration of mercury when applying PVG;
A photo-chemical reduction of inorganic mercury conducted in a single annular cascade DBD atomizer by applying 30% formic acid and utilizing DBD atomizer with 3.5 cm spectral path length.

Another PVG experimental set was conducted to investigate As, Sn, and Cu while applying several concentrations of formic acid (20 – 50 % v/v). The results are shown in **Figure (7-14)** which indicates 40% v/v is the optimal concentration. In comparison to the signals recorded previously from the HG scheme, the As signal has a lower intensity, whereas Sn signals are higher. No trusted signal was observed for Cu even when applying 50 % v/v formic acid.

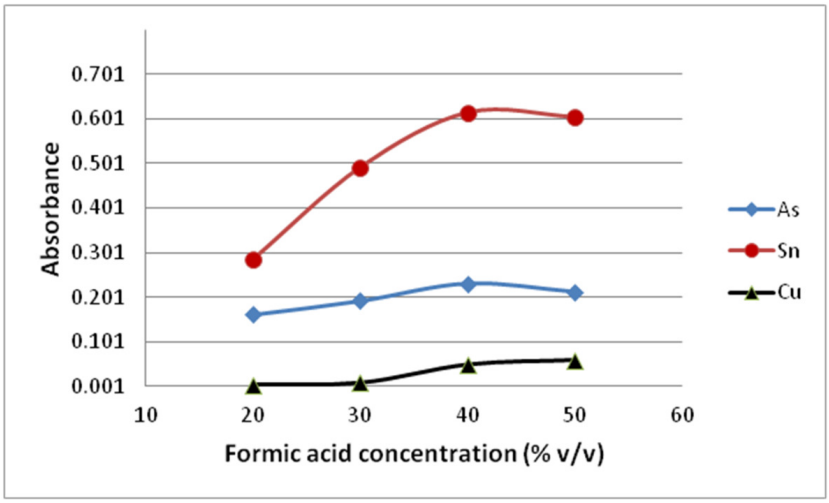

Figure 7-14 the effect of applying different concentrations of formic acid on the analyte absorbance recorded upon injecting100 µg/L of the examined elements at 150 watt power, 105 ml/min argon flow rate and two cascade DBD atomizers.

The signal recorded when injecting 100 µg/L of tin impregnated with 40 % v/v of formic acid is shown in **Figure (7-15)**.

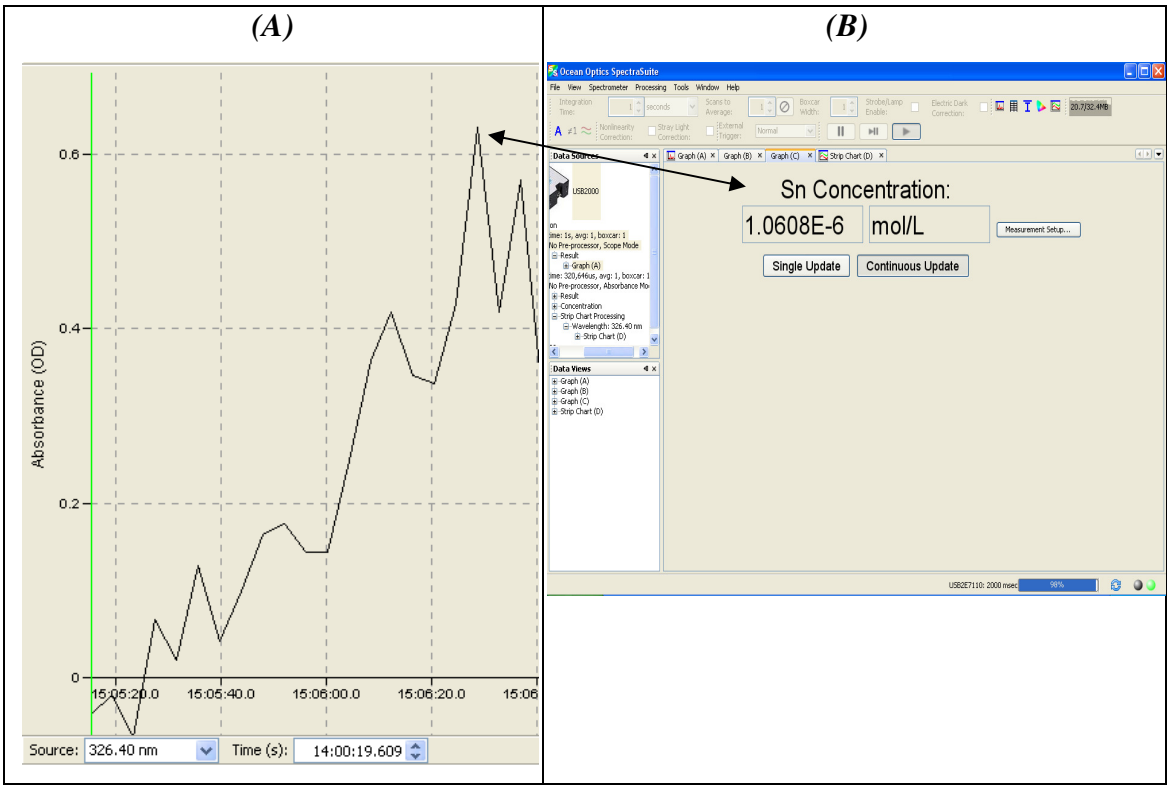

Figure 7-15 the photo-chemical reduction for a sample contains 100 µg/L tin;
The sample has been impregnated with 40% v/v formic acid and injected through two cascade DBD atomizers at 150 watt power; (A) a strip chart illustrates the recorded signal (B) the estimated concentration by applying 18.9×10^4 (L/mol/cm) molecular absorption coefficient.

It can be observed in **Figure (7-15)** that the estimated concentration based on applying the molecular absorption coefficient related to HG scheme results in a 20% error, which clearly indicates that a correction is required. The corrected molecular absorption coefficients for tin and arsenic are 21.5×10^4 and 6.3×10^4 (L/mol/cm) respectively.
According to the data, the estimated analytical figures of merit 3.6 (µg/L) LOD and 3.72% RSD for mercury, 5.73 (µg/L) LOD and 1.87% RSD for arsenic, as well as 3.27 (µg/L) LOD and 2.47% RSD for tin. The achieved detection limits are higher than those obtained from the HG technique but within the accepted limits in drinking water, shown in **Table (1-2)**.

7.6 Application of photo-chemical derivatization technique promoted with ultrasonic irradiation

As mentioned in **Section (2.4.3)**, it is hypothesized that UV radiation could be coupled with the ultrasonic irradiation for an integrated effect, which could be utilized to conduct both sample pre-treatment and analyte reduction. This section is devoted to test this hypothesis and to explore whether the proposed technique is applicable for derivatization of several elements. A sonic water bath (VWR ultrasonic cleaner, 45 kHz and 80 watt) was utilized to induce ultrasonic irradiation. The sample is injected through a peristaltic pump (2.8 ml/min) to the cascade annular DBD atomizer and to the later stages as described in **Section (7-5)**. A water sample containing (50 µg/L) Hg (II) was examined in the first instance, where the ultrasonic irradiation has been induced in parallel with injecting the sample to the DBD atomizer. The measured absorbance of the sample increased 22% upon being subjected to the coupled effects compared with effect from only UV radiation, (**Figure (7-16)**).
No enhancement was observed on the signals of 100 µg/L tin, arsenic, and copper upon coupling the aforementioned techniques. A clear amelioration on the absorbance signals of arsenic (by 2%) and tin (by 4.5%) was found when applying sonic irradiation for 15 minutes, whereas no signal is observed for copper even when applying longer periods.

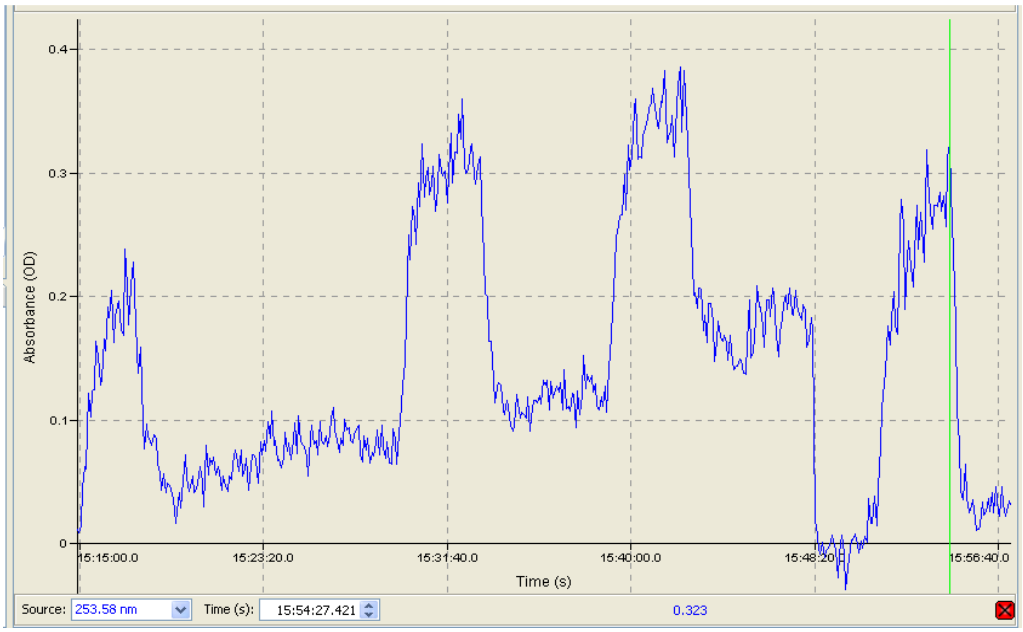

Figure 7-16 a strip chart illustrates two derivatization schemes for a water sample contains 50 µg/L Hg (II);
The first three peaks shows the signal recorded when applying the photo-chemical reduction of mercury through one annular cascade DBD atomizer at 150 Watt. The fourth peak shows the signal recorded upon emerging the sonic effect on the examined sample, which consequently magnifies the measured absorbance from 0.296 to 0.361.

The results could not be considered valuable for adoption in the final version of the integrated system. It is believed that, to induce considerable effects, the sonic effect must be inserted directly inside the sample. Practically, an online sonic effect could be implemented by utilizing miniaturized sonic probes inserted along the sample flow path before reaching the DBD atomizer.

7.7 Application of the proposed technology for the analysis of real water samples

A sample of drinking water (bottled natural mineral water – UK) has been tested to verify the measurements through the proposed techniques. **Table (7-1)** illustrates the values injected and recovered when applying $SnCl_2$, HG, and PVG schemes.

Table 7-1 the analytical results of a drinking water sample by applying three derivatization schemes ($SnCl_2$, HG and PVG – two stages)

Analyte	Amount detected µg/L	Added µg/L	Found µg/L			Recovery %		
			$SnCl_2$	HG	PVG	$SnCl_2$	HG	PVG
Hg (II)	NIL	10	9.1	9.3	8.8	91	93	88
As	NIL	10	--	8.6	8.3	--	86	83
Sn	NIL	10	--	9.1	8.7	--	91	87
Cu	>100	--	--	>100	--	--	--	--

It can be observed in **Table (7.1)** that the estimated copper concentration in the examined sample exceeds the limits of the workable range in the current study (100 µg/L). The reason can be attributed to interferences with unknown species which consequently lead to considerable fluctuations in the recorded spectrum, (**Figure (7-17)**). The determination of copper was repeated three times; one run showed a concentration of 66 µg/L (Absorbance = 0.265), whereas two runs showed copper concentrations exceeding 100 µg/L (Absorbance = 0.532, 0.57). In order to validate the measurements, the mineralized water sample has been analyzed via ICP-MS (Kroto research institute – The University of Sheffield). The results showed that traces of Hg (0.1 µg/L), As (0.4 µg/L), Sn (2.04 µg/L), and Cu (1.8 µg/L) are detected which are found below the detection limits of the proposed DBD system in this study. The results also show high concentrations of Ca (19392.8 µg/L), Mg (4291 µg/L), Fe (48.1 µg/L), Ba (40.3 µg/L), Sr (99.8 µg/L) and traces of other metals. The existence of other elements in the water sample results in interferences with the copper signal, (324.55 - 324.92 nm). Although Mg is known to be less active for chemical vapour generation procedures *(Matousek, 2007)*, the interferences most likely resulted from Mg (IV & VI), which is normally detected at spectral lines (324.253, 324.655, and 324.79 nm).

Further experiments were conducted by spiking the mineralized water sample with 100 µg/L copper and measuring the concentration via three techniques. Upon applying the HG technique in the DBD system, an absorbance of 0.653 is detected. The increased absorbance of copper indicates that the selected wavelength for copper determination is applicable for the test but interferes with other species in the sample, i.e. Mg.

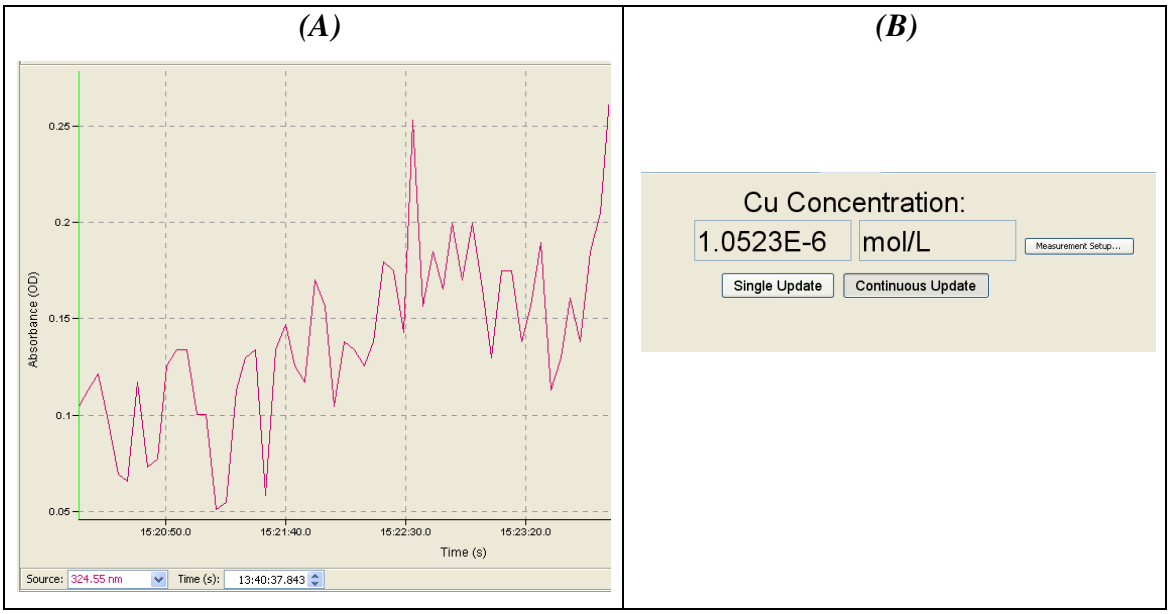

Figure 7-17 copper determination in the mineralized natural water sample; a molecular absorption coefficient equal to 9.5×10^4 (L/mol/cm) has been applied

A similar result is obtained when testing the spiked sample through ICP-MS, where a concentration of 121µg/L is determined. Further determination of the spiked sample via ICP-OES (Chemistry department – The University of Sheffield) shows 17.2 µg/L Cu (measured at 324.75 nm) is detected in the sample. Lower concentrations are determined at other wavelengths (e.g. 7.7 µg/L at 219.2 nm).

To sum up, the selection of appropriate wavelength for the examined analyte is crucial for the sensitivity of spectrometric analysis.

Other experiments were conducted to analyse a real waste water sample (digested sludge). The pre- treatment scheme was applied by utilizing one cascade atomizer and circulating the sample for 10 minutes. The biological oxygen demand (BOD_5) and the chemical oxygen demand (COD) were measured before and after treatment using reagents purchased from (Hach Lange - UK) and applying the protocol specified by the company, (**Appendix 11.10**). The results show a reduction of 30% and more than 70% in the values of COD and BOD_5 respectively after plasma treatment. **Figure (7-18)** shows a picture taken for the samples before and after treatment. The colour of the treated sample changed from dark brown to whitish, which emphasizes the extensive treatment action achieved.

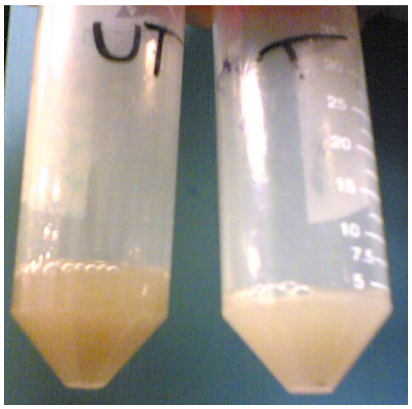

Figure 7-18 picture shows the digested sludge sample before treatment (UT) and after treatment (T);
The measured parameters before and after treatment are 3.11 and 2.2 g/L for COD and 550 mg/L and 150 mg/L for BOD_5.

The digested sludge sample has been analysed for mercury by applying the developed DBD system. No mercury signals were obtained from either untreated or treated samples. Hence, untreated samples were prepared by spiking 50 and 10µg/L Hg (II). These samples were examined with the $SnCl_2$ scheme and the measured values were 44 and 4.7 µg/L respectively. The absorbance was not stable, as shown in **Figure (7-19)**. The fluctuation in the signal could have resulted from other species in the examined sludge sample, which might scavenge the mercury.

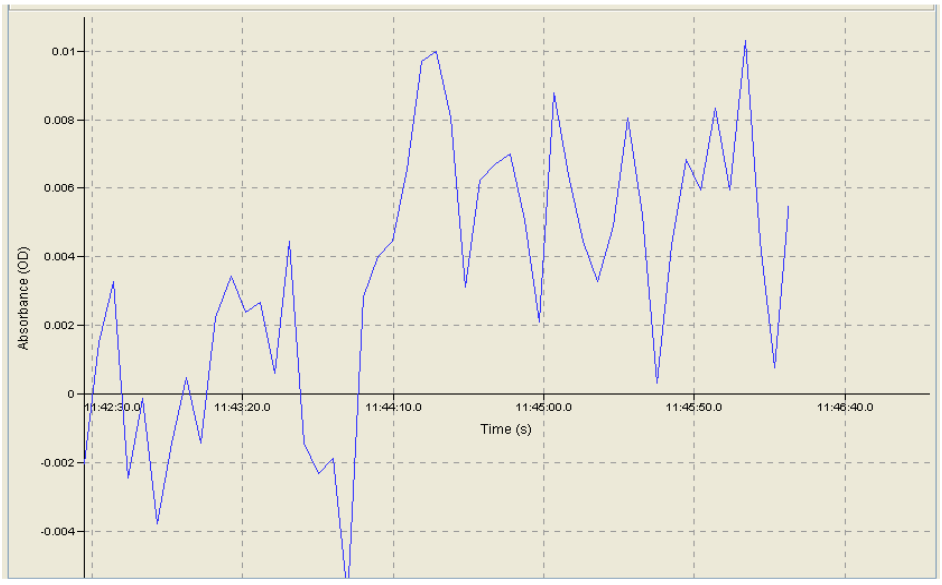

Figure 7-19 a strip chart for a mercury signal recorded upon injecting 10 µg/L Hg (II) in a digested sludge sample (before treatment);
According to the measured absorbance, 2.38×10^{-8} mol/L is estimated for the mercury concentration which is equivalent to 4.7 µg/L.

A similar experiment was conducted with a sample of treated digested sludge. The sample was been spiked with 50 µg/L Hg (II) and examined through the $SnCl_2$ scheme. The signal was more stable with lower fluctuation, which indicates the treatment results in more stable performance.

7.8 Summary of the findings from chapter seven

1- A cascade annular DBD atomizer has been utilized for sample pre-treatment and photo chemical reduction of the analytes.

2- Samples containing 0.5 OD_{595} *E.coli* grown in LB nutrient media and treated by circulating through the annular cascade DBD atomizer resulted in a reduction in viable cell number by three orders of magnitudes after only 5 minutes treatment.

3- The treatment scheme is found to be very effective on artificial samples spiked with various organic compounds. A 50% reduction in acetic acid occurs after 10 minutes treatment. It is also observed that the UV radiation inside the bulk of DBD atomizer is more effective compared with the effects produced from other factors such as increasing the power exerted on the atomizer.

4- The treatment scheme was also tested for the treatment of real wastewater (digested sludge); the results show a significant reduction in BOD_5 and COD, by more than 70% and 30% respectively, occurs after treating the sample for 10 minutes.

5- The application of several DBD atomizers for heavy metals determination was accomplished by coupling the annular DBD cascade atomizers with a final atomization stage based on a rectangular atomizer. The first stage atomizers were used for analyte photo chemical reduction, after which the generated vapour species were separated and carried to the final atomization stage for spectrometric analysis. Three out of four elements were measured by applying the aforementioned scheme with good accuracy. Efficiency was further increased by coupling online sonic irradiation. Since indirect and limited sonic irradiation is applied from a water bath, the enhancement in signal intensity is found to be valuable only in the case of mercury. Better results are obtained upon subjecting the sample to a longer irradiation period before introducing the sample to the cascade annular DBD atomizer.

6- The application of the proposed scheme for mercury determination in real waste water samples proved to be useful, obtaining good determination. Nonetheless,

considerable fluctuations are observed in the recorded signal, attributed to interferences from other species in the untreated digested sludge sample. Lower fluctuations in the signal are observed after treating the sample, indicating that treatment ameliorates the system performance.

8. A PROTOTYPE SYSTEM FOR HEAVY METALS DETERMINATION

8.1 Preface

This part of work is to assess a prototype system for heavy metals determination. The description of the proposed integrated design is presented in two main sections. In the first section, a design for a separation stage coupled with cryogenic trapping is discussed. By applying the cryogenic separation coupled with the controlled heating, better separation is induced in the system. The second section is devoted to utilize a combination of magnetization and ultrasonic irradiation, which are imposed on the sample flowing through a channel toward the cascade DBD atomizers. Finally, a custom design model for a portable device is presented based on the suggested stages.

8.2 Design, fabrication and test of the integrated cryogenic separation stage

It is mentioned earlier (**Section (2.5.10)**) that cryogenic trapping with liquid nitrogen has been applied in several studies and aimed at separating different species based on their boiling points. An integrated separation process based on two stages; where a miniaturized gas liquid separator of type (A) is coupled with a second separation stage based on the concept of cryogenic trapping was designed. The separated vapour species with a carrier or other gases generated in the system (e.g. hydrogen), are transferred from the gas separator into another separation media surrounded by an extreme cooling agent (liquid nitrogen). The separation space in the cryogenic stage is occupied by an adsorbing media (Chromosorb G/AW-DMCS 45-60 mesh, purchased from Sigma Aldrich) used to capture the vapour species and the gases having a boiling point higher than liquid nitrogen (-196˚C). The captured species are released by gradual heating via a Tungsten coil inserted inside the adsorbing media. The heat is supplied by applying electrical pulses for selected periods. The Tungsten coil is connected to the power supply operated through a microcontroller (Arduino – Mega) and PC software. The gradual heating method was adopted in order to overcome thermal effects in the adsorbing media.

Preliminary experiments were conducted using a custom made liquid nitrogen cold trap (3 litre), in which the examined stream is injected through a borosilicate glass U-tube (60 cm length and 6 mm ID) filled with the adsorbing media. The U-tube was immersed

in a Styrofoam container filled with liquid nitrogen and provided with a secure PTFE lid *(Abdul-Majeed et al., 2012)*. The heat was induced sequentially by electrical pulses through an electric rope heater wrapped on the U-tube and controlled by the microcontroller. The experiments investigate the use of helium gas as a carrier for the released species when applying the sequential heating. Since helium boiling point (-268.9˚C) is lower than that of liquid nitrogen, it passes through the U-tube directly without being trapped inside the bulk, provided that it is supplied with sufficient pressure. This step has been checked by recording the spectrum of helium plasma generated in a DBD atomizer. The results have shown that no change in the spectrum is observed before and after passing the cryogenic trap.

Further experiments were conducted for a mixture of helium-water vapour directed from a gas liquid separator toward the cold trap. The helium plasma was not affected due to the presence of water vapour in the inlet stream, which means the water vapour has been detained inside the cold trap.

Cryogenic trapping becomes more effective when hydrogen gas exists in the examined stream. Since the hydrogen boiling point (-252.87 °C) is lower than the liquid nitrogen, hydrogen is expected to pass through the U-tube while the accompanying vapour species is detained by the adsorbing media. After the hydrogen totally releases from the system, helium gas is injected into the cold trap while applying sequential heating in the same time; thereby the helium is carrying the released species gradually toward the plasma stage, based on their boiling points. Since the HG scheme is the most reliable scheme, integrated separation coupled with cryogenic trapping is believed to be the best way to overcome the hydrogen effect on the recorded spectrum mentioned in previous chapters. Moreover, the species of interest are distinguished based on their release time. Consequently, this technique offers the ability to discriminate between species of similar wavelengths.

Further experiments were applied to explore the feasibility of cryogenic separation for a system working in accordance with HG scheme. These experiments generate the hydrogen by catalytic decomposition of $NaBH_4$ using a cobalt catalyst in a small scale packed bed reaction column; (see **Appendix 11.11**). The generated hydrogen, with the accompanying residues of water vapour and alkaline mist, is forwarded to the U-tube liquid nitrogen cold trap. Hydrogen concentration is measured, before and after the cold trap. Although traces of water residues are found in the stream, utilization of the cold

trap leads to a reduction in water vapour and alkaline mist, and a consequent increase in hydrogen in the outlet stream. The encouraging results directed the author to design a prototype device based on coupling a gas-liquid separation stage with a cryogenic trapping (GLS-LNCT), as shown in **Figure (8-1)**. The full details of the design are presented in **Appendix 11.12**.

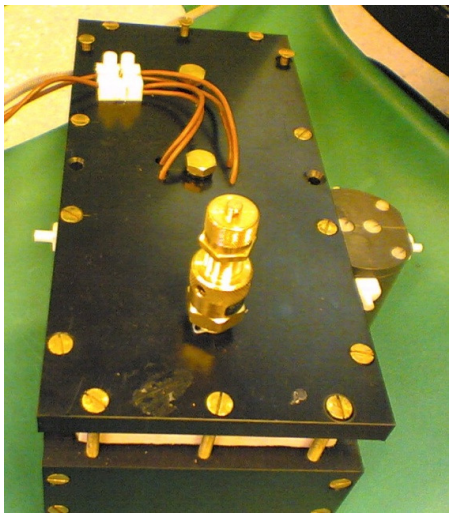

Figure 8-1 a picture shows the gas liquid separation stage coupled with cryogenic trapping, in one device, given a name (GLS-LNCT).

In the pre-commissioning test, the cryogenic section was filled with 200 ml liquid nitrogen times and subjected to continuous heating through the Tungsten coil; it was observed that the liquid nitrogen run out in 8 – 10 minutes. Although this is enough time to implement at least one full test, it is still essential to increase the insulation efficiency to keep the liquid nitrogen for more time, especially when using the device for in-situ and online monitoring.

In the first instance, the GLS-LNCT was tested after loading the Chromosorb material in order to optimize the gas stream pressure required to pass through a 6 cm packed layer. The first test was with helium without loading the liquid nitrogen or heating. The results show a gauge pressure of 1.2 bar is required to pass through the Chromosorb layer; this is checked by forwarding the helium toward the DBD atomizer and igniting the helium plasma. Upon loading the liquid nitrogen, the intensity of helium decreases significantly as a result of a tiny amount of helium released from the trap. Accordingly, the inlet pressure of helium was increased to 1.5 bar which gives a stable performance of the GLS-LNCT. The other observation is that the plasma was extinguished due to the effect of cooling; hence, higher power is required to break down the cooled helium

stream released from the GLS-LNCT. One possible cause for extinguishing the plasma stems from traces of nitrogen vapour escaping from the liquid nitrogen reservoir and mixing with the helium gas in the separator, which consequently leads to an increased power requirement for the breakdown. Some changes are observed in the helium spectrum recorded after loading the liquid nitrogen, represented by the appearance of several peaks (e.g. 215.38, 226.76, 236.98, 246.8, 258.1, 266.36, 270.87, 284.73 nm) as shown in **Figure (8-2)** which were not observed before. These peaks are attributed to the γ band of NO_x at 220-280 nm *(Hong et al., 2008, Zhu et al., 2008a)*. The formation of NO_x is possible at high energy levels such as a plasma and is expedited by increasing the power and the humidity *(Iskenderova et al., 2001)*.

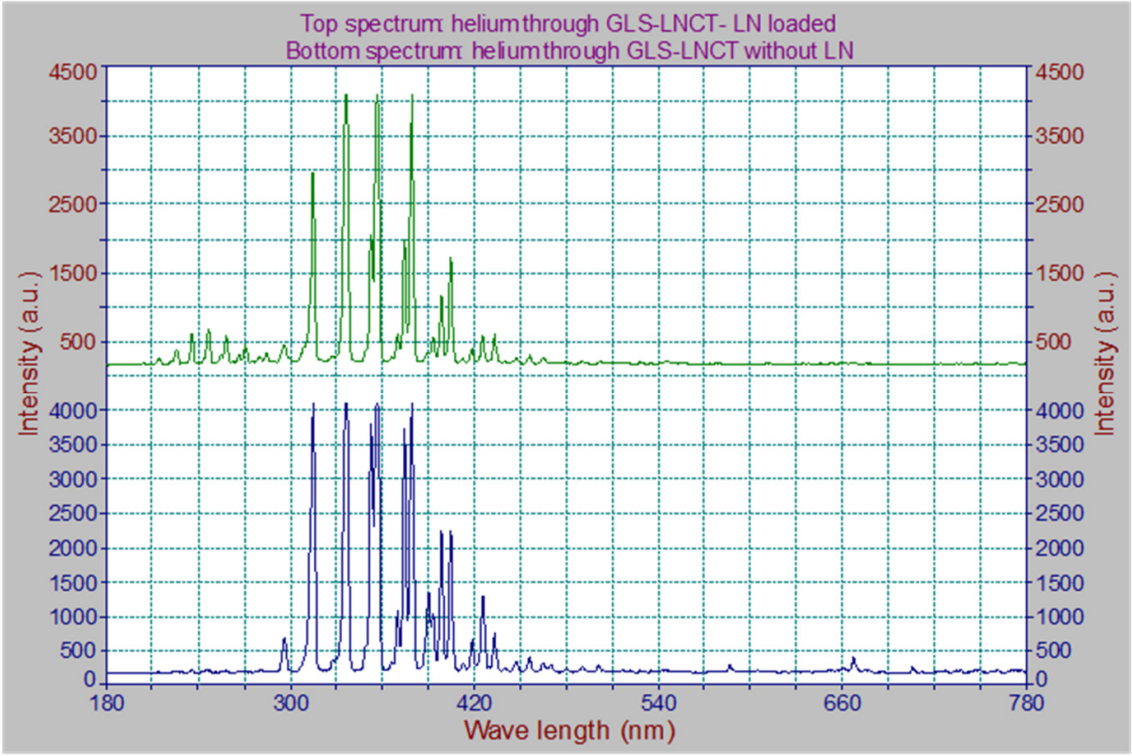

Figure 8-2 a comparison between the helium spectrums obtained before (bottom spectrum) and after loading the liquid nitrogen (top spectrum) to the GLS-LNCT.

The vaporized nitrogen from the liquid nitrogen reservoirs transfers to the centre reservoir, shown in **Figure (11-6)** – (**Appendix 11.12**), because of leakage from the top insulation layer. This indicates that the constructed top section of the GLS-LNCT is not

secure, and requires some modifications. However, the appearance of the abovementioned peaks, which occurs due to the nitrogen, supports the interpretation given in chapter four (**Section (4.4.3)**) regarding the spectra shown in **Figure (4-7)**. Hence, a conclusion is drawn the peaks to the left hand side of the spectra could be related to pure nitrogen or unknown species generated from surface reactions.

The GLS-LNCT, loaded with liquid nitrogen, was tested for inorganic mercury determination. The recorded spectra are shown in **Figure (8-3)**.

(A)

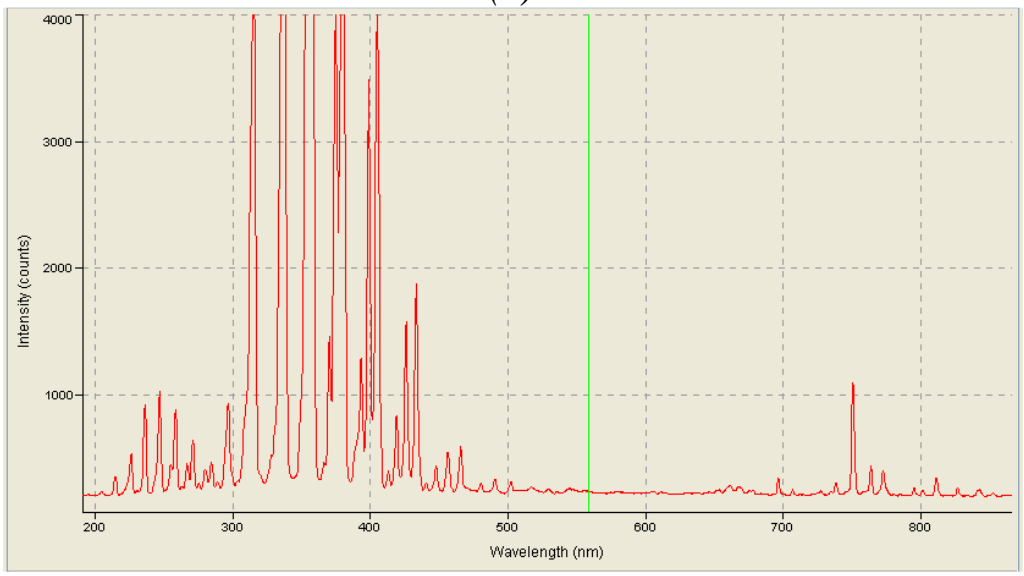

(B)

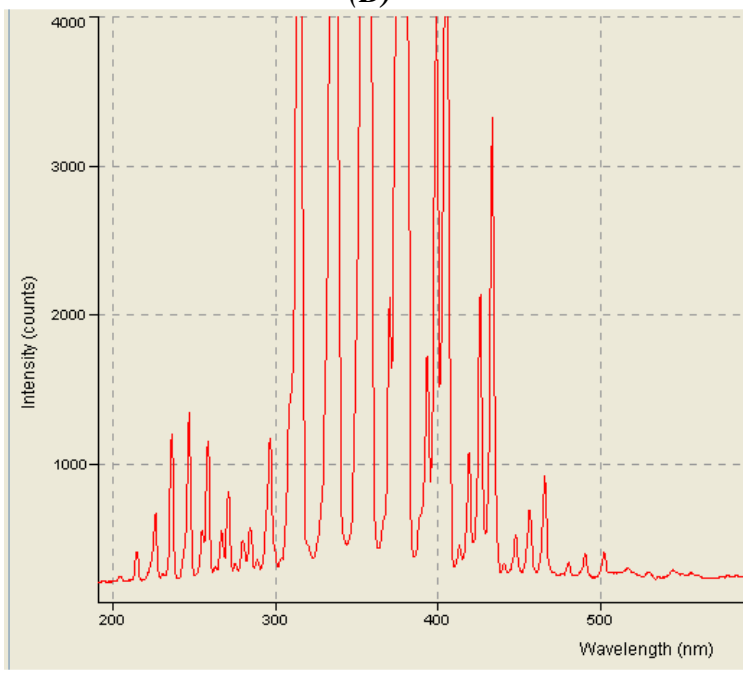

(C)

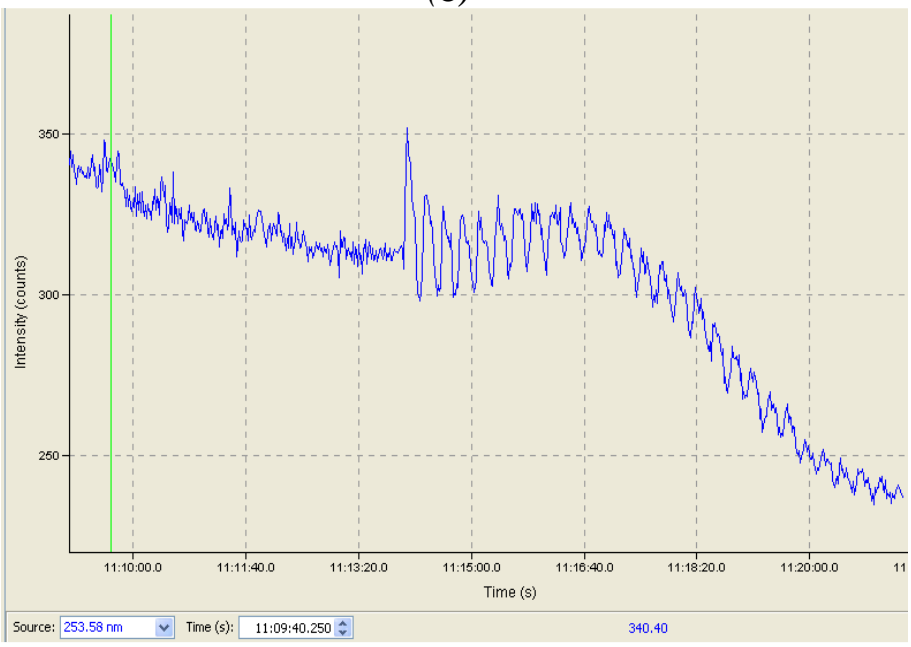
350
300
250
Intensity (counts)
11:10:00.0
11:11:40.0
11:13:20.0
11:15:00.0
11:16:40.0
11:18:20.0
11:20:00.0
Time (s)
Source: 253.58 nm
Time (s): 11:09:40.250
340.40

(D)

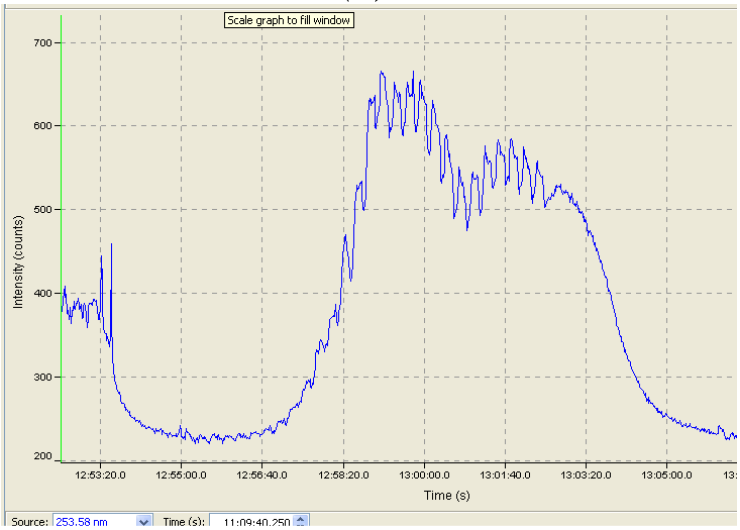
Scale graph to fill window
700
600
500
400
300
200
Intensity (counts)
12:53:20.0
12:55:00.0
12:56:40.0
12:58:20.0
13:00:00.0
13:01:40.0
13:03:20.0
13:05:00.0
Time (s)
Source: 253.58 nm
Time (s): 11:09:40.250

(E)

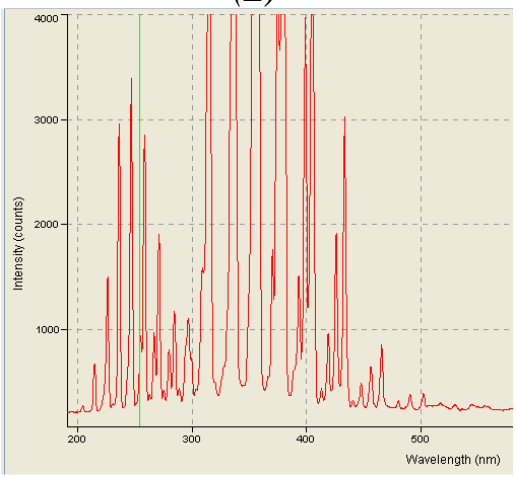
4000
3000
2000
1000
Intensity (counts)
200
300
400
500
Wavelength (nm)

(F)

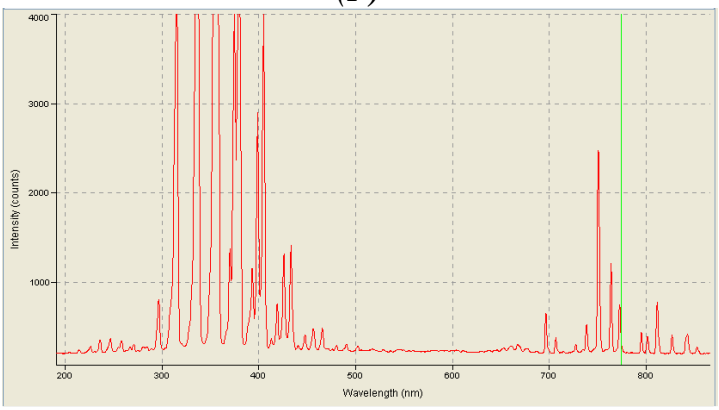

Figure 8-3 the recorded spectrums for a mercury vapour generation process coupled with GLS-LNCT;
The experiments conducted by injecting water solution contain 50µg/L Hg (II) acidified with (1 *M* HCL) and applying hydride generation scheme by using (1.5 % m/v $NaBH_4$). (A) the spectrum recorded when only argon and helium gases entered through the GLS-LNCT in presence of liquid nitrogen, (B) the spectrum recorded upon injecting the mercury sample and $NaBH_4$ streams to the system, (C) a strip chart for mercury signal at 253.58 nm recorded when applying 10 seconds heating pulses, (D) a strip chart for mercury signal recorded when applying 25 seconds heating pulses, (E) the recorded spectrum when applying 25 seconds heating pulses show the significant increase in the peaks' intensity to the left hand side, (F) the recorded spectrum after the liquid nitrogen escaped from the system, the case represented by the increased signal intensities of the peaks to the right hand side and diminished peaks to the left hand side

Figure (8-3/A) shows the spectrum recorded for a system running in presence of argon and helium before introducing $NaBH_4$ to the system. Clear signals of argon and other species (probably oxygen) at low intensities are observed in the spectrum, which means the applied cooling rate is not enough to retain these species inside the cold trap (The boiling points of oxygen and argon are -183 and -186 ^{o}C respectively). The introduction of $NaBH_4$ to the system results in hydrogen generation, which is represented by the magnification effect on the peaks below 400 nm, as shown in **Figure (8-3/B)**. The later stage is related to the mercury species release from the adsorbing agent with aid of heating pulses. Since extreme cooling is expected to occur inside the trap, mercury vapour condensation on the adsorbing agent is highly possible. Mercury species release commences after evacuating most of the hydrogen from the cold trap, aided by purging by helium, which is estimated to take place within 30 – 60 seconds after stopping the sample injection to the system. The heat supply to the trap was applied in a sequential

form in order not to affect the adsorbing media. Two schemes of heating strategy were tried. The first adopted 10 seconds for the heat pulse with a 3 second gap between pulses. The second scheme applied a 25 second heating pulse with a 5 second gap between pulses. Results are shown in **Figure (8-3/C-D)**, where longer heating pulses result in higher signal intensities for mercury. The heating pulses affect all the peaks in the spectrum; however, more effect is observed for peaks to the left hand side as shown in **Figure (8-3/E)**. Peak intensity increases when heat is supplied to the trap, while the signal decreases in the period between the pulses, which consequently produces a sinusoidal shape for the recorded signal, as shown in **Figure (8-3/C-D)**. There are three stages. The intensity decreases in the first stage as a result of the hydrogen effect. The second stage begins after hydrogen is totally released from the system, where the mercury intensity increases with the heating pulse length and then starts to decrease and increase again in a sinusoidal form due to the applied heat. The third stage is a continuous decrease in signal intensity, which indicates that all mercury has been released out of the trap. In this final stage, the intensity of the peaks to the right hand side of the spectrum increase while the peaks to the left hand side decrease as a result of the liquid nitrogen running out from the system, (**Figure (8-3/F)**).

Further experiments targeted the simultaneous determination of mercury and tin. The recorded strip chart (**Figure (8-4)**) shows three stages as described above.

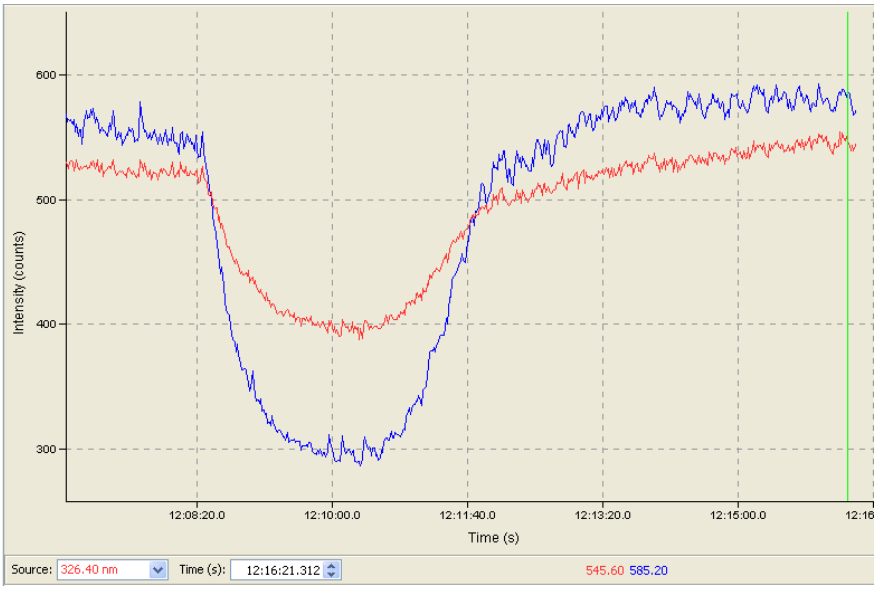

Figure 8-4 a strip chart show the signals of mercury and tin that determined simultaneously by applying the hydride generation scheme coupled with GLS-LNCT; The examined stream contains 50µg/L of both *Hg (II)* and *Sn*, acidified with (1 *M* HCL) and applying (1.5 % m/v $NaBH_4$) as a reducing agent.

According to *(Grüter et al., 2000)*, the boiling point of tin hydride (SnH_4) and mercury species is -55 ^oC and 80 ^oC respectively. Since there is a considerable difference between the boiling points, it is expected to observe a clear signal for tin hydride. However, the increase in the signal intensity is limited even when increasing the heating pulse length to 30 seconds. Most importantly the increase in the signal intensity of mercury which is very limited compared with the result obtained when only mercury is applied in the system, (**Figure (8-3/D)**).

This result could be attributed to a limited efficiency when applying heating and cooling inside the cold trap, or to the instability of the spectrum demonstrated by the peaks appearing to the left hand side.

This result indicates that the design of the interior section of GLS-LNCT requires two modifications: the first is to enhance the insulation between the interior section and the outside environment. The second is to the container of the adsorbing media. It is believed that a miniaturized U-tube wrapped with a Tungsten wire or rope heater, (**Appendix 11.11**), will be efficient for the cryogenic separation. The U-tube is loaded with the adsorbing agent (Chromosorb) and inserted directly in the liquid nitrogen. The gaseous stream from the GLS will pass through the U-tube and reach the DBD atomizer. By applying this methodology, the generated hydrogen and helium are expected to leave the U-tube directly whereas hydrides are retained inside the trap. The captured species could be released through a gradual heating as mentioned earlier. This modification is planned for future work.

8.3 A novel approach to heavy metals detection and determination based on photo chemical reduction promoted with physical effects

The aim of the current work is to integrate all techniques studied in this research to produce a fully integrated system for heavy metals determination. According to the results of the previous sections, the hydride generation scheme is the most reliable technique for the metals, studied even with practical limitations due to the generated hydrogen and the alkaline mist in the system. Although a solution to the hydrogen problem has been attempted through GLS-LNCT, the continuous consumption of liquid nitrogen is still a barrier, therefore further work is required to produce a system with sufficient thermal insulation. An alternative technique to the HG scheme is to apply

photo chemical reduction of the elements which is promoted with ultrasonic irradiation. This technique may enhanced by applying sample magnetization.

An integrated system based on the proposed stages is shown in **Figure (8-5)**, where the examined sample is injected through a channel subjected to the effects of a strong magnetic field and ultrasonic irradiation. In order to induce these effects, a channel with sufficient length is required; therefore a corrugated rectangular or circular channel is proposed. An aluminium alloy block might be the best option, in which a strong magnetic field through a coil wrapped along the corrugated channel could be imposed. If other alternatives such as lined ferrous alloys resistant to corrosion from aqueous acidic media are used, then permanent magnetic poles could be attached around the channel to induce the required magnetic field.

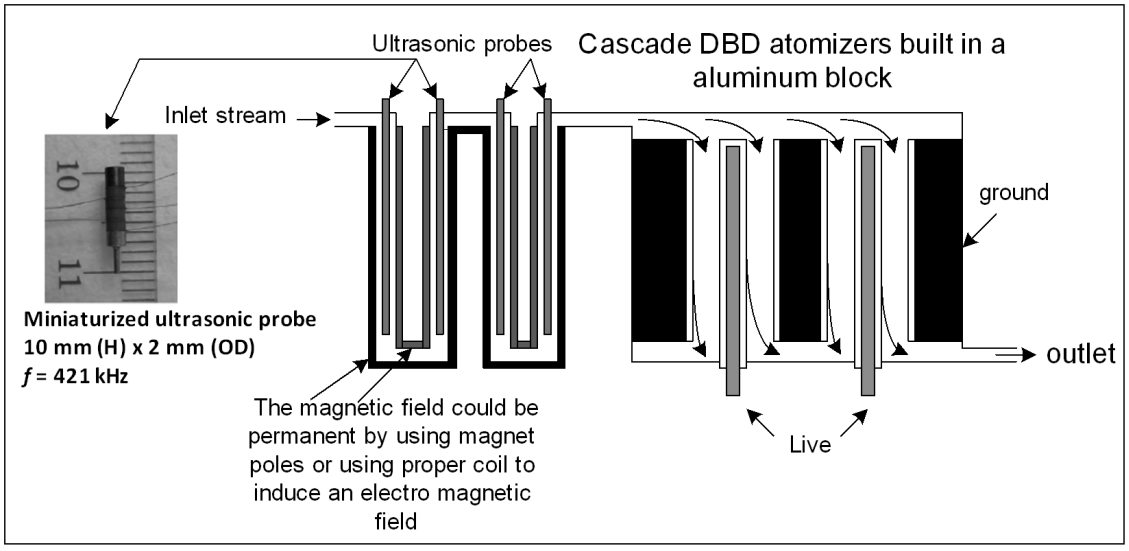

Figure 8-5 a proposed design for a chemical photo reduction stage preceded by physical effects induced by magnetization and ultrasonic irradiation stages.

Practically, the electromagnetic field is more preferable for sample magnetization compared with the permanent field because the field strength and the exposure time can be controlled through changing the applied power via the microcontroller used earlier in this research. Since advantageous effects are observed in **Section (5.6)** and **Section (6.2.1)** upon subjecting the sample to 0.3 Tesla magnetic fields for 14 hours, therefore it is speculated that the required field strength should not be less than 1.0 Tesla, which could be generated through a coil wrapped along the channel of interest.

Ultrasonic irradiation is planned through specific miniaturized probes available commercially. In order to introduce extreme irradiation in direct contact with the aqueous bulk, it is preferable to use immersion-type ultrasonic transducers. The advantage of this type is uniform performance and sensitivity as well as high speed response.

The transducers must be able to induce at least 200 kHz which is expected to be highly effective since the probe will be in direct contact with water sample. The expected performance is folds higher than the indirect ultrasonic irradiation applied in previous experiments (45 kHz).

An acidified sample (by applying 30 – 40 % v/v formic or acetic acid) should be injected to the DBD system, the photo chemical reduction of the analytes then occurs through the consecutive stages of DBD cascade atomizers shown in the last part of the suggested design. In addition to PVR, an extra treatment of biological and organic contaminants is achieved in the DBD atomizers; eventually, producing fragmented species. The fragments dissociate in the final rectangular DBD atomizer for spectrometric analysis.

8.4 Summary of the findings from chapter eight

1- Two approaches are presented to enhance the performance of the technology. In the first approach, the coupling of a gas liquid separation stage with cryogenic trapping is investigated. In the second approach, a novel design, based on coupling the photo-chemical vapour generation with two physical effects is described and utilized for producing a fully integrated system rather than the traditional hydride generation scheme.

2- A considerable discrepancy was observed upon testing the developed GLS-LNCT, attributed to deficiencies in the constructed prototype as well as the design itself. Nitrogen escaping from the reservoirs mixes with the applied gases (helium and argon), which consequently extinguishes the DBD plasma as well forming *NO* species, represented by the peaks appeared to the left hand side of the spectrum.

3- Although the disruption occurs, the developed GLS-LNCT proves useful when used for mercury determination by the hydride generation scheme. In this regard, the system performs as expected and the generated hydrogen is released from the trap, while the mercury species are retained by the adsorbing agent. In a later stage, the mercury species are released from the system by applying sequential heating.

4- Nonetheless, the performance of the GLS-LNCT is found to be very poor for the simultaneous determination of mercury and tin. The signals are produced with lower intensities even when applying longer heating pulses. The results indicate that some modifications to the prototype are essential for better system performance.

5- Two changes are proposed, the first is the use of an efficient insulation material for the interior section, the second is a glass U-tube wrapped with a heating coil to achieve the cryogenic trapping and release.

9. CONCLUSIONS AND RECOMMENDATIONS FOR FUTURE WORK

9.1 General conclusions

Several techniques and different strategies are described in the literature for heavy metal determination in different solid and liquid samples, achieving low detection limits. In practice, most of these techniques have many operational problems such as limited speed of detection and non stable performance, which makes them impractical to use for continuous online – real time analysis of wastewater from industrial applications. Plasma spectrochemistry devices (e.g. ICP-OES) have shown better performance and proved to be robust for long term operations inside laboratories. The working principal of these equipments utilizes spectrometric analysis that totally depends on the atomic structure rather than monitoring changes in the chemical properties of the examined species. This feature led to the wide spread use of plasma analytical devices in recent years. Nevertheless, plasma spectrochemistry devices are still expensive bulky instruments that require skilled labour, high analytical costs, additional pre-concentration procedures, and long operational times. Such instruments are found to be impractical for online and in situ analysis.

Alternatively, we attempted in this research to utilize dielectric barrier discharge plasma atomizers for heavy metal determination in water samples. Several reasons are behind the selection of this type such as high electron energy and low operating temperature, which suggests the possibility of embedding the atomizer with other components in proximity. Eventually, a DBD atomizer could be utilized as a basis for producing a portable device.

The production of a miniaturized portable system, based on plasma spectral analysis, requires an efficient sample introduction technique. The chemical vapour generation (CVG) technique was selected for the current research as an alternative to the desolvation/nebulisation processes which is normally applied in traditional spectrochemistry devices. The CVG technique could achieve efficient sample introduction as well as having other advantages such as limited consumables and space requirements.

Since the proposed technology combines multiple stages and starts with chemical derivatization procedures to be finalized with species atomization in the DBD atomizer, it was essential to deduce the optimal design and operational parameters required for

best system performance. Accordingly, several mathematical investigations were conducted in this research exploring the chemical reaction mechanism, the gas liquid separation stage and the atomization stage. The results show that a reaction mechanism based on the hydroboron intermediate species formation is the best for design integrity; the calculation shows that a 5 cm length of reaction coil is required to achieve full conversion of the analyte into the vapour hydride. Further mathematical investigations are dedicated to examine the performance of a custom design nebulizer-gas liquid separator and the atomization processes in two kinds of atomizers. The computations show that a 200 ml/min gas flow rate is appropriate to dilute the hydrogen gas before entering the DBD atomizer. The simulation of the atomization process in a DBD atomizer shows that arsenic hydride is totally dissociated into free arsenic atoms before reaching the electrode section of the DBD atomization channel. Another informative result is related to the free analyte concentration distribution along the atomization channel, which shows that the concentration of free arsenic atoms saturates to a maximum in the first section of the atomizer and does not change in the following parts of the channel. This result conceives the ability to apply spectral data acquisition radially from any position along the atomizer, which has been verified in later experimental investigations. The results show that similar signal intensities were obtained from two different positions along the channel, whereas a higher signal intensity (by 40%) is obtained from an axial position at the end of the atomization channel. Hence, the axial position was adopted for the experimental investigations in this research.

The proposed design for a rectangular DBD atomizer is shown to be efficient for analytical purposes; this is deduced by estimating the operational parameters and plasma characteristics. The estimated electron temperature (T_e = 0.849 eV) is found to be higher than the excitation temperature (T_{exc} = 0.55 eV) and the rotational temperature (T_{rot} = 0.064 eV), which indicates a non-thermal plasma is generated in the proposed chip. The estimated electron number density (3.1×10^{17} m^{-3}) shows good agreement with the range reported in literature, which denotes a bulk of high dissociation energy. The generated characteristic diagram, the Lissajous figure, demonstrates that filamentary discharges are produced in the examined system; this has been interpreted by the parallelogram shape produced in the charge/voltage characteristic diagram.

Operational parameters such as gas flow rate and applied power are found to be key factors affecting the appearance and consistency of the spectral lines of interest. An optimization study and statistical analysis shows that the gas flow rate is a critical factor needed to be controlled accurately during the course of the analytical run, whereas the applied power is found to be a key factor for best system performance.

The rectangular DBD atomizer has been coupled with the reaction scheme and used for mercury determination in water samples by applying tin chloride ($SnCl_2$) and sodium hydroborate ($NaBH_4$). Both schemes act efficiently for inorganic mercury determination and accordingly reasonable detection limits obtained from both schemes in accordance with the standard limits of mercury in drinking water. Nevertheless, the $NaBH_4$ scheme found lower detection limits of 2.19 µg/L compared with 2.8 µg/L from applying $SnCl_2$ scheme.

The $NaBH_4$ scheme has also been shown to have a major problem related to hydrogen generated in the system. The hydrogen affects the recorded spectrum and misleads the interpretation. The problem is solved by using two experiments for each studied case. In the first experiment, only acidified water is injected in parallel with $NaBH_4$ solution to the reaction coil and the signal intensity recorded due to the hydrogen magnification effect. In the second experiment, the analyte was spiked in the acidified water and the recorded signal has included the effects from the examined analyte as well as the hydrogen effect. The difference between the two signals is attributed to the injected analyte. The quantitative determination of mercury has also been conducted by applying the abovementioned schemes and adopting an absorption spectroscopy technique. The results are obtained with a 10% error.

Other investigations are conducted for a group of hydride forming elements and transition elements by applying the hydroborate scheme, achieving acceptable detection limits except for cadmium which is slightly high. The hydrogen magnification error has been treated by applying the same technique used for mercury. The quantitative determination of three selected elements is conducted using the same scheme, achieving reasonable determination accuracies. The estimated figures of merit for the examined group are illustrated in **Table (9-1)**.

Table 9-1 the figures of merit estimated for the examined group of elements by applying $NaBH_4$ scheme;
(*LOD* is the achieved limit of detections, *RSD%* is the relative standard deviation, and *QD-AAEE%* represents the average absolute error of estimate for the elements determined quantitatively)

Examined element (µg/L)	*LOD* (µg/L)	*RSD%*	*QD-AAEE%*	Std. limits in drinking water
Hg	2.19	2.19	9.13	6 (WHO)
As	3.7	1.82	11.8	10 (WHO)
Sn	2.13	1.29	9.51	<150 mg/kg
Cd	3.8	1.37		3 (WHO)
Pb	2.67	1.0		10 (WHO)
Cu	3.03	1.55	10.38	1000 (ECD)
Ni	6.04	2.19		10 (ECD)
Zn	4.08	1.54		5 (NCU)
Cr	6.02	2.52		50 (ECD)

In order to assess the developed system, the achieved detection limits of copper in the current research are compared with data extracted from literature for other technologies. The results are shown in **Figure (2-1)** - chapter two, which certainly indicate a competitive accuracy achieved from the developed technique. The privilege of the developed system is the ability to apply for in-situ or online analysis, as well as a possibility for connecting the device with control loops.

Conducting simultaneous determination for the examined elements is found to be a difficult task due to a variety in the derivatization conditions. Accordingly, an expanded experimental plan is conducted and the optimum values of the chemicals (1.46% m/v $NaBH_4$ and 1.2 M HCl) are deduced with aid of principal component analysis. The application of the concluded optimal values facilitates the qualitative determination of nine elements simultaneously, achieving reasonable accuracy. The achieved figures of merit denotes that the hydroborate scheme as a unique technique for heavy metals determination; however, extra work has been required to refine the results from the hydrogen magnification problem.

Practically, the adoption of HG scheme for the targeted portable device requires an efficient technique through which the hydrogen should be separated from the hydride before entering the DBD plasma atomizer. We applied a design for an integrated gas-

liquid separation stage coupled with a cryogenic trapping stage. The aim is to retain the hydrides on an adsorbing agent occupied in a bulk subjected to extreme cooling with aid of liquid nitrogen. While the hydrides trapped on the adsorbing agent surface, the hydrogen releases since its boiling point is lower than the liquid nitrogen. After releasing all hydrogen from the system, the hydrides released based on their boiling points with aid of sequential heating. The system has been tried in the first instance for inorganic mercury determination, where the results show that the system performs as expected. This conclusion is interpreted by monitoring the mercury signal during the experiment time, in which the effect of hydrogen on the mercury signals has been elucidated by a sharp reduction in the signal intensity. The intensity has increased in the later step, in a sinusoidal form, due to the sequential heating applied in the bulk, and finally the signal reduced sharply when the analyte has totally released from the trap. Nonetheless, the performance of the proposed separation technique is found not efficient when two elements examined simultaneously. The weakness in performance is attributed to shortages in both cooling and heating strategies applied in the system as well as some fabrication deficiencies. According to the obtained results, an alternative design for the interior section is proposed which is expected to implement higher separation efficiency.

Another technique is investigated based on applying the photo-chemical vapour (PVG) generation for the examined analyte by utilizing UV radiation generated inside the plasma reactor. Hence, a design for an annular cascade DBD atomizer has been proposed, fabricated, and explored as an alternative for the hydroborate scheme. The aim is to overcome the disruption occurs due to the hydrogen effect. The proposed PVG technique has been applied for mercury, two hydride forming elements (arsenic and tin) and one transition element (copper) determination. The application of the proposed scheme achieves competitive reduction efficiency compared with HG scheme in the case of mercury, whereas better reduction results obtained for tin. The reduction of arsenic by PVR technique results in lower reduction efficiency compared with HG scheme, while PVR scheme failed to achieve the expected results when applied for copper.

Further investigations applied to enhance the performance of the technique. In this sense, PVR scheme has been stimulated by the effect of ultrasonic irradiation generated from ultrasonic water bath. The application of PVR promoted with ultrasonic irradiation

proves useful for mercury determination, where the ultrasonic irradiation is induced in parallel with the sample injection. The results have shown the mercury signal enhanced by 22% due to the ultrasonic effect. Further experiments conducted in this sense to examine the arsenic and tin determination. The coupled PVR-ultrasonic scheme failed to achieve enhancement for arsenic and tin online reduction, whereas an increase in the signal intensity by 4.5% has been observed for tin upon subjecting the sample into local ultrasonic irradiation for 15 minutes before introducing the sample to the annular DBD atomizer. This result indicates that applying an optimized ultrasonic irradiation in direct contact with the sample might produce valuable effects rather than using only local irradiation effect from a sonic bath.

Other physical effects, gained from magnetizing the examined sample, are investigated. The results of magnetizing tap water sample for 14 hours via 0.3 Tesla magnetic fields have shown considerable permanent changes in the water physical properties. The electrical conductivity increases by 8% whereas a reduction in the interfacial tension and pH has also been observed. The reduction of interfacial tension lead to considerable increase in the mercury signal intensity by 7.5%, whereas 8% increase in the signal intensity observed for arsenic reduction aided with a pre-reducing agent. Increasing the magnetic field strength and the magnetization period is expected to induce further effects on the sample derivatization efficiency. Hence, an optimized magnetization conditions might act beneficially as an alternative for expensive chemicals normally used to enhance the reduction processes (e.g. surfactants).

It is believed that coupling optimized physical effects from sample magnetization and ultrasonic irradiation with further effects of UV radiation could be a unique combination for an effective reduction scheme. Hence, a design is proposed on that basis aiming to introduce all these effects while the sample being transferred through an introduction channel connected with the annular DBD atomizer. The application of this combination has been planned for future work.

The pre-treatment of the examined sample is investigated since a presence of several compounds may lead to significant interferences on the recorded spectral signals. The proposed pre-treatment scheme has been tested for treating artificial samples prepared by spiking organic and biological contaminants. A significant reduction observed in the concentration of acetic acid (by 50%) and the live cells of *E.coli* by 3 orders of magnitude upon circulating the sample through the DBD atomizer for 10 minutes.

The proposed system has been examined for determination of heavy metals in real water samples taken from two sources. The examination of bottled natural mineral water sample shows that no mercury, arsenic or tin detected in the sample, whereas more than 100 (µg/L) copper has been determined by applying HG scheme. Alternatively, 10 (µg/L) of mercury, arsenic, and tin are spiked in separate samples and determined quantitatively by applying several schemes. Higher recovered values are obtained relatively when applying the HG scheme compared with other schemes; however, more effort has been required to refine the results from the hydrogen effects. The analysis of the mineralized water sample is conducted through ICP-MS for analysis verification. The ICP-MS analysis show that only traces of (Hg, Sn, As, and Cu) are detected in the sample. The shift in the predicted copper concentration, via HG scheme, is attributed to interferences (e.g. with Mg).

Another real sample, a digested sludge collected from a wastewater treatment plant, has been examined by applying the developed system. The pre-treatment stage leads to a reduction in the values of BOD_5 and COD by more than 70% and 30% respectively. On the other hand, no mercury could be determined in the examined sample. Alternatively, the real samples spiked with inorganic mercury and examined by using $Sncl_2$ scheme without treatment. Lower determination accuracy achieved for the samples spiked with low mercury concentration (10 µg/L), which has been attributed to the interferences occurs due to the existence of unknown species in the sample. This result has been confirmed by repeating the determination for a sample treated by plasma effect. The recorded signals have shown more stability and less fluctuation obtained in the signal. Therefore it becomes certain that sample pre-treatment enhances the determination accuracy.

9.2 Directions for future work

It is required to apply more experimental investigations to explore the performance of the developed system after applying the modifications in the design of GLS-LNCT, as suggested in **Section (8-2)**, as well as testing the novel approach described in **Section (8-3)**. Further investigations could be devoted to explore the effect of coupling the hydride generation scheme with PVG scheme promoted by the aforementioned physical

effects. Moreover, other derivatization schemes by applying other reducing agents such as ethylation and propylation agents is also required to be examined especially for samples include organic species.

It is also important to develop a power supply that can fit in a portable device. Many attempts are shown elsewhere in the literature which describes the production of miniaturized power supply *(Valdivia-Barrientos et al., 2009)*; however, the ambition is to produce a robust power source for long term operations.

10. REFERENCES

ABDUL-MAJEED, W. S., PARADA, J. H. L. & ZIMMERMAN, W. B. 2011. Optimization of a miniaturized DBD plasma chip for mercury detection in water samples. *Analytical and Bioanalytical Chemistry,* 401 (9)**,** 2713-2722

ABDUL-MAJEED, W. S. & ZIMMERMAN, W. B. 2012a. The study of the impact of mercury sample magnetization prior to detection by emission spectroscopy. *Journal of Environmental Science and Engineering,* 1 (3A)**,** 380-387.

ABDUL-MAJEED, W. S., SERDAROGLU, G. M., ZIMMERMAN, W. B. 2012. Application of liquid nitrogen cold trap for purification of hydrogen gas stream generated from NaBH4. *Journal of chemistry and chemical engineering,* 6 (5), 425-434.

ABDUL-MAJEED, W. S. & ZIMMERMAN, W. B. 2012b. Computational modelling of the hydride generation reaction in a tubular reactor and atomization in a quartz cell atomizer. *Journal of Analytical Sciences, Methods and Instrumentation,* 2 (3), 126-139.

ABRANKÓ, L., JÓKAI, Z. & FODOR, P. 2005. Investigation of the species-specific degradation behaviour of methylmercury and ethylmercury under microwave irradiation. *Analytical and bioanalytical chemistry,* 383**,** 448-453.

AGTERDENBOS, J. & BAX, D. 1986. Mechanisms in hydride generation AAS. *Fresenius' Journal of Analytical Chemistry,* 323**,** 783-787.

AISBL 2011. E.I.G.A., Code of practice - Arsine [online] Last accessed 4 August 2011 at: http://www.eiga.org/fileadmin/docs_pubs/Doc_163_10_E.pdf. .

ALDER, J., BOMBELKA, R. & KIRKBRIGHT, G. 1980. Electronic excitation and ionization temperature measurements in a high frequency inductively coupled argon plasma source and the influence of water vapour on plasma parameters. *Spectrochimica Acta Part B: Atomic Spectroscopy,* 35**,** 163-175.

ALEKSANDROV, N., KINDYSHEVA, S., KIRPICHNIKOV, A., KOSAREV, I., STARIKOVSKAIA, S. & STARIKOVSKII, A. Y. 2007. Plasma decay in N2, CO2 and H2O excited by high-voltage nanosecond discharge. *Journal of Physics D: Applied Physics,* 40**,** 4493.

ANDREWS, G. H. A. 2006. Heavy metal pollution and agriculture – TSM 424 public information Bulletin [online]. Last accessed 13 Mar. 2011 at: http://www3.abe.iastate.edu/tsm424/TSM424TermProj2006/AndrewsOliveiraTermPaper.pdf.

ARBAB-ZAVAR, M. H., CHAMSAZ, M., YOUSSEFI, A. & ALIAKBARI, M. 2006. Mechanistic aspects of electrochemical hydride generation for cadmium. *Analytica Chimica Acta,* 576**,** 215-220.

ATSDR-WEBSITE. . Toxic substances portal [online]. Last accessed 13 Mar. 2011 at: http://www.atsdr.cdc.gov/

AVTAEVA, S., GENERAL, A. & KEL'MAN, V. 2010. Kinetic model for low-density non-stationary gas discharge in water vapour. *Journal of Physics D: Applied Physics,* 43**,** 315201.

BEERE, H. & JONES, P. 1994. Investigation of chromium (III) and chromium (VI) speciation in water by ion chromatography with chemiluminescence detection. *Analytica Chimica Acta,* 293**,** 237-243.

BELLAN, P. M. & EBRARY, I. 2006. *Fundamentals of plasma physics*, Cambridge university press Cambridge.

BENDL, R. F., MADDEN, J. T., REGAN, A. L. & FITZGERALD, N. 2006. Mercury determination by cold vapor atomic absorption spectrometry utilizing UV photoreduction. *Talanta,* 68**,** 1366-1370.

BENTLIN, F. R. S., DUARTE, F. A., DRESSLER, V. L. & POZEBON, D. 2007. Arsenic determination in marine sediment using ultrasound for sample preparation. *Analytical Sciences,* 23**,** 1097-1101.

BOGAERTS, A., GIJBELS, R. & VLCEK, J. 1998. Modeling of glow discharge optical emission spectrometry: Calculation of the argon atomic optical emission spectrum. *Spectrochimica Acta Part B: Atomic Spectroscopy,* 53**,** 1517-1526.

BPO-WEBSITE Ultrasonic transducers [online] last accessed 9 Jan. 2012 at: http://www.bostonpiezooptics.com/?D=15.

BRAININA, K. Z., STOZHKO, N. Y., BELYSHEVA, G., INZHEVATOVA, O., KOLYADINA, L., CREMISINI, C. & GALLETTI, M. 2004. Determination of heavy metals in wines by anodic stripping voltammetry with thick-film modified electrode. *Analytica Chimica Acta,* 514**,** 227-234.

BRERETON, R. G. 2003. *Chemometrics: data analysis for the laboratory and chemical plant*, John Wiley & Sons Inc.

BRETT, C. M. A. 2001. Electrochemical sensors for environmental monitoring. Strategy and examples. *Pure and applied chemistry,* 73**,** 1969-1978.

BROEKAERT, J. A. C. & WILEY, J. 2005. *Analytical atomic spectrometry with flames and plasmas*, Wiley Online Library.

CAI, Q. Y. & ZELLERS, E. T. 2002. Dual-chemiresistor GC detector employing monolayer-protected metal nanocluster interfaces. *Analytical chemistry,* 74**,** 3533-3539.

CAI, W., LI, Y., GAO, X., GUO, H., ZHAO, H. & WANG, P. Year. An Automated Electronic Tongue for In Situ Quick Monitoring of Trace Heavy Metals in Water Environment. *In:* Olfaction and Electronic Nose: Proceedings of the 13 International Symposium, 2009. 493-496.

CAI, Y., RAPSOMANIKIS, S. & ANDREAE, M. O. 1993. Determination of butyltin compounds in river sediment samples by gas chromatography-atomic absorption spectrometry following in situ derivatization with sodium tetraethylborate. *Journal of Analytical Atomic Spectrometry,* 8**,** 119-125.

CALZADA, M. D. 2005. Spectroscopy of the discharges created and maintained by a surface-wave. *Memorie della Societa Astronomica Italiana Supplementi,* 7**,** 198.

CANTLE, J. E. 1982. *Atomic absorption spectrometry*, Elsevier Science Ltd.

CAPELO, J., LAVILLA, I. & BENDICHO, C. 2000. Room temperature sonolysis-based advanced oxidation process for degradation of organomercurials: application to determination of inorganic and total mercury in waters by flow injection-cold vapor atomic absorption spectrometry. *Analytical chemistry,* 72**,** 4979-4984.

CHAUDHARY, K., INOMATA, K., YOSHIMOTO, M. & KOINUMA, H. 2003. Open-air silicon etching by H2-He-CH4 flowing cold plasma. *Materials Letters,* 57**,** 3406-3411.

CHEN, H., DU, P., CHEN, J., HU, S., LI, S. & LIU, H. 2010. Separation and preconcentration system based on ultrasonic probe-assisted ionic liquid dispersive liquid-liquid microextraction for determination trace amount of chromium (VI) by electrothermal atomic absorption spectrometry. *Talanta,* 81**,** 176-179.

CHEN, H., WU, J. & BRINDLE, I. D. 1995. Simultaneous reduction of arsenic and lead to hydrides by sodium tetrahydroborate (III) for inductively coupled plasma-atomic emission spectrometry: An investigation into the reaction medium. *Talanta,* 42**,** 353-360.

CHEN, G., ZHOU, M., CHEN, S. & CHEN, W. 2009. The different effects of oxygen and air DBD plasma byproducts on the degradation of methyl violet 5BN. *Journal of hazardous materials,* 172**,** 786-791.

CHIPER, A., APETROAEI, N. & POPA, G. 2005. Correlation between surface modifications induced on PET/TiO2 sample by DBD plasma produced in He/N2 gas mixture and plasma parameters. *Journal of Optoelectronics and Advanced Materials,* 7**,** 2561-2570.

CHUNG, H. & DALGARNO, A. 2002. Diffusion of hydrogen atoms in helium gas and helium atoms in hydrogen gas. *Physical Review A,* 66**,** 012712.

COCHRAN, W. G. & COX, G. M. 1992. Experimental designs. second edition.

COMSOL 2008. Chemical Engineering Module User's Guide - version 3.5

COOK, A., SHAPIRO, M. & TEMKIN, R. 2010. Pressure dependence of plasma structure in microwave gas breakdown at 110 GHz. *Applied Physics Letters,* 97**,** 011504.

CORNELIS, R., HEUMANN, K. G., CARUSO, J. & CREWS, H. 2003. *Handbook of elemental speciation: techniques and methodology*, Wiley Online Library.

CSGNETWORK-WEBSITE Dielectric Constants Of Various Materials [online] Last accessed 15 May 2011 at: http://www.csgnetwork.com/dieconstantstable.html

DEAN, J. R. 2005. *Practical inductively coupled plasma spectroscopy*, John Wiley & Sons Inc.

DEDINA, J. & RUBESKA, I. 1980. Hydride atomization in a cool hydrogen--oxygen flame burning in a quartz tube atomizer. *Spectrochimica Acta Part B: Atomic Spectroscopy,* 35**,** 119-128.

DEDINA, J. 1986. Optimization of hydride generation methods for AAS. *Fresenius' Journal of Analytical Chemistry,* 323**,** 771-782.

DEDINA, J. & TSALEV, D. 1995. *Hydride generation atomic absorption spectrometry,* Chichester, John Wiley &Sons Ltd.

DEDINA, J., D'ULIVO, A., LAMPUGNANI, L., MATOUSEK, T. & ZAMBONI, R. 1998. Selenium hydride atomization, fate of free atoms and spectroscopic temperature in miniature diffusion flame atomizer studied by atomic absorption spectrometry. *Spectrochimica Acta Part B: Atomic Spectroscopy,* 53**,** 1777-1790.

DEDINA, J. 2007. Atomization of volatile compounds for atomic absorption and atomic fluorescence spectrometry: On the way towards the ideal atomizer. *Spectrochimica Acta Part B: Atomic Spectroscopy,* 62**,** 846-872.

DE SMAELE, T., MOENS, L., DAMS, R., SANDRA, P., VAN DER EYCKEN, J. & VANDYCK, J. 1998. Sodium tetra (n-propyl) borate: a novel aqueous in situ derivatization reagent for the simultaneous determination of organomercury,-lead and-tin compounds with capillary gas chromatography-inductively coupled plasma mass spectrometry. *Journal of Chromatography A,* 793**,** 99-106.

DESHPANDE, K. B. & ZIMMERMAN, W. B. 2005. Experimental study of mass transfer limited reaction--Part I: Use of fibre optic spectrometry to infer asymmetric mass transfer coefficients. *Chemical engineering science,* 60**,** 2879-2893.

DIETZ, C., MADRID, Y., CAMARA, C. & QUEVAUVILLER, P. 1999. Simultaneous determination of As, Hg, Se and Sb by hydride generation-microwave induced plasma atomic emission spectrometry after preconcentration in a cryogenic trap. *J. Anal. At. Spectrom.,* 14**,** 1349-1355.

DONG, L., RAN, J., YIN, Z. & MAO, Z. 2005. Electron excitation temperature of argon dielectric barrier discharge at atmospheric pressure [Abstract]. *Guang pu xue yu guang pu fen xi* 25**,** 1184.

DRAPER, N. R. & PUKELSHEIM, F. 2000. Ridge analysis of mixture response surfaces. *Statistics & Probability Letters,* 48**,** 131-140.

DUFFUS, J. H. 2002. "HEAVY METALS"—A MEANINGLESS TERM? *Pure Appl. Chem,* 74**,** 793-807.

D'ULIVO, A. & CHEN, Y. 1989. Determination of cadmium in aqueous samples by vapour generation with sodium tetraethylborate (III) reagent. *Journal of Analytical Atomic Spectrometry,* 4**,** 319-322.

D'ULIVO, A. & DEDINA, J. 1996. Interferences in hydride atomization studied by atomic absorption and atomic fluorescence spectrometry. *Spectrochimica Acta Part B: Atomic Spectroscopy,* 51**,** 481-498.

D'ULIVO, A. & DEDINA, J. I. 2002. The relation of double peaks, observed in quartz hydride atomizers, to the fate of free analyte atoms in the determination of arsenic and selenium by atomic absorption spectrometry. *Spectrochimica Acta Part B: Atomic Spectroscopy,* 57**,** 2069-2079.

D'ULIVO, A., ONOR, M. & PITZALIS, E. 2004. Role of hydroboron intermediates in the mechanism of chemical vapor generation in strongly acidic media. *Analytical chemistry,* 76**,** 6342-6352.

D'ULIVO, A., MESTER, Z. & STURGEON, R. E. 2005. The mechanism of formation of volatile hydrides by tetrahydroborate (III) derivatization: A mass spectrometric study performed with deuterium labeled reagents. *Spectrochimica Acta Part B: Atomic Spectroscopy,* 60**,** 423-438.

D'ULIVO, A., MESTER, Z., MEIJA, J. & STURGEON, R. E. 2007. Mechanism of generation of volatile hydrides of trace elements by aqueous tetrahydroborate (III). Mass spectrometric studies on reaction products and intermediates. *Analytical chemistry,* 79**,** 3008-3015.

D'ULIVO, A., DĚDINA, J., MESTER, Z., STURGEON, R. E., WANG, Q. & WELZ, B. 2011. Mechanisms of chemical generation of volatile hydrides for trace element determination (IUPAC Technical Report). *Pure and Applied Chemistry,* 83**,** 1283.

FAIRES, L. M., PALMER, B. A., ENGLEMAN JR, R. & NIEMCZYK, T. M. 1984. Temperature determinations in the inductively coupled plasma using a Fourier transform spectrometer. *Spectrochimica Acta Part B: Atomic Spectroscopy,* 39**,** 819-828.

FANG, M., VETELINO, K., ROTHERY, M., HINES, J. & FRYE, G. C. 1999. Detection of organic chemicals by SAW sensor array. *Sensors and Actuators B: Chemical,* 56**,** 155-157.

FARAJI, M., YAMINI, Y., SALEH, A., REZAEE, M., GHAMBARIAN, M. & HASSANI, R. 2010. A nanoparticle-based solid-phase extraction procedure followed by flow injection inductively coupled plasma-optical emission spectrometry to determine some heavy metal ions in water samples. *Analytica chimica acta,* 659**,** 172-177.

FAROUK, T. I. 2009. *Modeling and Simulations of DC and RF Atmospheric Pressure Non-thermal Micro Plasma Discharges: Analysis and Applications.* PhD thesis, Drexel university.

FENG, Y. L., LAM, J. W. & STURGEON, R. E. 2001. Expanding the scope of chemical vapor generation for noble and transition metals. *Analyst,* 126**,** 1833-1837.

FOUND, C. G. 1920. Ionization Potentials of Argon, Nitrogen, Carbon Monoxide, Helium, Hydrogen and Mercury and Iodine Vapors. *Physical Review,* 16**,** 41-53.

FRAGUEIRO, S., LAVILLA, I. & BENDICHO, C. 2006. Hydride generation-headspace single-drop microextraction-electrothermal atomic absorption spectrometry method for determination of selenium in waters after photoassisted prereduction. *Talanta,* 68**,** 1096-1101.

FRANK, J., KRACHLER, M. & SHOTYK, W. 2005. Determination of arsenic in peat samples using HG-AFS and L-cysteine as pre-reductant. *J. Anal. At. Spectrom.,* 21**,** 204-207.

FRIDMAN, A. 2008. *Plasma chemistry*, Cambridge Univ Pr.

GAO, J., ZHANG, X., YANG, W. & KANG, J. 2002. Highly sensitive spectrofluorimetric kinetic determination of ultratrace amounts of vanadium (V) based on the oxidation of 1, 8-diaminonaphthalene by bromate. *Analytica Chimica Acta,* 455**,** 159-165.

GAO, S., KOSHIZAKI, N., KOYAMA, E., TOKUHISA, H., SASAKI, T., KIM, J. K., CHO, Y., KIM, D. S. & SHIMIZU, Y. 2009. Innovative Platform for Transmission Localized Surface Plasmon Transducers and Its Application in Detecting Heavy Metal Pd (II). *Analytical chemistry,* 81**,** 7703-7712.

GEERDINK, R. B., BREIDENBACH, R. & EPEMA, O. J. 2007. Optimization of headspace solid-phase microextraction gas chromatography-atomic emission detection analysis of monomethylmercury. *Journal of Chromatography A,* 1174**,** 7-12.

GIELNIAK, B., FIEDLER, T. & BROEKAERT, J. 2011. Study of a new direct current atmospheric pressure glow discharge in helium. *Spectrochimica Acta Part B: Atomic Spectroscopy,* 66**,** 21-27.

GIL, S., LAVILLA, I. & BENDICHO, C. 2006. Ultrasound-promoted cold vapor generation in the presence of formic acid for determination of mercury by atomic absorption spectrometry. *Analytical chemistry,* 78**,** 6260-6264.

GIL, S., LAVILLA, I. & BENDICHO, C. 2008. Mercury removal from contaminated water by ultrasound-promoted reduction/vaporization in a microscale reactor. *Ultrasonics Sonochemistry,* 15**,** 212-216.

GOLUBOVSKII, Y. B., MAIOROV, V., BEHNKE, J. & BEHNKE, J. 2003. On the stability of a homogeneous barrier discharge in nitrogen relative to radial perturbations. *Journal of Physics D: Applied Physics,* 36**,** 975.

GOLUBOVSKII, Y. B., MAIOROV, V., BEHNKE, J., TEPPER, J. & LINDMAYER, M. 2004. Study of the homogeneous glow-like discharge in nitrogen at atmospheric pressure. *Journal of Physics D: Applied Physics,* 37**,** 1346.

GORDILLO-VÁZQUEZ, F., CAMERO, M. & GÓMEZ-ALEIXANDRE, C. 2006. Spectroscopic measurements of the electron temperature in low pressure radiofrequency Ar/H2/C2H2 and Ar/H2/CH4 plasmas used for the synthesis of nanocarbon structures. *Plasma Sources Science and Technology,* 15**,** 42.

GRAS, R., LUONG, J., HAWRYLUK, M. & MONAGLE, M. 2010. Analysis of part-per-billion level of arsine and phosphine in light hydrocarbons by capillary flow technology and dielectric barrier discharge detector. *Journal of Chromatography A,* 1217**,** 348-352.

GRINBERG, P., CAMPOS, R. C., MESTER, Z. & STURGEON, R. E. 2003. A comparison of alkyl derivatization methods for speciation of mercury based on solid phase microextraction gas chromatography with furnace atomization plasma emission spectrometry detection. *J. Anal. At. Spectrom.,* 18**,** 902-909.

GROTTI, M., LAGOMARSINO, C. & FRACHE, R. 2005. Multivariate study in chemical vapor generation for simultaneous determination of arsenic, antimony, bismuth, germanium, tin, selenium, tellurium and mercury by inductively coupled plasma optical emission spectrometry. *J. Anal. At. Spectrom.,* 20**,** 1365-1373.

GRÜTER, U., KRESIMON, J. & HIRNER, A. 2000. A new HG/LT-GC/ICP-MS multi-element speciation technique for real samples in different matrices. *Fresenius' journal of analytical chemistry,* 368**,** 67-72.

GUO, X., HUANG, B., SUN, Z., KE, R., WANG, Q. & GONG, Z. 2000. Preliminary study on a vapor generation technique for nickel without using carbon monoxide by inductively coupled plasma atomic emission spectrometry. *Spectrochimica Acta Part B: Atomic Spectroscopy,* 55**,** 943-950.

GUO, X., RALPH, E., MESTER, Z. & GARDNER, G. J. 2003. UV vapor generation for determination of selenium by heated quartz tube atomic absorption spectrometry. *Analytical chemistry,* 75**,** 2092-2099.

GUO, X., STURGEON, R. E., MESTER, Z. & GARDNER, G. J. 2005. Photochemical alkylation of inorganic arsenic. *J. Anal. At. Spectrom.,* 20**,** 702-708.

HAAK, H. & STUHL, F. 1984. Argon fluoride (193 nm) laser photolysis of HN3, methylamine (CH3NH2), and hydrazine (N2H4): formation of excited imidogen (NH) radicals. *The Journal of Physical Chemistry,* 88**,** 3627-3633.

HAGELAAR, G., KROESEN, G., VAN SLOOTEN, U. & SCHREUDERS, H. 2000. Modeling of the microdischarges in plasma addressed liquid crystal displays. *Journal of Applied Physics,* 88**,** 2252.

HAGENDORFER, H. & GOESSLER, W. 2008. Separation of chromium (III) and chromium (VI) by ion chromatography and an inductively coupled plasma mass spectrometer as element-selective detector. *Talanta,* 76**,** 656-661.

HATTORI, S., WATANABE, M., OSONO, H., TOGII, H. & SASAKI, K. 2001. Effects of an external magnetic field on the flock size and sedimentation of activated sludge. *World Journal of Microbiology and Biotechnology,* 17**,** 833-838.

HE, Y., LV, Y., LI, Y., TANG, H., TANG, L., WU, X. & HOU, X. 2007. Dielectric barrier discharge-induced chemiluminescence: Potential application as GC detector. *Analytical chemistry,* 79**,** 4674-4680.

HEISTERKAMP, M. & ADAMS, F. C. 1999. In situ propylation using sodium tetrapropylborate as a fast and simplified sample preparation for the speciation analysis of organolead compounds using GC-MIP-AES. *J. Anal. At. Spectrom.,* 14**,** 1307-1311.

HILL, S. J. 2006. *Inductively coupled plasma spectrometry and its applications*, Wiley-Blackwell.

HOERL, A. E. 1959. Optimum solution of many variables equations. *Chemical Engineering Progress,* 55**,** 69-78.

HOERL, A. E. 1962. Application of ridge analysis to regression problems. *Chemical Engineering Progress,* 58**,** 54-59.

HONG, Y. C., UHM, H. S. & YI, W. J. 2008. Atmospheric pressure nitrogen plasma jet: Observation of striated multilayer discharge patterns. *Applied Physics Letters,* 93**,** 051504-051504-3.

HOWARD, A. & SALOU, C. 1996. Cysteine enhancement of the cryogenic trap hydride AAS determination of dissolved arsenic species. *Analytica chimica acta,* 333**,** 89-96.

HOWARD, A. & SALOU, C. 1998. Arsenic speciation by cryogenic trap hydride generation atomic absorption spectroscopy: performance enhancement by pre-derivatization. *J. Anal. At. Spectrom.,* 13**,** 683-686.

HUANG, C. & HU, B. 2008. Silica-coated magnetic nanoparticles modified with [gamma]-mercaptopropyltrimethoxysilane for fast and selective solid phase extraction of trace amounts of Cd, Cu, Hg, and Pb in environmental and biological samples prior to their determination by inductively coupled plasma mass spectrometry. *Spectrochimica Acta Part B: Atomic Spectroscopy,* 63**,** 437-444.

INVITROGEN-WEBSITE Fluorescence fundamentals [online], last accessed 2-June.-2011 at: http://www.invitrogen.com/site/us/en/home/References/Molecular-Probes-The-Handbook/Introduction-to-Fluorescence-Techniques.html.

IONASCUT-NEDELCESCU, A., CARLONE, C., KOGELSCHATZ, U., GRAVELLE, D. & BOULOS, M. 2008. Calculation of the gas temperature in a throughflow atmospheric pressure dielectric barrier discharge torch by spectral line shape analysis. *Journal of Applied Physics,* 103**,** 063305.

ISKENDEROVA, K., CHIROKOV, A., GUTSOL, A., FRIDMAN, A., SIEBER, K., GRACE, J. & ROBINSON, K. Year. Simulation of NOx Formation in Dielectric Barrier Discharge. *In*, 2001. 443-448.

JAYARAMAN, B., CHO, Y. C. & SHYY, W. 2008. Modeling of dielectric barrier discharge plasma actuator. *Journal of Applied Physics,* 103**,** 053304.

JOVIEVI, S., IVKOVI, M., PAVLOVI, Z. & KONJEVI, N. 2000. Parametric study of an atmospheric pressure microwave-induced plasma of the mini MIP torch--I. Two-dimensional spatially resolved electron-number density measurements. *Spectrochimica Acta Part B: Atomic Spectroscopy,* 55**,** 1879-1893.

KADARA, R. O. & TOTHILL, I. E. 2004. Stripping chronopotentiometric measurements of lead (II) and cadmium (II) in soils extracts and wastewaters using a bismuth film screen-printed electrode assembly. *Analytical and bioanalytical chemistry,* 378**,** 770-775.

KARADJOVA, I. B., LAMPUGNANI, L., ONOR, M., D'ULIVO, A. & TSALEV, D. L. 2005. Continuous flow hydride generation-atomic fluorescence spectrometric determination and speciation of arsenic in wine. *Spectrochimica Acta Part B: Atomic Spectroscopy,* 60**,** 816-823.

KARANASSIOS, V. 2004. Microplasmas for chemical analysis: analytical tools or research toys? *Spectrochimica Acta Part B: Atomic Spectroscopy,* 59**,** 909-928.

KHAN, H., AHMED, M. J. & BHANGER, M. I. 2005. A simple spectrophotometric determination of trace level mercury using 1, 5-diphenylthiocarbazone solubilized in micelle. *Analytical sciences,* 21**,** 507-512.

KOGELSCHATZ, U., ELIASSON, B. & EGLI, W. 1997. Dielectric-barrier discharges. Principle and applications. *Journal de physique. IV,* 7**,** C4. 47-C4. 66.

KOSTOV, K., HONDA, R., ALVES, L. & KAYAMA, M. 2009. Characteristics of dielectric barrier discharge reactor for material treatment. *Brazilian Journal of Physics,* 39**,** 322-325.

KRZEMIENIEWSKI, M., DEBOWSKI, M., JANCZUKOWICZ, W. & PESTA, J. 2004. Effect of the Constant Magnetic Field on the Composition of Dairy Wastewater and and W Domestic Sewage. *Polish Journal of Environmental Studies,* 13**,** 45-53.

KUMAR, M. S. H., NAGARAJA, P. & YATHIRAJAN, H. 2003. Copper (II)-catalysed oxidative coupling reaction of 3-hydroxyacetanilide with 3-methyl-2-benzothiazolinone hydrazone for the spectrophotometric determination of traces of copper (II). *Analytical and bioanalytical chemistry,* 375**,** 315-318.

KUMARANA, V. 2011. Diffusion [online] , Last accessed 11 March 2011 at: http://chemeng.iisc.ernet.in/kumaran/chap2.pdf.

LABORDA, F. 2002. Hydride generation in analytical chemistry and nascent hydrogen: when is it going to be over? *Spectrochimica Acta,* 57**,** 797-802.

LABUDA, J., SAUR, D. & NEEB, R. 1994. Effect of ethylenediamine on the anodic stripping voltammetric determination of heavy metals in the presence of humic acid. *Fresenius' journal of analytical chemistry,* 349**,** 294-297.

LE, X. C., CULLEN, W. R., REIMER, K. J. & BRINDLE, I. D. 1992. A new continuous hydride generator for the determination of arsenic, Antimony and tin by hybride generation atomic absorption spectrometry. *Analytica chimica acta,* 258**,** 307-315.

LEAL, L., FORTEZA, R. & CERDA, V. 2006. Speciation analysis of inorganic arsenic by a multisyringe flow injection system with hydride generation-atomic fluorescence spectrometric detection. *Talanta,* 69**,** 500-508.

LEERMAKERS, M., BAEYENS, W., QUEVAUVILLER, P. & HORVAT, M. 2005. Mercury in environmental samples: Speciation, artifacts and validation. *TrAC Trends in Analytical Chemistry,* 24**,** 383-393.

LI, G., WU, L., XIN, J. & HOU, X. 2004. Chemical vapor generation by reaction of cadmium with potassium tetrahydroborate and sodium iodate in acidic aqueous solution for atomic fluorescence spectrometric application. *J. Anal. At. Spectrom.,* 19**,** 1010-1013.

LI, T., CHEN, Y. & MA, J. 2009. Development of a miniaturized piezoelectric ultrasonic transducer. *Ultrasonics, Ferroelectrics and Frequency Control, IEEE Transactions on,* 56**,** 649-659.

LI, W., ZHENG, C., FAN, G., TANG, L., XU, K., LV, Y. & HOU, X. 2011. Dielectric Barrier Discharge Molecular Emission Spectrometer as Multi-channel GC Detector for Halohydrocarbons. *Analytical chemistry,* 83**,** 5050-5055.

LI, Y., HU, J., TANG, L., HE, Y., WU, X., HOU, X. & LV, Y. 2008. Miniaturized dielectric barrier discharge induced chemiluminescence for detection of volatile chlorinated hydrocarbons separated by gas chromatography. *Journal of Chromatography A,* 1192**,** 194-197.

LIEBERMAN, M. A. & LICHTENBERG, A. J. 2005. *Principles of plasma discharges and materials processing*, Wiley Online Library.

LIM, K.-B., LEE, DUCK-CHOOL 2004. Surface modification of glass and glass fibres by plasma surface treatment. *SURFACE AND INTERFACE ANALYSIS,* 36**,** 254-258.

LIN, M., WANG, Y. & WAN, C. 1986. Determination of optimal formation conditions for tubular positive electrodes of lead/acid batteries. *Electrochimica acta,* 31**,** 565-571.

LIN, T. J. & CHUNG, M. F. 2009. Detection of cadmium by a fiber-optic biosensor based on localized surface plasmon resonance. *Biosensors and Bioelectronics,* 24**,** 1213-1218.

LIU, Y., GUO, Y., MENG, S., FENG, F. & CHANG, X. 2007. Determination of trace heavy metals in waters by flame atomic absorption spectrometry after preconcentration with 2, 4-dinitrophenyldiazoaminoazobenzene on Amberlite XAD-2. *Microchimica Acta,* 157**,** 209-214.

LIU, Z., ZHU, Z., WU, Q., HU, S. & ZHENG, H. 2011. Dielectric barrier discharge-plasma induced vaporization and its application to the determination of mercury by atomic fluorescence spectrometry. *Analyst,* 136**,** 4539-4544.

LOCKE, B., SATO, M., SUNKA, P., HOFFMANN, M. & CHANG, J. S. 2006. Electrohydraulic discharge and nonthermal plasma for water treatment. *Industrial & engineering chemistry research,* 45**,** 882-905.

LOZANO PARADA, J. H. 2007. *Design, Simulation and Fabrication of an Atmospheric Pressure Microchannel Plasma Reactor.* PhD thesis, University of Sheffield.

LUQUE, J., CALZADA, M. & SAEZ, M. 2005. A new procedure for obtaining the Voigt function dependent upon the complex error function. *Journal of Quantitative Spectroscopy and Radiative Transfer,* 94**,** 151-161.

MACH, M. H., NOTT, B., SCOTT, J. W., MADDALONE, R. F. & WHIDDON, N. T. 1996. Metal speciation: Survey of environmental methods of analysis. *Water, Air, & Soil Pollution,* 90**,** 269-279.

MAHESHWARI, B. L. & GREWAL, H. S. 2009. Magnetic treatment of irrigation water: Its effects on vegetable crop yield and water productivity. *Agricultural Water Management,* 96**,** 1229-1236.

MALEKI, N., SAFAVI, A. & RAMEZANI, Z. 1999. Determination of lead by hydride generation atomic absorption spectrometry (HGAAS) using a solid medium for generating hydride. *Journal of analytical atomic spectrometry,* 14**,** 1227-1230.

MANAHAN, S. E. 2005. *Environmental chemistry*, CRC.

MANISANKAR, P., VEDHI, C., SELVANATHAN, G. & ARUMUGAM, P. 2008. Differential pulse stripping voltammetric determination of heavy metals simultaneously using new polymer modified glassy carbon electrodes. *Microchimica Acta,* 163**,** 289-295.

MANISANKAR, P., VEDHI, C., SELVANATHAN, G. & GURUMALLESH PRABU, H. 2006. Electrochemical synthesis and characterization of novel electrochromic poly (3, 4-ethylenedioxythiophene-co-Diclofenac) with surfactants. *Electrochimica acta,* 51**,** 2964-2970.

MANNING, T. J. & GROW, W. R. 1997. Inductively coupled plasma-atomic emission spectrometry. *The Chemical Educator,* 2**,** 1-19.

MARCUS, R. K., BROEKAERT, J. A. C. & EBRARY, I. 2003. *Glow discharge plasmas in analytical spectroscopy*, Wiley Online Library.

MARIN, A., LOPEZ-GONZALVEZ, A. & BARBAS, C. 2001. Development and validation of extraction methods for determination of zinc and arsenic speciation in soils using focused ultrasound:: Application to heavy metal study in mud and soils. *Analytica chimica acta,* 442**,** 305-318.

MASSINES, F., MESSAOUDI, R. & MAYOUX, C. 1998. Comparison between air filamentary and helium glow dielectric barrier discharges for the polypropylene surface treatment. *Plasmas and polymers,* 3**,** 43-59.

MATHWORKS-WEBSITE. 2011. Ordinary differential equations [online], Last accessed 4 August 2011 at: http://www.mathworks.com/moler/odes.pdf.

MATOUSEK, T. & DEDINA, J. 2000. Fate of free selenium atoms in externally heated quartz tube atomizers for hydride generation atomic absorption spectrometry and their reatomization at tube ends studied by means of the determination of longitudinal free atom distribution. *Spectrochimica Acta Part B: Atomic Spectroscopy,* 55**,** 545-557.

MATOUŠEK, T. 2007. The efficiency of chemical vapour generation of transition and noble metals. *Analytical and Bioanalytical Chemistry,* 388**,** 763-767.

MATOUSEK, T., HERNÁNDEZ-ZAVALA, A., SVOBODA, M., LANGROVÁ, L., ADAIR, B. M., DROBNÁ, Z., THOMAS, D. J., ST BLO, M. & DEDINA, J. 2008. Oxidation state specific generation of arsines from methylated arsenicals based on L-cysteine treatment in buffered media for speciation analysis by hydride generation-automated cryotrapping-gas chromatography-atomic absorption spectrometry with the multiatomizer. *Spectrochimica Acta Part B: Atomic Spectroscopy,* 63**,** 396-406.

MATUSIEWICZ, H. & SLACHCINSKI, M. 2006. Simultaneous determination of hydride forming elements (As, Sb, Se, Sn) and Hg in sonicate slurries of biological and environmental reference materials by hydride generation microwave induced plasma optical emission spectrometry (SS-HG-MIP-OES). *Microchemical journal,* 82**,** 78-85.

MCSHEEHY, S., GUO, X. M., STURGEON, R. E. & MESTER, Z. 2005. Photochemical alkylation of inorganic arsenic. *J. Anal. At. Spectrom.,* 20**,** 709-716.

MECHANIST-WEBSITE Engineering tables [online]. Last accessed 8 May 2011 at: http://www.machinistmaterials.com/comparison_table_for_plastics.htm

MEDODOVIC, S. & LOCKE, B. 2009. Primary chemical reactions in pulsed electrical discharge channels in water. *Journal of Physics D: Applied Physics,* 42**,** 049801.

MESTER, Z., STURGEON, R. E. & LAM, J. W. 2000. Sampling and determination of metal hydrides by solid phase microextraction thermal desorption inductively coupled plasma mass spectrometry. *J. Anal. At. Spectrom.,* 15**,** 1461-1465.

MICLEA, M., KUNZE, K., MUSA, G., FRANZKE, J. & NIEMAX, K. 2001. The dielectric barrier discharge--a powerful microchip plasma for diode laser spectrometry. *Spectrochimica Acta Part B: Atomic Spectroscopy,* 56**,** 37-43.

MILI , B., NOVAKOVI , N. & STOJILKOVI , S. 1987. Transport properties and weak non-ideality in xenon and argon plasmas of intermediate degree of ionization. *Czechoslovak journal of physics,* 37**,** 1238-1247.

MOLLAH, M., SCHENNACH, R., PATSCHEIDER, J., PROMREUK, S. & COCKE, D. 2000. Plasma chemistry as a tool for green chemistry, environmental analysis and waste management. *Journal of hazardous materials,* 79**,** 301-320.

MOOR, C., LAM, J. W. H. & STURGEON, R. E. 2000. A novel introduction system for hydride generation-inductively coupled plasma mass spectrometry: determination of selenium in biological materials. *J. Anal. At. Spectrom.,* 15**,** 143-149.

MORAVEJ, M., BABAYAN, S., NOWLING, G., YANG, X. & HICKS, R. 2004. Plasma enhanced chemical vapour deposition of hydrogenated amorphous silicon at atmospheric pressure. *Plasma Sources Science and Technology,* 13**,** 8.

MOTRET, O., HIBERT, C., PELLERIN, S. & POUVESLE, J. 2000. Rotational temperature measurements in atmospheric pulsed dielectric barrier discharge-gas temperature and molecular fraction effects. *Journal of Physics D: Applied Physics,* 33**,** 1493.

MUSIL, S. & MATOUSEK, T. 2008. On-line pre-reduction of pentavalent arsenicals by thioglycolic acid for speciation analysis by selective hydride generation-cryotrapping-atomic absorption spectrometry. *Spectrochimica Acta Part B: Atomic Spectroscopy,* 63**,** 685-691.

NAGHMUSH, A. M., PYRZYNSKA, K. & TROJANOWICZ, M. 1994. Determination of chromium in different oxidation states by selective on-line preconcentration on cellulose sorbents and flow-injection flame atomic absorption spectrometry. *Analytica Chimica Acta,* 288**,** 247-257.

NAPARTOVICH, A. 2001. Overview of atmospheric pressure discharges producing nonthermal plasma. *Plasmas and polymers,* 6**,** 1-14.

NAVRATIL, J. & SHING, T. M. T. 2003. Magnetic separation of iron and heavy metals from water. *Water science and technology: a journal of the International Association on Water Pollution Research,* 47**,** 29.

NCSU-WEBSITE Heavy metals. [online], Last accessed 18 Feb. 2010 at: http://www.water.ncsu.edu/watershedss/info/hmetals.html#revise.

NEHRA, V., KUMAR, A. & DWIVEDI, H. 2008. Atmospheric Non-Thermal Plasma Sources. *International Journal of Engineering (IJE),* 2**,** 53.

NIST-WEBSITE 2010. National Institute of Standards and Technology - Atomic spectroscopy data base, Last accessed 15 Dec. 2010 at http://www.nist.gov/pml/data/atomspec.cfm

NSENGIMANA, H., CUKROWSKA, E. M., DINSMORE, A., TESSIER, E. & AMOUROUX, D. 2009. In situ ethylation of organolead, organotin and organomercury species by bromomagnesium tetraethylborate prior to GC ICP MS analysis. *Journal of separation science,* 32**,** 2426-2433.

OCEANOPTICS 2010. Installation and Operation Manual - SpectraSuite operating software.

OGNIER, S., IYA-SOU, D., FOURMOND, C. & CAVADIAS, S. 2009. Analysis of Mechanisms at the Plasma–Liquid Interface in a Gas–Liquid Discharge Reactor Used for Treatment of Polluted Water. *Plasma Chemistry and Plasma Processing,* 29**,** 261-273.

OHIOSTATE-WEBSITE Ohio state education, Measures of toxic metals in water [online] accessed 17 May. 2011 at : http://tycho.knowlton.ohio-state.edu/heavyinfo.html

OHNO, S., TESHIMA, N., WATANABE, T., ITABASHI, H., NAKANO, S. & KAWASHIMA, T. 1996. Determination of ultratrace amounts of copper (II) by its catalytic effect on the oxidative coupling reaction of 3-methyl-2-benzothiazolinone hydrazone with N-ethyl-N-(2-hydroxy-3-sulfopropyl)-3, 5-dimethoxyaniline. *Analyst,* 121**,** 1515-1518.

HOWARD,P. 2005. Partial differential equations in Matlab 7.0 [online],Last accessed 23 June 2011 at: http://www.tem.uoc.gr/~marina/pdemat.pdf.

PAL, U., KUMAR, M., TYAGI, M., MEENA, B., KHATUN, H. & SHARMA, A. Year. Discharge analysis and electrical modeling for the development of efficient dielectric barrier discharge. *In*, 2010. IOP Publishing, 012142.

PAL, U. N. & ET AL. 2010. Discharge analysis and electrical modeling for the development of efficient dielectric barrier discharge. *Journal of Physics: Conference Series,* 208**,** 012142.

PANAKAMOL DEEYAI, P. J., WASUSATE SOONTHONCHAIKUL, MANOP SUPHANTHARIKA, AND & DANGTIP, S. 2010. Effect of Atmospheric Argon Plasma on Morphology of Tapioca Starch Granule. *Journal of the Microscopy Society of Thailand,* 24**,** 112-116.

PANOUSIS, E., CLÉMENT, F., LOISEAU, J., SPYROU, N., HELD, B., THOMACHOT, M. & MARLIN, L. 2006. An electrical comparative study of two atmospheric pressure dielectric barrier discharge reactors. *Plasma Sources Science and Technology,* 15**,** 828.

PANTA, Y. M., JING, L., CHENEY, M. A., JOO, S. W. & SHIZHI, Q. 2009. Ultrasensitive detection of mercury (II) ions using electrochemical surface plasmon resonance with magnetohydrodynamic convection. *Journal of colloid and interface science.,* 333**,** 485-490.

PARK, J., HENINS, I., HERRMANN, H., SELWYN, G. & HICKS, R. 2001. Discharge phenomena of an atmospheric pressure radio-frequency capacitive plasma source. *Journal of Applied Physics,* 89**,** 20.

PEÑA-VÁZQUEZ, E., BERMEJO-BARRERA, A. & BERMEJO-BARRERA, P. 2005. Use of lanthanum hydroxide as a trapping agent to determine of hydrides by HG-ICP-OES. *J. Anal. At. Spectrom.,* 20**,** 1344-1349.

PILON, L. & VISKANTA, R. 2004. Minimum superficial gas velocity for onset of foaming. *Chemical engineering and processing,* 43**,** 149-160.

POHL, P. & ZYRNICKI, W. 2001. On the transport of some metals into inductively coupled plasma during hydride generation process. *Analytica chimica acta,* 429**,** 135-143.

POHL, P. & PRUSISZ, B. 2007. Chemical vapor generation of noble metals for analytical spectrometry. *Analytical and bioanalytical chemistry,* 388**,** 753-762.

POHL, P., ZAPATA, I. J., BINGS, N. H., VOGES, E. & BROEKAERT, J. A. C. 2007b. Optical emission spectrometric determination of arsenic and antimony by continuous flow chemical hydride generation and a miniaturized microwave microstrip argon plasma operated inside a capillary channel in a sapphire wafer. *Spectrochimica Acta Part B: Atomic Spectroscopy,* 62**,** 444-453.

QUEVAUVILLER, P. & THOMPSON, K. C. 2006. *Analytical methods for drinking water: advances in sampling and analysis*, John Wiley & Sons Inc.

RADMILOVI -RADJENOVI , M., RADJENOVI , B. & SAVI , M. 2010. Breakdown Phenomena in Water Vapor Microdischarges. *ACTA PHYSICA POLONICA A,* 117**,** 752-755.

RAMESH KUMAR, A. & RIYAZUDDIN, P. 2005. Mechanism of volatile hydride formation and their atomization in hydride generation atomic absorption spectrometry. *Analytical sciences,* 21**,** 1401-1410.

RAPSOMANIKIS, S., DONARD, O. & WEBER, J. H. 1986. Speciation of lead and methyllead ions in water by chromatography/atomic absorption spectrometry after ethylation with sodium tetraethylborate. *Analytical chemistry,* 58**,** 35-38.

RIBEIRO, A. S., VIEIRA, M. A., WILLIE, S. & STURGEON, R. E. 2007. Ultrasound-assisted vapor generation of mercury. *Analytical and Bioanalytical Chemistry,* 388**,** 849-857.

RIO-SEGADE, S. & BENDICHO, C. 1999. On-line high-performance liquid-chromatographic separation and cold vapor atomic absorption spectrometric determination of methylmercury and inorganic mercury. *Talanta,* 48**,** 477-484.

ROUESSAC, F. & ROUESSAC, A. 2007. *Chemical analysis: modern instrumentation methods and techniques*, Wiley.

RUDNITSKAYA, A., LEGIN, A., SELEZNEV, B., KIRSANOV, D. & VLASOV, Y. 2008. Detection of ultra-low activities of heavy metal ions by an array of potentiometric chemical sensors. *Microchimica Acta,* 163**,** 71-80.

SAFAVI, A., MALEKI, N. & FARJAMI, F. 2001. Selective kinetic spectrophotometric determination of copper at nanograms per milliliter level. *Talanta,* 54**,** 397-402.

SCHUTZE, A., JEONG, J. Y., BABAYAN, S. E., PARK, J., SELWYN, G. S. & HICKS, R. F. 1998. The atmospheric-pressure plasma jet: A review and comparison to other plasma sources. *Plasma Science, IEEE Transactions on,* 26**,** 1685-1694.

SERDAROGLU, G. 2011. *Study The Hydrogen Generation From Sodium Borohydride System Using a Liquid Nitrogen Cold Trap As a Separation Step.* Master thesis, Chemical and Biological Engineering Department - The University of Sheffield.

SETTLE, F. A. 1997. *Handbook of instrumental techniques for analytical chemistry*, Prentice Hall PTR.

SHIH, K. Y. & LOCKE, B. R. 2010. Optical and Electrical Diagnostics of the Effects of Conductivity on Liquid Phase Electrical Discharge. *Plasma Science, IEEE Transactions on***,** 1-10.

SMITH, C., COETZEE, P. & MEYER, J. 2004. The effectiveness of a magnetic physical water treatment device on scaling in domestic hot-water storage tanks. *Water SA,* 29**,** 231-236.

SMITH, L. 2002. A tutorial on Principal Components Analysis [online], accessed 8 Sep. 2011 at: http://www.cs.otago.ac.nz/cosc453/student_tutorials/principal_components.pdf.

STEFECKA, M., KORZEC, D., SIRY, M., IMAHORI, Y. & KANDO, M. 2001. Experimental study of atmospheric pressure surface discharge in helium. *Science and Technology of Advanced Materials,* 2**,** 587-593.

STURGEON, R., LIU, J., BOYKO, V. & LUONG, V. 1996. Determination of copper in environmental matrices following vapor generation. *Analytical chemistry,* 68**,** 1883-1887.

SUN, H., SUO, R. & LU, Y. 2002. Determination of zinc in food using atomic fluorescence spectrometry by hydride generation from organized media. *Analytica Chimica Acta,* 457**,** 305-310.

SUN, Y., CHANG, Y. & SU, C. 2006. On-line HPLC-UV/Nano-TiO2-ICPMS system for the determination of inorganic selenium species. *Analytical chemistry,* 78**,** 2640-2645.

TAKAKI, K. & FUJIWARA, T. 2001. Multipoint barrier discharge process for removal of NOx from diesel engine exhaust. *Plasma Science, IEEE Transactions on,* 29**,** 518-523.

TENDERO, C., TIXIER, C., TRISTANT, P., DESMAISON, J. & LEPRINCE, P. 2006. Atmospheric pressure plasmas: A review. *Spectrochimica Acta Part B: Atomic Spectroscopy,* 61**,** 2-30.

TORRES, J., JONKERS, J., SANDE, M. J., MULLEN, J., GAMERO, A. & SOLA, A. 2003. An easy way to determine simultaneously the electron density and temperature in high-pressure plasmas by using Stark broadening. *Journal of Physics D: Applied Physics,* 36**,** L55.

TSALEV, D. L., D'ULIVO, A., LAMPUGNANI, L., DI MARCO, M. & ZAMBONI, R. 1996. Thermally stabilized iridium on an integrated, carbide-coated platform as a permanent modifier for hydride-forming elements in electrothermal atomic absorption spectrometry. Part 2. Hydride generation and collection, and behaviour of some organoelement species. *Journal of analytical atomic spectrometry,* 11**,** 979-988.

VALDIVIA-BARRIENTOS, R., PACHECO-PACHECO, M., PACHECO-SOTELO, J., ESTRADA-MARTÍNEZ, N., RAMOS-FLORES, F., GARCÍA-GARCÍA, J. & FRETON, P. 2009. A high efficiency bipolar pulsed power source for DBD discharges. *ICPIG, Cancún, México*.

VAN WAGENEN, S., CARTER, D. E., RAGHEB, A. & FERNANDO, Q. 1987. Kinetic control of peak shapes in atomic absorption arsenic determinations by arsine generation. *Analytical chemistry,* 59**,** 891-896.

VANDENTOP, G., KAWASAKI, M., NIX, R., BROWN, I., SALMERON, M. & SOMORJAI, G. 1990. Formation of hydrogenated amorphous carbon films of controlled hardness from a methane plasma. *Physical Review B,* 41**,** 3200.

VIEIRA, M. A., RIBEIRO, A. S., CURTIUS, A. J. & STURGEON, R. E. 2007. Determination of total mercury and methylmercury in biological samples by photochemical vapor generation. *Analytical and Bioanalytical Chemistry,* 388**,** 837-847.

WAGNER, H., YURGELENAS, Y. V. & BRANDENBURG, R. 2005. The development of microdischarges of barrier discharges in N2/O2 mixtures—experimental investigations and modelling. *Plasma physics and controlled fusion,* 47**,** B641.

WANG, F. T. & JOLLY, W. L. 1972. Kinetic study of the intermediates in the hydrolysis of the hydroborate ion. *Inorganic Chemistry,* 11**,** 1933-1941.

WANG, X. 1986. A mathematical model for continuous hydride generation with inductively coupled plasma spectrometry analysis--I. Hydride transfer. *Spectrochimica Acta Part B: Atomic Spectroscopy,* 41**,** 967-977.

WANG, X. & BARNES, R. M. 1987. A mathematical model for continuous hydride generation with inductively coupled plasma spectrometry--II. pH dependence of hydride forming elements. *Spectrochimica Acta Part B: Atomic Spectroscopy,* 42**,** 139-156.

WEBER, J. H. 1997. Speciation of methylarsenic, methyl-and butyltin, and methylmercury compounds and their inorganic analogues by hydride derivatization. *TrAC Trends in Analytical Chemistry,* 16**,** 73-78.

WELZ, B. & MELCHER, M. 1983. Investigations on atomisation mechanisms of volatile hydride-forming elements in a heated quartz cell. Part 1. Gas-phase and surface effects; decomposition and atomisation of arsine. *Analyst,* 108**,** 213-224.

WELZ, B. & SCHUBERT-JACOBS, M. 1986. Investigations on atomization mechanisms in hydride-generation atomic absorption spectrometry. *Fresenius' Journal of Analytical Chemistry,* 324**,** 832-838.

WHITE, C. 2011. Atomic absorption determination of zinc and copper in a multivitamin [online]. Last accessed 31 May. 2011 at:

http://www.scribd.com/doc/10513921/Atomic-Absorption-Determination-of-Zinc-and-Copper-in-a-Multivitamin.

WHO 2008. Guidelines for drinking-water quality, third edition, incorporating first and second addenda, Volume 1 – Recommendations [online], accessed 13 March 2011 at: http://www.who.int/water_sanitation_health/dwq/fulltext.pdf.

WICKSTRØM, T., LUND, W. & BYE, R. 1996. Transport of nickel, cobalt, iron and chromium to the atom cell during a hydride generation process. *Analyst,* 121**,** 201-204.

WILKE, C. 1950. A viscosity equation for gas mixtures. *The Journal of Chemical Physics,* 18**,** 517.

WILKE, C. & CHANG, P. 1955. Correlation of diffusion coefficients in dilute solutions. *AIChE Journal,* 1**,** 264-270.

WILSON, D. M., HOYT, S., JANATA, J., BOOKSH, K. & OBANDO, L. 2001. Chemical sensors for portable, handheld field instruments. *Sensors Journal, IEEE,* 1**,** 256-274.

WU, P., HE, L., ZHENG, C., HOU, X. & STURGEON, R. E. 2010. Applications of chemical vapor generation in non-tetrahydroborate media to analytical atomic spectrometry. *J. Anal. At. Spectrom.,* 25**,** 1217-1246.

WU, Q., ZHU, Z., LIU, Z., ZHENG, H., HU, S. & LI, L. 2012. Dielectric barrier discharge-plasma induced vaporization for the determination of thiomersal in vaccines by atomic fluorescence spectrometry. *J. Anal. At. Spectrom.,* 27**,** 496-500.

WU, X., YANG, W., LIU, M., HOU, X. & ZHENG, C. 2011. Vapor generation in dielectric barrier discharge for sensitive detection of mercury by inductively coupled plasma optical emission spectrometry. *J. Anal. At. Spectrom.*

XING, Z., WANG, J., ZHANG, S. & ZHANG, X. 2009. Determination of bismuth in solid samples by hydride generation atomic fluorescence spectrometry with a dielectric barrier discharge atomizer. *Talanta,* 80**,** 139-142.

Y TEMPRANO, M. C. V. H., DE LA CAMPA, M. R. F. & SANZ-MEDEL, A. 1993. Generation of volatile cadmium species with sodium tetrahydroborate from organized media: application to cadmium determination by inductively coupled plasma atomic emission spectrometry. *Journal of Analytical Atomic Spectrometry,* 8**,** 847-852.

Y TEMPRANO, M. C. V. H., DE LA CAMPA, M. R. F. & SANZ-MEDEL, A. 1994. Sensitive inductively coupled plasma atomic emission spectrometric determination of cadmium by continuous alkylation with sodium tetraethylborate. *J. Anal. At. Spectrom.,* 9**,** 231-236.

YING, X. & FANG, Z. 2006. Experimental research on heavy metal wastewater treatment with dipropyl dithiophosphate. *Journal of hazardous materials,* 137**,** 1636-1642.

YU, Y., DU, Z., CHEN, M. & WANG, J. 2008a. Atmospheric Pressure Dielectric Barrier Discharge as a Radiation Source for Optical Emission Spectrometry. *Angewandte Chemie International Edition,* 47**,** 7909-7912.

YU, Y. L., DU, Z., CHEN, M. L. & WANG, J. H. 2008b. A miniature lab-on-valve atomic fluorescence spectrometer integrating a dielectric barrier discharge atomizer demonstrated for arsenic analysis. *J. Anal. At. Spectrom.,* 23**,** 493-499.

YUBERO, C., GARCIA, M. & CALZADA, M. 2006. On the use of the H [alpha] spectral line to determine the electron density in a microwave (2.45 GHz)

plasma torch at atmospheric pressure. *Spectrochimica Acta Part B: Atomic Spectroscopy,* 61**,** 540-544.

ZHANG, C. 2007. *Fundamentals of environmental sampling and analysis*, LibreDigital.

ZHANG, Y., WEN, X. H. & YANG, W. H. 2007. Excitation temperatures of atmospheric argon in dielectric barrier discharges. *Plasma Sources Science and Technology,* 16**,** 441.

ZHENG, C., STURGEON, R. E. & HOU, X. 2009. UV photochemical vapor generation and in situ preconcentration for determination of ultra-trace nickel by flow injection graphite furnace atomic absorption spectrometry. *J. Anal. At. Spectrom.,* 24**,** 1452-1458.

ZHENG, C., MA, Q., WU, L., HOU, X. & STURGEON, R. E. 2010a. UV photochemical vapor generation-atomic fluorescence spectrometric determination of conventional hydride generation elements. *Microchemical Journal,* 95**,** 32-37.

ZHENG, C., STURGEON, R. E., BROPHY, C. & HOU, X. 2010b. Versatile Thin-Film Reactor for Photochemical Vapor Generation. *Analytical chemistry,* 82**,** 3086-3093.

ZHENG, C., STURGEON, R. E., BROPHY, C. S., HE, S. & HOU, X. 2010c. High-yield UV-photochemical vapor generation of iron for sample introduction with inductively coupled plasma optical emission spectrometry. *Analytical chemistry,* 82**,** 2996-3001.

ZHU, Z., ZHANG, S., LV, Y. & ZHANG, X. 2006a. Atomization of hydride with a low-temperature, atmospheric pressure dielectric barrier discharge and its application to arsenic speciation with atomic absorption spectrometry. *Analytical chemistry,* 78**,** 865-872.

ZHU, Z., ZHANG, S., XUE, J. & ZHANG, X. 2006b. Application of atmospheric pressure dielectric barrier discharge plasma for the determination of Se, Sb and Sn with atomic absorption spectrometry. *Spectrochimica Acta Part B: Atomic Spectroscopy,* 61**,** 916-921.

ZHU, Z., CHAN, G. C. Y., RAY, S. J., ZHANG, X. & HIEFTJE, G. M. 2008a. Microplasma Source Based on a Dielectric Barrier Discharge for the Determination of Mercury by Atomic Emission Spectrometry. *Analytical chemistry,* 80**,** 8622-8627.

ZHU, Z., LIU, J., ZHANG, S., NA, X. & ZHANG, X. 2008b. Determination of Se, Pb, and Sb by atomic fluorescence spectrometry using a new flameless, dielectric barrier discharge atomizer. *Spectrochimica Acta Part B: Atomic Spectroscopy,* 63**,** 431-436.

ZHU, Z., LIU, J., ZHANG, S., NA, X. & ZHANG, X. 2008c. Evaluation of a hydride generation-atomic fluorescence system for the determination of arsenic using a dielectric barrier discharge atomizer. *Analytica Chimica Acta,* 607**,** 136-141.

ZHU, Z., LIU, Z., ZHENG, H. & HU, S. 2010. Non-chromatographic determination of inorganic and total mercury by atomic absorption spectrometry based on a dielectric barrier discharge atomizer. *J. Anal. At. Spectrom.,* 25**,** 697-703.

ZIMMERMAN, W. B. J. 2006. *Multiphysics modelling with finite element methods,* London, World scientific publishing Co. Pte. Ltd.

ZOOROB, G. K., MCKIERNAN, J. W. & CARUSO, J. A. 1998. ICP-MS for elemental speciation studies. *Microchimica Acta,* 128**,** 145-168.

11. APPENDICES

11.1 Matlab code for solving the systems of ODE

The systems of ordinary differential equations are analyzed by using the ordinary differential equation solver (ode 23) in Matlab *(Mathworks-Website, 2011).* The following two codes are generated to treat two sets of ordinary differential equations according to nascent hydrogen and hydroboron intermediates hypotheses, described in **Section (3.3.2)**.

Matlab code for mechanism 1:

1-M.file// **hgode44bb.m**

```
function dy = hgode44bb(t,y)
k1=2033;ca0=1.347;k2=32;
k3=3.5;
dy=zeros(8,1);
dy(1)=-k1*0.1*y(1)^2;
dy(2)=k1*0.1*y(1)^2-
k2*y(2)^6*y(3);
dy(3)=-k2*y(2)^6*y(3);
dy(4)=1.5*k2*y(2)^6*y(3);
dy(5)=k2*y(2)^6*y(3)-k3*y(5);
dy(6)=k3*y(5);
dy(7)=-k1*0.1*y(1)^2*y(7)/ca0;
dy(8)=y(7);
```

2-Matlab code//

```
tspan = [0:0.01:2];
ynot = [1.347;0;2.66e-4;0;0;0;0.074;0];
[t,y] = ode23(@hgode44,tspan,ynot);
fprintf('%f\n',t)
fprintf('%f\n',y)
```

Matlab code for mechanism 2:

1-M.file// **hgode45bbbb.m**

```
function dy = hgode45bbbb(t,y)
kHyd=1.6e3;k1=32;k2=3.5;
ca0=1.347;
dy=zeros(9,1);
dy(1)=-kHyd*0.1*y(1)^2;
dy(2)=kHyd*0.1*y(1)^2-
k1*y(2)*y(3);
dy(3)=-k1*y(2)*y(3);
dy(4)=k1*y(3)*y(2)-k2*y(4);
dy(5)=k2*y(4);
dy(6)=4*kHyd*0.1*y(1)^2;
dy(7)= k1*y(2)*y(3);
dy(8)=-kHyd*0.1*y(1)^2*y(8)/ca0;
dy(9)=y(8);
```

2-Matlab code//

```
tspan = [0:0.00001:2];
ynot = [1.347;0;2.66e-4;0;0;0;0;0.074;0];
[t,y] = ode23(@hgode45bbbb,tspan,ynot);
fprintf('%f\n',t)
fprintf('%f\n',y)
```

11.2 Diffusion coefficients estimation

1- In the liquid phase (water):

According to *(Wilke and Chang, 1955)*, the diffusion coefficients of solutes in dilute solutions can be estimated from the following equation :

$$D = 7.4x10^{-8} \frac{(c\,M)^{0.5}T}{\eta V^{0.6}} \qquad (11\text{-}1)$$

Where;
D = Diffusion coefficient (cm^2/sec)
c = association parameter = 2.6 (for water)
M = Molecular weight of solvent, (gm/gmole)
T = Temperature , (^oK)
η = viscosity of solution , (centipoise)
V = Molal volume of solute at normal boiling point, ($cm^3/gmol$)

An approximation made that this formula is applicable for a gas diffuses in water, therefore applying the values of arsenic hydride ($2.66x10^{-4}$ mol/m^3) in a water solution at 303 ^oK , gives the value of $3.45x10^{-10}$ cm^2/sec. For a value 5.388 mol/m^3 of hydrogen, the diffusion coefficient has been estimated equal to ($1.32x10^{-7}$ cm^2/sec).

2- In the gas phase (Helium)

Based on the kinetic theory of gases, the following formula has been applied to calculate the diffusion coefficient of a spherical molecule in a mixture of gases *(Wilke, 1950, Chung and Dalgarno, 2002, Kumarana, 2011)* :

$$D_{12} = \frac{3}{8\,n\,d_{12}^2}\left[\frac{kT(m_1+m_2)}{2\,\pi\,m_1 m_2}\right]^{0.5} \qquad (11\text{-}2)$$

Where;
D_{12} = Diffusion coefficient
d_{12} = molecular diameter = $(d_1 + d_2)/2$
m_1 & m_2 = component masses

n = number of gas molecules per unit volumes
k = 1.3087×10^{-23} (J/ ^{o}K)
T = Tempearture (^{o}K)

The diffusion coeffient of small molecules diameter (1.372×10^{-10} m) such as hydrogen and helium at room temperature is reported equal to (1.132×10^{-4} m^2/sec) *(Kumarana, 2011)*, whereas the diffusion coefficient of the large molecules ($\approx 3.7 \times 10^{-10}$ m diameter) such as nitrogen and oxygen is found to be ten times less than the diffusion coefficient of small molecules. The arsenic hydride molecule shape is reported to be a trigonal pyramidal *(AISBL, 2011)*; however, it is approximated in this study with a sphere geometry having a diameter (3.5×10^{-10} m) which is in the range of large molecules diameter. Thus , the diffusion coefficient of the arsenic hydride has been assumed equal to (1.81×10^{-5} m^2/sec) which is the same value of nitrogen and oxygen. On the other hand, a value of (1.132×10^{-4} m^2/sec) has been considered applicable for the hydrogen gas diffusion in a bulk of helium gas.

11.3 Principles of the central composite rotatable design

In practice, the experimental planning and the data modelling has been done with a lot of success in several kinds of researches, shown in literature, based on the central composite design. The concept is to code the parameters (factors) that dominate the system performance, and it is always necessary to select sensible physical values for each of the effective factors. First important assumption is that the central point for each factor is equal to zero and the design is symmetric around the central point. The following figure illustrates the components of central composite design for a system composed of three factors.

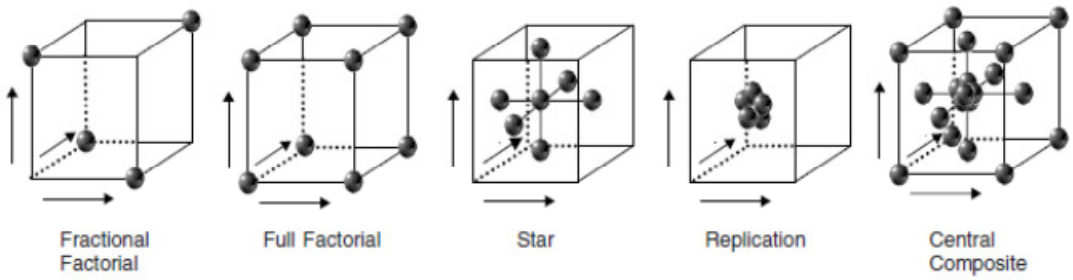

Figure 11-1 Elements of three factors central composite design *(Brereton, 2003)*

The simplest design for a system composed of three factors is based on a fractional factorial, in which four experiments are required to conceive the three linear terms and the intercept; however, no estimations for the interactions or the squared terms could be provided. Extending the number of experiments into eight converts the design into a full factorial and provides estimation for all interaction terms. In the full factorial design, the intended experiments are placed on the corners of the cube that represents the response space. In order to fit the system data quite well, a star design is required to plan the experiments, in which three levels at least are required for each factor, often denoted by +1, 0 and –1, with level (0) placed in the centre. The star design is relevant to estimate the squared terms; and consists of a centre point in addition to six points each of them is located in the centre of the cube faces. Further replicates (typically five) are required to

estimate the experimental error. These replicates are performed in the centre of the response surface, assuming that same error is repeated throughout the response surface.

In the central composite design, the total number of experiments (N) in the set is estimated by adding (2^k) factorial points (often represented by the corners of the cube) to (2k + 1) star points (often represented by the axial points on or above the faces of the cube plus one in the centre) as well as the specified number of replicate points; where (k) represents the number of factors.

For a system of three variables, the central composite design plan is conducted by performing a full factorial design (8 experiments), a star design (7 experiments) and five replicates, which results in 20 experiments as a total.

The full experimental system could be represented by a quadratic multivariable model combines the single effect of the variables in addition to the effects resulted from the interactions of the variables, as shown in the following equation:

$$Y = B_0x_0 + B_1x_1 + B_2x_2 + B_3x_3 + B_{11}x_1^2 + B_{22}x_2^2 + B_{33}x_3^2 + B_{12}x_1x_2 + B_{13}x_1x_3 + B_{23}x_2x_3 \quad (11\text{-}3)$$

Where; Y is the objective function, B_0 represents the level of response at the origin of the response space, x_0 is a dummy variable which has the value +1 for every observation in the set, B_i represents the linear terms coefficients $\frac{\delta y}{\delta x_i}$, whereas $B_{ii}\ and\ B_{ij}$ represent the coefficients of the quadratic terms $\frac{\delta^2 y}{\delta x_i^2}$ and the cross product terms $\frac{\delta^2 y}{\delta x_i x_j}$ that refers to the interaction effects.

The quadratic terms are important to obtain a maximum or minimum for the response space whereas the interaction terms shows whether the influence of two factors on the response is dependent or not.

Practically, the total number of terms in the resulted polynomial is estimated as follows:

$$No.of\ terms = \frac{(k+1)(k+2)}{2}$$

Another important parameter in the central composite design is the level adopted for each factor. As mentioned previously, -1, 0 and +1 are usually adopted to represent the levels of each factor. Nonetheless, another criterion is adopted in this research which is known as *rotatability*. The rotatable design implies a similar standard error for all points that are at the same distance from the centre of the region; which is so useful for a kind of exploratory work with non advanced knowledge. In order to make the design rotatable, a value of $2^{k/4}$ should be adopted for the levels of each factor. Therefore the levels of each examined factor becomes (-1.414, 0, and +1.414) in a rotatable central composite design. It is well known that increasing the levels of the factor in the examined system would result in a higher fitting accuracy and low error of estimate from the produced model, which is essential for statistical analysis. Therefore the author adopted five levels to implement the rotatable design throughout this research. Hence, the rotatable plans are generated as shown in the following table:

Table 11-1 Plans according to the central composite rotatable design

No. of variables	No. of experiments	Level 1	Level 2	Level 3	Level 4	Level 5
2	13	-1.414	-1	0	+1	+1.414
3	20	-1.682	-1	0	+1	+1.682
4	31	-2	-1	0	+1	+2

The estimation of the generated model coefficients has been achieved through a multi variable regression analysis. The algorithms shown below were applied to conduct a multi variable regression analysis for systems composed of two, three and four variables *(Cochran and Cox, 1992).*

- System of two variables

$$\left.\begin{aligned} B_0 &= 0.2(0Y) - 0.1\sum(iiY) \\ B_i &= 0.125(iY) \\ B_{ii} &= 0.125(iiY) + 0.01875\sum(iiY) - 0.1(0Y) \\ B_{ij} &= 0.25(ijY) \end{aligned}\right\} \quad (11\text{-}4)$$

- System of three variables

$$\left.\begin{aligned} B_0 &= 0.166338(0Y) - 0.056791\sum(iiY) \\ B_i &= 0.073224(iY) \\ B_{ii} &= 0.0625(iiY) + 0.006889\sum(iiY) - 0.056791(0Y) \\ B_{ij} &= 0.125(ijY) \end{aligned}\right\} \quad (11\text{-}5)$$

- System of four variables

$$\left.\begin{aligned} B_0 &= 0.142857(0Y) - 0.035714\sum(iiY) \\ B_i &= 0.041667(iY) \\ B_{ii} &= 0.031250(iiY) + 0.003720\sum(iiY) - 0.035714(0Y) \\ B_{ij} &= 0.0625(ijY) \end{aligned}\right\} \quad (11\text{-}6)$$

The standard error of the coefficients for a system of four variables is calculated as follows:

$$\left.\begin{aligned} Standard\ error\ of\ (B_i) &= 0.204\ (SES) \\ Standard\ error\ of (B_{ii}) &= 0.185\ (SES) \\ Standard\ error\ of \left(B_{ij}\right) &= 0.250\ (SES) \end{aligned}\right\} \quad (11\text{-}7)$$

Where;

SES = Standard error of the experimental set

$$SES = \frac{S}{\sqrt{N}} \quad (11\text{-}8)$$

S = Standard deviation

N = number of experiments = 13, 20, and 31 for systems composed of two, three, and four variables respectively

The average absolute error of the empirical model is estimated from the following formula:

$$Average\ absolute\ error\ (AAE) = \frac{\sum ABS\ \frac{(Y_{obs} - Y_{calc})\ x\ 100}{Y_{obs}}}{N} \qquad (11\text{-}9)$$

On the other hand, the coefficient of determination (R^2) which is used to assess the accuracy of the linear regression equation has been estimated as follows:

$$R^2 = 1 - \frac{SSE}{SS_{yy}} \qquad (11\text{-}10)$$

SS_{yy} measures the deviations of the observations from their mean, whereas *SSE* measures the deviations of the observations from their predicted value:

$$Sum\ of\ squares\ of\ the\ model = SS_{yy} = \sum_i (y_i - \bar{y})^2$$

$$Sum\ of\ squares\ of\ the\ error = SSE = \sum_i (y_i - \hat{y}_i)^2$$

As a general guideline, the higher the R^2 is, the more useful the model.

11.4 Constrained optimization algorithm

In order to maximize the objective function (Y), a minimization of the objective function (-Y) is performed. The resulting point where the minimum of (-Y) occurs is also representing the point where the maximum of (Y) occurs. The general description of the constrained optimization problem is shown as follows:

Maximize f(x)

Subject to: $g_i(x) = c_i$ (for i = 1 to n) Equality constraints

$h_j(x) \leq d_i$ (for j = 1 to m) Inequality constraints

Where; x is a vector residing in a n-dimensional space; f(x) is the objective function

The bound limits of the variables are shown as follows:

- System of two variables : $(x_1 \; to \; x_2)$ were applied between -1.414 and +1.414
- System of three variables: $(x_1 \; to \; x_3)$ were applied between -1.682 and +1.682
- System of four variables: $(x_1 \; to \; x_4)$ were applied between -2 and +2.

The algorithm is applied in Matlab as shown by the following code (e.g. for a system of two variables):

M. files:

```
function f = objfun11(x)
f=B0+B1*x(1)+B2*x(2)+B11*x(1)^2+B22*x(2)^2-B12*x(1)*x(2);
function[c,ceq]=confun11(x)
% Nonlinear inequality constraints
c=(x(1)^2+x(2)^2)^0.5;
% Nonlinear equality constraints
ceq=[];
```

Matlab code:

```
x0=[-1.414  -1.414];
options=optimset('LargeScale','off','Display','iter');
[x,fval,exitflag,output]=fmincon(@objfun11,x0,[],[],[],[],[
],[],@confun11,options);
```

Solution:

```
x (press enter to see x values)
fval (press enter to see the calculated objective function
for the optimized (x) values)
```

11.5 Ridge analysis technique

Principally, the ridge analysis technique is based on calculating the distance from the centre of the response space, defined to be the ridge value (R_v), which can give an insight on the variables response in the tested system. The method defines a series of paths outward from the origin ($x_1, x_2, ..., x_n$) = (0,0,....,0) of the factor space *(Draper and Pukelsheim, 2000)*. Let's adopt the following format for the second order fitted equation for a system consists of four variables:

$$Y = B_0x_0 + B_1x_1 + B_2x_2 + B_3x_3 + B_4x_4 + B_{11}x_1^2 + B_{22}x_2^2 + B_{33}x_3^2 + B_{44}x_4^2 + B_{12}x_1x_2 + B_{13}x_1x_3 + B_{14}x_1x_4 + B_{23}x_2x_3 + B_{24}x_2x_4 + B_{34}x_3x_4 \quad (5\text{-}1)$$

The outward paths could be represented by a sphere around the origin, $x = (0,0,0,0)$ of radius R_v. The points of the maximum and minimum responses could be found in the sphere by adopting the following definition for the ridge value for a system of four variables and one response function:

$$R_v^2 = x_1^2 + x_2^2 + x_3^2 + x_4^2 \quad (11\text{-}11)$$

Then,

$$x_4 = \mp\sqrt{R_v^2 - x_1^2 - x_2^2 - x_3^2} \quad (11\text{-}12)$$

Substitute eq. (11-12) in eq. (5-1), differentiate with respect to x_1, x_2 and x_3, equalize the derivatives to zero, then back substitution of x_4 in the resulted derivatives ($\frac{dy}{dx_1}$, $\frac{dy}{dx_2}$, $\frac{dy}{dx_3}$) produces the following formulas:

$$x_1\left[\frac{-(B_4 + B_{14}x_1 + B_{24}x_2 + B_{34}x_3)}{x_4} + 2B_{11} - 2B_{44}\right] + B_{14}x_4 + B_{12}x_2 + B_{13}x_3 = -B_1 \quad (11\text{-}13)$$

$$x_2\left[\frac{-(B_4+B_{14}x_1+B_{24}x_2+B_{34}x_3)}{x_4}+2B_{22}-2B_{44}\right]+B_{24}x_4+B_{12}x_2+B_{23}x_3=-B_2 \quad (11\text{-}14)$$

$$x_3\left[\frac{-(B_4+B_{14}x_1+B_{24}x_2+B_{34}x_3)}{x_4}+2B_{33}-2B_{44}\right]+B_{34}x_4+B_{13}x_1+B_{23}x_2=-B_3 \quad (11\text{-}15)$$

Assume $$\frac{(B_4+B_{14}x_1+B_{24}x_2+B_{34}x_3)}{x_4}=\lambda \quad (11\text{-}16)$$

Substitute λ in equations (11-13) to (11-15) then re-arrange, produces the following forms:

$$x_1(2B_{11}-2B_{44}-\lambda)+B_{12}x_2+B_{13}x_3+B_{14}x_4=-B_1 \quad (5\text{-}2)$$

$$B_{12}x_1+x_2(2B_{22}-2B_{44}-\lambda)+B_{23}x_3+B_{24}x_4=-B_2 \quad (5\text{-}3)$$

$$B_{13}x_1+B_{23}x_2+x_3(2B_{33}-2B_{44}-\lambda)+B_{34}x_4=-B_3 \quad (5\text{-}4)$$

Re-arrange eq. (11-16) gives the following form:

$$B_{14}x_1+B_{24}x_2+B_{34}x_3-\lambda x_4=-B_4 \quad (5\text{-}5)$$

In the solution strategy, the set of equations, (5-2) to (5-5), is solved for a specific value of λ to determine the values of x_1 to x_4 , and then calculating the ridge value from equation (11-11). The first step in the solution should be devoted to identify the working range of λ in the examined system.

11.6 Determination of (F - factor)

The value of (F-factor) is utilised to elucidate the interaction effect of two variables on the objective function in a system of multi-variables. As a general, F-factor has been defined for each individual and interaction coefficients according to the following formula *(Lin et al., 1986)*:

$$F - factor = \frac{mS}{Se} \tag{11-17}$$

Where;

$$mS = \frac{S}{freedom} \tag{11-18}$$

S = Variance, can be represented by the following general description:

$$S = \sum_{i=1}^{n}(y_i - \bar{y})^2 = \sum_{i=1}^{n} y_i^2 - \frac{1}{n}\sum_{i=1}^{n} y_i^2 = \sum_{i=1}^{n} y_i^2 - Cf \tag{11-19}$$

y_i = the response value of such experiment
n = number of experiments in the examined set
Cf = correction factor

$$S_e = S_T - (S_{x1} + S_{x2} + S_{x3} + S_{x4} + S_{x1.x2} + S_{x1.x3} + S_{x1.x4} + S_{x2.x3} + S_{x2.x4} + S_{x3.x4}) \tag{11-20}$$

$$S_T = Variance\ of\ the\ total\ experimental\ set = \sum_{i=1}^{n} y_i^2 - Cf \quad , n = 31 \tag{11-21}$$

The variance of the individual and interaction coefficients, S_{xi} *and* $S_{xi.xj}$, are estimated from the following relations:

- Individual parameter, the variable (1) is taken as an example:

$$S_{x1} = A + B + C + D + E - Cf$$

Where;

$$A_{x1} = \left(\frac{(\sum y_{(-2)})^2}{1}\right)$$

$$B_{x1} = \left(\frac{(\sum y_{(-2)})^2 + (\sum y_{(-1)})^2}{1+8}\right)$$

$$C_{x1} = \left(\frac{(\sum y_{(-2)})^2 + (\sum y_{(-1)})^2 + (\sum y_{(0)})^2}{1+8+13}\right)$$

$$D_{x1} = \left(\frac{(\sum y_{(-2)})^2 + (\sum y_{(-1)})^2 + (\sum y_{(0)})^2 + (\sum y_{(+1)})^2}{1+8+13+8}\right)$$

$$E_{x1} = \left(\frac{(\sum y_{(-2)})^2 + (\sum y_{(-1)})^2 + (\sum y_{(0)})^2 + (\sum y_{(+1)})^2 (\sum y_{(+2)})^2}{1+8+13+8+1}\right)$$

The values shown in the subscript parentheses of the numerator (terms A to E) indicate the treatment levels while the numbers shown in the denominator determines the number of the experiments at that level.

- Interaction parameters

$$S_{x1.x2} = AA + BB + CC - Cf$$

$$AA = \left(\frac{(\sum y_{(-1)})^2_{(variable1)} \times (\sum y_{(-1)})^2_{(variable2)}}{8}\right)$$

$$BB = \left(\frac{\left(\sum y_{(-1)}\right)^2_{(v.1)} \times \left(\sum y_{(-1)}\right)^2_{(v.2)} + \left(\sum y_{(0)}\right)^2_{(v.1)} \times \left(\sum y_{(0)}\right)^2_{(v.2)}}{8 + 13} \right)$$

$$CC = \left(\frac{\left(\sum y_{(-1)}\right)^2_{(v.1)} \times \left(\sum y_{(-1)}\right)^2_{(v.2)} + \left(\sum y_{(0)}\right)^2_{(v.1)} \times \left(\sum y_{(0)}\right)^2_{(v.2)} + \left(\sum y_{(+1)}\right)^2_{(v.1)} \times \left(\sum y_{(+1)}\right)^2_{(v.2)}}{8 + 13 + 8} \right)$$

The degrees of freedom represent the number of coordinates required to describe the system (e.g. specify the position on the response space); hence, for individual and interaction parameters, the degrees of freedom are shown as follows:

$freedom$ = 2 , for individual variable effect

= 4 , for interaction effect of two variables

11.7 The analytical figures of merit

The experimental data quality indicators can be summarized by the following factors:

a) Precision

The precision is defined as "*the degree of mutual agreement among individual measurements as the result of repeated applications under the same condition*" *(Zhang, 2007)*. Precision is normally expressed by either the standard deviation or the relative standard deviation.

For a finite set of data ($n < 30$), the standard deviation is defined as:

$$S = \sqrt{\frac{\sum (x_i - x_a)^2}{n-1}} \qquad (11\text{-}22)$$

Where; $x_a = \text{arithmetic mean} = \frac{\sum x_i}{n}$

The relative standard deviation is defined as follows:

$$\text{RSD} = \frac{S}{x_a} \times 100 \qquad (11\text{-}23)$$

b) Standard calibration plot

The calibration plot illustrates the relation between the instrumental response and the concentration of the examined analyte. It is normally obtained by preparing at least five solutions of known chemical concentrations, injecting them into the tested system and recording the measurements. If a linear dependency present in the system, then a linear regression equation of the form ($y = a\,x + b$) can be used to describe the curve.

Where; *y*: response, *x*: concentration, a: slope (the reciprocal of the calibration sensitivity), and b: intercept (represents the instrument response at $x = 0$).

c) The limits of detection (LOD) and the practical quantification limit (PQL)

LOD is defined as "*the minimum concentration that can be measured and reported with 99% confidence that the analyte concentration is greater than zero*" *(Zhang, 2007)*. Formally, the procedure of LOD determination consists of spiking an analyte free matrix with the concentration of the target analyte equals (3-5) times the estimated LOD. The sample is then measured at a minimum of seven times. The standard deviation (*S*) is calculated from these measurements and the LOD is calculated according to the following formula *(Zhu et al., 2008a, Li et al., 2011, Wu et al., 2011)*:

$$LOD = 3\,\frac{S}{m} \qquad (11\text{-}24)$$

Where; m = the slope of the calibration plot

PQL is defined as "*the lowest concentration that can be reliably achieved within specified limits of precision and accuracy during routine operating condition*" and is normally selected to be (2 to 10) times LOD value. Thus, PQL value in reality represents the lowest point in the calibration plot.

11.8 Operational code for the microcontroller (Arduino-Mega)

The following code has been uploaded to the microcontroller to control the equipments (pumps and solenoid valves) when running the automated mode for the quantitative determination of inorganic mercury. The language used is a writing – based language similar to C++ with some simplifications and modifications according to the operational software requirements.

The timing shown in the code shows the optimal value, which is applicable for most of the examined elements.

```
int solenoid1 = 1;
int pump1 = 2;
int solenoid2 = 3;
int light = 4;
void setup() {
  pinMode(solenoid1,
OUTPUT);
  pinMode(pump1,
OUTPUT);
  pinMode(solenoid2,
OUTPUT);
  pinMode(light,
OUTPUT);
}
void loop() {
   analogWrite(1,255);
   delay(4000);
   analogWrite(1, 0);
  delay(3000);
// repeat on/off for 3 times
  analogWrite(1,255);
   analogWrite(2,255);
   delay(4000);
   analogWrite(1, 0);
  delay(3000);
  analogWrite(1,255);
  delay(4000);
   analogWrite(1, 0);
  delay(3000);
// repeat on/off for 17 times
   analogWrite(2,0);
   analogWrite(4,255);
  analogWrite(1,255);
   delay(4000);
   analogWrite(1, 0);
  delay(3000);
  analogWrite(1,255);
   delay(4000);
   analogWrite(1, 0);
  delay(3000);
  analogWrite(4, 0);
   analogWrite(3,255);
   analogWrite(1,255);
  delay(4000);
   analogWrite(1, 0);
  delay(3000);
// repeat on/off for 9 times
  analogWrite(3, 0);
 while(1) { }// stopping the
pump completely
}
```

11.9 Principal component analysis (PCA) technique

PCA is a multivariate data analysis technique which is applied abundantly in different types of analysis in order to extract the required information from the data set. In practice, PCA can identify patterns in data and express the similarities and differences in such a data set. By applying the technique, the data set can be reduced into lower dimension which reveal a simple structure and a clear way to obtain the required interpretations *(Brereton, 2003)*. Practically, PCA analysis is based on calculating the covariance matrix of a data set, then estimating the eigenvalues and the eigenvectors of the covariance matrix. In conclusion from these calculations, the estimated eigenvector with the highest eigenvalue is considered to be the principal component of the data set *(Smith, 2002)*. The procedures of PCA analysis can be summarized for two dimensions (x,y) data set as follows:

- Subtract the mean from each of the data dimensions in order to produce a data set with a mean equal zero.
- Calculate the covariance matrix; for a two dimensions data set, the covariance matrix is 2×2 as shown below:

$$C = \begin{pmatrix} cov(x,x) & cov\,(x,y) \\ cov(y,x) & cov(y,y) \end{pmatrix}$$

Where;

$$cov(x,y) = \frac{\sum_{i=1}^{n}(x_i - x_m)(y_i - y_m)}{(n-1)} \qquad (11\text{-}25)$$

x_m , y_m : represents the mean of the data dimension
n : represents the number of points in the data set

- Calculate the eigenvectors and the eigenvalues of the covariance matrix, where the vector (x) is an eigenvector of the matrix (C) with an eigen value (λ) provided that the following relation applies:

$$C\,x = \lambda\,x \qquad (11\text{-}26)$$

For a two dimension data set, the result could be represented in **Figure (11-2)** in which two diagonal lines perpendicular to each other provides the information about the patterns in the data and characterize the data. The solid line represents an eigenvector goes through the middle of the points and indicates how the data set is related along the line whereas the dotted line represents the second eigenvector which shows less important pattern in the data. Practically, the solid line is considered to be the principal component which gains the highest eigenvalue compared with the other eigenvector (dotted line).

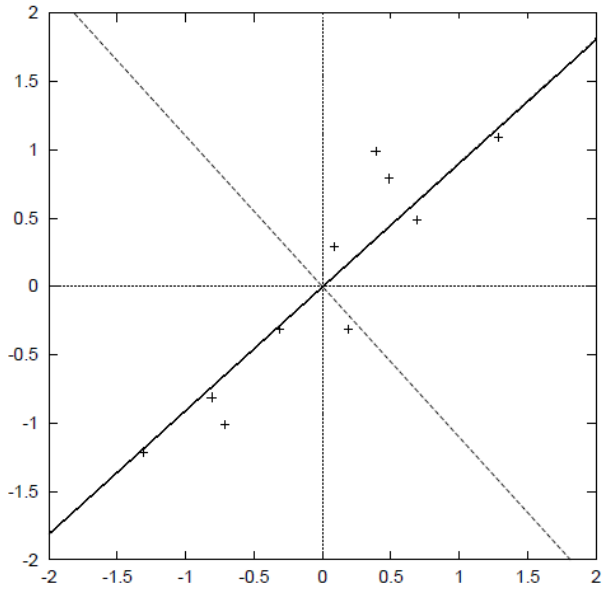

Figure 11-2 a plot shows the mean subtracted data (+) as well as two diagonal lines represent the calculated eigenvectors for a two dimension covariance matrix *(Smith, 2002)*

In order to achieve the full PCA analysis, the significance of the components in the covariance matrix is normally identified according to the values of eigenvalues that estimated for each of the eigenvectors. For instance, if the original data set contains (n) dimensions, then (n) eigenvectors and eigenvalues could be estimated for the set. Some of the components could be neglected because of less importance, and then the final data set will be converted into (p) dimensions which represent the most significant components in the set.

- The final step of PCA analysis is to form the feature vector and then deriving the new data set.

Practically, the feature vector could be formed by adopting some components in the set or using only the first component as the most important in the set. Upon deciding the required feature vector, the transpose is taken for it and multiplied by the transpose of the mean subtracted original data (+) to get the final new version of the data set. The new data set become in terms of the two selected eigenvectors instead of the (x,y) form.

In the final result of the analysis, the data are transformed into a form showing the pattern between them; i.e. the values of the data points exactly identifies where the data from the trend line.

In this research, PCA analysis has been utilized to characterize each of the examined analytes from the applied derivatization conditions, and accordingly the optimal experimentation conditions that applied for all analytes are decided.

The calculations are conducted by using the Matlab software, in which the distribution of the analytes according to the significant component is produced in a graph form. On the other hand, the percentage variance of the components is calculated to identify the significance of each principal component.

The following code is applied in Matlab for PCA analysis, in which (D) represents the data matrix:

```
load D
 stdr = std(D);
sr = D./repmat(stdr,9,1);
[coefs,scores,variances,t2] = princomp(sr);
c3 = coefs(:,1:2)
I = c3'*c3
plot(scores(:,1),scores(:,2),'+')
xlabel('1st Principal Component')
ylabel('2nd Principal Component')
grid on
axis([-4 10 -0.7 0.7])
gname
variances
percent_explained=
100*variances/sum(variances)
pareto(percent_explained)
xlabel('Principal Component')
ylabel('Variance Explained (%)')
[st2, index] = sort(t2,'descend'); % Sort in descending order.
extreme = index(1)
biplot(coefs(:,1:2), 'scores',scores(:,1:2),...
'varlabels',categories);
axis([-.26 1 -.51 .51]);
grid on
```

11.10 Protocols for artificial samples preparation and COD/BOD_5 evaluation in real wastewater sample

a) Preparation of organic and biological water samples

Two kinds of samples, biological and organic are prepared and treated by using the DBD plasma treatment scheme described in chapter seven. It should be mentioned that the *E. coli* experiments were assisted by a group member of the Engineering and Physical Sciences Research Council (EPSRC). The biological samples are prepared from (bacteria – *E. coli*) while three organic compounds (isopropyl-alcohol, phenol and acetic acid) are used for organic samples preparation, as follows:

- *E. coli* samples

All safety issues were taken into consideration when applying the full set of experiments in this part of work. The effect of the treatment on the viability of *E. coli* is assessed in this study using two methods, 1) by monitoring the lag in the batch growth curve during culturing treated cells in rich medium (Luria broth) and 2) by viable plate count technique.

1) Monitoring the growth of E. coli:

Escherichia coli K-12 MG1655 has been used in these experiments. *E. coli* was grown on LB agar medium (BPE1425, Fisher Scientific, UK; tryptone 10 g/L, yeast extract 5 g/L, sodium chloride 10 g/L, agar 15 g/L) from glycerol stocks (20% glycerol) stored in -80°C. The cells were transferred from LB agar to 5 ml LB broth (BPE1426, Fisher Scientific, UK; tryptone 10 g/L, yeast extract 5 g/L, sodium chloride 10 g/L) and were grown for 16 hours at 37°C with aeration (orbital shaking at 200 rpm) for use as starter culture. The cells are diluted in fresh LB broth to the required concentrations measured as optical density at 595 nm (OD_{595}). The diluted cell suspensions are treated for different times in the annular DBD atomizer. The treated cells are incubated at 37°C and the increase in the optical density is measured at 595 nm every 30 minutes for 24 hours using a Tecan multi-well plate reader (Genios, UK). The growth curve is obtained as a plot of OD_{595} against time. Un-inoculated LB broth and untreated LB broth containing *E. coli* were set up as controls in the experiment. The results are reported as an average and standard deviation of OD_{595} of cultures setup in 8 separate wells in a 96-well plate

(TKT-180-070U, Fisher Scientific, UK) after a single round of treatment. The viability of cells after treatment is interpreted as being inversely proportional to the length of the lag phase in the growth curve of treated cells when compared to that of the untreated controls.

2) *Viable plate counts*:

Starter cultures of *E. coli* were grown in 5 ml of LB medium for 16 hours at 37°C. After incubation, the cells are harvested by centrifugation at 5000 xg for 10 minutes. The supernatant containing spent culture medium was discarded and the cells were washed and re-suspended in 5 ml sterile distilled water. The OD_{595} of the cell suspension is measured and the starter culture is diluted to 0.5 OD_{595}. The diluted cell suspensions were treated for different times in the annular DBD atomizer. An untreated control was setup in the experiment. The controls and the samples were serially diluted (dilution factor of untreated control 10^6; dilution factor of treated samples 10^4) and plated on LB agar plates. The dilution factors differed between the untreated control and the treated samples to account for the potential reduction in the number of viable cells in the sample. The agar plates were incubated overnight at 37°C. The resulting colonies were counted and adjusted with the appropriate dilution factors to obtain the number of viable cells in the samples and the untreated control.

- organic samples

Three organic compounds were used to prepare artificial samples through a dilution with distilled water: acetic acid concentrate (CH_3COOH, 99.8% - from BDH), liquefied Phenol (≥89.0% from Sigma Aldrich), and isopropyl alcohol (HPLC grade $(CH_3)_2$ CHOH from Fisher scientific). The applied concentrations were kept in the miscibility range for the case of phenol (8.3 gm per 100 ml water) whereas higher ranges used for isopropyl alcohol and acetic acid as they are miscible with water.

b) COD and BOD_5 evaluation

The determination of the chemical oxygen demand (COD) and the five days biological oxygen demands (BOD_5) was applied by using reagents from (Hach Lange united for water quality - UK). The concept behind the COD determination is that the oxidizable substances react with sulphuric acid – potassium dichromate solution in the presence of

silver sulphate as a catalyst. The chloride is masked by mercury sulphate whereas the colour of Cr^{3+} is evaluated (appeared to be dark orange). In the COD determination procedures, a total of two cuvettes of the reagent (LCK 014, range 1 – 10 g/L) used; one cuvette for the sample before and after plasma treatment. A 0.5 ml of well mixed digested sludge samples before and after treatment (CS1 and CS2) were added to the sample cuvettes and mixed, then the cuvettes were put in a thermostat heater set at 148 ^{o}C for 2 hours and left to cool to the room temperature. The spectrometry device (DR 2800, Hach Lange) was used for measurement, in which the sample cuvettes were put in the device and the COD determined according to the measured absorbance and appeared on the device LCD in g/L. It is worth noting that the device automatically identifies the type of the measurement required according to the cuvette bar code.

The BOD_5 test measures the dissolved oxygen which is analysed in an alkaline solution with a pyrocatechol derivative in the presence of Fe^{2+}, under which conditions a dark red dye is formed. In the BOD_5 determination, three cuvettes of the reagent (LCK 555, range 100 – 1650 mg/L) used, in which two sample cuvettes applied for the sample before and after plasma treatment whereas the third one filled with distilled water and used as a reference for the device calibration. A 0.4 ml of the sample (well mixed digested sludge), before and after plasma treatment was diluted by using 2.8 ml distilled water to prepare the diluted samples (DB1 and DB2). A 0.5 ml of DB1 and DB2 was put in the sample cuvette which was then filled to the brim with distilled water in order to release all air bubbles. The prepared samples closed and checked to ensure no air bubbles left inside, then kept for five days in darkness at 20 ^{o}C. After five days, tablets of the reagent (Dosi Cap Zip, supplied with each sample cuvette) added through a suitable funnel to the cuvette and mixed with the liquid contents for three minutes by shaking the cuvette. Afterwards, the BOD_5 evaluated through the spectrometry device (DR 2800) which appears on the device LCD in mg/L.

11.11 Application of liquid nitrogen cold trap for hydrogen stream purification

The full details of this work are described in *(Abdul-Majeed et al., 2012)*. A part of this work has been undertaken in collaboration with other committee, *(Serdaroglu, 2011)*, to investigate the feasibility of using a liquid nitrogen cold trap (LNCT) for the removal of water vapour and other possible residues, which accompanying the generation of hydrogen gas from the catalytic decomposition of sodium borohydride ($NaBH_4$). The target application is mobile fuel cells based on the hydrogen production from storage in chemical hydrides.

It is hypothesized in this work that a liquid nitrogen cold trap is able to increase the potential of the hydroborate system for fuel cell applications. The LNCT is aimed to be used as a one step purification method with less cost and space requirements instead of applying the conventional multiple stages purification technique (e.g. chilled water heat exchanger – two stage gas liquid separation – dryer – filter). This approach could eliminate the requirements for additional equipments and hence space; it is also capable of increasing the overall system efficiency by decreasing the total energy consumption and cost.

A simple hydrogen generation system from $NaBH_4$ solution hydrolysis on a catalyst in a packed bed column was to meet the targets of the project. It is planned to produce the hydrogen in controlled amounts. Therefore, apparatus choice and design are based on a small-scaled study as a first try.

The experimental setup used for the undertaken study is illustrated in **Figure (11-3)**.

A glass tube (28 mm length and 10 mm ID) used to reside the catalyst in order to act as a packed adsorption bed. A peristaltic pump with a calibrated feed rate of 1.15 ml/min (Williamson Manufacturing Company – UK) has been used to feed $NaBH_4$ solution from the fuel container. The generated hydrogen and the accompanying water vapour and other residues are then directed into a gas-liquid separator made of 50 ml glass bottle provided with a plastic lid and two glass tubes served as an inlet and outlet. The separated hydrogen and other vapour species are forwarded into a U-tube liquid nitrogen cold trap which is used to capture the water vapour as well as other residues

through an adsorbing media (Chromosorb G/AW-DMCS 45-60 mesh, purchased from Sigma Aldrich).

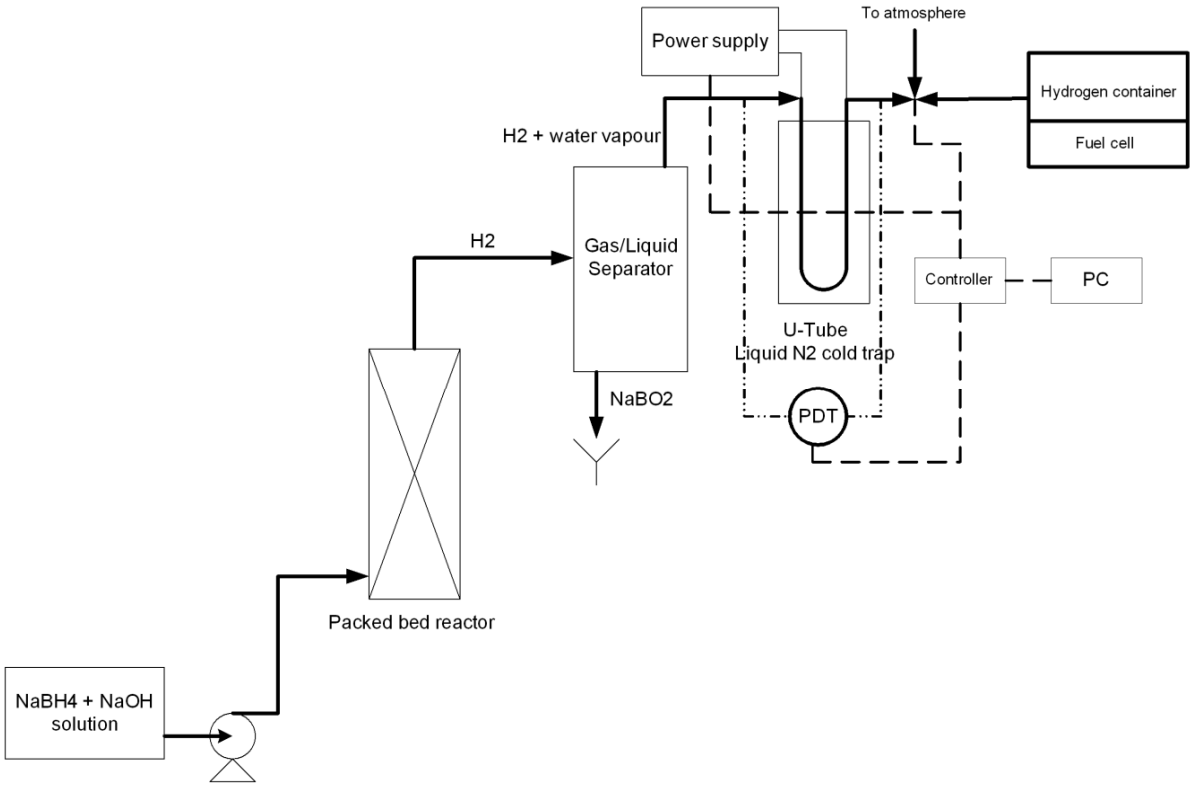

Figure 11-3 a schematic diagram illustrates the system used to test the feasibility of LNCT for hydrogen stream purification

A borosilicate U-tube (60 cm length and 6 mm ID) passed through a lid made of PTFE is immersed in a Styrofoam container (3 L volume) and used to reside the liquid nitrogen. The evaporated nitrogen has been released from LNCT through a tube open to the atmosphere; nonetheless, the lid is also provided with a pressure safety valve set at 0.5 barg and a pressure gauge for safety reasons. The U-tube is wrapped with an electric rope heater which is applied to heat the tube in order to release the condensed residues.

The whole system was designed, fabricated and operated through (Arduino-mega) microcontroller run by a PC software. The idea is to control the rope heater and the three way valve, shown in **Figure (11-3)**, in order to keep a free path for passing the hydrogen out of the cold trap. Accordingly, the electric rope is supplied with pulses of 230 V AC in a sequence form according to the requirements.

As soon as the cold trap is being clogged with the condensed/solidified residues (this should be indicated by a differential pressure transducer), the electric field should be

supplied to the rope heater. At the same moment, the three way valve should close the path to the hydrogen container and release the stream coming from the cold trap into the atmosphere. The targeted fuel cell is planned to supply from the hydrogen container attached to it during the regeneration step.

Two catalysts (cobalt pieces and cobalt boride powder) are investigated for the production of hydrogen from the aqueous solution of $NaBH_4$ in a small scale packed bed reaction column. The results have shown a concentration of 10 wt % $NaBH_4$ stabilized with 1 wt % NaOH is proper to produce 17.7 and 0.69 (ml H_2/min/g catalyst) upon using cobalt boride and cobalt pieces, achieving conversion ratios of 98.48% and 15.06% respectively. The results also show that a high activity and fast exhaustion period recorded for the cobalt boride compared with cobalt pieces whereas a stable performance, better durability and easy recovery are observed for the cobalt pieces. Although low quantity of water vapour has accompanied the hydrogen generated from the current reaction system, the application of LNCT for H_2 purification has proved useful and leads to a reduction in the content of water vapour and consequently increased the concentration of hydrogen in the outlet stream up to 99.71%, as shown in **Figure (11-4)**.

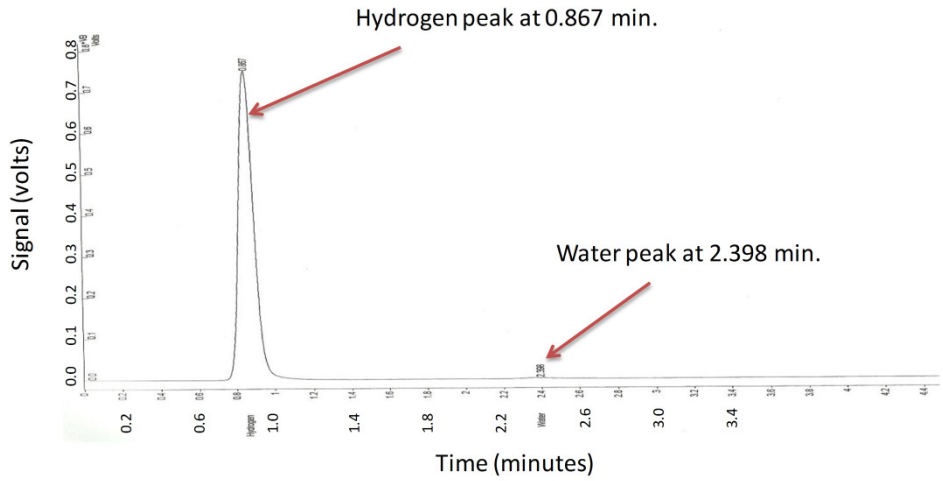

Figure 11-4 a GC chromatogram for a sample collected after passing the LNCT.

Because of limited water vapour generated in the system, the performance of the cold trap could not be evaluated accurately. Therefore an acidic decomposition of $NaBH_4$ is conducted by using the reaction system described in **Figure (11-5)**, in which higher elaboration of water vapour and alkaline mist is expected. In these experiments, an HCl

solution (1.5 M) and $NaBH_4$ solution (2% m/v stabilized by using 0.5% m/v NaOH) are used.

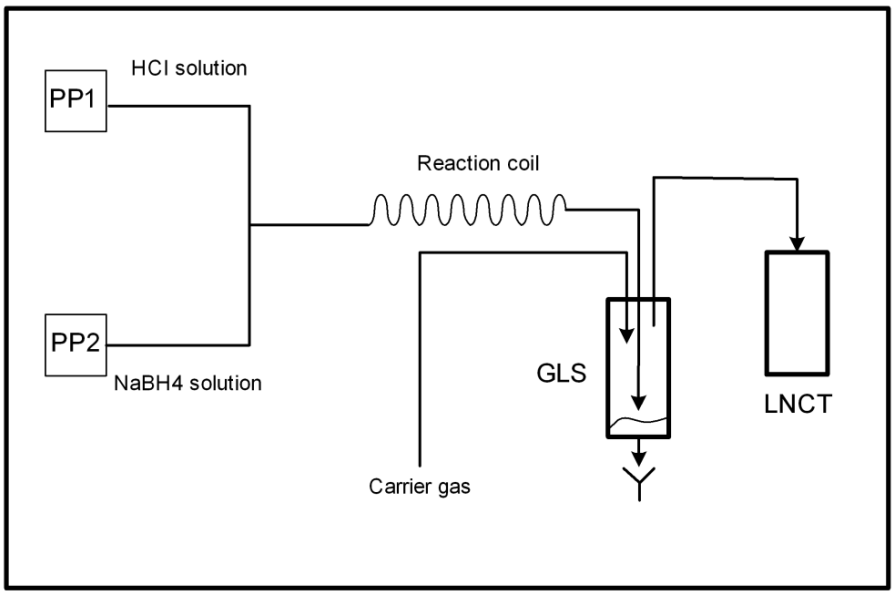

Figure 11-5 a schematic diagram illustrates the reaction system used for the acidic decomposition of $NaBH_4$.

The mixed solutions through a tee junction are directed into a helical reaction coil (1 m length, 2.5 mm ID silicon tube) and then into a gas/liquid separator (GLS). The hydrogen gas stream, accompanied by traces of water vapour and alkaline mist has been carried with aid of carrier gas (helium) into LNCT through a (20 cm length, 2.5 mm ID silicon tube). The GC analysis conducted for the stream after LNCT have shown a reduction in the water content by more than 5% as illustrated in **Table (11-2)**, which emphasizes the advantageous effect of LNCT.

Table 11-2 comparison between the contents of the samples collected before and after LNCT from the acidic decomposition of $NaBH_4$.

	Before LNCT	**After LNCT**
Hydrogen	93.12 %	98.76 %
Water vapour	6.88 %	1.24 %

11.12 Design details of the GLS-LNCT

The details of the separation stage integrated with a cryogenic trapping (GLS-LNCT) are shown in the following detailed drawings. The two stages are fabricated in one piece of equipment shown in **Figure (11-6)**.

(A)

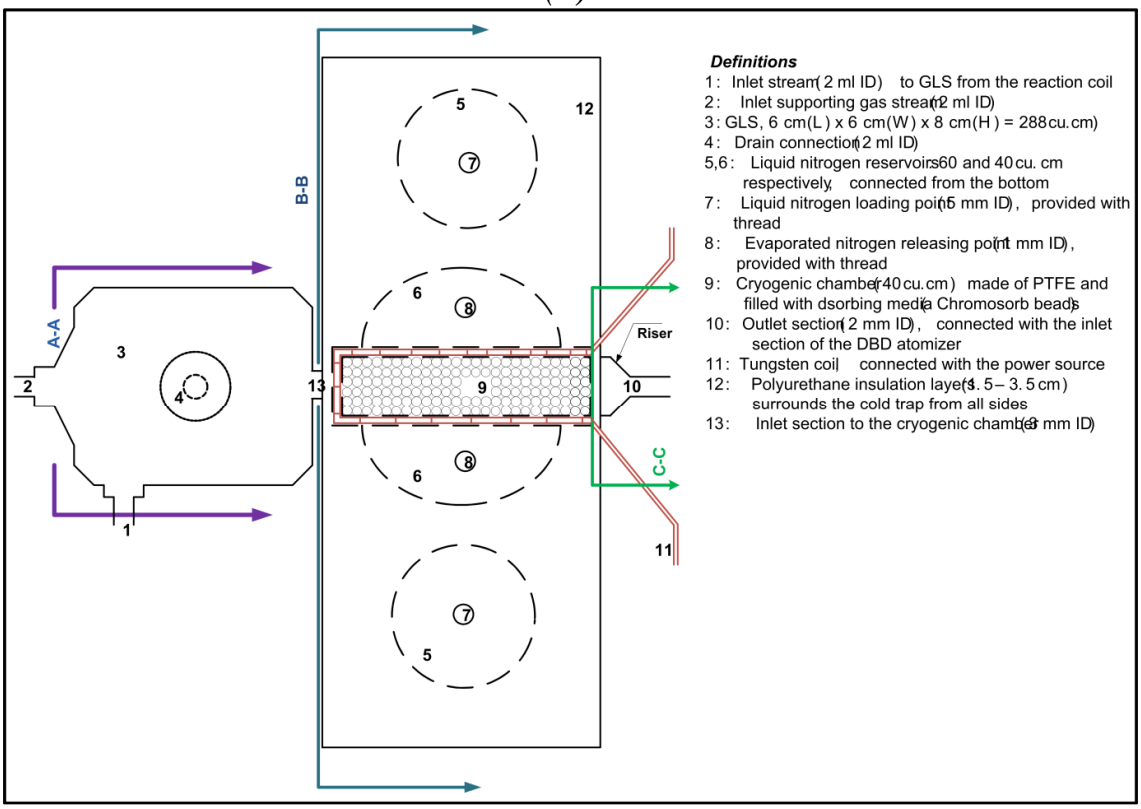

Definitions

1: Inlet stream (2 ml ID) to GLS from the reaction coil
2: Inlet supporting gas stream (2 ml ID)
3: GLS, 6 cm (L) x 6 cm (W) x 8 cm (H) = 288 cu. cm)
4: Drain connection (2 ml ID)
5,6: Liquid nitrogen reservoirs 60 and 40 cu. cm respectively, connected from the bottom
7: Liquid nitrogen loading point (5 mm ID), provided with thread
8: Evaporated nitrogen releasing point (1 mm ID), provided with thread
9: Cryogenic chamber (40 cu. cm) made of PTFE and filled with dsorbing media (Chromosorb beads)
10: Outlet section (2 mm ID), connected with the inlet section of the DBD atomizer
11: Tungsten coil connected with the power source
12: Polyurethane insulation layer (3. 5 – 3. 5 cm) surrounds the cold trap from all sides
13: Inlet section to the cryogenic chamber (3 mm ID)

(B)

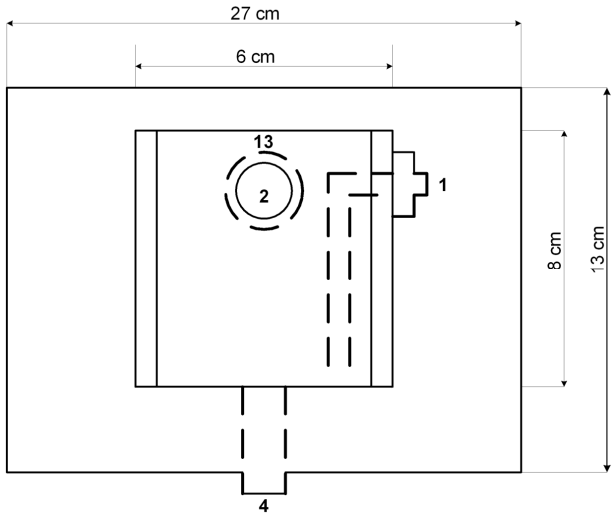

Section A-A

(C)

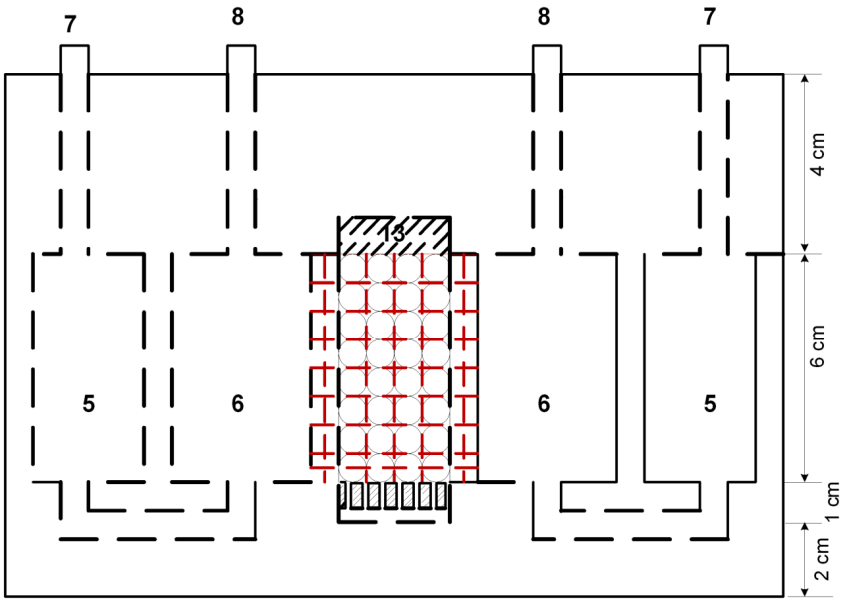

Section B-B

(D)

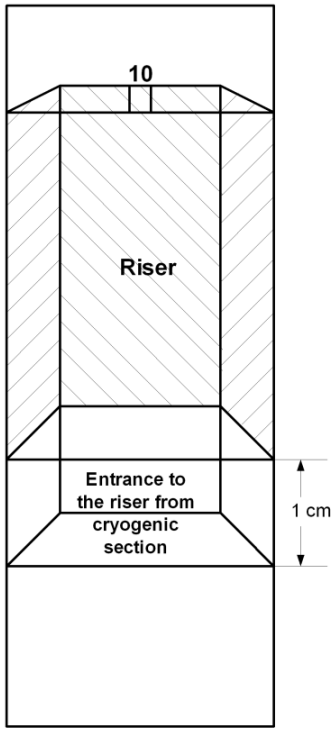

Section C -C

Figure 11-6 the detailed drawings show the separation stage integrated with cryogenic trapping (not to scale);
(A) top view, **(B)** section A-A, **(C)** section B-B, **(D)** section C-C

The walls of the gas-liquid separator were constructed from a plastic sheet, 6 mm thickness, through which many holes and threads were used to connect to outside tubes. The cryogenic trapping stage has been totally constructed inside high quality insulation material (polyurethane of low thermal conductivity < 0.4 W/m/^{o}C). The polyurethane foam has been injected inside a rectangular mould, where a block was produced after drying. The polyurethane block was machined by using CNC drilling device to produce the reservoirs and the channels, while plastic sheets, 10 mm thickness, were used to form the outside covers. The full combination was fastened by using screws.

The liquid nitrogen is loaded to the cryogenic section through a special funnel from one opening, while the other opening is left open to release the air and vapours. The release of the evaporated nitrogen is conducted through a pressure safety valve, set at 0.5 barg, connected to the cryogenic section. It should be mentioned that a tiny mesh steel membrane has been put at the base of the cryogenic section. The membrane allows only the gases to pass out from the beneath section through (≈0.02 mm) holes to the riser section, as illustrated in **Figure (11-6/B&C)**.

A picture illustrates the interior parts of GLS-LNCT is shown in **Figure (11-7)**.

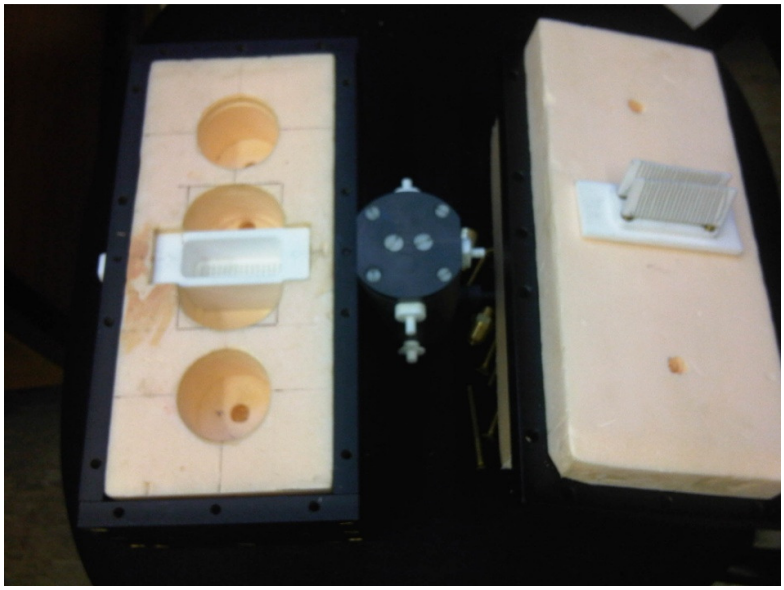

Figure 11-7 a picture shows the interior sections of the fabricated integrated separation stage with cryogenic trapping, named as (GLS-LNCT)

11.13 Other achievements

a) Publications:

The author published four journal articles, cited in the references section, and a conference paper entitled "Application of cascade dielectric barrier discharge plasma atomizers for wastewater" in the proceedings of the 6th International Conference on Environmental Science and Technology (25th – 29th June, 2012 / Houston –USA). Moreover, the author has submitted a journal article entitled "Computational modelling of the volatile hydride fragmentation in a dielectric barrier discharge atomizer" which is currently under consideration. Furthermore, the author has collaborated as co-author in a work entitled "Hydrogen production from water vapour plasmolysis using DBD-corona hybrid reactor" which is currently under consideration.

b) Conferences:

1. European winter conference on plasma spectrochemistry, Zaragoza, Spain 2011

Poster presentation title: Application of a miniaturized DBD plasma chip for mercury detection in water samples.

2. Spectroscopy – Detective in Science, Rostock, Germany 2011

Oral presentation title: Study the atomization of the generated hydride species in a dielectric barrier discharge atomizer. (The author won a conference scholarship prize valued Euros 400)

3. The 6th International Conference on Environmental Science and Technology (25 – 29 June) 2012 / Houston –USA

Oral presentation title: Application of cascade dielectric barrier discharge plasma atomizers for wastewater.

c) Other activities

- Served as a referee for a scientific article upon invitation from the Journal of Plasma Science and Technology (November 2011).
- Served as a research mentor for the following research projects (master dissertations):

1) Water quality sensor development: online, continuous heavy metals detection, 2010.

2) Study the hydrogen generation from sodium borohydride system using a liquid nitrogen cold trap as a separation step, 2011.